Microstructure-Sensitive Investigation of Plasticity and Fatigue of Magnesium Alloys

A Thesis

Submitted to the Faculty

of

Drexel University

By

Kavan Hazeli

in partial fulfillment of the

requirements for the degree

of

Doctor of Philosophy

March 2014

Doctoral Committee

Dr. Antonios Kontsos Chair and Advisor	*P.C. Chou Endowed Assistant Professor in Mechanical Engineering* *Department of Mechanical Engineering & Mechanics, Drexel University*
Dr. Anthony Rollett	*Professor* *Department of Materials Science & Engineering, Carnegie Mellon University*
Dr. Antonios Zavaliangos	*A. W. Grosvenor Professor in Materials Science Engineering* *Department of Materials Science & Engineering, Drexel University*
Dr. Christopher Weinberger	*Assistant professor* *Department of Mechanical Engineering & Mechanics, Drexel University*
Dr. E. Caglan Kumbur	*Assistant professor* *Department of Mechanical Engineering & Mechanics, Drexel University*
Dr. Alan Lau	*Professor* *Department of Mechanical Engineering & Mechanics, Drexel University*

Dedication

To

Farinaz, Kavian, Sima and Shahpour

For

the limitless support and unconditional love

Acknowledgments

Working on PhD was a wonderful and often unexplainable moments of my life. I missed and achieved many valuable things at the same time. On top of everything, it was extremely difficult to be away from my parents and brother; there is no replacement for those moments. PhD is not a journey one can complete on one's own, without a strong network of support. I know I would never have finished without that support.

First and foremost, I would like to thank my advisor Dr. Antonios Kontsos for his understanding and his exemplary support during my PhD. It has been an honor to be his first PhD student. I have been fortunate to have an advisor who gave me the freedom to explore on my own, and at the same time the guidance to recover my mistakes. He oriented me with promptness and extreme care, and he was patient and encouraging in times of new ideas and difficulties. He always listened to my ideas and our discussion often led to key insights. Importantly, he always gave me an opportunity to discuss my ideas in social and scientific events from which I build up a great deal of confidence by identifying my strength and weakness. It is not exaggeration to say that he changed my life profoundly. He, indeed, fulfilled the definition of an excellent advisor, if he did not go beyond.

I must also thank my PhD thesis committee: Dr. Anthony Rollett, Dr. Christopher Wheinberger, Dr. Antonios Zavaliangos, Dr. Caglan Kumbur and Dr. Alan Lau for their constructive comments and discussion during my PhD. I would like to present a special thanks to Dr. Anthony Rollett for introducing me many different aspects of life and science.

With enough reasons, my family without you, I would never have begun such a bold undertaking and would certainly never have had the disposition, strength, and will to finish. Thanks Sima, Shahpour for making who I am. Thanks Kavian for being such a supportive brother. You have been taking care of my parent since I left our home. I would never be able to make up your intense devotion and kindness. Kavian, I am and I will always be the happiest person ever since I have you. One more time, thanks again my dearest family for believing in me, encouraging me in all of my pursuits and your emotional supports to follow my dreams. These dissertation stands as a testament to your unconditional love. I

would also like to present my deepest gratitude to my wife, Farinaz, for standing beside me during the past few years and for her love and patience. You did everything in your power to support me. Farinaz, I wouldn't be who I am today if you were not there.

I am also indebted to my lab mates that I had a pleasure to work with. You have been an invaluable friends and support during these years. You guys made a lot of amazing memories for me. As you were, you will always be, treasured forever in my mind. This is why I would like to see your names in first page of my thesis: Prashanth Abraham, Jefferson Cuadra, Eric Scwartz, Shane Esola, Andrew Ellenberg, Daniel Christie, Satish Rajaram, Rami Carmi, Raghavendra Saralaya, and Michael Cabal.

I have been privileged to get to know many precious friends. Thanks Babak and Bita for the critical role you played in my life. Without you I would not have experienced many things. Rob Yucha, I learned a lot from you about life. You are one of the best people I have ever met and I do everything for our friendship. I would like to thanks Salar Sallahieh, Askan Zardoee and Babak Davoudi for being so nice to my family and I during these years.

This thesis would not be completed with extensive support of Department of Mechanical Engineering and Mechanics (MEM) at Drexel University. MEM not only supported the scientific part of my activities, they also trusted me by giving me an opportunity of conducting many academic and social events where I gained a valuable set of experiences. It is, of course, important to magnify the support of Office Graduate Studies (OGS) directing by D. Lim. Besides the remarkable contribution of OGS on graduate student life, which I benefited as well, I was honored to working with OGS closely by holding responsibility for executing many academic events. Thank you very much OGS. Thanks to Drexel library staff for making continues effort to provide us with rich resources of references, articles and standards.

Thank You
Kavan

Spring 2014
Philadelphia, PA, USA

This page intentionally left blank

List of Figures

Abstract

Microstructure-Sensitive Investigation of Plasticity and Fatigue of Magnesium Alloys

Kavan Hazeli

Research Advisor: Dr. Antonios Kontsos

This dissertation identifies and quantifies the correlation between strain localizations at different scales and both macro- as well as microplasticity of Magnesium (Mg) based alloys. The extension of the work in the case of cyclic mechanical loading further enabled the investigation of reversible and irreversible microstructural processes that are ultimately linked to progressive fatigue damage development. To accomplish these goals, this dissertation presents a systematic experimental mechanics methodology combining multi-scale mechanical testing, *in situ* nondestructive evaluation (NDE) and targeted microstructure quantification. The presented research benefited from the novel integration between mechanical testing and multimodal NDE comprising both full field deformation measurements by using the digital image correlation method and time-continuous recordings of acoustic. Specific contributions of this work include the direct identification of the dominant effect of twinning in early stages of plasticity which is demonstrated in this research to be responsible for macroscopic effects on the monotonic and cyclic plasticity, as well as for microscopic processes that include slip-twin interactions and fatigue crack incubations. Such observations both enabled and were validated by careful texture evolution and grain-scale effects including pronounced intrusions/extrusions on the surface which are demonstrated to be responsible for micro-level strain accumulations that eventually, under cyclic loading conditions, lead to the onset of cracking. Surface morphology changes were found to be attributed to an evolving twinning-detwinning-retwinning activity which operates from early stages of the low cycle fatigue life up until later stages, while it was found to be

associated with progressive damage development. Furthermore, the role of twinning in plasticity and fatigue of Mg alloys was verified using a Continuum Dislocation Dynamics Viscoplastic self-consistent (CDD-VPSC) polycrystal model. The simulation results reveal that the detwinning mechanism is in fact responsible for the anisotropic hardening behavior for various imposed strain amplitudes. Experimental results were further used to modify strain-based modeling approaches of fatigue life estimation. A number of the insights enabled with this research were further verified by performing a mechanical behavior characterization investigation of Mg alloys with Strontium (Sr) additions, which are currently considered for industrial applications. The presented results demonstrate that the major research accomplishments described in this dissertation could improve current manufacturing processes, which further allow extensions and applications of this research in fundamental and applied aspects of plasticity and fatigue of polycrystalline metals.

Contents

Chapter 1

1. Introduction

This dissertation presents results based on recent theoretical and experimental investigation of the nature of plastic deformation during monotonic and cyclic loading of Magnesium (Mg) based alloys. This investigation further focuses on the microstructural effects that lead to heterogeneous deformation, plastic instabilities and the activation of dominant damage mechanisms. First, this study identifies and quantifies the main source of plastic strain heterogeneities and damage nucleation by investigating the local deformation behavior of polycrystalline aggregates at different length-scales. Then, particular attention is given on a possible solution for predicting material behavior as well as indication and development of damage mechanisms under various loading conditions.

1.1 Magnesium Alloys

Magnesium is the fourth most common element on Earth (behind iron, oxygen and silicon), accounting for 13% of the planet's mass and a large fraction of the planet's mantle [1]. Mg is the lightest of all metals [2], having a density of $1.74\,g/cm^3$. It is, therefore, 35% lighter than Aluminum (Al) and over four times lighter than commercial steels $7.86\,g/cm^3$. Due to Mg's high specific strength (also known as strength-to-density ratio) shown in Figure 1 and Table 1, where it is compared to several aluminum alloys and several types of steels [3, 4], Mg is currently the basis material for several commercial alloys that have found successful use in a wide variety of applications. The low density of Mg alloys permits thicker sections to be used in parts, eliminating the need for a large amount of stiffening, simplifying the part and its

manufacturing processes. Moreover, since reducing the weight of vehicles is one of the primary means by which fuel consumption could be lowered, and Mg is well suited for transportation applications.

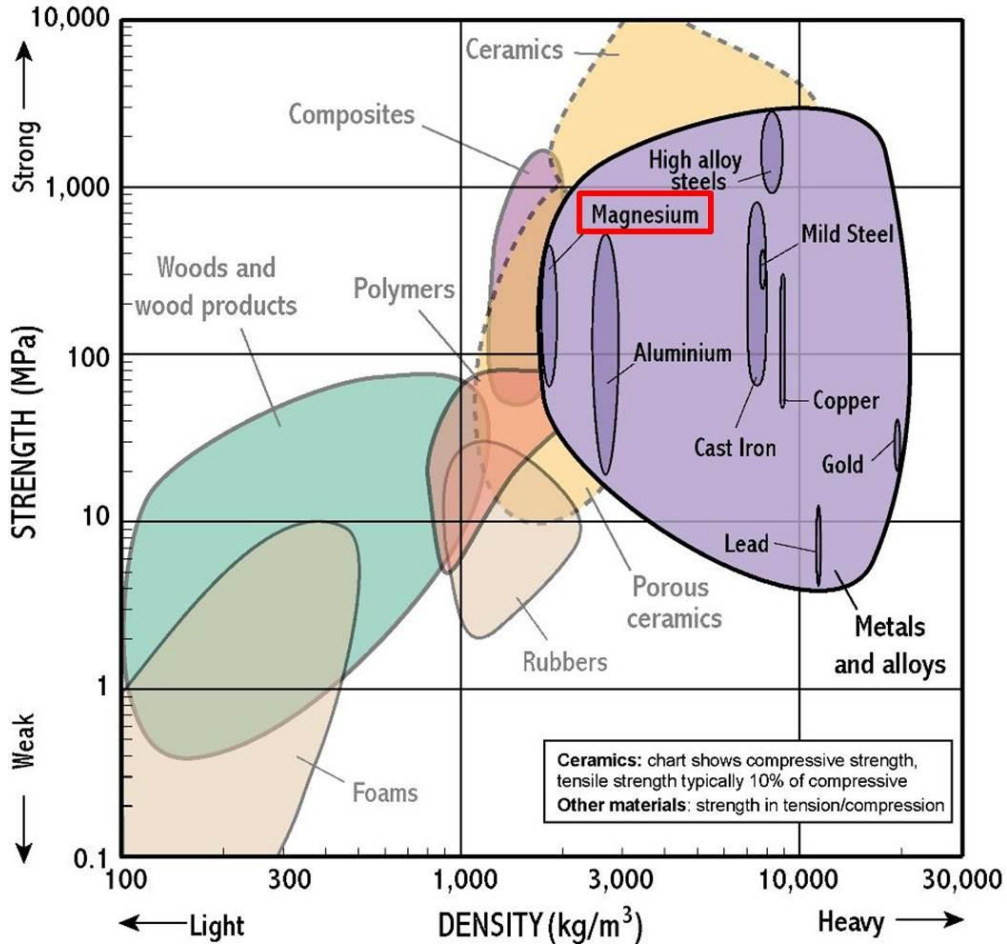

Figure 1 Specific strength-specific stiffness of various materials with emphasize on metallic metals, including Mg.

In addition to the promising mechanical and physical properties reported in Table 1, Magnesium's good noise and vibrational damping properties as well as excellent castability make it a candidate material for aircraft and surface-vehicle frames, panel, brackets, wheels and engine components [5]. For similar reasons, low inertia due to its low density and considerable

damping characteristics, gives Mg a distinct advantageous over other materials in the manufacturing of disk drives. Furthermore, high thermal conductivity and recyclability make Mg alloys a competitive choice over polymer products used in portable device applications [2]. Mg based alloys are also being used to manufacture hand-held devices such as camera and sport goods. Moreover, Mg has been suggested as a potential biodegradable orthopedic material for trauma surgery applications [6]. Orthopedic devices, required for the immobilization and fixation of bone fractures, are conventionally metallic as they need to maintain structural integrity and biocompatibility for the duration of the bone healing period. The elastic modulus of Mg is reported as 45MPa [7] which is very close to the elastic modulus of natural bone. This favorable property of Mg could decrease the incidences of stress shielding reported in literature [6]. Additionally, screws and plates made of Mg alloys could provide stable implant materials that degrade *in vivo*, eliminating the need for a second operation for implant removal [7].

Table 1 Physical and mechanical properties of Magnesium versus Aluminum and steel[8]

Material	**Tensile strength (MPa)**	**Density at 20°C (gr/cm^3)**	**Specific strength (MPa cm3/gr)**
Automotive steel (SPFC440)	*440*	*7.85*	*56.1*
Aluminum (5000 series)	*275*	*2.71*	*101.5*
Magnesium (AZ31)	*260*	*1.78*	*146.1*

Due to good mass production characteristics, a large number of Mg components (automobile, aircraft, housing and electric) are produced by die-casting. However, the better mechanical properties of wrought alloys are essential for high-performance structural applications. Thus, developing wrought Mg products is highly desirable. Compared to cast magnesium alloys,

wrought magnesium alloys could enable further engineering applications, explaining why research and development of high performance wrought Mg alloys is becoming increasingly prevalent. In order to produce wrought Mg alloys, adequate forming operations such as bending, drawing and extrusion are required to yield metal sheets or extruded bars. Contrary to Aluminum alloys, in which texture changes are observed to occur during recrystallization due to strong selective recrystallization mechanisms (depending on alloy composition), in conventional Mg alloys texture forms during mechanical process [9, 10]. The definition of texture and the method to determine texture will be presented in the material characterization section of this dissertation. In fact in Mg alloys a strong basal texture forms during rolling and remains unchanged during recrystallization annealing. This affects subsequent sheet formability, mainly by the related plastic anisotropy of strength, ductility and related phenomena such as yield locus and forming limits.

1.2 Microstructure-sensitive mechanics

Mechanical design of metals can be conducted more precisely when considering directly the polycrystalline microstructure as a continuous design parameter [11]. To achieve this goal, it is crucial to understand the association between microstructural properties and material performance. Microstructures consist of features at length scales from nanometers to several hundred micrometers. Microstructural features usually have complex geometry and varying orientations; thus spatial correlations occur. As a result, fatigue and fracture are complex evolutionary processes dependent on multiscale microstructural evolution [12, 13]. It is noted that in polycrystalline metals, local deformation differs from the globally imposed strain, especially in crystals of lower symmetry such as Hexagonal Close-packed (HCP) crystal [14]. In fact, these local heterogeneities induced by unequal shear stress effects to deformation resistance

as well as microstructure evolution could further cause remarkable changes on the overall mechanical behavior. In this regard, plastic strain localizations in this dissertation are demonstrated to be associated with heterogeneous deformation and they are shown to constitute a necessary condition and a precursor for the nucleation of fatigue cracks [15]. For these reasons, the effect of various microstructure attributes on fatigue life requires quantitative assessment through accurate experimental examination at the grain scale. Here, the main emphasis is placed on a selection of forward-thinking approaches to study the vital microscopic evolution parameters, which influence *plastic deformation* and *fatigue indicator parameters* in Mg alloys. It is noted that in polycrystalline metals, local deformation differs from the globally imposed strain [14]. Such local heterogeneities induced by the microstructure evolution influence the overall mechanical behavior during manufacturing processes such as metal forming. In addition, special attention is paid to the effect of deformation twinning on both heterogeneous strain concentrations at either at grain or twin boundaries during monotonic and cyclic loading. The reported observations provide opportunities to advance in microstructure sensitive design of materials.

1.3 Thesis objective and hypothesis

The objective of this dissertation is to identify and quantify underlying microscopic and crystallographic effects that govern strain heterogeneities and their effect on plasticity and fatigue life of Mg alloys. It is of particular interest to determine microstructure level mechanisms that cause plastic instability and to quantify the resultant local and global mechanical states of stress and strain. This is crucial for establishing linkages between small-scale deformation and constitutive relations of material performance for the macro-scale. In addition, identification of

microscopic-driven mechanisms that results into local decohesion and crack initiation is regarded as an important task in quantitative understanding of fatigue crack initiation.

Deformation mechanism selectivity within polycrystalline aggregate, as well as their spatial correlations between the grains leads to strain gradients. As a consequence of external loading, a broad yet limited range of deformation systems can operate at the grain scale in the case of Mg alloys. Each deformation system can be resolved into a certain components of plastic strain, which need not be similar to other deformation components operating within the same grain. This state of affairs leads to the development of internal stress mismatching, and therefore strain heterogeneity. There are two competing mechanisms through which a material can plastically deform, slip and mechanical twinning. The mechanism that dominates has the greatest resolved shear stress when on the corresponding crystallographic plane. In fact, tension twins frequently obey this rule, known as Schmid's law. Deformation twinning occurs in a broad group of materials to accommodate plastic deformation without the formation of cracks in the grains. Another source of displacement is grain boundary sliding, which consists of a substantially large number of dislocations, yet limited shear orientation. Mechanical twinning generally occurs at low angle grain boundaries, and sometimes occurs even inside grains without any connection to the surrounding grain boundary. Mechanical twinning always supplements dislocation based slip systems, each contributing to plastic shape changes of the grain. However, comparatively fewer degrees of freedom exist in the grain boundaries. This strain mismatch could become the driving force for crack formation [16]. Mechanical twinning creates new grain boundaries within the grain. Fresh grain boundaries due to mechanical twinning play a key role in overall plasticity and fracture by affecting strain hardening and creating another source of crack initiation, respectively. Furthermore, mechanical twinning is a reversible phenomenon; the reverse process

known as detwinning. This means that, mechanical twinning can be disappeared upon reverse loading. This phenomenon can occur even after a large number of loading cycles without permanent localized evidence (for example surface marks such as the one which creates by slip bands). Mechanical twinning involves out of plane strain components that produce considerable surface steps. This means that shear is only permitted in one direction, in contrast to dislocation slip. Detwinning can reduce the previously formed surface steps through the reverse shearing mechanism on the same plane of shear; hence it does not result in another surface feature. The continuous occurrence of twinning-detwinning under cyclic loading results in local exhaustion, which gives rise to the fatigue crack initiation. The experimental evidences of the described microstructure-based phenomena will be presented in chapter 6.

To realize this goal, extensive access to microstructural information is necessary. Therefore, it is vital to exclude unnecessary microstructural features and precisely eliminate grain size disparity effects by effective thermo-mechanical processes. In fact, it is very challenging to monitor microstructure evolution and relate it to the mechanical state of stress while following suggested American Standard Testing Material (ASTM) dimensions. To reduce complexity, the first phase of the study is conducted solely under monotonic loading conditions. When the comprehensive correlation between overall mechanical properties and corresponding underlying microstructure is found, relevant hypotheses are formulated and examined in the case of additional alloying elements, which are common in engineering design. The information obtained from this part can help develop a length scale specific understanding of deformation in polycrystalline aggregates, yielding new insights that inform future mechanical and structural designs, especially in metal forming processes. In addition, such research could be an important step towards investigating material behavior under cyclic loading conditions. In this regard, fatigue life prediction,

microstructural changes as a consequence of reverse loading, surface roughness and finally crack initiation and incubation are explored in this dissertation.

1.4 In situ mechanical properties evaluation

Real time study of micromechanical phenomena, particularly microstructure evolution, is essential for filling the large gap in the mechanistic understanding of material plasticity under different loading paths. In situ nondestructive evaluation of mechanical behavior of materials offers a way to understand the physics and mechanics of solids. The purpose of this section is to introduce the in situ and ex situ methods that were used in this dissertation to investigate microstructure induced plasticity. Acoustic Emission (AE) as a non-destructive approach has been historically used to detect crack initiation and growth during mechanical loading. AE are essentially elastic stress waves, produced by rapid release of energy from localized source within a material under loading. In general, the form of the primitive wave changes during propagation through the medium, and the amplified signal recorded generally by piezoelectric sensor, in the form of voltage versustime, bears little resemblance to the original emission [17]. Recently, many attempts have been made towards determining the AE signature of various deformation and damage processes during straining. The aim of the AE method is to correlate certain empirical parameters of the recorded waveform to characteristics of the material [17]. Furthermore, to obtain real time grain level deformation mechanisms information, other non-destructive experimental diffraction techniques have been proposed, including for example neutron and synchrotron x-ray diffraction. In neutron diffraction, the sample is placed within a neutron beam and the angles at which the neutrons are deflected or scattered by the material are recorded to generate a so-called diffraction pattern, from which structural information can be extracted. Specifically, the evolution of *hkl* diffraction intensities and the development of *hkl*

elastic lattice plane strains in the grains oriented with their $\{hkl\}$ plane normal to the loading direction can be measured [18]. More recently, X-ray diffraction (XRD) has been suggested to measure lattice strains for different families of planes to understand the micromechanical response to a known macroscopic loading. In this connection, high intensity synchrotron x- rays, however, can interrogate samples in transmission to determine crystallographic texture as well as lattice strain [19]. Hence, it is possible for a non-destructive approach to perform local studies within the bulk of the materials.

1.5 Thesis overview

This dissertation is organized in the following manner. ***Chapter 2*** provides essential background on plastic deformation, fatigue parameters and important aspects of crack initiation. ***Chapter 3*** presents the most recent endeavors to develop deeper knowledge of polycrystalline deformation and fatigue criteria in Mg alloys. ***Chapter 4*** describes the effect of twinning on early plasticity and strain localizations in Mg alloys. The significance of deformation twinning on localized heterogeneities and surface morphology is discussed in ***Chapter 5***. ***Chapter 6*** summarizes the key microstructural-sensitive parameters on fatigue life and fatigue crack initiation in Mg alloys. ***Chapter 7*** presents the effect of Strontium (Sr) on plasticity and damping of Mg alloys. ***Chapter 8*** states the conclusion of the current investigation. ***Chapter 9*** describes future works

Chapter 2

Deformation Mechanisms and Material Characterization Methods

2.1. Introduction

This chapter describes the deformation mechanisms of polycrystalline materials with an extensive discussion about the deformation modes in Mg alloys from different perspective. The first part of this chapter shows the required mathematical framework to describe plasticity. In continue, plastic deformation will be discussed from the crystallographical point of view. The mathematical as well as the crystallographical perspective of the plastic deformation will together be used to the general concept of plasticity. Finally, section 2.4 explains the constitutive equations in incremental form based on the crystallographical events, to predict the behavior of solids subjected to large loads, sufficient to cause plastic strains.

2.2 Mathematical description of deformation

This section briefly describes the framework to explain shape changes in solids. In general, Deformation is a change in the shape or size of an object due to an applied force. If the applied stress is small enough such that the object returns to its original dimensions upon removal of the stress, it is known as *elastic deformation.* A directly measured property, Young's modulus, relates stress to strain in the elastic region. *Plastic deformation* describes the deformation of a material undergoing non-reversible shape changes in response to applied stress. Note that in plastic deformation there is no easily measured constant relating stress to strain. It must be also recognized that plasticity has enormous practical implications for various metals forming process such as rolling, extrusion, drawing and sheet-metal forming. Furthermore, the study of plastic

deformation may lead to improved understanding and analysis of permanent strain, residual stress, and yielding during cyclic loading (fatigue conditions). It is expected that the remaining residual stress after unloading profoundly affects quality and component life by either decreasing or increasing the subsequent resistance during manufacturing and working condition. Thus, in addition to the significance of plastic deformation for metal manufacturing and design, plastic deformation parameters such as tensile and compressive residual stresses caused by local yielding and strain hardening and softening during cyclic stress-strain hysteresis affect the fatigue life computations.

In continuum mechanics, deformation is transformation of a body from a reference configuration to a current configuration. The change in configuration is the result of a displacement of the body. Shape changes near a point can always be characterized by six numbers. These could be the six independent components of the Lagrangian, Eulerian or infinitesimal strain tensor. Given the complete set of six numbers for any deformation measure, one can always calculate the components of other strain measures. The reason that so many different deformation measures exist is partly because different material models adopt different strain measures, and partly because each measure is useful for describing a particular type of shape changes.

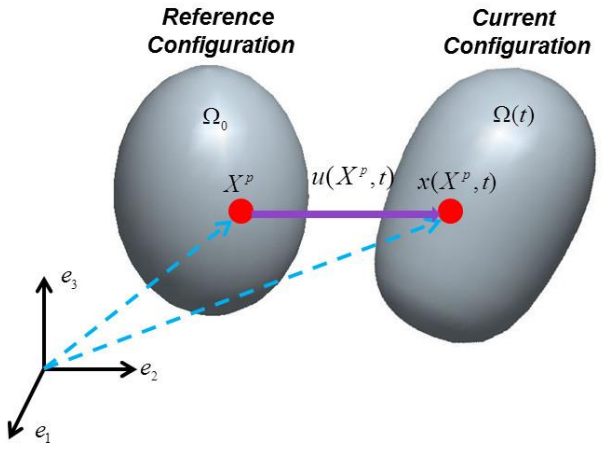

Figure 2 Illustration of the reference and current body configurations of a continuum body

Consider a continuum body made up of a collection of material points, shown in Figure 2. As a consequence of a force, the reference body configuration Ω_0 deforms and the material moves to a new configuration $\Omega(t)$. In order to map the position of each point, a mapping function must be defined. Here, the mapping function is the displacement vector $u(X,t)$ which describes the motion of each point in the solid. Deformation takes place at every point as the solid moves as a direct result of an applied stress. For instance, a point at position X in the undeformed solid might move to new position x at time t in the deformed body. The corresponding displacement vector is thereby defined as

$$u(X,t) = x - X \tag{2.1}$$

The material description u is considered as a function of X and t, so that

$$u(X,t) = x(X,t) - X \tag{2.2}$$

And in the spatial description $_U$ is regarded as a function of x and t, so that

$$u(x,t) = x - X(x,t) \tag{2.3}$$

The *displacement field* completely specifies changes in shape of the solid, where the *velocity field* describes the rate of change of displacement. If we focus our attention on a specific particle, for example a point in the undeformed body such as X^p, the velocity vector v of particles describes the rate of change in particle displacement. Due to the fact that the hypothetical point X^p is constant at a fixed particle, it is more convenient to use the material description so that, from (2.2)

$$v(X,t) = \frac{\partial u(X,t)}{\partial t} = \frac{\partial x(X,t)}{\partial t} \tag{2.4}$$

Of course, the initial particles of a body cannot arbitrarily move independently of one another. In particular, no two particles can occupy the same location in space at a given time. Furthermore, for smooth motions it is typical to consider any two particles arbitrarily close in the reference configuration and in all other configurations. Considering this, the *deformation gradient* is a measure of the local relative displacement occurring between material points. More specifically, the deformation gradient transforms material line elements into spatial line elements.

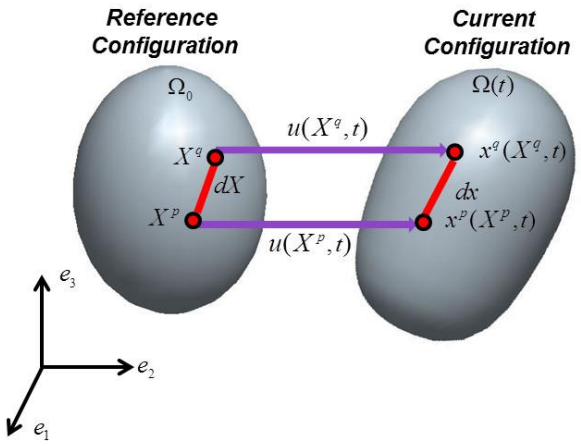

Figure 3 Illustration of a material and spatial line element

A material line element, dX , shown in Figure 3, is a vector that connects two infinitesimally close points, X^p and X^q, within the reference configuration where $dX = X^q - X^p$. A spacial line element, dx is the vector that connects points x^p and x^q in the current configuration such that

$$dx = x^q(X^q,t) - x^p(X^p,t) \tag{2.5}$$

The current position of point x^q can be presented as follows

$$x^q(X^q,t) = x^p(X^p,t) + dx \text{ or } x^q(X^q,t) = x^p(X^p + dX,t) \tag{2.6}$$

Therefore,

$$x^p(X^p,t)+dx=x^p(X^p+dX,t) \tag{2.7}$$

A Taylor expansion of the right hand side equation (2.7) gives

$$x^p(X^p,t)+dx=x^p(X^p,t)+\left.\frac{\partial x(X,t)}{\partial X}\right|_{X^p}.dX+0\left(\left|dX\right|^2\right) \tag{2.8}$$

Since we have an infinitesimal material line element, the last term in equation (2.8) can be neglected. Therefore, the relation between the material and spatial line elements becomes

$$dx=\left.\frac{\partial x(X,t)}{\partial X}\right|_{X^p}.dX \tag{2.9}$$

The deformation gradient is defined as a second order tensor, which describes the motion of a continuum body. Hence, the deformation gradient describes how each material point is displaced. *i.e.* it associates a displacement u with each point in the material. Thus, the deformation gradient is defined as

$$F=\frac{\partial x(X,t)}{\partial X}=\frac{\partial x_i}{\partial X_J}e_i\otimes E_j \tag{2.10}$$

As noted, this is a so-called second order tensor, which relates dx to dX, such that

$$x=F\cdot dX \tag{2.11}$$

Since the deformation gradient, F includes rigid body rotation, it is not a direct measure of deformation. Therefore, the concept of strain is used to evaluate how much a given displacement differs locally from a rigid body displacement. Thus, looking at the change in length of the squared line-element between two material points during deformation gives,

$$\begin{aligned}(dx)^2-(dX)^2 &= (FdX)(FdX)-dXdX \\ &= F_{ij}dX_jF_{ik}dX_k-dX_kdX_k \\ &= F_{ij}dX_jF_{ik}dX_k-\delta_{kj}dX_jdX_k \\ &= (F_{ij}F_{ik}-\delta_{kj})\,dX_jdX_k \\ &= dX\,(F^TF-1)dX\end{aligned} \tag{2.12}$$

This result leads to the definition of the *Lagrangian strain tensor*,

$$E=\frac{1}{2}(F^TF-I)\ or\ E_{ij}=\frac{1}{2}(\frac{x_J}{X_i}\frac{x_i}{X_J}-\delta_{ij}) \tag{2.13}$$

The component of Lagrange strain tensor can also be expressed in terms of the displacement gradient, so

$$E_{ij}=\frac{1}{2}(\frac{\partial u_i}{\partial x_i}+\frac{\partial u_j}{\partial x_i}+\frac{\partial u_k}{\partial x_j}\frac{\partial u_k}{\partial x_i}) \tag{2.14}$$

The Lagrangian strain tensor quantifies the change in length of material points and angles between the pairs points in a deformable solid. It is used in calculation in which large shape changes are expected.

If the numerical values of all components of the displacement and the displacement gradient tensors are very small relative to the gradient, we may neglect the square and products of these quantities. . Hence, the *infinitesimal strain tensor* is an appropriate tool utilized to describe small shape changes. Since the higher order components of these calculations are neglected, infinitesimal strain tensor is linear and thereby more convenient to use than the Lagrangian strain. The infinitesimal strain tensor is defined as

$$\varepsilon_{ij}=\frac{1}{2}(\frac{\partial u_i}{\partial x_j}+\frac{\partial u_j}{\partial x_i}) \tag{2.15}$$

Where u represents the displacement vector, written out in full,

$$\varepsilon_{ij} = \begin{pmatrix} \dfrac{\partial u_1}{\partial x_1} & \dfrac{1}{2}\left(\dfrac{\partial u_1}{\partial x_2} + \dfrac{\partial u_2}{\partial x_1}\right) & \dfrac{1}{2}\left(\dfrac{\partial u_1}{\partial x_3} + \dfrac{\partial u_3}{\partial x_1}\right) \\ \dfrac{1}{2}\left(\dfrac{\partial u_2}{\partial x_1} + \dfrac{\partial u_1}{\partial x_2}\right) & \dfrac{\partial u_2}{\partial x_2} & \dfrac{1}{2}\left(\dfrac{\partial u_2}{\partial x_3} + \dfrac{\partial u_3}{\partial x_2}\right) \\ \dfrac{1}{2}\left(\dfrac{\partial u_3}{\partial x_2} + \dfrac{\partial u_1}{\partial x_3}\right) & \dfrac{1}{2}\left(\dfrac{\partial u_3}{\partial x_2} + \dfrac{\partial u_2}{\partial x_3}\right) & \dfrac{\partial u_3}{\partial x_3} \end{pmatrix} \tag{2.16}$$

For a general strain tensor (which could be any of Lagrangian strain tensor ($\boldsymbol{E}$) or infinitesimal strain tensor ($\boldsymbol{\mathcal{E}}$), the diagonal strain components are referred to as "normal" strain, whereas the off-diagonal terms are known as "shear" strains. The *shear strains* are sometimes reported as "engineering shear strain", defined as twice the tensorial shear strain. Generally, $\gamma_{12}, \gamma_{13}\ \gamma_{23}$ are used for engineering shear strain components. Hence, engineering shear strain may be expressed as

$$\gamma_{12} = 2\varepsilon_{12} \quad \gamma_{13} = 2\varepsilon_{13} \quad \gamma_{23} = 2\varepsilon_{23} \tag{2.17}$$

If one considers the infinitesimal cuboid, projecting its deformation on the X-Y plane, the resulting coordinates of the point A, B, C, D are as shown in Figure 4.

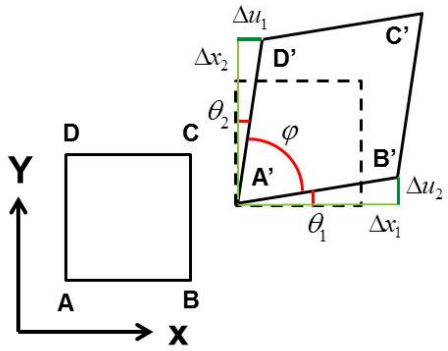

Figure 4 The physical meaning of component of strain tensor in the X-Y plane

As can be seen in Figure 4, the lone segment of the initial length AB and AD gets deformed to A'B' and A'D', respectively. The relative change in length can be can be defined as

$$\gamma_{12} = \frac{\pi}{2} - \varphi = \theta_1 + \theta_2 \tag{2.18}$$

Where

$$\begin{aligned} \tan\theta_1 = \frac{\Delta u_2}{\Delta x_1} &\xrightarrow{small\ angle} \tan\theta_1 \approx \theta_1 \approx \frac{\Delta u_2}{\Delta x_1} \\ \tan\theta_2 = \frac{\Delta u_1}{\Delta x_2} &\xrightarrow{small\ angle} \tan\theta_2 \approx \theta_2 \approx \frac{\Delta u_1}{\Delta x_2} \end{aligned} \tag{2.19}$$

Therefore

$$\frac{1}{2}\gamma_{12} = \varepsilon_{12} = \frac{1}{2}\left(\frac{\Delta u_2}{\Delta u_1} + \frac{\Delta u_1}{\Delta u_2}\right) \approx \frac{1}{2}(\theta_1 + \theta_2) \tag{2.20}$$

Equation (2.20) demonstrates that the tensorial shear strain component is the average of the changes in the angles of the two perpendicular line elements. Consequently, the strain rate tensor can be presented as follows,

$$\varepsilon^{\bullet} = \begin{pmatrix} \varepsilon_{11}^{\bullet} & \frac{\varepsilon_{12}^{\bullet}}{2} & \frac{\varepsilon_{13}^{\bullet}}{2} \\ \frac{\varepsilon_{21}^{\bullet}}{2} & \varepsilon_{22}^{\bullet} & \frac{\varepsilon_{23}^{\bullet}}{2} \\ \frac{\varepsilon_{31}^{\bullet}}{2} & \frac{\varepsilon_{32}^{\bullet}}{2} & \varepsilon_{33}^{\bullet} \end{pmatrix} \tag{2.21}$$

In plastic deformation, the volume of the solid changes negligibly (conservative of volume). This statement means that hydrostatic component of the strain tensor is zero so,

$$\varepsilon_{11}^{\bullet} + \varepsilon_{22}^{\bullet} + \varepsilon_{33}^{\bullet} = 0 \tag{2.22}$$

Therefore, in order to solve the total six unknown strain rate components, only five states of strain are required. The discussed state of strain can be computed from the crystallographical perspective, which will be discussed in the next section. In this dissertation a computer program based on the described correlation formulation was deployed for the determination of the displacement components and deformation gradients of an object surface due to deformation by

assisting optical digital imaging. Several analyses were performed to validate the viability of the correlation method in experimental mechanics results. The details of using continuum based digital image correlation to quantify strain field due to deformation are presented in section 2.5.2

2.3 Crystallographic description of deformation

Plasticity describes the deformation of a material undergoing non-reversible changes of shape in response to applied forces. It is important to notice that the load can be applied externally or internally (phase transformations). Behavior at the *macrolevel*, in particular *plastic anisotropy*, is controlled by microscopic features; i.e. crystals and dislocation within crystals. Thus, plastic deformation and plastic anisotropy, similar to many other physical processes, can be well-defined by properly linking the operating grain level mechanisms responsible for macro scale mechanical behavior. Crystalline solids (most metals and alloys) generally consist of millions of individual crystals, known as grains. Each grain contains a systematic arrangement of atoms. Therefore, each grain has different orientation, separated from the neighboring grain by a *grain boundary*. As a result of this fact, the physical mechanisms that cause plastic deformation can vary widely. Nevertheless, this broad spectrum of physical mechanisms is being studied using two major approaches. First, developing a mechanistic-based understanding of grains (conventionally regarded as single crystals) appears to be essential for identifying the active slip systems and quantifying the required driving force in a single crystal, which can build knowledge surrounding the plasticity of a polycrystalline aggregate. Hence, mechanical testing on single crystals is required to determine the characteristics of operating deformation mechanisms, mainly slip and deformation twinning with respect to the loading condition. Several former and recent [20-22] studies have contributed to this topic by describing the active deformation modes, specifically slip and twinning system, and the magnitude of critical resolved

shear stress (CRSS) (Schmid's law) in single crystals. Meanwhile, polycrystalline aggregate behavior of polycrystalline materials, and particularly Mg based alloys has also been examined extensively by paying close attention to the role of crystal orientation and average over the aggregate of stress and strain [23-26]. Despite this intense effort, the local strain distribution due to the grain interaction as well as the interaction between dislocation slip and deformation twin are poorly understood.

2.3.1 Deformation by slip

The objective of this section is first to give a brief description of slip and differentiate slip from twinning. Then, the significant effect of slip on elongation at the early stage of plastic flow and also the role of strain transfer in the activation of deformation twinning in grain boundaries are discussed. Finally, an example will be given to show stress concentration as a result of slip bands formation.

It is known that plasticity in crystalline materials, especially metals with HCP unit cell structure, greatly depends on the preferred crystallographic orientation of individual grains, known as texture. Texture mostly develops during thermo-mechanical processing and becomes more pronounced during forming processes. Therefore, the nature of plastic deformation is closely referred to understanding the mechanical state of stress and strain in individual crystals, which can be quantified to within a good approximation by Schmid's law. It should be noted that Schmid's law neglects crystal interaction (crystal compatibilities). Schmid's Law states that for yield in crystals: a single crystal yields on any particular slip system (plane and direction comprise what is known as a deformation/slip system) if the shear stress resolved on that slip plane and slip direction reaches a critical value, the "yield strength" on that slip system (details are given in section 2.3.3) [27]. Of special interest regarding slip is the establishment of a

criterion for predicting the onset of plasticity. According to Schmid's law [28], if a polycrystal is stressed, initial yield stress varies from crystal to crystal as a function of the relative positions of the crystal lattices with respect to the loading axes. Accordingly, slip begins when the shear stress on a slip system reaches a CRSS. The prevalence of deformation modes greatly depends on the (CRSS) of each deformation mode, which is significantly influenced by crystal orientation with respect to the loading direction. Consequently, both CRSS values and texture define the sequential deformation modes by introducing slip, twinning and their interactions [29-31].

Table 2 Slip direction and planes[32]

Structure	Slip direction	Slip planes
FCC	$\langle 110 \rangle$	$\{111\}$
BCC	$\langle 111 \rangle$	$\{110\}, \{112\}, \{123\}$
HCP	$\langle 11\bar{2}0 \rangle$	$\{1\bar{1}01\}$

Slip regularly arises as a consequence of dislocation glide. It is an experimental fact that in metallic crystals, slip occurs on planes of high-atomic density [33]. Nevertheless, this statement does not mean that slip cannot occur in planes other than the mostly close packed plane [34]. The slip planes and direction for the most common crystalline structures are tabulated in Table 2. There are number of ways that dislocations may be created as a result of an exerted load. If dislocations are not generated by dislocation sources such as the Frank-Read source, then they must be created by a nucleation process. Complete descriptions of dislocation sources can be found in references [33] and [34]. In a slip mechanism, external loading causes plastic deformation to occur in well-defined slip planes. The planes on which slip occurs are called *slip*

planes and the directions of the shear are the *slip directions*. These are crystallographic planes

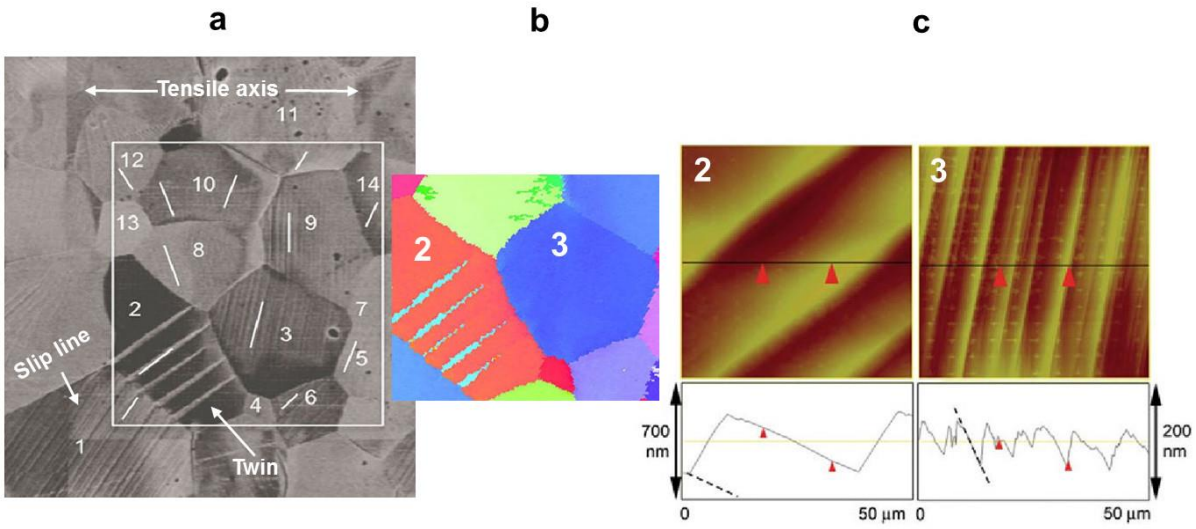

Figure 5 (a) Microstructure study of commercial purity titanium sample after ~1.5 % tensile strain, showing distinct slip bands and twinning. (c)Examples of surface topography measured by atomic force microscopy in grain 2 (left) and grain 3 (right) after deformation. Line section profiles reveal that much larger and more homogeneous surface steps result from twins (left) than from slip lines (right). The dashed line is interpreted as the undistorted surface inclination and serves as the basis for evaluating the overall height change along the section. surface steps form because that slip is an inhomogeneous phenomenon on an atomic scale [32].

and directions that are characteristic of the crystal structure. The magnitude of the shear displacement is an integral number of interatomic distances, so that the lattice is left unchanged. When plastic deformation takes place by slipping, visual examination of the surface of a deformed crystal will usually reveal slip lines. Figure 5a clearly shows slip bands and deformation twinning on the surface grain of commercially pure titanium alloy as a result of 1.5% tensile straining [35]. It is evident that the density and directions of the slip traces and twins vary strongly from one grain to another. For instance, grains 3, 6, and 9 display the most obvious slip traces, while less pronounced slip bands are found in grains 8 and 10. This observation can be attributed to the fact that the grains 3, 6, and 9 are more favorable to slip (Schmid's law). The thick lenticular crystallographycal feature appearing in grain 2 was

confirmed to be deformation twinning using Electron Backscatter Diffraction (EBSD) (Figure 5b). Atomic force microscopy scans of grains 2 and 3 shown in Figure 5c are being used here to quantify slip and twin traces on the surface. As it can be observed in Figure 5c, surface step occurs as a consequence of slip and twinning. However, the line scan provided in the same image indicates that the twinning effect is more pronounced on the surface morphology. Deformation twinning will be discussed with more detail in the following section.

Displacements of thousands of atomic diameters must occur on discrete or closely spaced planes to create visible steps on the surface. A *slip band* is a group of closely spaced slip lines that appear at low magnification. Hence, if a single crystal of a metal is stressed in tension or compression beyond its elastic limit, elongation/compression is usually accompanied by step appearance on the surface. This is accepted to be possibly given through the intersection of dislocations with surface dislocations [34]. If the step lies on the slip plane of a dislocation, the generated step is commonly referred to as a *kink.* If the step is normal to the slip plane of dislocation, the step is referred to as a jog. Close inspection of Figure 6 shows that slip bands tend to appear in an irregular wavy pattern. This can be attributed to the fact that the dislocations that produce the bands are not restricted to motion in a single plane. Shifting of dislocations from one slip plane to another usually results from cross-slipping of screw dislocations[34].

Besides the importance of slip bands for plasticity, direct evidence also indicates that slip bands have an effect on fatigue crack development. In this regard, one of the most visible features of cyclic saturation is the localization of slip along certain bands. For example, observation of structural details underlying the fatigue surface revealed that slip bands in fatigued copper mono- and polycrystals were persistent [36]. They are termed persistent because if one polishes the sample, the slip bands would reappear at their former sites whenever fatigue resumes.

Conventionally, fatigue slip bands are referred to as Persistent Slip Bands (PSB). It thus became gradually evident that fatigue damage in the form of irreversible microscopic changes at the surface resulted from the accumulation of very small irreversible plastic cyclic micro-strains and that metal fatigue was actually a problem of micro-plasticity [37]. It is crucial to note that although the surface slip steps form in proportion to the average plastic amplitude, the displacement between the bands is not fully reversible [38]. This leads to formation of slip offset and a rough topography within the bands (shown also earlier in Figure 5c) which appears to be a precursor to crack nucleation [39]. Figure 6a demonstrates crack propagation along PSB in the fatigued sample. PSBs consist of extrusions and intrusions on surface, which can potentially become incipient fatigue crack sites. Figure 6b&c clearly demonstrate that the extrusions and intrusions are closely related to the specific dislocation structure of the PSBs, and that this dislocation structure is present even in the extruded region of the material. Close attention to Figure 6c shows that very short incipient cracks start from intrusions adjacent to extrusions and initially grow parallel to the PSB [40].

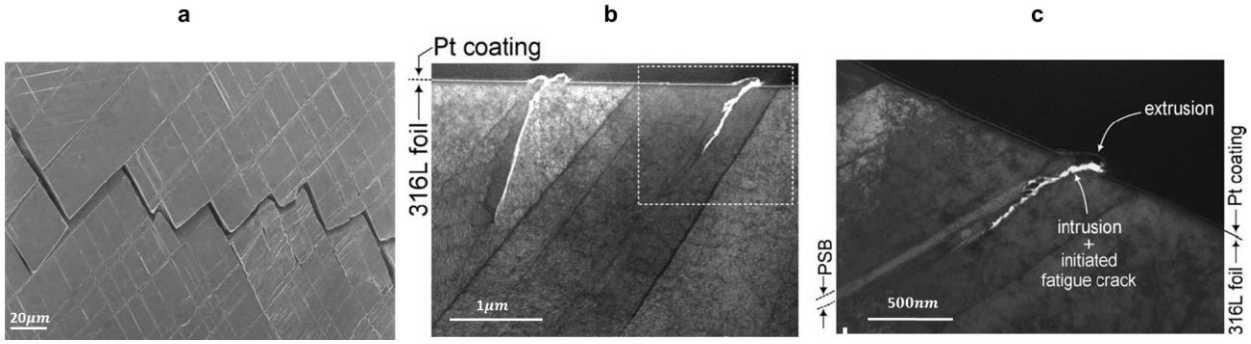

Figure 6 (a) Crack propagating along PSB in tungsten monofilament-reinforced multi-crystalline copper composites [41]. Scanning Transmission Electron Microscopy (STEM) overview (b) and TEM detail (c) of initiated fatigue cracks imaged in a foil covered by Pt coating. Foil taken from fatigued 316L steel [40].

2.3.2 Deformation by mechanical twinning

It is generally accepted that mechanical twinning is one of the two major modes of plastic deformation in crystalline solids, becoming prevalent at high strain rates and/or low temperature deformation [29]. For simplicity, mechanical twinning will be referred to as twinning henceforth in the manuscript. It is widely believed that the stress required for formation of twinning is controlled by the value of Stacking-fault Energy (SFE). It is also demonstrated that the twinning stress increases directly proportional to the SFE value [42]. This statement is particularly accurate in FCC materials [43]. Twinning usually occurs to accommodate strain in low-symmetry crystal structure materials (restricted deformation systems) [44], and in materials with lower SFEs [45]. It has been showed that unlike carbon steels, austenitic steels deformed plastically through mechanical twinning [46]. This observation has been further attributed to the relatively low SFE characteristics of austenitic steels when compared to carbon steels. Despite the broad agreement in literature with regard to the great tendency of low SFE materials to deform by twinning, another set of experimental evidence reports indications of twinning during plastic deformation of a high SFE material such as nanocrystaline aluminum [47]. This explanation relies on a comparison between the critical shear stress required to nucleate a perfect dislocation with an approximation of the source size equal to the grain size, with that needed to initiate Shockley partial dislocation to generate stalking fault and deformation twinning. In this framework, the effect of several alloying element on SFE in Mg alloys was subjected to the recent computational study [48]. This investigation shows by adding some specific alloying elements such as Aluminum (Al) and Zinc (Zn) to Mg, deformation energy of twinning decreases in compare to pure alloy. These elements are of particular interests as the Mg AZ 31, with a nominal chemical composition of 3 wt%. Al and 1 wt.% Zn, is the highest volume

wrought Mg alloy in production [49]. This underscores the fact that AZ31 readily deforms through twinning. It is, however, important to notice that the twinning operation is extremely sensitive to the material texture [50, 51], grain size [52, 53], alloying elements[54, 55], testing temperature[56], and strain rate[57].

In HCP metals like beryllium, magnesium, cadmium and zinc the Critical Resolved Shear Stress (CRSS) for basal slip is low, therefore slip takes place mainly on the $\{0001\}$ basal plane [58]. Depending on the c/a ratio of a particular material, as well as the deformation stage and mode of loading, the $\{1010\}$ prismatic plane may also become an important glide plane [59]. It should be noted that both prism and basal slip resolves in a plastic response along $\langle a \rangle$ directions (see Figure 7), thus the aforementioned slip systems cannot resolve to strain along to the c-axis. Moreover, due to the large Burgers vector and small interplanar spacing of slip on pyramidal planes along the $\langle a \rangle$ directions, slip then is significantly difficult, and even more difficult on the pyramidal planes along the $\langle c+a \rangle$ direction [29]. Figure 7 schematically shows the slip plane and its corresponding direction in HCP unit cell structure. The specified slip systems provide only a total of four independent slip systems. Therefore, it appears that Mg alloys with their HCP crystal structure fail to satisfy the Taylor criterion [60] requiring five independent slip systems for homogeneous, generalized deformation of a polycrystalline aggregate [29]. Note that the mathematical justification of this statement is presented in section (2.2). It is also important to recognize that the basal slip does not produce any elongation or shortening parallel to the c-axis [29]. Consequently, only twinning [30, 61] or pyramidal slip [62, 63], which are shown in Figure 7, can potentially accommodate inelastic shape changes along the c-axis direction. As indicated,

at room temperature Mg exhibits a strong propensity for twinning since the twinning has a lower threshold than $\langle c+a \rangle$ slip.

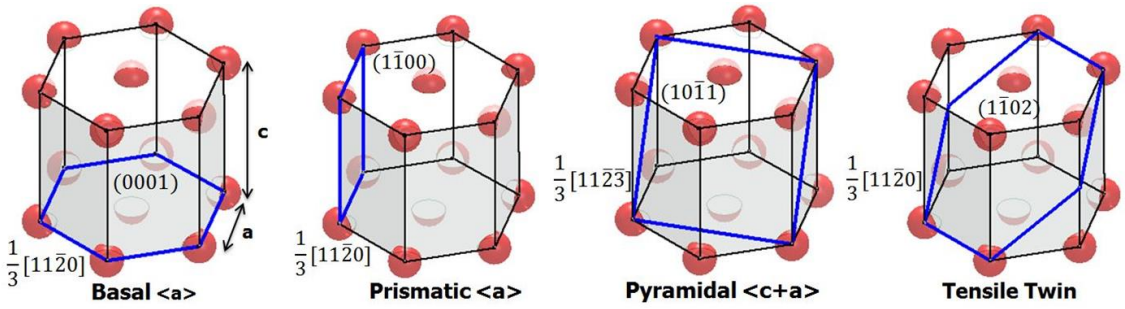

Figure 7 Basal, prismatic, pyramidal and twins with the corresponding operational directions.

Twinning is a polar [64] shearing mechanism [34] of the lattice by which atoms are shifted parallel to the so-called twinning plane, which consequently leads to a noticeable reorientation of the crystal structure [65]. This means that as a result of twinning, a region of the crystalline body undergoes a homogeneous shape deformation in such a way that the resulting product structure is identical to that of the parent, *but oriented differently*. Figure 8a displays an atomistic level description of deformation twin (which is marked with T) and the loading direction relative to the crack plane, using a combination of tensile straining and in-situ High-Resolution Transmission Electron Microscopy (HRTEM) [66]. In this respect, Figure 8b shows HRTEM image of the twin (T) and the original matrix (M) ahead of the crack tip. The importance of twinning becomes increasingly apparent in explaining certain elusive mechanical behavior of many polycrystalline materials. For example, when twinning occurs, the lattice inside the twin is realigned into a specific orientation where the slip planes are more favorably aligned with respect to the applied stress [34]. Figure 8a and particularly Figure 8b, provide an insightful example of homogeneous atoms shuffling of a portion of the crystal due to twinning in aluminum. Another experimental examination exclusively demonstrates high resolution of atomic rearrangement in the twinning region in Mg [67]. In this study the authors used in situ mechanical testing of a

magnesium single crystal in the presence of TEM. As it is shown, multiple twins formed along the gage section (Figure 8d). Figure 8e exhibits twinning results in the atoms of the original (parent) crystal, and those of the original crystal (twin) is being mirror images of each other. This concept will be revisited later in this chapter.

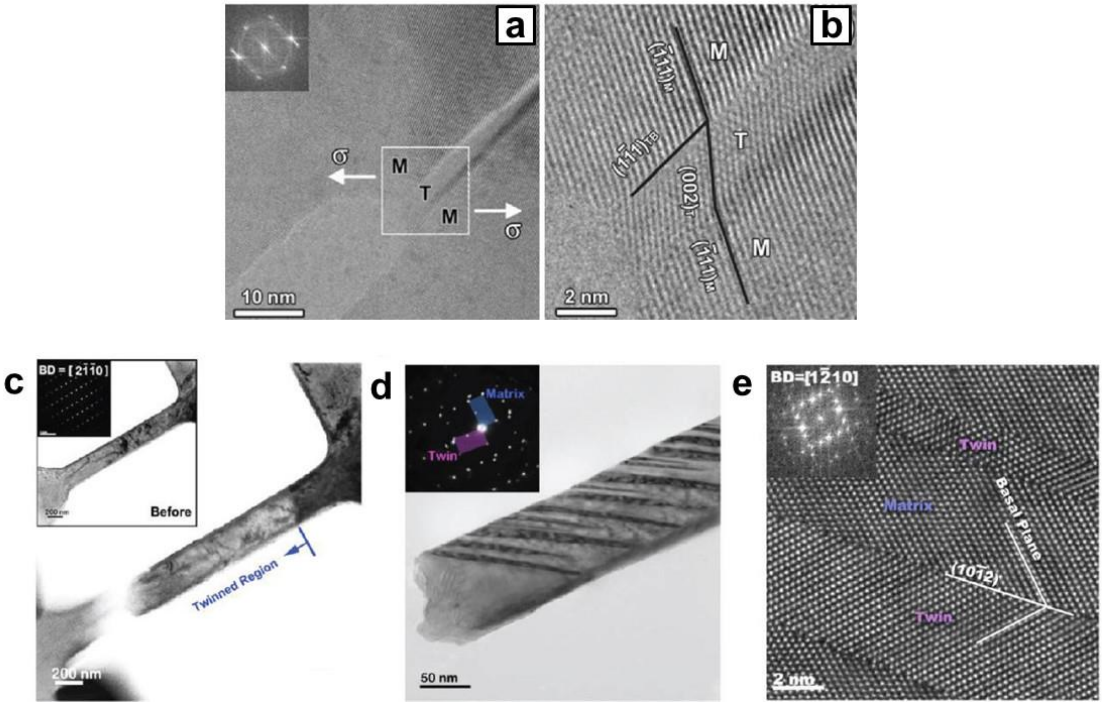

Figure 8. (a) TEM observation of the thin area produced by straining at the crack tip (marked by a white arrow) [66](b) HRTEM image of the twin ,T, and the matrix ,M [66] (c) image of tensile deformation showing the region of extension twinning (the loading axis is normal to the basal plane) [67]. (d) Nano twin array in a tensile sample[67]. (e) HRTEM image of twinned structure [67].

Twin nucleation has been explained by a heterogeneous model involving dissociations of perfect $\langle a \rangle$ and $\langle c+a \rangle$ slip dislocations into glissile twinning dislocations [68]. Dislocation piles-ups can further drive such dissociations, propagate the twin fault and aid twin formation by generating stress concentration [69]. There are seven twinning modes in HCP metals by which two types of twins are frequently reported in magnesium alloys: $\{10\bar{1}2\}\langle 10\bar{1}\bar{1} \rangle$ *tension* and $\{10\bar{1}1\}\langle 10\bar{1}\bar{2} \rangle$ *contraction* twins. Tension twins are formed and cause an extension strain

component parallel to the c-axis, i.e they can only be activated by tension but not by compression in the c direction [70]. In contrast, contraction twins are activated to produce contraction strain components parallel to this axis [30, 31, 71]. Figure 9a shows the occurrences of several tension twins in a rolled Mg AZ31alloy [72]. In this instance, twin and parent grains are indicated by T and P, respectively. Figure 9b shows that due to the lattice reorientation caused by tension twin occurrence, the lattice inside the twin region moves to a position about ~86 degrees away from the parent grain. Despite the presented twins in Figure 9 all characterized as $\{10\bar{1}2\}$ tension twins [72], they have reoriented the lattice plane to different places, demonstrating the activation of twins on different crystallographycal planes (twin variants).

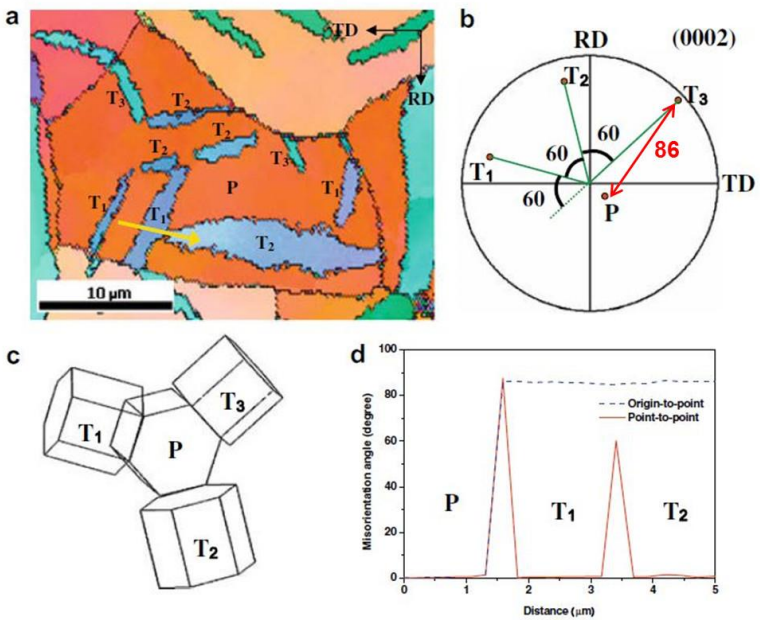

Figure 9 (a) Crystallographic orientation map obtained by tensioning to 6% along the ND; (b) crystallographic orientations of a parent grain and twin bands; (c) crystallographic relationship between the parent grain and twin bands; and (d) line profiles of the misorientation angle along the direction indicated as an arrow in (a) Here, P, T1, T2 and T3 represent the parent grain and three different types of twins, respectively [72].

The activation of different twin variants is dependent on the strain path. Figure 10 displays texture evolution and activation of different twin variants for samples on which tension loading was applied along to the c-axis (Figure 10a-d) and the sample which compression loading is applied perpendicular to the c-axis (Figure 10e-h) [73]. Thus, tension twinning is expected to occur in both tension and compression modes. Figure 10a exhibits the formation of three distinct tension twin variants at the onset of yielding (66MPa) during tensile loading. Then, as deformation progressed (Figure 10b), the twinning process is dominated by the nucleation of fresh twins rather than the development of the existing twin. As a result, higher stress state configuration depicts all six possible tension twin variants shown in Figure 10c &d. Nevertheless, in the case of compression test, yielding (Figure 10e), is followed by twinning growth of existing ones (Figure 10f). It is also apparent that only two different twin variants are recognized in this instance (Figure 10g &h).The operation of all six twin variants and the distinct relationship between all six twin variants increases the possibility of twin intersection that would restrict the twin growth by creating high misorientation grain boundaries. The extension twin variants can be selected based on the Schmid's law principle [73, 74].

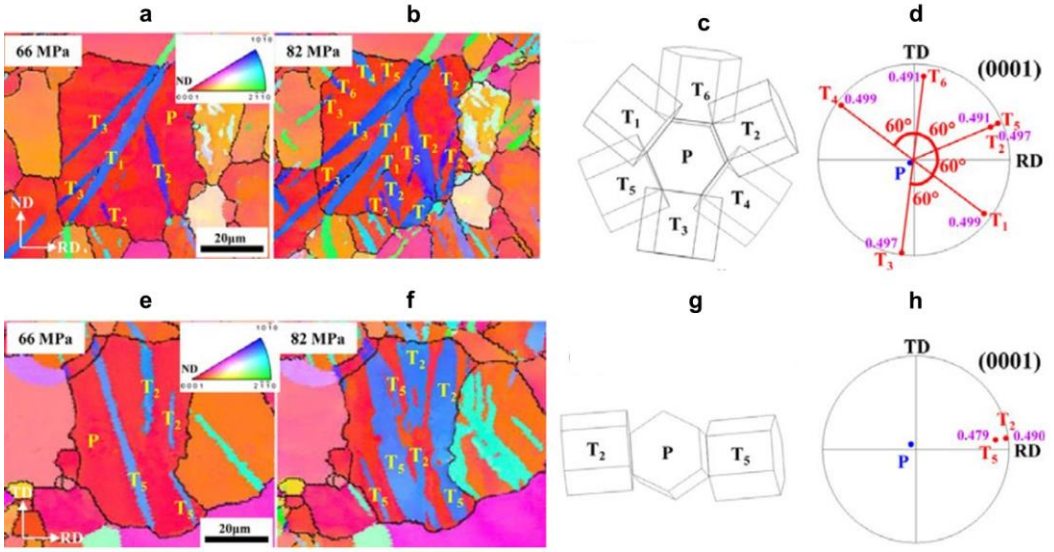

Figure 10 In situ EBSD of the specimen tensioned along c-axis to (a) 66 MPa and (b) 82 MPa. (c) Crystallographic relationship between the parent grain and the twin bands (d) crystallographic orientation of the parent grain and the twin bands, where the corresponding SF values of the twin variants are indicated as digits. (e) In situ EBSD of the specimen tensioned perpendicular to the c-axis to e) 66 MPa and (f) 82 MPa. (g) Crystallographic orientation of the parent grain and the twin bands. (h) Crystallographic orientation of the parent grain and the twin bands, where the corresponding SF values of the twin variants are indicated as digits [73].

Magnesium compressed along the c-axis would not undergo $\{10\bar{1}2\}$ twinning because this mode does not produces an extension along the c-axis [75]. Moreover, the $\{0001\}\langle 10\bar{1}\bar{2}\rangle$ basal slip, non-basal slip such as $\{10\bar{1}1\}\langle\bar{1}2\bar{1}0\rangle$ prismatic slip, and $\{11\bar{2}2\}\langle 11\bar{2}3\rangle$ pyramidal slip are also suppressed in accordance to (Schmid's law) [28]. However, the CRSS for basal slip is considerably low (~0.5MPa in pure Mg and ~2MPa in Mg AZ31 [76]) . Therefore, Schmid's law would apply when the angle between the compression and c-axis is at least 4^{o} [70, 75, 77]. This implies that a slight misalignment of the basal plane can activate the $\{0001\}\langle 10\bar{1}\bar{2}\rangle$ basal slip. In some studies, $\langle c+a\rangle$ slip on $\langle 11\bar{2}\bar{2}\rangle$ planes has also been observed [62]. In others, it has been emphasized that compression along the c-axis favors contraction twins on the $\{10\bar{1}1\}$, and

$\{10\bar{1}3\}$ planes [78, 79]. Although different modes have been observed, it is most common for twinning to occur on the $\{10\bar{1}1\}$ plane [80, 81]. In many cases, retwinning or secondary twinning follows this on the $\{10\bar{1}2\}$ plane. Secondary twinning will be discussed in greater detail shortly. Figure 11a shows the primary $\{10\bar{1}1\}$ twins were followed by $\{10\bar{1}2\}$ twin in AM30 Mg alloy [82]. The evidence provided in Figure 11b & c shows that the contraction twin reorients the crystal lattice by ~56.2^{o}. It is also apparent from the same diagram that primary twinning followed by secondary twinning gives a net reorientation of ~38^{o}. As noted, in addition to primary twinning, secondary twinning can occur within the reoriented primary twins, known as double twinning. In this instance, contraction twins tend to form first, after which $\{10\bar{1}2\}$ extension twins propagate within the original contraction twins [71]. Note that, only one variant associated with double twinning has been reported in the literature, where the nest result is always a reorientation of the basal planes by 38^{o} around $\langle 1\bar{2}10\rangle$ [83].

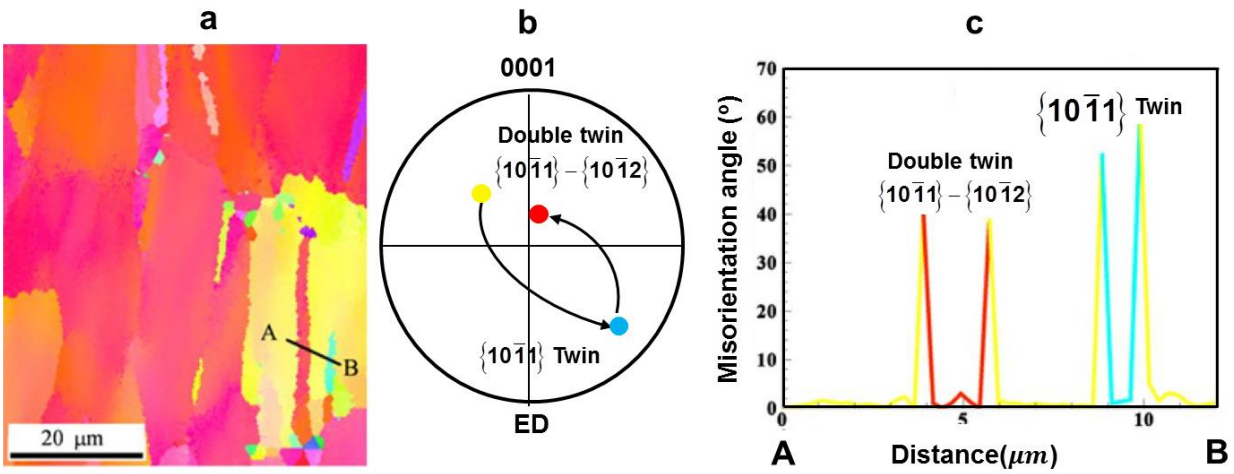

Figure 11. (a) The primary contraction $\{10\bar{1}1\}$ twin and $\{10\bar{1}1\}-\{10\bar{1}2\}$ double twin. (b) pole responding to primary $\{10\bar{1}1\}$ and secondary twin $\{10\bar{1}1\}-\{10\bar{1}2\}$ (c) the characteristic misorientation of ~56° for $\{10\bar{1}1\}$ and 38° for $\{10\bar{1}1\}-\{10\bar{1}2\}$ double twinning [82].

These twins become more prevalent at higher magnitude of strain. It must be recognized that due to the fine size and also high level of strain it is usually difficult to index contraction and double twinning [31]. Chun and Davis [84] deformed a highly textured Mg plate to fracture in which the c-axis was perpendicular to the loading direction. Deformed microstructure shown in Figure 12a exhibits two distinct contraction twin variants, marked as ct1 and ct2. Furthermore, Figure 12a presents tension twins (tt1, tt2, tt3 and tt4) formed within the contraction twins and thus double twins (ct1-tt1, ct1-tt2, ct2-tt3 and ct2-tt4). Hartt and Reed-Hill [85], and later Barnett et al.[81] experimentally showed that the c-axis of the double twins are aligned roughly 38° away from the c-axis of parent grain. The primary $\{10\bar{1}1\}$ contraction twin reorient the basal plane by ~56° around the $\langle 1\bar{2}10\rangle$ axis; in this case, the secondary $\{10\bar{1}2\}$ twin (tension twin) rotates the pole "back" by ~86° around the same axis and the net results is a reorientation of the original c-axis by 38° degree around the $\langle 1\bar{2}10\rangle$ axis. The pole figure (Figure 12b) shows that the reoriented

lattice places as a direct result of double twins place the basal plane on a position more favorable for basal $\langle a \rangle$ slip (the traces of c-axes with the maximum Schmid factor for basal $\langle a \rangle$ slip shown as red circles in Figure 12b). Similar statement has been proposed in Ref.[31]. It should be noted that double twins lead to a net contraction along the c-axis [80].

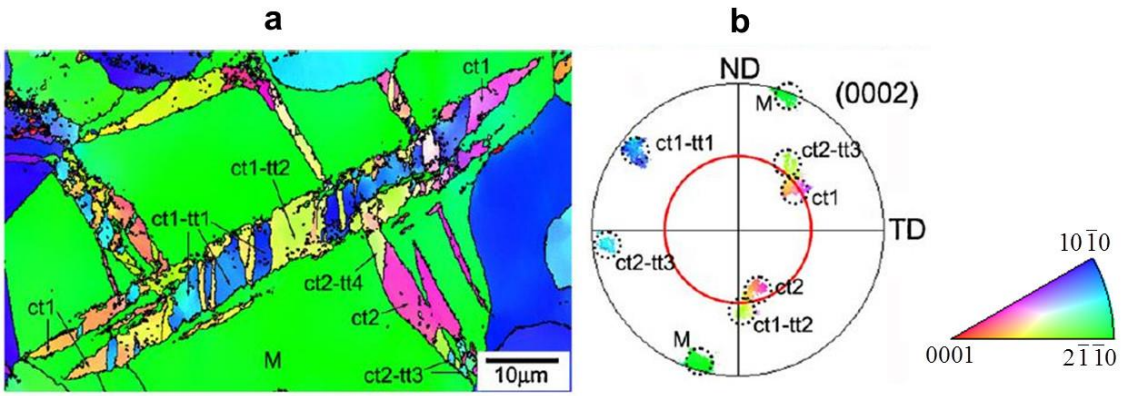

Figure 12 inverse pole figure map for the section normal to the loading directionshowing the coexistance fo contraction and double twins. Shown in (a and b) are the shapes and (0002) pole distributions of a parent grain (M), two variants of contraction twin (ct1 andct2), and tension twins (tt1, tt2, tt3 and tt4) formed in the contraction twins and thus double twins (ct1-tt1, ct1-tt2, ct2-tt3 and ct2-tt4) [84].

2.3.3 Plastic deformation

To establish the connection between dislocation behavior and yield strength as measured in tension, the deformation of single crystal is considered here first, and then it will be linked to a polycrystal. Slip occurs by dislocation motion. To move dislocations, a certain stress must be applied to overcome the dislocation's resistance to motion [33]. In this regard, slip occurs when the shear stress acting along the slip direction on the slip plane reaches a critical value. This critical shear is related to the stress required to move dislocations across the slip planes. The important question is, how big an applied stress is required for slip to occur? Consider the crystal illustrated in Figure 13, which is under tension due to the applied force (F) along the cylinder axis. If cross sectional area is A the tensile stress parallel to F is $\sigma=F/A$. To obtain the resolved shear stress based on an applied tensile stress, F, one can take the component of the stress along

the slip direction, given by $F\cos\lambda$, and divide by the area over which the (shear) force is applied, $A\cos\phi$. The two angles are not complementary unless the slip direction, slip plane normal and tensile direction happen to be co-planar.

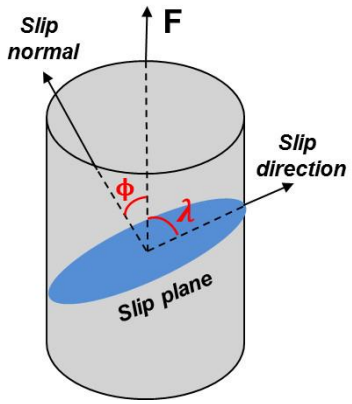

Figure 13 Illustration of the geometry of slip in a crystal

The tensile yield stress of a material is the applied stress required to initiate plastic deformation. Thus, the shear stress (τ) resolved on the slip plane in the slip direction, is

$$\tau = \frac{F}{A}\cos\phi\cos\lambda \tag{2.23}$$

Where $\cos\phi\cos\lambda$ is known as the Schmid Factor (m) and τ represents the shear stress resolved in this way. Schmid and Boas postulated [28] that the initial yield stress various from sample to sample depending on several factors, including the position of the crystal lattice relative to the loading axis. It is the shear stress resolved along the slip direction on the slip plane that initiates plastic deformation. Thus, yield will begin on a slip system when the shear stress on this system first reaches a critical value (Critical Resolved Shear Stress, CRSS), independent of the tensile stress or any other normal stress on the lattice plane [28]. The CRSS is verified by measuring the yield stress of single crystal as a function of orientation. The relationship between the Schmid factor to the axial and the shear strain is therefore given by

$$\varepsilon = \gamma \cos\theta \cos\lambda \tag{2.24}$$

where ε is the strain along the direction of the applied stress, and γ is the magnitude of the shear in the slip system. Note the strain for a specific slip system ($\langle uvw \rangle \{hkl\}$) is given by

$$\varepsilon = \gamma \begin{bmatrix} u.v & \frac{v.h+u.k}{2} & \frac{u.l+w.h}{2} \\ \frac{v.h+u.k}{2} & v.k & \frac{w.k+v.l}{2} \\ \frac{u.l+w.h}{2} & \frac{w.k+v.l}{2} & w.l \end{bmatrix} \tag{2.25}$$

For polycrystals, in which the grains are randomly orientated, Equation (2.33) is generalizes to

$$\sigma = M\tau \tag{2.26}$$

where M is known as the "*Taylor factor*". This equation functions by averaging the stress over the grains. In Equation (2.24), the term $\cos\theta$ can be obtained from the scalar product of two unit vectors $n = (\cos\beta, \sin\beta, 0)$ and $v = (\sin\psi, 0, \sin\psi)$, see Figure 14a).

$$\cos\theta = n \cdot v = \cos\beta \sin\psi \tag{2.27}$$

For any possible value of β and ψ, in a grain with one of the slip directions $\langle 11\bar{2}0 \rangle$ lying optimally, i.e in the plane defined by the normal to the basal plane and the stress axis. In this instance, the sume of the angles θ and λ_{opt} equals to $\pi/2$ and thus $\cos\lambda_{opt}$ is

$$\cos\lambda_{opt} = \sin\theta = \sqrt{1-\cos^2\theta} \tag{2.28}$$

In order to consider all possible grain orientations, a factor of $3/\pi$ is introduced to the Equation (2.28), this coefficient corresponds to the average of the cosine function from $-\pi/6$ to $\pi/6$, and obtains

$$\cos\lambda = \frac{3}{\pi}\sqrt{1-\cos^2}\theta \tag{2.29}$$

Therefore, by combining Equations (2.23), (2.27) and (2.29) the rotation factor as a function of β and ψ can be written as [70]

$$\mu(\beta,\psi)=\frac{3}{\pi}\cos\beta\sin\psi\sqrt{1-\cos^2\beta\sin^2\psi} \tag{2.30}$$

If one assume that β can takes any value from 0 to $\pi/2$, calculating the average of the mean orientation factor as a function of the tilt angle ψ respect to the loading axis is equal to

$$\mu(\psi)=\frac{6}{\pi^2}\int_0^{\pi/2}\cos\beta\sin\psi\sqrt{1-\cos^2\beta\sin^2\psi}\,d\beta \tag{2.31}$$

Figure 14b shows that the mean orientation factor increases with increasing the tilt angle until 57^o and its decline afterward. Similarly, the strain which can be accommodated by twinning in a single crystal can be obtained from [70, 77]

$$\varepsilon_{tw}=s\mu_{tw} \tag{2.32}$$

where s the twinning is shear and μ_{tw} is the orientation factor for twinning. For pure magnesium the twinning shear is reported to be 0.1289 [29]. Note that the orientation factor for twinning is defined as $\mu_{tw}=\cos\theta_{tw}\cos\lambda_{tw}$, where θ_{tw} represents the angle between the normal to the $\{10\bar{1}2\}$ twinning plane and the loading axis and λ_{tw} is the angle between the direction of the shear and the stress axis. Figure 14c demonstrates the calculated strain caused by twinning in Mg. This plot is obtained by averaging over all possible grain orientations for the ring fiber texture [70]. The discussion about the strain caused by twinning and its global and local consequences will be continued in chapter 4 and 6 respectively.

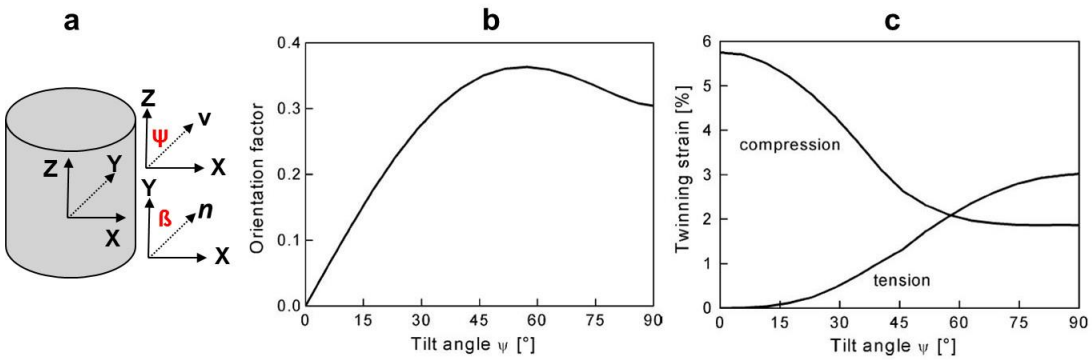

Figure 14 (a) coordinate system to illustrates n and v vectors in Equation (2.27). (b) Mean orientation factor (Schmid factor) for basal slip as a function of the tilt angle respect to the loading axis. (c) mean twinning strainunder compressive and tensile loading a s function of the tilt angle between longitudinal extusion axis and longitudenal specime axis (loading direction) [70].

2.4 Crystal plasticity

Crystal plasticity is a micromechanics-based approach to combine a variety of mechanical effects, which are dependent on the underlying crystalline structure to estimate overall mechanical behavior. Therefore, crystal plasticity methods allow one to incorporate crystallographic deformation mechanisms and their interactions to investigate plasticity of metals [86]. Crystal plasticity-based simulations can be used both at microscopic and macroscopic scales [87]. It is suggested that indirect approaches for interrogating the microstructure, such as crystal plasticity, may yield new insights which are perhaps unattainable relying solely upon traditional experimental techniques of single crystal [88]. Several examples of small-scale applications are inter/ intra grain mechanics, damage initiation, mechanics at interfaces, simulation of micromechanical experiments and the prediction of local lattice curvatures and mechanical slip-dominated are given in reference [86]. For instance, it is hard to experimentally quantify spatial distribution of relative amount of slip and twin activity and their interaction as a function of strain increment, which is vital to enhance understanding of heterogeneous distribution of both deformation slip and twin as well as stress concentration. This subject was recently investigated by coupling a microscopic mapping technique that considers grain size

distribution and texture together with crystal plasticity based on constitutive law scheme in the commercial finite element package, ABAQUS [89]. Figure 15 a &b show the 3D spatial distribution of effective stress and twinned regions in deformed configuration by compression to a 0.05 and 0.1 strains respectively.

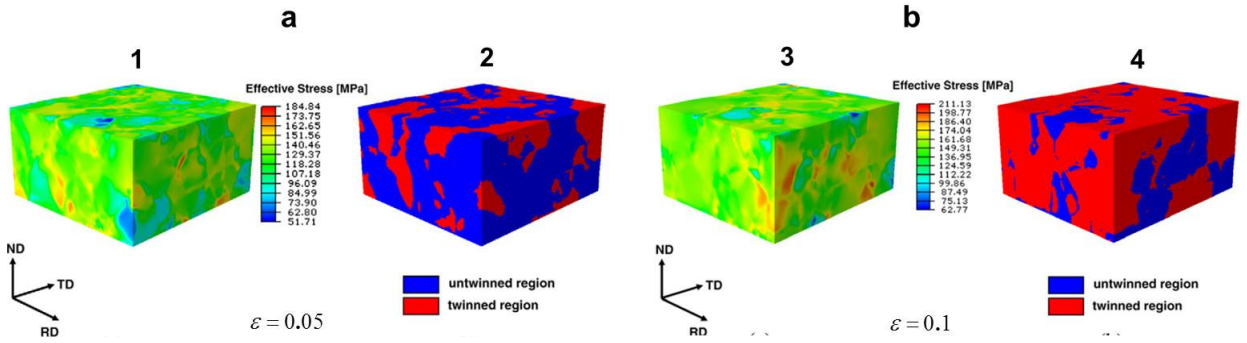

Figure 15 (a) 3-D spatial distribution of (1) effective stress and (2) twinned regions in the deformed microstructure ($\varepsilon = 0.05$) (b) 3-D spatial distribution of (3) effective stress and (4) twinned regions in the deformed microstructure ($\varepsilon = 0.1$) [89].

Comparison of Figure 15a and Figure 16a reveals that the tensile twin and basal $\langle a \rangle$ slip are the dominant deformation modes in the un-twinned region. However, the twinned regions exhibit significant activation of the pyramidal $\langle c+a \rangle$ slip. The major cause of high pyramidal $\langle c+a \rangle$ slip activity in the twinned region can be attributed to the reorientation induced by deformation twinning. The same result was concluded for the case where $\varepsilon = 0.1$, as shown in Figure 15 b and Figure 16b. In concurrence with the result obtained by the X-ray diffraction peak profile analysis (section 2.3), a-type dislocations (basal a) were found to be the dominant deformation mode up to the fracture point. It is important to note that a-type dislocations were found to be active at ε=0.05 and ε=0.1 (Figure 16a&b). Interestingly, good agreement can be observed between the experimental [18, 90] and simulation results in regards to the significant effect of twinning at early stages of plastic deformation.

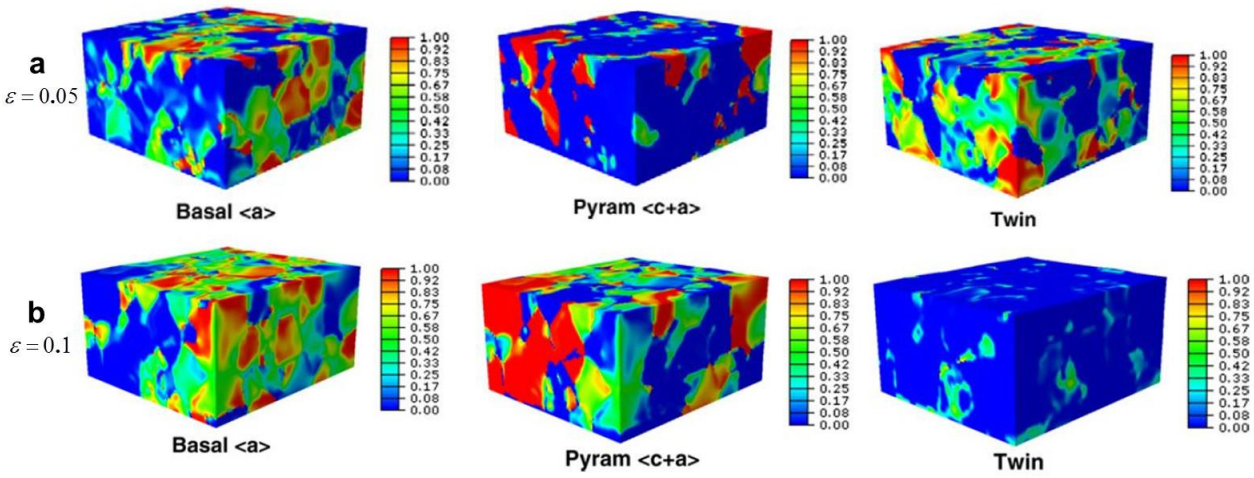

Figure 16 3-D spatial distribution of the relative activity of each deformation mode in the deformed microstructure (a) $\varepsilon = 0.05$ (b) $\varepsilon = 0.1$ [89].

2.4.1 Phenomenological constitutive law

As noted earlier, due to the diverse crystallographic slip in each crystal respect to the neighboring grains, each crystalline lattice experiences elastic stretching, rotation and plastic strain, not necessary similar to those of adjacent grains. Three parameters describe the orientation of each crystal axes with respect to sample axes, a set of Euler angles $g = \{\varphi_1, \phi, \varphi_2\}$. The crystallographical texture represents by an Orientation Distribution Function (ODF) $f(g)$ defined as follows: $f(g)dg$ is the volume fraction of all grains that have a crystallographic orientation belonging to a volume element dg around g in Euler space. The ODF can be computed from EBSD or X-ray technique.

Based on a multiplicative decomposition of the deformation gradient, F, into a plastic part which is characterized by shearing rates on active slip and twin systems [89, 91], as well as a part that accounts for the rotation and elastic distortion of the crystal lattice, the deformation gradient can be given as:

$$F = F^e F^p \tag{2.33}$$

This formula leads to additive decomposition of the velocity gradient into elastic and plastic parts:

$$L = L^e + L^p \tag{2.34}$$

The plastic part of the velocity gradient is determined from the slip rates, $\dot{\gamma}^{\alpha}$ on slip/twin systems with normal, m^{α}, and slip/twin directions, s^{α}

$$L^p = \sum_{\alpha=1}^{n} \dot{\gamma}^{\alpha} s^{\alpha} \otimes m^{\alpha} \tag{2.35}$$

The summation represents all of the deformation modes, $N = N_s + N_t$, corresponding to slip, N_s and twin, N_t. For rate-dependent materials, the *shear rates* are given explicitly in terms of the *resolved shear stress* on the active slip systems, τ_r^s, and the resistance of the active slip systems to shear, τ_{cr}^{α}. Resolved shear stress on a deformation system which is characterized by a vector n (normal to the slip or twinning plane) and a vector b (Burgers vector in the case of slip and twin shear direction in the case of twinning) is given

$$\tau_r^s = m_k^s \sigma_k^{'} \tag{2.36}$$

The Schmid factor of system (s) defined as $m_{ij}^s = (n_i b_j + n_j b_i)$. The plastic strain rate associated with the shear rate is specified

$$\dot{\varepsilon_k} = m_k^s \sigma_k^{'} \tag{2.37}$$

The shear rate induced in the hypothetical system (s) by a given applied stress described by a rate sensitive criterion, which formally amounts to assuming a non-linear viscous response [92]

$$\dot{\gamma}^s = \dot{\gamma}_o \left(\frac{\tau_r^s}{\tau_{cr}^s} \right)^n = \dot{\gamma}_o \left(\frac{m_j^s \sigma_i^{'}}{\tau_{cr}^s} \right)^n \tag{2.38}$$

Where $\dot{\gamma}_o$ is a reference rate, τ_{cr}^s, is the threshold stress (linked to $\dot{\gamma}_o$) and n is the inverse of the rate sensitivity . When $n \gg 1$the activity of system is negligible unless τ_r^s is very close to τ_{cr}^s. Substituting equation (2.28) in (2.27) gives a kinematic equation for each grain of the polycrystal [92]

$$\dot{\varepsilon_k} = \dot{\gamma}_o \sum_{s=1}^{s} m_k^s \left(\frac{m_j^s \sigma_i^{'}}{\tau_{cr}^s} \right)^n \qquad (k = 1,5) \tag{2.39}$$

Summation operation carries over all the systems in the grain. This non-linear system of five equations contains ten unknowns, where the five of which are strain rate and the other five being deviatoric stresses.

2.4.2 Self-consistent polycrystal model

The differences in stress experienced by differently orientated grains in a polycrystal are mainly due to the orientation and interactions between grains. This means that a simple assumption proposed by Taylor [93] does not accurately capture the relationship between macroscopic quantities (average flow stress, average plastic strain) and microscopic ones (stresses and plastic strains at the level of the individual grains) during plastic deformation of polycrystalline aggregate. Self-consistent formulations represent each grain as a visco-plastic anisotropic ellipsoidal inclusion embedded in a visco-plastic anisotropic Homogeneous Effective Medium (HEM). This interaction is, of course, dependent on the self-consistent scheme which is developed above (section 2.4.1). The total strain rate obtained in Equation (2.39) in a crystal can be written as the sum of contributions from all potentially active systems and can be pseudolinearized as follows [94].

$$\dot{\varepsilon}_k = \left\{ \dot{\gamma}_o \sum_{s=1}^{s} \frac{m_i^s m_j^s}{\tau_{cr}^s} \left(\frac{m_k^s \sigma_k^{'}}{\tau_{cr}^s} \right)^{n-1} \right\} \sigma_j^{'} = M_{ij}^{c(\sec)}(\sigma^{'}) \sigma_j^{'} \tag{2.40}$$

Where $\dot{\varepsilon}_k$ is the plastic strain rate of the grain, $\dot{\gamma}_o$ a reference strain rate, τ_{cr}^s a reference stress for the slip system, m^s the geometrical Schmid tensor, σ' deviatoric stress tensor, and $M_{ij}^{c(\sec)}$ is the secant visco-plastic compliance of the crystal which gives the instantaneous relation between stress and strain rate. The relation between the macroscopic plastic strain rate tensor $\dot{E}$ and the macroscopic stress deviator $\bar{\Sigma}'$ can therefore be described by a secant visco-plastic compliance tensor $M_{ij}^{c(\sec)}$

$$\dot{E} = M_{ij}^{c(\sec)} \bar{\Sigma}' \tag{2.41}$$

According to the Eshelby solution for an ellipsoidal inclusion and its approximate extension to power-law materials, one obtains the following relation between the macroscopic stress $\bar{\Sigma}'$ and stress in the grain scale σ' [92]

$$\sigma^{'} = B^c \bar{\Sigma}' \tag{2.42}$$

Where B^c is the accommodation tensor, which also appears in the self-consistency equation

$$M^{(\sec)} = \langle M^{c(\sec)} B^c \rangle \tag{2.43}$$

Here brackets indicate the average over all grains. Provided that the macroscopic plastic strain rate is prescribed, the stresses in each grain are calculated in the following iterative fashion: the iteration is started by making the Taylor assumption that the plastic strain rate in each grain is equal to the macroscopic plastic strain rate. The associated stresses are calculated by solving equation (2.40). Next, the self-consistency equation (2.43) is solved through two nested iterative procedures. In the inner loop, the crystal secant moduli $M^{c(\sec)}$ are calculated according to Equation (2.40), and a Vigot average is calculated as a first guess for $M^{(\sec)}$ [95].

$$\left(M^{(\mathrm{sec})}\right)^{-1} = \langle \left(M^{c(\mathrm{sec})}\right)^{-1} \rangle \tag{2.44}$$

Then the value for $M^{(\mathrm{sec})}$ derived in the previous step is used to calculate the accommodation tensor B^c. Finally, Equation (2.43) is solved iteratively by using the average $\langle M^{c(\mathrm{sec})} B^c \rangle$ as an improved guess for $M^{(\mathrm{sec})}$. The iteration continues until the average becomes equal to the input tensor (within certain limits). Then the inner loop is terminated and the new macroscopic stress is calculated using the new $M^{(\mathrm{sec})}$

$$\bar{\Sigma}' = \left(M_{ij}^{(\mathrm{sec})}\right)^{-1} \dot{E} \tag{2.45}$$

In the outer loop, the stress in each grain is recalculated and the iterations are stopped if the average of the grain stresses coincides with the macroscopic stress and the microscopic stresses converge.

2.4.3 Several challenges

Although Mg alloys are excellent candidates for such applications due to their low density and remarkable noise and vibration dampening characteristics [96], their widespread use has not been yet achieved. The reason for this delay is rooted in the multi-faceted nature of plasticity in Mg alloys that includes plastic anisotropy, tension-compression asymmetry and complex hysteretic fatigue behavior. These phenomena complicate room temperatures Mg based alloy forming procedures, a necessary condition for mass industrial fabrication. In general, the sheet formability of metals is limited by their resistance to plastic instability [97]. In addition, understanding the large strain plastic behavior of sheet alloys along non-proportional strain path, usually leading to Baushinger effect, is an important requirement for sheet metal forming that can be evaluated by fatigue criteria. Additionally, increasing the safety and reliability of structures relies on detailed material characterization and identification of fatigue criteria [98].

Yet, reliable prediction of fatigue durability of structure remains a major challenge in mechanical engineering design [39]. Absence of reliable fatigue life prediction is directly related to the stochasticity of microstructure [99].

To mitigate the lack of fundamental knowledge surrounding the mechanical behavior, modern experimental evaluation based on in/ex situ monitoring has been used for detection, identification and quantification of relations between the microstructure and observed mechanical behavior. However, due to the inability to relate the multiple length and time scales associated with characteristic stages of the mechanical behavior of Mg alloys, no direct link has been formed between microstructural features (grain size, orientation, alloying structure, etc) and properties near yielding and hardening. In particular, the role of deformation twinning in comparison to competitive activation of slip-based plastic deformation is still unknown in most aspects, although, it is expected theoretically to be dominant. The mechanical behavior of Mg alloys is controlled by the activation and development of a variety of slip and twinning modes, which further depend on temperature [100] and crystallographic grain orientation (also known as texture) [64]. Such microscale characteristics are ultimately linked to internal strains and stresses, the evolution of which therefore affects their forming capabilities. Hence, understanding the underlying microstructure-properties-behavior relations can provide critical insights necessary to further develop processing routes suitable for Mg alloys. Based on this context, the objective of the presented investigation is to use in situ deformation observations coupled with both nondestructive acoustic information and microscopic quantification to identify the role of microstructuraldeformation mechanisms in the plasticity of Mg alloys. In particular, a detailed experimental plan is presented to acquire high resolution data that can be used to understand the

role of key microstructural features that affect deformation and damage development and validate relevant model predictions.

2.5 Material Characterization

2.5.1 Acoustic Emission (AE)

Acoustic Emissions (AE) are elastic waves produced by sudden movement in stressed materials, which can be detected with appropriate surface-mounted sensors. The dominant sources of acoustic emissions in materials are defect-related deformation processes such as crack initiation, growth and plastic deformation [101]. Of particular interest to this thesis include crack initiation and growth, dislocation motion, slip, twinning, grain boundary sliding as well fracture and inclusion decohesion. Familiar examples of the phenomenon occur when a twig breaks or a piece of paper is torn. We can hear these examples without the use of specialized sensors since these types of emissions are in the audible range. AE testing differs foremost from other non-destructive testing methods in two significant respects. First, AE testing is passive; this means the energy that is detected is released from within the specimen, rather being actively supplied by the test method, as ultrasonic testing, x-rays or radiographic testing. Second, the AE method can detect the dynamic process associated with the progressive damage development. Material related AE are caused by external stimuli such as changes in load pressure, strain or temperature [102, 103]. In this framework, AE has held promise for quantitative evaluation of the crack initiation and growth in metals during fracture and fatigue. For instance, by finding a correlation between AE hits and the stress intensity factor, a relationship is proposed to predict the crack growth [104]. In addition, several studies have attempted to reframe Paris-Erdogan equation by relating AE parameters such as events, count, amplitude and energy to material behavior [104-106]. In fatigue the crack growth rate can be described using Paris-Erdogan equation

$$\frac{da}{dn} = C(\Delta K)^m \tag{2.46}$$

where da/dn is the change of the crack length per load cycle is (a is the crack length and n is the number of fatigue cycles). Furthermore, Δk is the stress intensity factor range, C and m are assumed to be constant for particular material. These studies suggest a linear relationship between the log of the crack propagation rate da/dn and the log of the AE count rate.

The detectability of the mechanism depends on the amplitude of the elastic wave emitted by the source of background noise over the frequency range of the sensors. To discriminate the AE emission from background noise, data processing techniques are necessary. The first part of data processing includes the Fourier spectral analysis of each recorded AE event. Aspects of spectral signal processing is explained in Ref. [107] and their implementation to AE is reported in Ref. [108]. After obtaining digital time-domain data, Fast Fourier transform is applied to AE waveform in order to convert it to the frequency-domain. Better estimation of AE power spectral density $G(f)$ can be calculated when the noise spectrum $G_n(f)$ is subtracted from each power spectral density $G_i(f)$

$$G(f) = G_i(f) - G_n(f) \tag{2.47}$$

From the AE power spectral density function, the energy and median frequency are computed for each event: E is the energy measured as an integral of $G(f)$ over a whole frequency range of 50-1000 kHz: $E = \int_{f_{\min}}^{f_{\max}} G(f)df$ and f_m is the median frequency given by [109].

$$\int_{f_{\min}}^{f_{\max}} G(f)df = \int_{f_m}^{f_{\max}} G(f)df \tag{2.48}$$

Friesel and Carpenter [110] found that deformation twinning and dislocation glide are the major sources of AE in pure magnesium and AZ31 magnesium alloys. Based on this result Lu et al. [111] associated AE signals with different deformation mechanisms in Mg alloys. AE generated by twinning was characterized by short rise time and high amplitude, both of which lead to the burst type emissions shown in Figure 17b. In contrast, deformation caused by slip results in continuous type emissions similar to the ones displayed in Figure 17a [111].

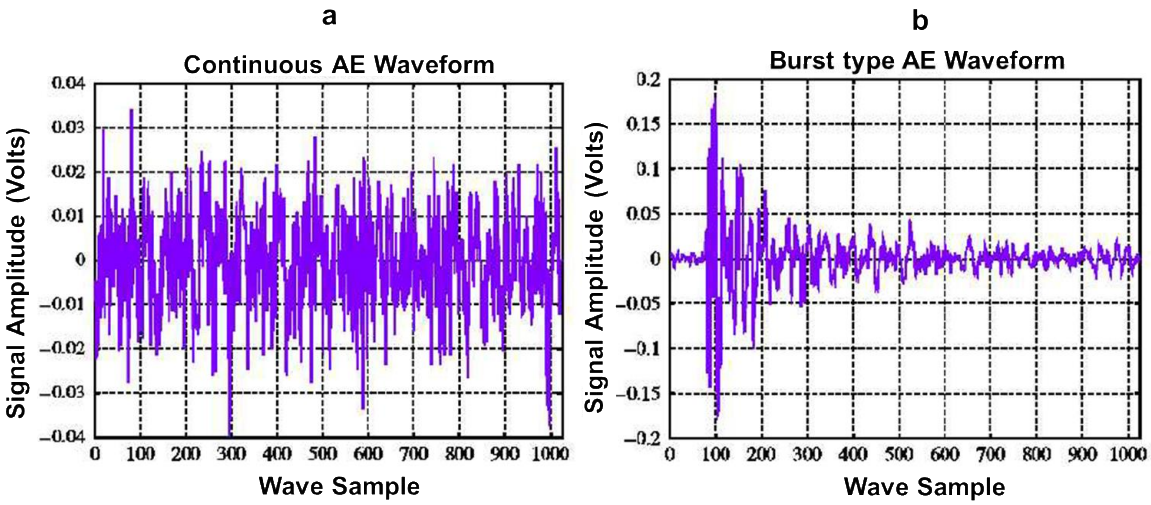

Figure 17 AE signal waveform (a) sliding (b) twinning [111].

The appearance of burst type AE can be conveniently identified by introducing a parameter known as the '*peakedness*' of the waveform in the time domain. This parameter quantifies a shape of a random signal in the same way that the forth moment of a random variable describes the sharpness of its probability distribution. The AE signal is considered as a set of fluctuation of random amplitude U_j, mean amplitude $\bar{U}$ and variance σ_U^2. Thus, kurtosis (q) of the AE signal as given in mathematical statistics is [111].

$$q = \frac{1}{N}\sum_{j=1}^{N}\left[\frac{U_j - \bar{U}}{\sigma_U}\right]^4 - 3 \tag{2.49}$$

Processes with normal amplitude distribution, i.e. noise-like continuous signals, have q-values close to zero. Those continuous signals, which have a 'flatter' amplitude distribution than normal, have negative kurtosis. The signals with $q \gg 0$ have the amplitude distribution 'sharper' than normal, and they will be recognized therefore as burst-type signals. The deviation of the positive q magnitude from zero serves as a measure of peakedness of the signal.

First, assume that different sources produce the AE signals with different waveforms and power spectral densities. Since AE is a random process, there will be some scatter in spectra and waveforms that makes it difficult sometimes to distinguish between different sources. This distinction, however, can be feasible by grouping signals of a similar kind. One possibility is to determine all records in terms of a limited number of parameters such as an energy, peak amplitude, median or central frequency, etc., measured in both time and frequency domain, without limiting ourselves to any a priory assumptions concerning characteristics of AE events caused by sources of different nature. Vinogradov et al. [109] proposed a following statistical procedure for unsupervised categorizing or 'clustering'. As a measure of the distance between two events A and B in the n-dimensional space of AE parameters, a simple metric is chosen as

$$r^2(A,B) = \sum_{i=1}^{n} \left(\frac{a_j - b_i}{\sigma_U} \right)^2 \tag{2.50}$$

Where $(a_1, a_2, ...a_n)$ and $(b_1, b_2, ...b_n)$ are the set of parameters of event A and B respectively, and $(\sigma_1, \sigma_2, ...\sigma_n)$ are the standard deviations of these parameters calculated over all data. Several recent works successfully grouped the AE signals generated from microscopic phenomena using a similar approach, for example see references [109, 112, 113].

2.5.2 Digital Image Correlation (DIC)

DIC is one of the most widely used methods for collecting surface strain measurements and for detection and examination of surface damage, which are particularly important because of their relationship to materials and structural failure mechanisms. DIC technique directly provides full-field 3D displacements to sub-pixel accuracy and full-field strains by comparing the digital images of a test object surface acquired before, during and after deformation. Principally, the 3D image correlation stems from the combination of two-camera stereo imaging and photogrammetry. A random or regular geometric pattern with strong contrast is applied to the surface of the test object (Figure 18). The test object is then monitored continuously as it deforms, while surface correlation areas known as facets or subsets (typically 5-20 pixels squared) are tracked with sub-pixel accuracy. Importantly, DIC can be used to estimate the components of the displacement field as defined by continuum mechanics. Thus, in order to describe the numerical procedure for deformation analysis using DIC, we will consider a small subset of the object centered at point P before deformation. After deformation, the subset center moves to point p. In order to compute displacement of point P, "*square reference subset"* is suggested. A square subset is preferred rather than an individual pixel because the grayscale value of single pixel can also be found at thousands of other pixels, meaning there is no unique solution. By choosing a subset, we can comprise a wider variation in gray level which will be distinguishable from that of other subsets and thereby more uniquely identifiable in the deformed image. In accordance with the deformation definition (displacement formulation in continuum mechanics), the intensity values at positions P and p (Figure 18) can be expressed as

$$F(P) = F(X, Y) \tag{2.51}$$

$$f(p) = f[X + u(P), y + v(P)] \tag{2.52}$$

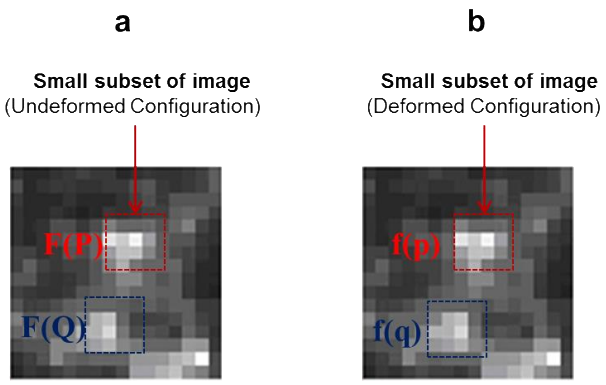

Figure 18 Intensity field for un-deformed and deformed configurations.

Similarly, for point Q at position $(X+dX, Y+dY)$ on the object prior to deformation, the position after deformation can be given by

$$F(Q) = F(X+dX, Y+dY) \tag{2.53}$$

$$f(q) = f[X+u(Q)+dx, Y+v(Q)+dy] \tag{2.54}$$

Finally, an assumption is made that $F(Q) = f(q)$ (i.e., that the intensity pattern deforms without altering its local value due to deformation). Therefore,

$$f(P) = f[X+u(P), y+v(P)] \tag{2.55}$$

$$f(Q) = [fX+u(Q)+dx, Y+v(Q)+dy] \tag{2.56}$$

Accordingly,

$$f[q] = f[X+u(P)+\frac{\partial u}{\partial x}(P)dx+\frac{\partial u}{\partial y}(P)dy+dx, Y+v(P)+\frac{\partial v}{\partial x}(P)dx+\frac{\partial v}{\partial y}(P)dy+dy] \tag{2.57}$$

Thus, if displacement of the center point P of a subset is known, $\frac{\partial u}{\partial x}(P)$ and $\frac{\partial u}{\partial y}(P)$ can be calculated. As a result, the position of any nearby point p and q is determined. Full field displacement, and consequently strain calculations, provides the necessary global and local density of data required to quantify material behavior and assist in the development of realistic models.

2.5.2.1 Measurement reliability

It is reasonable to assume that the shape of the reference square subset changes in the deformed image. However, based on the assumption of deformation continuity in a solid deformable object, a set of neighboring points in a reference subset remains as neighboring points in the target subset. Before evaluating the similarity between references and after deformation, the light fields intensity of these points must be calculated. Given the assumption above, sub pixel interpolation schemes such as bilinear and polynomial interpolation are suggested [114]. Then, to evaluate the degree of similarity between the reference subset and the deformed subset (gray intensity changes), a Cross-Correlation (CC) or Sum-Squared Difference (SSD) correlation criterion must be defined. Pan et al. [115] reported commonly used CC and SSD algorithm and the interested readers are referred to this reference. The accuracy of subset domain can be evaluated by a fine pixel by pixel search routine. In Fourier domain, the correlation between two subsets is calculated as the complex multiplication of the first subset's Fourier spectrum by the complex conjugate of the second subset. The aforementioned methods can be applied accurately to most displacement cases. The complexity occurs when a large distortion takes place between two subsets, by which some pixel of the reference subset goes away from the deformed subset. Figure 19a displays a simple case of displacement, when only rigid body motion is involved [115]. As it can be observed, if only rigid body motion exists between the reference and deformed subsets, a single peak can be found in the correlation coefficient distribution. Conversely, when a 20^{o} relative rotation occurs between the reference image and the deformed image, there will not be a single sharp peak in the correlation coefficient distribution map (see Figure 19b). As noted, pixel displacement searching becomes a challenging task when a significant displacement takes place. To address this particular concern, it is critical to develop a

matching algorithm that can accurately measure the correct correspondence between subsets, even if the intensity values undergo significant changes.

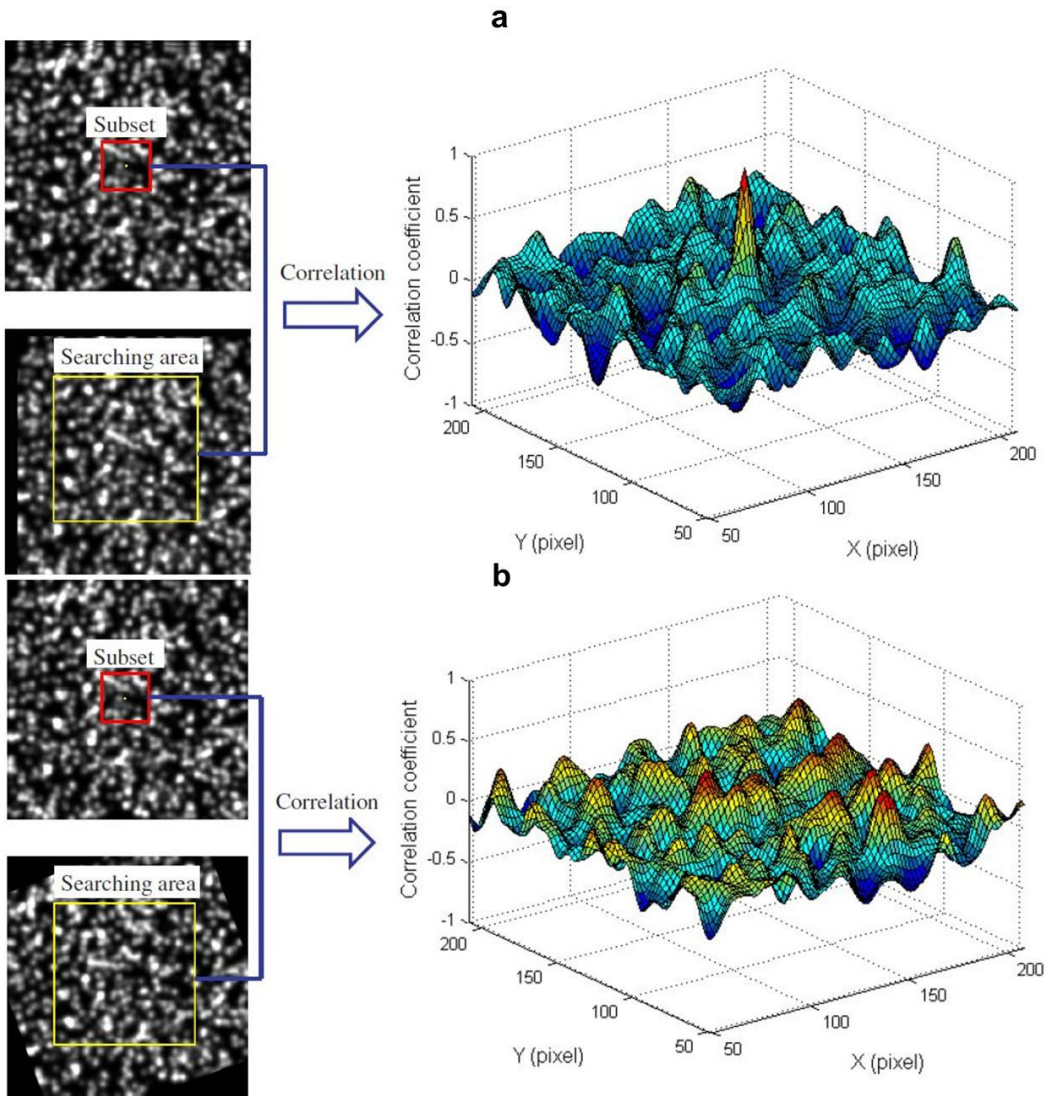

Figure 19 Computed whole-field cross-correlation when the deformed image is subjected to (a) rigid body motion, and (b) 20° relative rotation [115].

As specified, the SSD method is one of the optimization criteria than can be used for template matching [116]. Principally, the intention is to determine how far the original subset moves. It is found that the SSD motion estimation method, which is based on minimizing the grayscale value

difference between a small subset from on the template (reference) image and the displaced image, works well. Sutton et al.[116] implemented this method by assuming that no lighting changes occur between two images, i.e., the template and its displaced version differ by Gaussian random noise. Referring to Figure 18, the image template is represented by F , and the image after displacement by f . In order to minimize the squared difference in gray values, known as SSD, over a neighborhood [116]

$$\bar{d}_{opt} = \arg\min \sum \left| f(x+\bar{d}) - F(x) \right|^2 \tag{2.58}$$

To solve for the optimal displacement vector ,an iterative algorithm obtained by expanding the function into first-order Taylor series is suggested [116]

$$\chi^2(\bar{d}_x + \Delta_x, \bar{d}_y + \Delta_y) = \sum \left| f(x+\bar{d}) - \frac{\partial f}{\partial x}\Delta_x - \frac{\partial f}{\partial y}\Delta_y - F(x) \right|^2 \tag{2.59}$$

Where $\bar{d}_x$ and $\bar{d}_y$ indicate the current estimates for the average motion of the subset. Here, Δ_x and Δ_y are the incremental motion updates sought in the current iteration. Taking the partials of (2.59) with respect to Δ_x, Δ_y and setting them equal to zero to yields the following linear system for incremental updates of each iteration.

$$\begin{bmatrix} \Delta_x \\ \Delta_y \end{bmatrix} = \begin{bmatrix} \sum \left(\frac{\partial f}{\partial x}\right)^2 & \sum \frac{\partial f}{\partial x}\frac{\partial f}{\partial y} \\ \sum \frac{\partial f}{\partial x}\frac{\partial f}{\partial y} & \sum \left(\frac{\partial f}{\partial y}\right)^2 \end{bmatrix}^{-1} \begin{bmatrix} \sum \frac{\partial f}{\partial x}(F-f) \\ \sum \frac{\partial f}{\partial y}(F-f) \end{bmatrix} \tag{2.60}$$

Equation (2.60) can be used to iteratively improve the estimate average motion in the p^{th} iteration using $\bar{d}^{\,p+1} = \bar{d}^{\,p} + \Delta$ until convergence to the optimal motion vector $\bar{d}_{opt}$ is reached.

2.5.2.2 DIC to measure macro-scale strain field

As specified, DIC is a method that identifies 3D-coordinates of surface points, extracting displacement fields and strain distributions by correlating subsequent sets of the image's surface coordinates. In addition to measuring full-field strain, DIC can be also used to detect localized plastic instabilities such as the Potevin-Le Chatelier (PLC) effect or fatigue-induced damage, and monitor their evolution. In this framework, Halim et al.[117] studied PLC banding as a function of prior deformation under positive strain rate sensitivity of Aluminum AA5754 alloy. A series of full-field strain maps obtained from DIC measurement on the surface of the tested sample (12.5 mm width and 1500mm length) in different conditions is provided along, with the stress-strain map in Figure 20. In the interest of the current section, which is to analyze the nature of DIC-measured mechanical properties of materials, only two testing conditions will be presented (details can be found in Ref.[117]). Nevertheless, few points should be brought up; including the fact that the mechanical response of this material depends on the strain path, as shown in Figure 20. Moreover, the PLC effect is manifested by the serrated stress-strain curve occurring over the whole range of stress-strain map. Figure 20A shows that the amplitude of the serrations increases as the strain rate decreases. Figure 20b demonstrates the full-field strain map for the sample tested at room temperature with strain rate of $6\times10^{-4}s^{-1}$; and Figure 20c represents the similar measurement for a sample pre-strained up to a true strain of 0.15 with a strain rate $6\times10^{-4}s^{-1}$. The obtained strain maps unambiguously differentiate the nature of PLC bands. The computed full-field strain map shows that in the none pre-strained samples, PLC bands are nucleated at random locations followed by discontinuous short-distance propagation. On the contrary, random nucleation of PLC bands is replaced by distinct propagation of single deformation bands in the pre-strained samples.

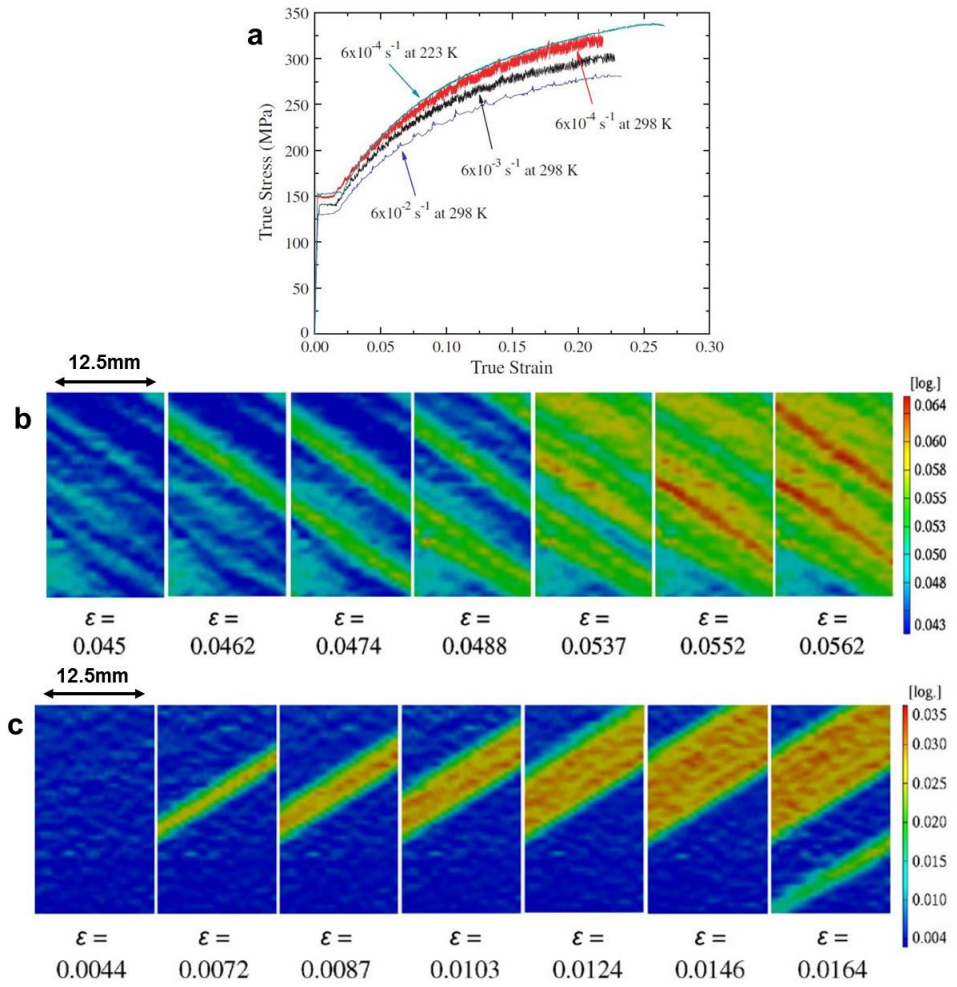

Figure 20 (A) true stress-strain curve of Al AA5754 alloy at various strain rates and temperatures. The recorded serration is manifested by PLC banding. (b) Full-field train map for the sample tested at room temperature with strain rate of 6×10-4s^{-1}. PLC banding is observed which is marked my nucleation of deformation band. (c) Full-field sample pre-strained up to a true strain of 0.15 with a strain rate 6×10-4s^{-1} followed by loading. It suggest a distinct deformation band [117].

In addition, DIC has been also suggested for detecting fatigue-induced damages. For instance, the in situ DIC analysis presented in Figure 21, depicts the damage evolution on the side surface a miniature dog bone shape fatigue specimen (8mm×3mm×1.5mm) of a UFG IF steel, under cyclic stress-controlled conditions.[118]. The crack initiation site is detected by monitoring the high strain localization zones with DIC. These result shows that DIC is capable of capturing damage features associated with highly localized strain along with full-field strain.

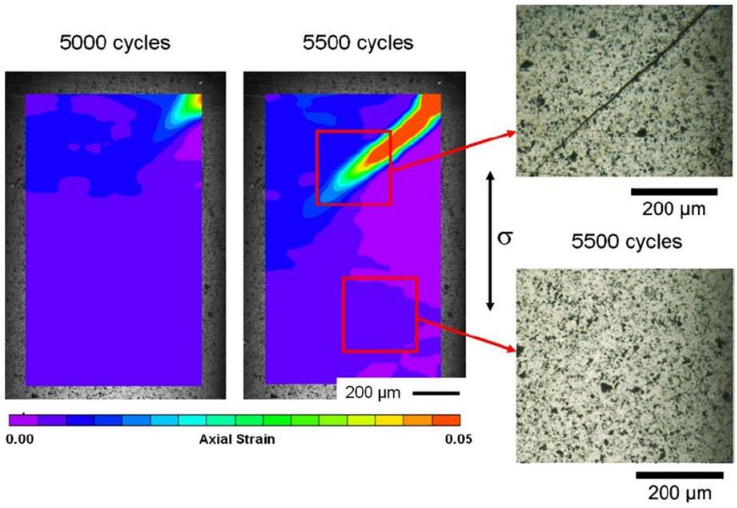

Figure 21 DIC images displaying the evolution of local strain fields on the side surface of IF steel sample the images were captured at the maximum stress level of 450MPa. Two optical micrographs are presented: the upper micrograph displays the vicinity of the crack tip; the lower micrograph shows an un-cracked reference area. The black arrow shows the loading direction for all images [118].

2.5.2.3 DIC to measure micro-scale strain field

The attractive feature of the image matching method is that it is scale independent, permitting full-field strain measurement at the micro-scale. Therefore, DIC can be employed as a practical non-contact tool to obtain accurate *ex situ* and *in-situ* full field strain measurements at grain scale in a single- or poly-crystalline material. Such grain scale information can be used to quantify full-field measurement of plastic strain caused by the operation of crystallographical events and their intimate effect on the neighbors and develop a microstructure-sensitive model, which has potential to better predict the material behavior than continuum-based models. When material characterization requires complex strain field measurement such as nonhomogeneous strain development, use of a specific technique is necessary. DIC can be directly used for quantitatively determining the deformation field and characterizing the deformation mechanisms of various material classes. Moreover, this technique has been suggested for measuring in-plane strain in presence of a strain gradient [119]. In the present section, to demonstrate a quantitative analysis of the interaction between microstructure and local strain, three examples of coupling of DIC

results with local orientation measurement are provided. First, the effect of neighboring grain orientation on elastic-plastic strain accumulation will be discussed. Next, the effect of plastic strain development on surface roughening and fatigue crack characteristics will be surveyed. These examples are selected because their objective aligns with the focal objective of this thesis.

Carroll et al.[120] examined the evaluation of heterogeneous deformation in 99.9% pure tantalum by paying particular attention to correlate effective strain to the crystallographycal information by loading the tensile sample inside the SEM. Prior to the loading, the local orientation of the grains was measured using EBSD (see Figure 22a). The sample was deformed to 25% of strain incrementally in six steps. At each load level, the targeted microstructure was imaged and the collected images are utilized to compute local strain field. Figure 22b illustrates effective strain ε_{eff} obtained from all three measured strain components, $\varepsilon_{xx}, \varepsilon_{yy}, \varepsilon_{xy}$ into a scalar quantity (the mathematical algorithm of this calculation will be given in chapter 6). Specifically, Figure 22b shows the effective strain field of for the targeted microstructure at 25% applied axial strain. The results show a distinct strain distribution, even within the grains. It is noticeable that the strain fielded is considerably heterogeneous as some regions were 0% strain, while the neighbor may experience strains as high as 50%. Note the macroscopic strain in the experiment is 25%. As noted earlier, EBSD data can be further used to determine local crystallographic slip preferences. This possibility enabled Carroll and coworkers [120] to obtain a statistical correlation between the average effective strain (Figure 22b) and Schmid factor on the $\{110\}\langle 111\rangle$ slip system, shown in Figure 22c. The result of this correlation is given in Figure 22d, where the average effective strain within each grain is plotted against the Schmid factor.

The same correlation for other slip systems is reported in the same reference, highlighting the contribution of $\{110\}\langle 111\rangle$ on effective strain.

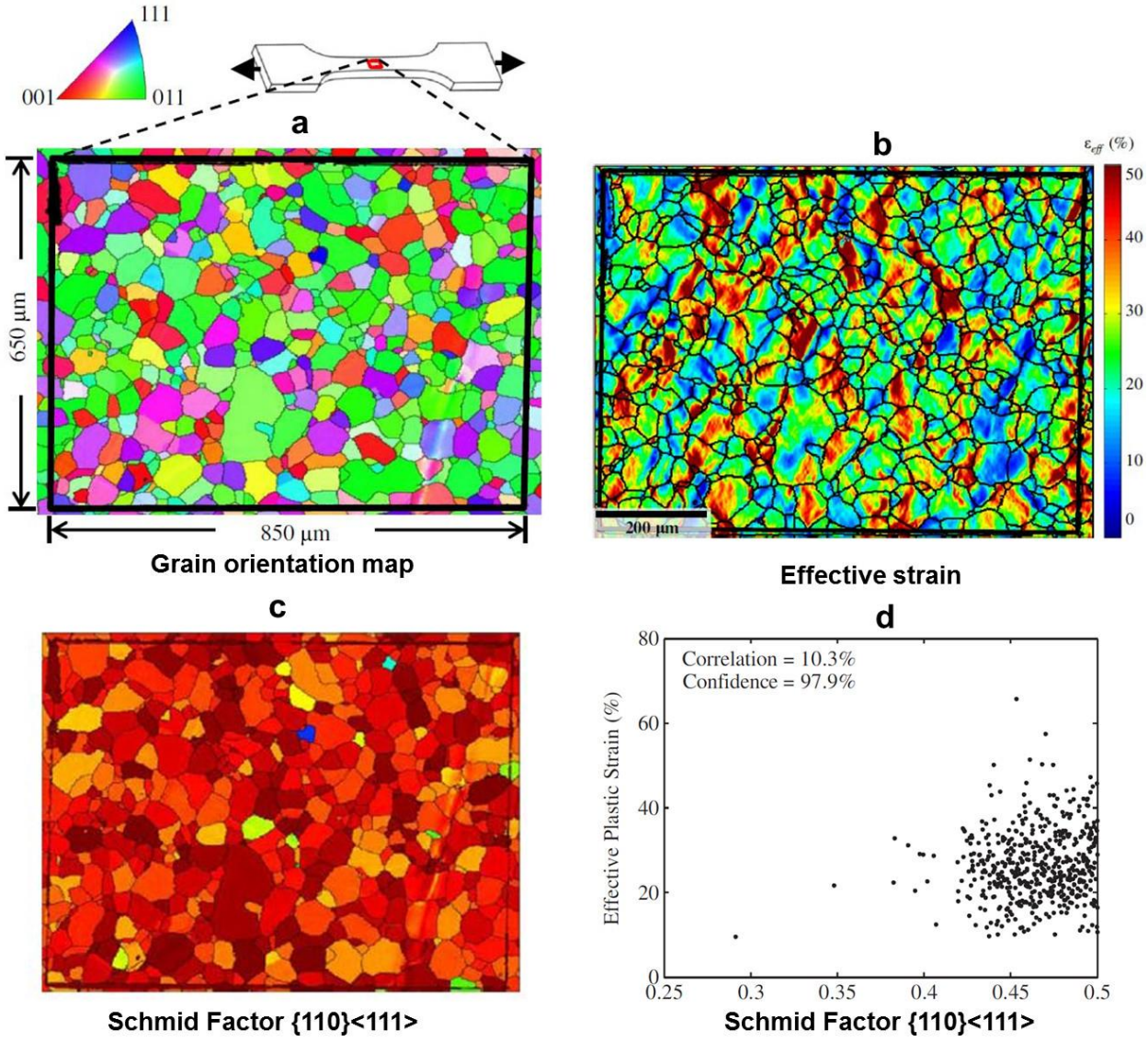

Figure 22 (a) Grain orientation map for the pure polycrystal Tantalum with respect to the loading axis. (b) Effective strain field, ε_{eff} in the specimen at 25% applied tension strain. (c) Schmid factor for slip in the $\langle 111\rangle$ direction on the $\{110\}$ plane. (d) Correlation between the average effective strain within each grain as a function of Schmid factor for $\{110\}\langle 111\rangle$ sip system [120].

One of the major impacts of non-uniform strain distribution at micro scale level is to induce surface roughening. Zhao et al. [121] addressed this concern by recording the history of strain

localization, surface roughening microstructure parameters and in-grain fragmentation during deformation for the region of interest simultaneously. To accomplish this goal they strained tensile specimens made of a pure aluminum consisting of a quasi-2D layer of grain. In this example, load was continuously applied and the digital images were taken at 10s intervals. To capture the development of strain localization, speckles pattern were placed on the surface using a fine paint mist. In addition, 3D surface topography of the specimen was measured and correlated to the grain orientation shown in Figure 23a. The evolution of the plastic strain field at different stage of the strain obtaining by DIC is displayed in Figure 23b. The strain field shows an instant localization effect at the grain number 6 (labeled in Figure 23a). It is evident that the localization progressively increases as strain increases, whereas the plastic heterogeneity appears to be subtle in the other grains. It is pointed out that this localization is mostly arises from the interaction between the grains (strain incompatibility). Figure 23c presents the overall roughening profile on the surface after 10.50%. A significant surface difference is observable in grain 6, overlaid with the reported localization in the same grain. Notably, a strong softening tendency is also reported in grain 6. According to the EBSD results, the Schmid factors for all the grains are comparable, indicating that the grains should have a similar softening/hardening property. Therefore, other parameters such as grain boundary misorientation or the geometry of grain boundary may account for this observation [121].

As discussed earlier, it is of great interest to identify and quantify the interaction between crack growth and the microstructure. One possible way to achieve this goal is to compute the resulting strain field from various deformation mechanisms (slip and twinning), which are associated to the plastic instabilities, and thus to measure driving force for fatigue crack initiation and growth. The following work is constructed on microstructural measurement from EBSD, aligning with

deformation measurement from DIC, to investigate accumulated plastic strain near a growing fatigue crack in Nickel based super-alloy.

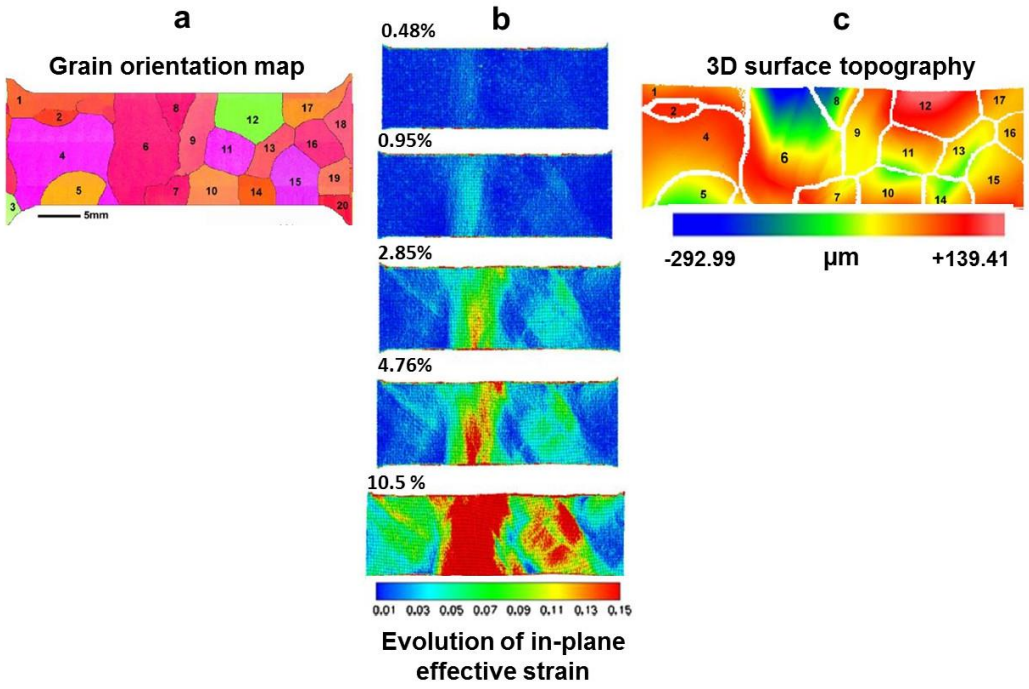

Figure 23 (a) surface grain orientation measured by EBSD. (b) Evolution of in-plane effective strain on the surface during tensile test. The strain map is computed by in situ DIC. (c) Roughening profile after 10.5% strain (tensile test). Surface topography is obtained using a-light confocal microscope [121].

This is accomplished by cyclically loading of the pre-notched customized tension sample. So, the EBSD is collected prior to the loading and crack is induced by fatigue loading. DIC data is collected at each stage of loading (A-F) and each image in these sequences is correlated to its corresponding image at zero load. The crack length and number of cycles for each of the specimen removal times are denoted A-F and shown in Figure 24a. The effective plastic accumulated strain associated with fatigue crack growth between image times C to D, D to E and E to F, are presented in Figure 24b. As crack grows from point C to D, strain is accumulation is visibly larger below the crack than that above the crack. During D to E, the crack generates large amount of strain above the crack. From E to F strain accumulation above the crack is relaxed and

addition strain accumulation appears below the crack. Apparently, effective plastic strain relaxes as the crack grows. The microstructure in response to the crack growth is demonstrated in Figure 24c. From this plot, transgranular crack growth characteristic can be seen, although there is some point where the crack growth occurs along the grain boundaries. In Figure 24c, the crack is seen to alter the direction as it meets a twin boundary marked with black arrow). This direction change is expected since the twin boundaries are of strain accumulation [122].

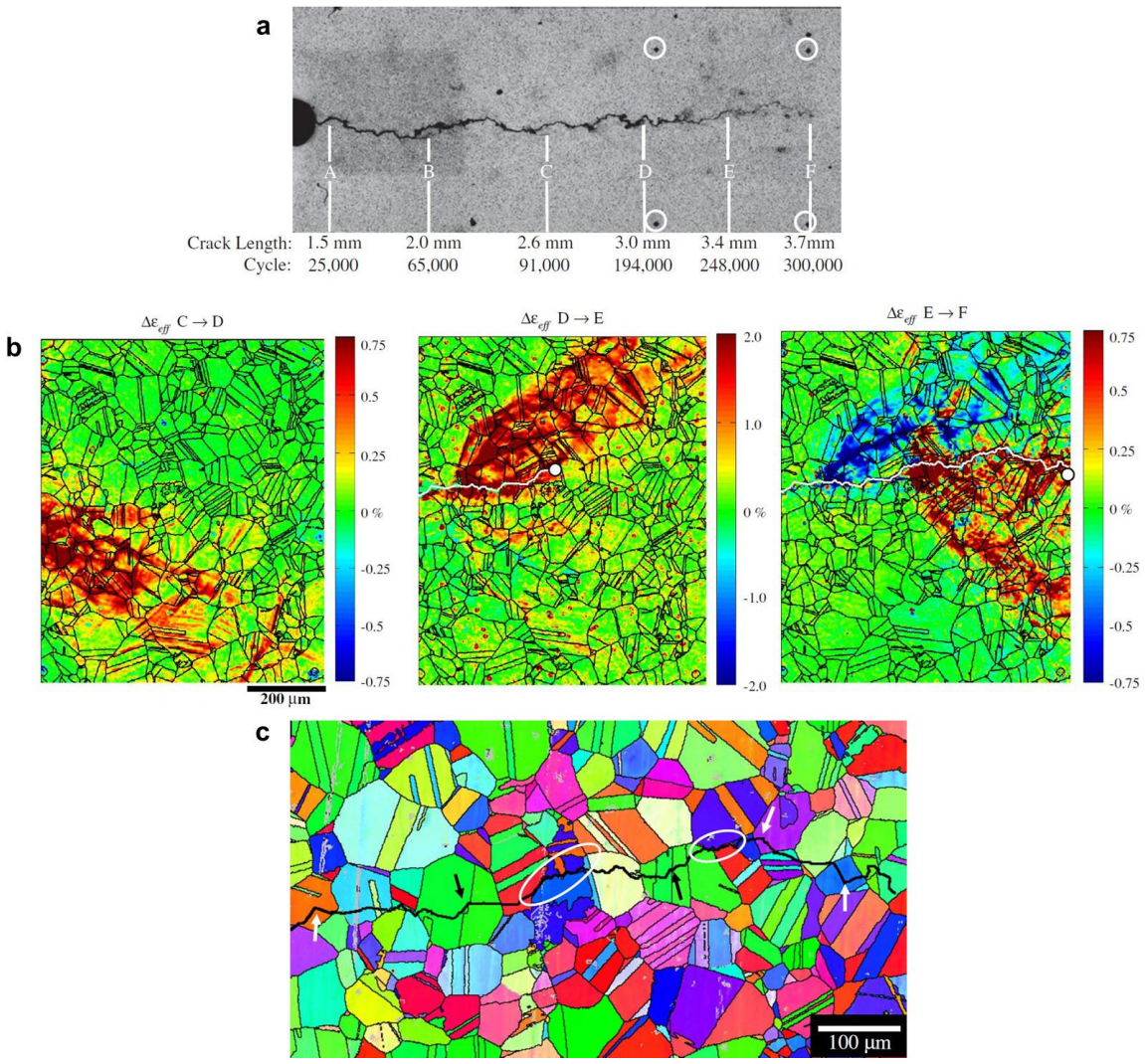

Figure 24 (a) Crack path at the tip of the pre-notched sample. The specimen was removed from the load frame at crack tip location (A to F). (b) Increments in effective plastic strain for different time intervals as indicated it above. (c) Surface crack path in relation to microstructure. Abrupt changes in crack direction are marked by white arrows, while changes in crack direction at twin boundaries are marked by black arrows. The region where intergranular crack growth was detected is circled [122].

In other instances, the directional change of the crack occurs in the middle of a grain at a considerable distance from boundaries (although there may be twin boundaries present at those locations at a length scale below the resolution of these EBSD measurements). This occurs several times within the small section of material here as indicated by white arrows. In most of these instances, the crack direction follows slip bands at a steep angle compared to mode I loading. This direction eventually becomes less energetically favorable and then the crack changes direction to follow a different slip band within the grain that is more closely aligned with the mode I direction [122].

2.6 Microscopy

Microscopy refers to the study of objects that are too small to be easily viewed by the unaided human eye. Accordingly, microscopes are devices that are used to magnify small objects. They come in a very wide range of shapes and sizes, and use many types of illumination sources such as light, electrons, ions, x-rays and mechanical probes, coupled with signal processing techniques to produce images. Some techniques yield qualitative information, such as an image of a surface, while others yield quantitative information such as the relative orientation of crystals in polycrystalline aggregates; the selected method depends on the nature of the investigation. This section will briefly introduce both the quantitative and qualitative techniques that are used to analyze the measured mechanical behavior in this study. The theoretical aspects and complete descriptions of these techniques can be found in many material characterization textbooks; see [123, 124].

2.6.1 Optical Microscopy

In an optical microscope, light passes through an objective lens which, if at the proper distance from the surface, will form an image of the surface to further magnify the observed image; this light passes through another lens, finally focusing on the retina of the eye. However, modern microscopes allow more than mere observation of transmitted light images of a sample. There are many techniques becoming available which can be used to extract other kinds of data; most of these techniques requiring equipment beyond that of a basic compound microscope. For instance, Confocal Microscopy (CM) or Optical Interferometry (OI) can produce quantitative descriptions of topographical details. Light interferometry systems offer fast, non-contact, high-precision 3D metrology of the surface features, capturing intensity data at a series of points along the vertical axis, determining where the surface is located by using the shape of white-light interferogram, the localized light of the interferogram, or a combination of both shape and phase. The white light interferogram actually consists of the superposition of fringes generated by multiple wavelengths, obtaining peak fringe contrast as a function of scan position. The ability of light interferometry systems to create sharp optical sections makes it possible to build 3D renditions of specimens from 2D images. Data gathered from a series of optical sections imaged at short and regular intervals along the optical axis are used to create the 3D reconstruction.

Diffraction of light determines the resolution limit of optical microscopes, roughly equal to a wavelength. For white light, the average wavelength is around 500nm, thus the best achievable resolution is a few hundred nm.

2.6.2 Electron microscopy

Electron waves are a unique medium that can be used in imaging. By accelerating electrons into a high energy beam (via a high voltage), the resulting wavelength is far shorter than that of white

light. For example, considering an electron beam produced from a 20kV gun, the wavelength is only 1240.7/20000(eV) = 0.06nm, corresponding to a resolution limit of $\lambda/2=0.3A^{o}$- theoretically implying that it can image species as small as 0.3 A^{o}. The generated high energy electrons (typically 5-40keV) penetrate the surface of specimen and interact with the atoms of material in a variety of elastic and inelastic scattering processes. Scattering continues until either the electrons escape from the specimen, or are absorbed by the material itself. Multiple scattering will result in a certain volume of material (the interaction volume) being irradiated, for instance see Figure 25 [125]. Note the diameter of this volume is much larger than the diameter of incident beam. As illustrated in Figure 25, a variety of signals are generated as a result of scattering. Secondary Electron (SE) are used to produce the classic electron microscopic images. This mode provides high-resolution imaging of surface and it's independent of the atomic number of the scattering atoms.

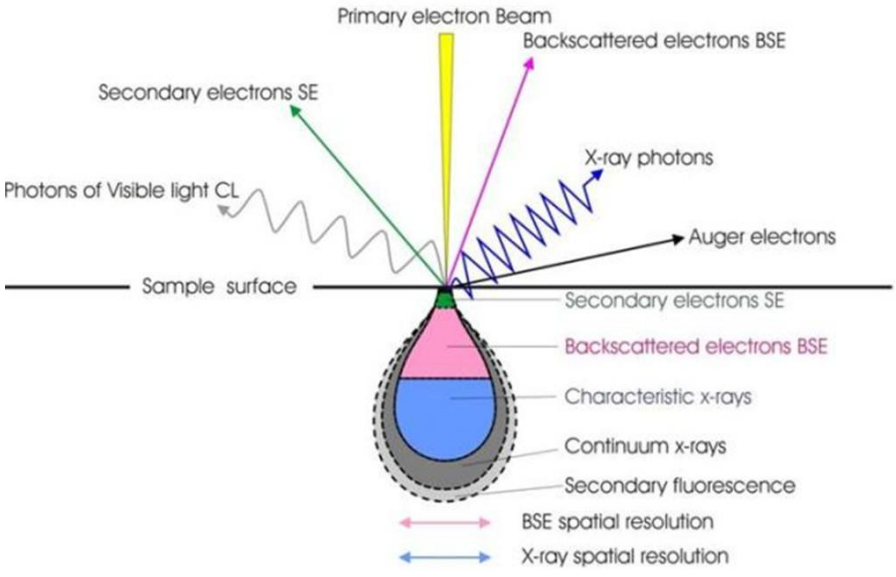

Figure 25 Interaction volume showing regions in a specimen that are primary source of secondary electrons, back-scattered electrons and x-ray in SEM

In addition to displaying the bright-field images from SE emission, back-scattered electrons (BSE) in a SEM may be used to determine the crystallography of (poly) crystalline samples. As schematically shown in Figure 25, when the beam penetrates the sample surface, some electrons are elastically scattered back out of the sample, retaining approximately their original energy- referred to as back-scattered electrons (BSE). BSE signals are widely used to examine the crystallographic orientation of materials. Unlike the SE mode, the number of backscattered electrons reaching a backscatter detector is proportional to the mean atomic number of the specimen. To do this, a flat/polished sample is placed in the SEM chamber at a tilted angle (70^o from the horizontal) towards the diffraction camera. The recommended 70^o angle degree is considered ideal because it maximizes the yield of backscattered electrons in the direction of phosphor screen. Hence, the tilted sample optimizes both the contrast in the diffraction pattern and the fraction of electrons scattered from the specimen. When the electrons impinge on the crystalline sample, they interact with individual lattice planes. When these interactions satisfy the Bragg condition, they exhibit backscattering diffraction and (due to the tilted sample) are directed toward a phosphor screen, where the CCD camera detects the fluorescent pattern. The resulting pattern consists of a large number of intersecting bands, known as Kikuchi lines, which represent the unique crystallographic properties of the crystal. Specifically, select crystallographic planes within the material, following Bragg's law, diffract the electrons. When a phosphor screen is placed in the SEM chamber, the diffracted electrons fluorescence the phosphor as they impact the screen. This phenomenon is schematically shown in Figure 26a. This interaction leads to the formation of a band pattern composed of "Kikuchi lines", characteristic of the sample crystal structure. Figure 26b illustrates the formation of a backscattered Kikuchi pattern by EBSD in SEM for a Copper sample [126]. Interpretation of the

Kikuchi patterns, needed to determine the crystallographic orientation of the sampled volume, is performed in two consecutive steps. First, the pattern has to be indexed, which means that the crystallographic indices of the Kikuchi bands and poles (more precisely, of the corresponding lattice planes) have to be determined. Next, the relative positions of the bands or poles with respect to an external reference frame - the crystallographic orientation of the sampled volume with respect to the specimen axes – will be redefined. Interested readers are encouraged to see Ref. [126]. Kikuchi patterns are analyzed automatically using commercially available software packages, especially in SEM settings.

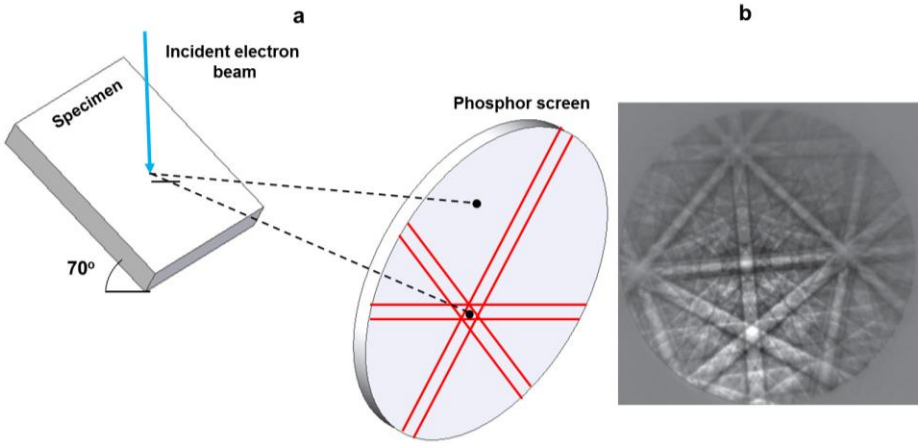

Figure 26 (a) Formation of backscattered Kikuchi patterns br EBSD in SEM. (b) Kikuchi pattern by EBSD in SEM for a Copper [126].

A Kikuchi diffraction pattern presents valuable information, such as lattice strains and grain/phase boundaries, which enables discrimination between low-angle boundaries from high angle types, and the estimation of the grain size distribution. Grain boundaries are characterized by the misorientation axis and angle and the boundary plane. In crystal orientation mapping, a grain is regarded by the collection of neighboring pixel in the map, which has a misorientation less than a certain threshold angle. Although the degree of rotation between neighboring pixels depends on the step size used in the EBSD grid as well as the intergranular rotation in the

sample, cumulative rotations may be discerned. There are several variations in this map, using different measures of intergranular lattice rotation.

One of the most common methods is the *Kernel* type, whereby the color of each pixel in the map a function of the degree of the orientation change with respect to its neighbor (this method is used in the current study). Many engineering materials are an aggregate of randomly oriented crystals and grains. The nature of the grain interface and their orientation is crucial for understanding microstructure-property relationships for alloy design, material characterization, fatigue and failure analysis [127].

The directional variation in diffracted intensities in the specimen is used to describe the orientation of a crystal relative to the embedding body. The graphical representation of the orientation distribution of crystallographic lattice plane is known as a "*Pole figure*". In other words, a pole figure is the density of a specific crystallographic direction with respect to a reference sample. More precisely, it is the frequency of occurrence of a given crystal plane normal per unit spherical area. For example, Figure 27a, considers a cubic crystal in a rolled sheet sample. The pole figure shown in Figure 27c demonstrates the orientation of the $\{110\}$ planes of the targeted crystal shown in Figure 27a with respect to the sample frame. Note that the circle dots shown in the pole figure map in Figure 27c, relates to the crystallographic plane with corresponding colors in Figure 27b. Whereas the pole figure shows sample directions aligned with a particular crystallographic pole, an "*inverse pole figure*" does the opposite, indicating the crystallographycal poles aligned with a specified sample direction[127]. Several examples with invoking the inverse pole figure will be presented in sections 4 to 7. This is often of interest for samples in which the processing history identifies a single direction, e.g. uniform distribution of HCP unit cells in wrought Mg alloys.

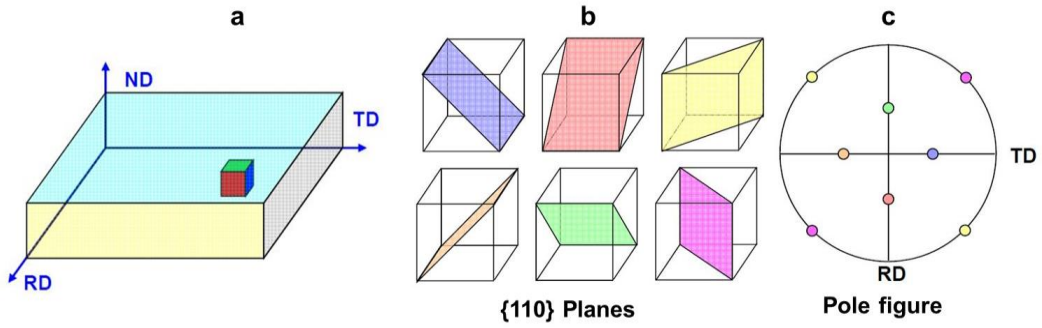

Figure 27 (a) A cube crystal embedded in a hypothetically drawn rolled sheet. (b) $\{110\}$ planes in the cubic structure. (c) Pole figure shows the orientation of a given plane in Figure 27b normal with respect to the sample axis. Note that the circle dots shown in the pole figure map in Figure 25c, correspond to the crystallographic planes of matching color in Figure 24b.

2.7 Novel hybrid experimental methodology

In conventional characterization of polycrystalline material behavior, local microstructure effects are usually neglected, as the material is assumed to be homogeneous and isotropic. While this assumption has proven sufficient for several circumstances, it is becoming increasingly evident (experimentally and numerically) that in many cases local microstructural features cannot be neglected [89, 121, 122, 128, 129]. This highlights a necessity for understanding the underlying physics of material deformation at different length scales. This understanding can be used in coupled structural-material design as well as microstructural-based models such as crystal plasticity. While these models demonstrate the capability to model material behavior, their accuracy is quite limited under certain circumstances. For instance, existing meso- and macroscale deformation models that include twinning do not include physical based mechanisms for twin nucleation [68]. Consequently, constitutive models for HCP metals heavily invoke empiricism to capture twins, the number of twins per grain, and the twin morphology. Advances in experimental and numerical techniques have greatly expanded the capabilities of experimental mechanics. The novel systematic characterization method used in this dissertation permits the

monitoring of deformation behavior across different length scales. The system is comprised of: i) mechanical testing targeting two different length scales; in the meso/macroscale a standard servo hydraulic loading frame that provides flexibility in applying complex loading profiles (monotonic and cyclic). In the microscale, a miniature loading stage (MTI/Fullam) that can operate within a SEM chamber or in the presence of optical microscope provides an opportunity to monitor grains embedded in a polycrystalline aggregate as they deform. ii) Mechanical testing was further coupled with both microstructure and in situ NDT characterization techniques. Specifically, ex situ (for MTS frame tests) and in situ (for MTI stage tests) microscopy and texture measurements provided by EBSD. Moreover, AE system (Physical Acoustic) for real time monitoring of volume-related reversible/irreversible changes in the tested material was used in parallel-simultaneously-to a DIC systems (Trilion, GOM) capable of in situ, full-field surface deformation/strain measurement. In addition, the relationship between micro strain heterogeneity and surface roughness in plastically strain tested specimen as function of strain and Schmid's factor was inspected using optical interferometry (3D Optical surface profilometers, Zygo) and atomic force microscopy (high resolution Dimension FastScan, Bruker).

The combination of the volume-inspection AE method with full-field surface deformation/strain measurement DIC technique created a robust characterization method capable of quantifying the relationship between loading induced microstructure evolution and bulk properties. In addition, strain mapping and its relationship to microstructural features, texture evolution, surface topography changes as well as mechanical behavior has enabled the current investigation to identify and quantify critical microstructural parameters that affect overall plasticity and fatigue damage criteria.

Chapter 3

State-Of-The-Art Plasticity and Fatigue Investigations of Mg Based Alloys

3.1 Introduction

The intention of this chapter is to survey recent findings surrounding the plastic deformation of Mg alloys. As specified earlier, the focus of this thesis is to identify and quantify localization and microstructure sensitive parameters that are associated with fatigue crack initiation and fatigue life. Chapters 4 to 7 are devoted to these interests, with more focused literature review related to the topic discussed in each one. Separating literature reviews by chapter was found to be effective and useful, to better connect relevant literature to the current work. The especially strong connection between the author's work to the former studies motivated the composition of the current section, discussing recent promising experimental and theoretical advances in the field which have not been sufficiently discussed elsewhere.

3.2 Deformation mechanisms in Mg Alloys

Plasticity behavior in Mg and its alloys is highly anisotropic. When Mg alloys are deformed under uniaxial tension at room temperature, reasonable elongation of 10-18% can be obtained. However, undesirable cracking occurs with very little reduction in cross sectional area. According to the measured data in single crystal Mg, the CRSS for the $\langle a \rangle$ basal slip system is approximately 1/100 of that for other slip systems, and it is generally accepted that the CRSS

follows the trend $CRSS_{basal} < CRSS_{twinning} < CRSS_{prismatic} \leq CRSS_{pyramidal}$ at room temperature. As

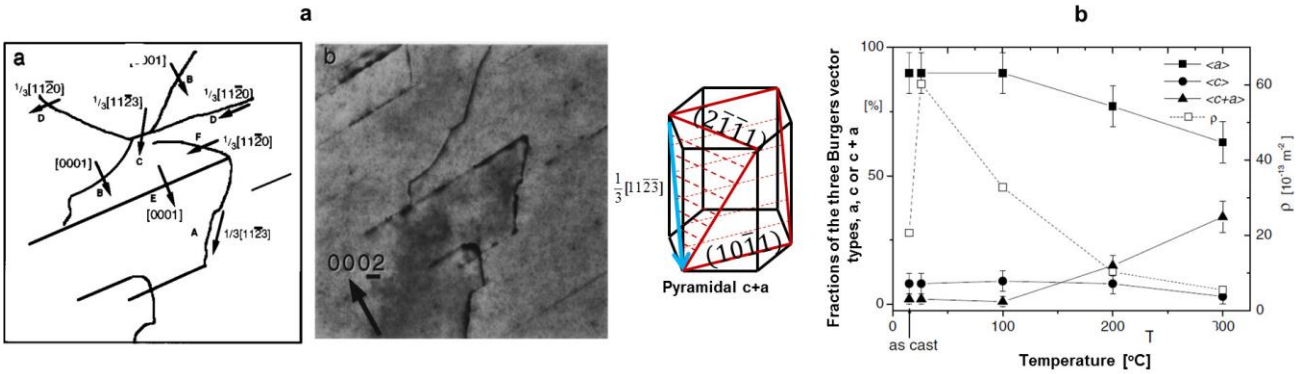

Figure 28 (a) Typical Burgers vector analysis emphasizing the presence of c+a dislocations in the Mg-Li alloy (b) Fraction of the three types Burgers vector types as a function of the deformation temperature [89].

noted, although prismatic and pyramidal slip systems operate in Mg, they require higher driving forces or elevated temperatures. The limited slip planes have been considered to be a major reason for ductility. Plastic properties of Mg single crystals were studied in detail during the 1960s through extensive application of *slip trace analysis*. Yoshinaga and Horiuchi [63] performed compression along the c-axis, but no evidence of non-basal slip was observed. Instead, some twinning mechanisms were observed to precede fracture [78]. *Transmission Electron Microscopy (TEM)* was applied to the problem during 1970s. Such results confirmed non-basal dislocation activity [62]. *Simulation analysis and texture measurements demonstrated* that the $\langle c+a \rangle$ dislocations play an important role in improving the ductility of Mg alloys [130], suggesting that the notable formability of Mg-Li is due to high density and more uniform distribution of $\langle c+a \rangle$ type dislocations (non-basal slip). For example, **Error! Reference source not found.**a shows the distribution of $\langle c+a \rangle$ dislocations in the Mg-Li alloy. Visualization of $\langle c+a \rangle$ type slip systems is presented in **Error! Reference source not found.**. Due to the significant implications of non-basal slip for ductility, *X-ray diffraction peak profile analysis* was

also utilized in **Error! Reference source not found.**b [131]. It was concluded that $\langle a \rangle$ type dislocations dominate up to the fracture point. However, at higher temperatures the fraction of non-basal type dislocations increased. Therefore, the remarkable formability of Mg-Li alloys at elevated temperature is attributed to the high activity of non-basal slip.

It is reported that fine-grained Mg AZ31 alloys can experience up to 40% elongation [4]. In regard to Mg polycrystals, this observation is not expected from the anisotropic data of single crystal Mg. This motivates further investigation of polycrystalline deformation mechanisms characteristics. Koike [132] designed a micro-scale experimental set up to better correlate elongation of the fine-grain polycrystals to the Grain Boundary Sliding (GBS). Figure 28 depicts a Focused Ion Beam (FIB) image of an Mg AZ31rolled sheet deformed to 10% in tension mode at room temperature. Prior to the tensile test, the electro-chemically polished samples were marked with a straight line using FIB. After 10% deformation, a discontinuous, micron-size shift of the lines can be seen at the grain boundary. Thus, it was concluded that the GBS contributes to plastic deformation. This reduction in grain size can explain the improvement of ductility.

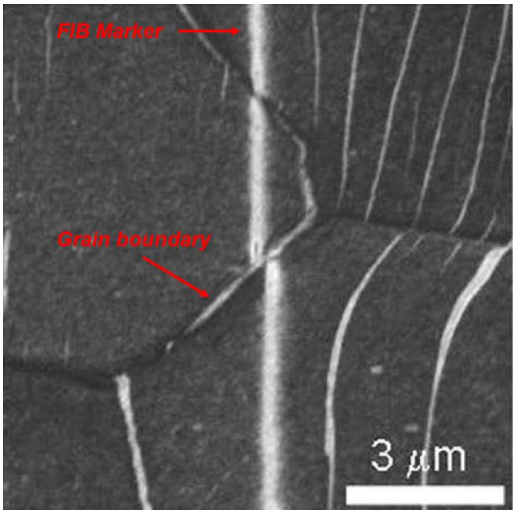

Figure 28 FIB image of a sample surface of AZ31 Mg after tensile deformation to 10% at room temperature. A straight vertical line was drawn by FIB before the test, and appreciably shifted after straining [132].

Grain boundary sliding requires accommodation mechanisms, without which, the microstructure would rapidly form voids as the grains slide past one another, leading to premature failure [133]. Slip is a proposed accommodation mechanism, particularly at room temperature. In this mechanism the deformation climbing along grain boundaries accommodates proceeds by slip and dislocation pile-ups. This produces some sliding across the grain boundaries, and its activation is limited by the climb rate of dislocations. Increasing the slip activities and dislocation pile-ups requires other accommodation mechanisms, which will be discussed in chapter 6. The effect of GBS is a controversial subject. Stanford et al. [133] quantified the contribution of GBS in plastic deformation at room and intermediate temperatures (150^{o}C). According to their findings, there is negligible grain boundary sliding at any test temperature. In contrast, Khan et al.[134] highlighted the contribution of GBS at elevated temperatures. Referencing the work done by Stanford and co-workers [133], the only significant change in deformation behavior between 25^{o}C and 150^{o}C is an increase in the homogeneity of slip at higher test temperatures. It is also concluded that the drop in normal anisotropy with increased

test temperature is unlikely to result from GBS, and more likely to be the result of an increase in pyramidal slip activity at higher test temperatures. Figure 29 shows the surface of the electrochemically polished tensile sample with a FIB grid milled onto the surface. After the grids were deposited, they were deformed to a strain of 0.15 [133]. Figure 29a indicates well-defined individual slip bands in some grains, whilst other regions developed only moderate surface relief in which the individual grains were not easily identifiable. After deformation at 150^{o}C, the grains were all well-defined, and there was little evidence of the highly localized slip banding that was evident at room temperature. The same study also reported that the shear is always larger in the tensile direction than in the transverse direction, with the largest shear occurring in room temperature. It will be shown (chapter 6) that the larger strain components along the loading axis in room temperature could originate from twinning. In that example, the strong effect of twinning on the plastic effective strain will be discussed.

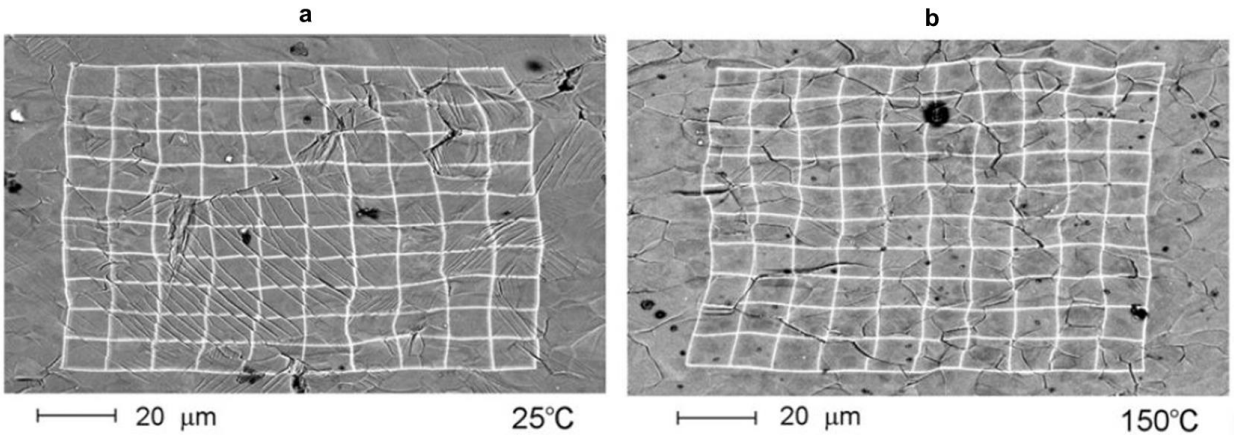

Figure 29 Scanning electron microscopy of the surface relief of a pre-polished surface resulting from deformation to a strain of 0.15 at (a) room temperature. (b) 150^{o}C. Grids with outer dimensions of 100 ×100 µm were deposited before deformation. The tensile direction is horizontal [133].

Moreover, it is reported that the distribution of these grain boundary shears is inhomogeneous and, particularly in the case of room temperature deformed specimens, these shears are found to

be concentrated along the diagonal line from the top left side of the grid where strong localized deformation is evident (see Figure 29) [133].

The evolution of the internal stresses due to the activation of various deformation mechanisms and different twinning variants leads to the non-homogeneous distortion of grains within a deforming polycrystal aggregate. Thus, intergranular strain arises from strain mismatching between grains of different orientations, and is associated with elastic and plastic anisotropy [23]. In chapters 4, 6 and 7, it will be shown that in addition to intergranular stresses resulting from slip and twinning, strong strain heterogeneities arise within the grains. Thus, understanding the underlying mechanisms may provide critical insights necessary to develop microstructure-sensitive criteria for both monotonic and cyclic behavior. Recent studies [49, 135] utilizing the *neutron diffraction technique* have quantified lattice strains and texture evolution caused by slip and twinning in Mg AZ31. One of the first in situ neutron diffraction work on this problem was led by Gharghouri et al. [136], who showed that twinning is primarily controlled by Schmid stresses, and that large, blocky precipitates in a Mg-Al alloy impeded twinning more than they do slip. Further studies by in-situ neutron diffraction were conducted by Muransky et al. [18]. In this study, neutron diffraction patterns were collected in situ by stepwise compressive loading up to 5% of macroscopic strain. These experimental results showed that yielding and immediate post-yielding plasticity in compression along the extrusion direction is governed primarily by twin nucleation, whereas plasticity at higher strains is presumably governed by twin growth and dislocation slip. Considering the importance of neuron diffraction, Figure 30 schematically shows the physical principal that enables collection of in situ diffraction and AE data. The instrument is equipped with a horizontal loading frame, mounted on a positioning table in such a way that its loading axis is oriented 45^{o} to the incident beam. Two detector banks placed on

either side of the load frame, at ±90^{o} to the incident beam, allow simultaneous collection of the full diffraction patterns with scattering vectors. The orientation of a typical grain prior to twinning is shown schematically in Figure 30. The position of the crystal lattice results in strong (0002) peak intensity in the transverse detector, $Q_{\perp}$ and absence of (0002) intensity in the parallel detector, $Q_{\parallel}$. In the given example, the stress axis is initially parallel to the basal plane (perpendicular to the basal pole), which facilitates twinning on the $\{10\bar{1}2\}\langle 10\bar{1}\bar{1}\rangle$ system. During twinning, the basal pole rotates (86.4^{o}), from perpendicular to the loading axis to nearly paralleling the axis. Thus, the transfer of intensity between the two detector banks is a direct measure of the twinned volume fraction and allows monitoring of the development of the twinned microstructure.

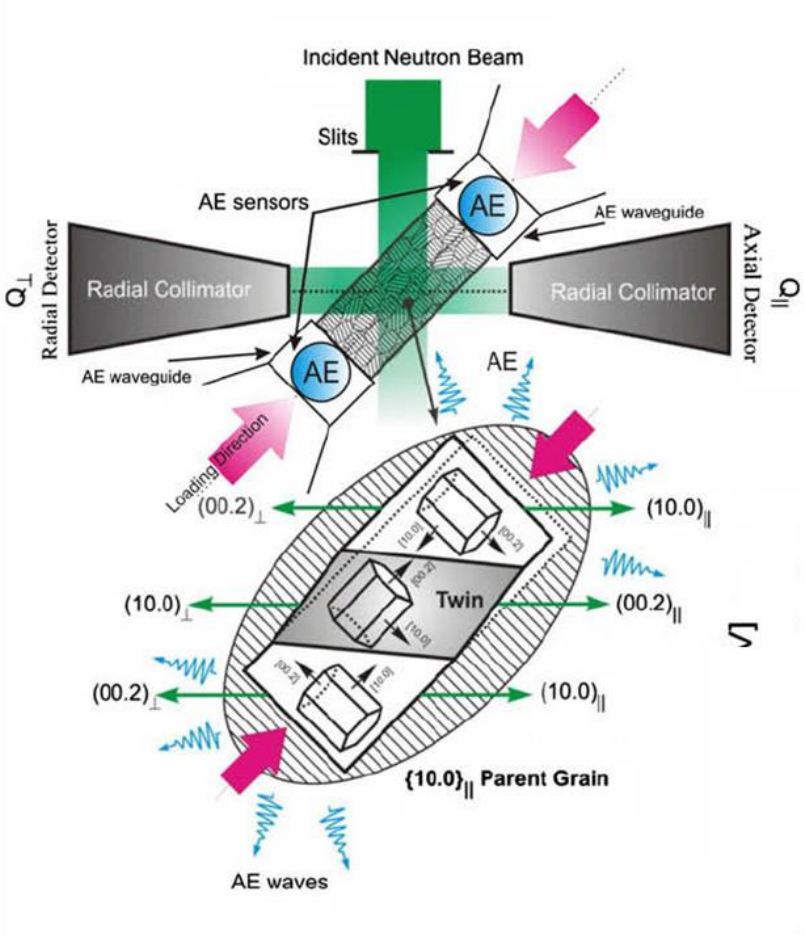

Figure 30 Schematic drawing of the diffraction geometry and the principal of the collecting the in situ neutron diffraction and in situ acoustic data in the same time [18].

Since AE and neutron diffraction information are extracted from separate signals, they can provide independent and complementary information. For example, Figure 31 b&c shows the high activation of twin nucleation at the onset of yielding. Neutron diffraction records multiple lattice plane (hkl) reflections for a specific sample orientation. During loading, neutron diffractograms are obtained at predetermined load intervals. The elastic lattice strain

measurements are calculated from the changes in the spectra peak positions. The average lattice

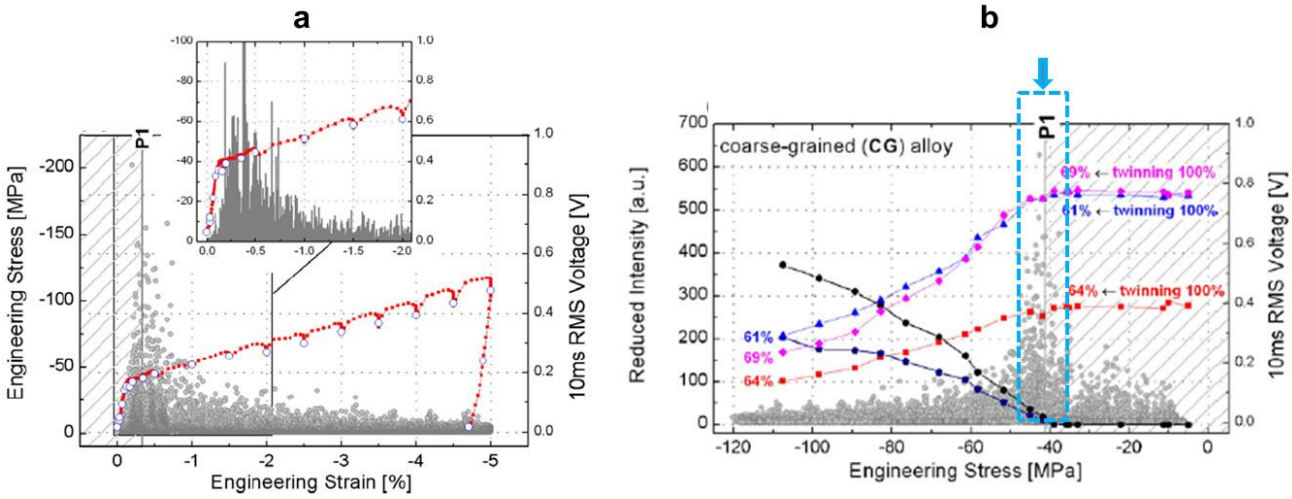

Figure 31 Microscopic stress-strain during in situ compression along the extrusion direction. (c) Twin fraction presented within the grains with respect to the grain direction [18].

strain can be calculated from inter-planar spacing between the loaded and unloaded pattern. The average lattice strain for such grains is given by:

$$\varepsilon = \frac{d^{hkl} - d_0^{hkl}}{d_0^{hkl}} \tag{3.1}$$

here d^{hkl} and d_0^{hkl} are the plane d-spacing in the loaded and unloaded conditions. Since the (0002) diffraction intensity is initially absent from the Q∥ detector, the position in $_d$-space of the initial (0002) diffracted intensity in this detector provides clear information about the initial strain state of the twinned region as they formed [49]. It should be noted that in this approach, each peak is uniquely poised to monitor the volume fraction of twins and the strains within the twins as they form. With such an approach, lack of unstrained lattice peaks and errors introduced by peak fitting result in uncertainties [49].

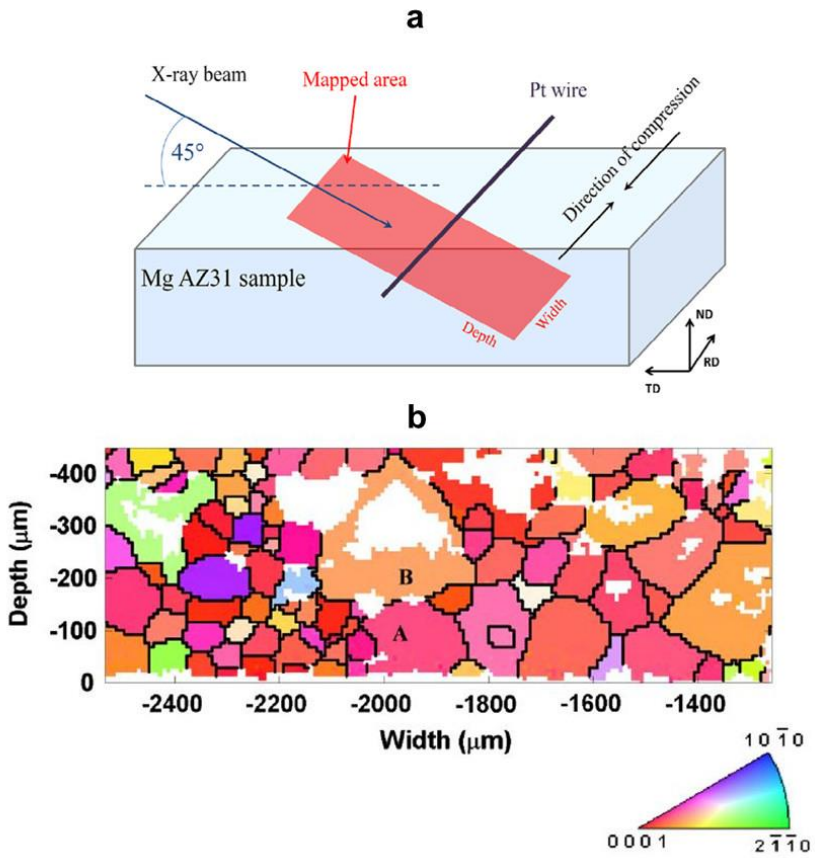

Figure 32 (a) The X-ray beam strikes the surface at a 45° angle and is directed parallel to the "depth" coordinates of the orientation maps. The compression direction is parallel to the surface of the sample and perpendicular to the X-ray beam. (b) Orientation map of the undeformed material reconstructed from Laue diffraction pattern [137].

Balogh et al. [137] measured the strain gradients across a grain containing twinning within the Mg AZ31 polycrystal. Differential-aperture X-ray microscopy (DAXM) is a synchrotron X-ray based technique for collecting spatially resolved diffraction data from the interior of a bulk sample. Depending on the material in question and photon energy, the beam may penetrate several tens or hundreds of microns into the sample. Similar to neutron diffraction, the monochromatic diffraction technique does not directly output the strain, but the lattice spacing. Hence, lattice strain for the grain orientations which contribute to a given (*hkl*) diffraction peak are calculated from the measured interplanar spacing using equation (3.1). It can be seen (Figure

32a) that the X-ray strikes the surface of the sample at 45° and thereby the mapped area penetrates into the bulk of the sample and intersects the surface with the same angle. Figure 32b illustrates that the direction of the depth coordinate has a 45° angle with the surface of the sample, as shown in Figure 32a. The sample was deformed to 1±0.5% and a new orientation map was created at the same location, shown in

Figure **33**b.

Figure **33**a and c show the regions below and above

Figure **33**b.

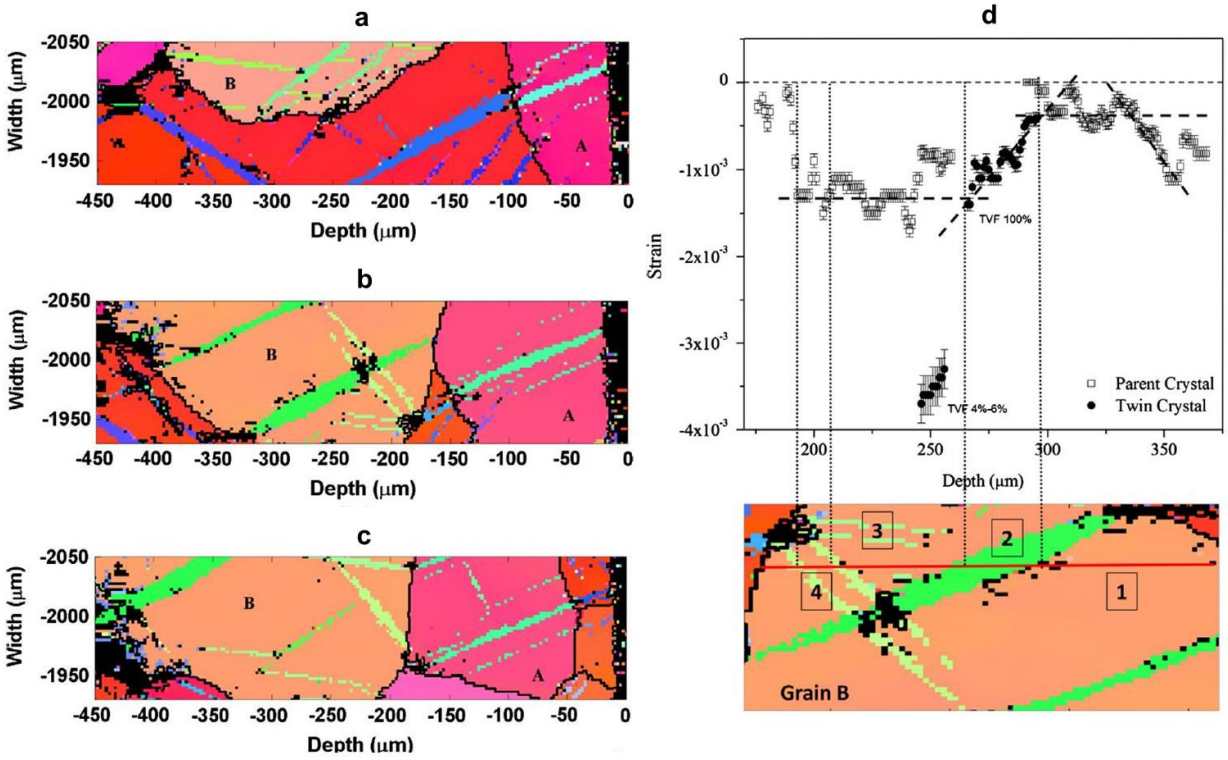

Figure 33 (a) orientation map after compression test below the zoomed in region shown in (b). (b) Zoomed in view of grain B. (c) zoomed out view of grain B shown in b. (d) the strain measured in grain B as a function of depth. The scale of the orientation map located below the graph is adjusted to the

horizontal axis of the graph to match the depth profile of the strain. The strain was mapped along the red line. The dashed lines are a guide to the eye to emphasize the role of the major twin lamella in the strain profile of the whole grain: the strain gradient across the twinned grain is localized in the twin lamella itself [137].

Figure 34 (a) orientation map after compression test below the zoomed in region shown in (b). (b) Zoomed in view of grain B. (c) zoomed out view of grain B shown in b. (d) the strain measured in grain B as a function of depth. The scale of the orientation map located below the graph is adjusted to the horizontal axis of the graph to match the depth profile of the strain. The strain was mapped along the red line. The dashed lines are a guide to the eye to emphasize the role of the major twin lamella in the strain profile of the whole grain: the strain gradient across the twinned grain is localized in the twin lamella itself [138].

The orientation map after deformation shows a noticeable amount of tension twinning in the microstructure. Based on the available orientation maps, grain B in

Figure **33**b was selected for the monochromatic strain measurement. The depth profile of the strain is along the width coordinate of -1960µm, as indicated by the straight line in the orientation map shown in

Figure **33**d.

Figure **33**d presents the strain measured in grain B as a function of depth.

3.3 Crystal plasticity modeling

Wu et al.[135] studied the internal stress (strain) evolution during cyclic deformation dominated by tension twinning and detwinning mechanisms within Mg ZK40 using in situ neutron

diffraction. They showed that once the matrix grains undergo twinning, that matrix and twin grains are relaxed relative to their neighbors. This load redistribution between the soft and hard grain orientations is attributable to plastic anisotropy. Texture evolution has been also suggested to play a role in plastic anisotropy. A reliable constitutive materials description must account for texture evolution associated with twin reorientation, the effect of the twin barriers on dislocation propagation, and the stress-strain response [138]. In other work, in-plane anisotropy of Mg AZ31 is attributed to the initial texture, and greater than the anticipated non-basal cross-slip dislocation with $\langle a \rangle$ type Burgers vector [64]. Simulation of the anisotropic stress-strain response and texture evolution are performed using the VPSC approach [92]. The "fitting parameters" in this approach are the critical resolved shear stresses (CRSSs) and hardening responses of the various deformation mechanisms. Because of the explicit connection with fundamental mechanisms of crystal plasticity, this approach is not considered to be merely phenomenological curve fitting. Agnew and Duygulu [139] used the same scheme and they found that dislocations having the $\langle a \rangle$ type Burgers vector in polycrystals are more active than those from a single crystal. They further justified this statement with TEM observations.

Most of the twinning based models for predicting mechanical stress-strain response such as [91, 92, 140] have been adopted to mainly describe the reorientation and hardening evolution associated with twinning. Most of these schemes accounted for twin reorientation using the concept of latent hardening to capture the role of twin interfaces in hardening. However, in the case of cyclic loading where detwinning has been reported to occur [135], the outlined modeling procedure will not be able to capture detwinning's effect on mechanical response. In 2007, Proust et al.[138] proposed a composite grain (CG) twin model that accounts for the orientation of slip and twin systems in each grain, which can describe the mechanical response for an

arbitrary deformation route. To model this mechanism, they favor the activation of the Predominant Twin System (PTS) inside the twin by setting a high CRSS value upon reloading for the other twin systems inside the twinned region. Such a procedure prevents them from being activated upon reloading. Once the PTS has been activated inside the twin, instead of creating a secondary twin, the volume of the twin that should be occupied by this secondary twin is transferred from the original twin to the matrix. It is important to note that the CG model assumes that strain is accommodated by twin growth inside the un-twinned matrix, and is driven by the average stress in the matrix. Whereas detwinning accommodate strains inside the twin region and is driven by average stress in the twin. Instead of attributing plastic deformation to the composite entity formed by the matrix and twin regions (Proust's model [138]), Wang et al.[141] proposed a model that assigns weighted contributions from twinning or detwinning to either the matrix or the twin, respectively. Therefore, this approach accounts for the average stress in the matrix and in the twin to calculate the twin growth and detwinning. In addition, this model allows more than one twin variant to exist within a grain. To better understand the example given below demonstrates a crystal plasticity model for an extruded MgAZ31 alloy including twinning and detwinning mechanisms. In this practice [141], the value of hardening parameters is estimated by fitting numerical simulations of monotonic tension and compression along the rolling direction to the corresponding experimental flow curves shown in Figure 34a. In order to incorporate the effect of the stress difference between the matrix and twin, and the compensation for twin shear among the matrix and the twin, twin growth is regarded as two parts: Matrix Reduction (MR) and Twin Propagation (TP), which are activated by the average stress in the matrix and in the twin, respectively. MR is accomplished through the migration of twin boundary induced by resolved shear stress in the matrix and reduces the current volume of the matrix. TP

occurs through the migration of twin boundary towards the matrix induced by the resolved shear stress in the twin, and has the effect of increasing the current volume of the twin. Note that detwinning takes place through gliding of twin boundaries on the same crystallographycal plane of twinning, but in the opposite operation of the twin growth. Therefore, detwinning is regarded as the opposite of twin growth, and thus consists of two parts: Matrix Propagation (MP) and Twin Reduction (TR). MP is accomplished through the migration of twin boundary towards the interior of the twin induced by the resolved shear stress in the matrix and increases the current volume of the matrix. On the other hand, TR is induced by the resolved shear stress in the twin and shrinks the current volume of the twin. Figure 34b shows the evolution of twin volume fraction and the accumulated twin/detwin volume fractions (f^{tw}) associated with twin growth and shrinkage. The twin volume fraction increases monotonically, saturating after approximately 7% strain, mainly due to MR and TP, i.e. initially dominated by MR and later dominated by TP after 3% strain, as shown in Figure 34c. The activities of various deformation mechanisms under uniaxial compression are compared in Figure 34d.

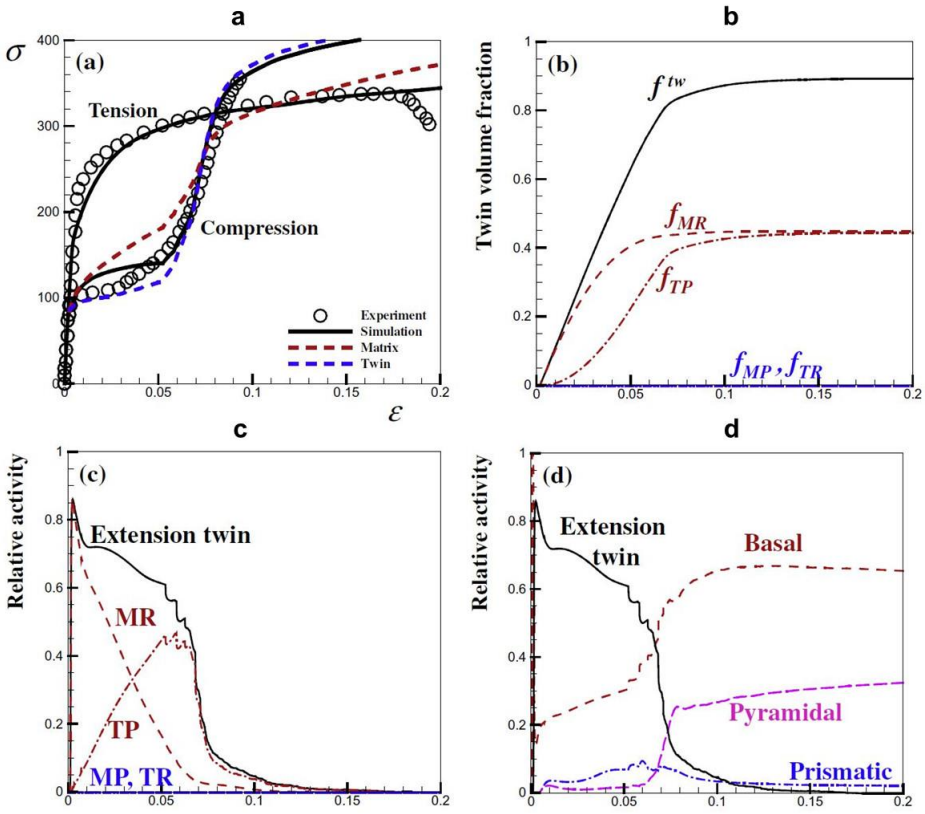

Figure 34 Uniaxial tension and compression of Mg alloy AZ31 plates along the rolling direction. (a) Measured and fitted stress-strain curve. (b) Evolution of twin volume fraction under uniaxial compression. (c) Relative shear activities of various mechanisms associated with tension twin under monotonic compression.(d) relative shear activities of slip deformation mechanisms under monotonic compression [141].

Figure 35a presents a comparison between modeling results and experimental data for the cyclic tension-compression loading [141],demonstrating the accuracy of the proposed model. According to this investigation, several deformation mechanisms operate during cyclic plasticity, indicated by P0–P1, P1–P2, P2–P3, P3–P5, P5–P7 and P7–P8 corresponding to twinning, de-twinning, slip, twinning, de-twinning and twinning, respectively. The twin volume fraction evolution as a function of the strain along RD is shown in Figure 35b. It can be observed that the twinning (MR and TP) and detwinning (MP and TR) are operating alternately during tension and

compression. In addition, the activity of different deformation mechanisms is compared in Figure 35 c and d.

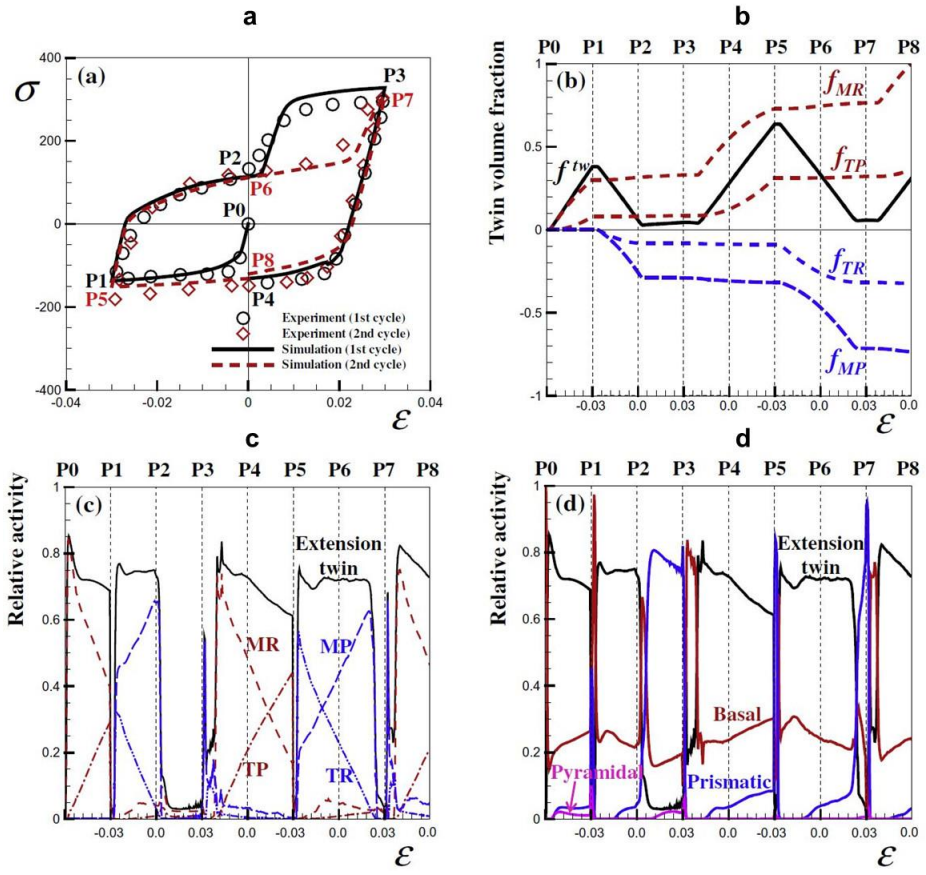

Figure 35 Measured and predicted stress/ strain curves of the AZ31B plate under cyclic loading along the RD, with a strain amplitude of 3.0%. The experimental data are taken from Wu et al. (2010); (b) Predicted twin volume fractions as a function of strain; (c) Relative shear activities of various mechanisms associated with extension twin; (d) Relative shear activities of slip deformation mechanisms [141].

3.3 Fatigue and fatigue crack characteristics

Twinning and detwinning are important deformation mechanisms in the single- and poly-crystalline HCP materials. For instance, the sudden nucleation of a twin in in fatigued cadmium single crystals gives rise to a large increase in damping [142]. As specified, twinning induces the lattice reorientation by ~86.4^{o} in the twin region, making the reoriented lattice favorable for detwinning under a subsequent load reversal. Proust et al.[143] experimentally studied the underlying mechanism for loading and reversal loading in Mg AZ31 sheet alloys. This study

involves two series of samples cutting in the plane of the sheet designated by IPC and through the thickness, designated by TTC. Note that it is expected the compression of IPC should be dictating by tension twinning. The dash line in Figure 36a shows the stress-strain curve for the compression of IPC sample. In recognition of the effect of dislocation structure and subsequent twinning for this particular orientation, they pre-strained two samples in opposite directions: up to 5% and 10% strain, and then reloaded them in the IPC direction (shown in Figure 36a). It is reported that in the loading along TTC direction (pre-straining condition in the presented example) plastic straining proceeds with $\langle a \rangle$ basal, $\langle c+a \rangle$ pyramidal and perhaps $\{10\bar{1}1\}$ contraction twinning [74]. It can be seen that the reload stress-strain curve following 5% and 10% TTC pre-straining displays behavior similar to the monotonic results shown in the same plot with dash line (see Figure 36a). The characteristic s-type strain-strain curve shows deformation is still largely accommodates by twinning. But, yielding occurs at larger stresses. In this case, during the pre-straining, $\langle a \rangle$ basal, $\langle c+a \rangle$ pyramidal are introduced. Thus, these dislocations may obstruct twin nucleation. This would explain both the increases of the stress corresponding to the onset of twinning with the increase in pre-strain, as well as more extended hardening plateau associated with twinning [30]. Proust et al. [143] also demonstrated the effect of twinning on subsequent deformation (Figure 36b). In this case, samples are pre-strained along the TTC direction up to 5% and 10%, which twinning is expected to control the onset of plasticity and then the pre-strained samples are loaded in the opposite direction. Figure 36b shows the stress-strain curve corresponding 5% pre-straining along IPC direction followed by10% reloading along the TTC direction. During monotonic TTC, primarily $\langle a \rangle$ basal, $\langle c+a \rangle$ pyramidal are active however, once twins have been introduced by previous IPC, the hardening behavior of the material reloaded in TTC changes drastically. The reload flow curves display the

characteristic sigmoidal shape associated with deformation twinning, a result of the fact that grains that have twinned during IPC are now properly oriented twin or detwin) during subsequent TTC, since the basal poles are roughly at ~86.4^{o} position.

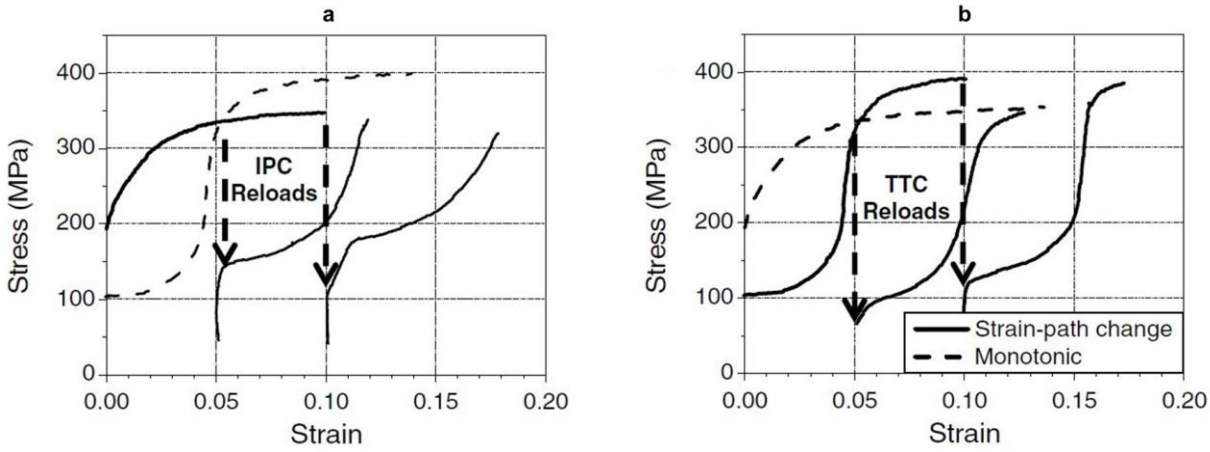

Figure 36 (a) strain –path change stress-strain curve for the samples deformed first in TTC to 5% and 10% strain and deformed in IPC (the monotonic IPC stress-strain property is represented by the dash line for comparison). (b) strain –path change stress-strain curve for the samples deformed first in IPC to 5% and 10% strain and then deforms in TTC (the monotonic TTC stress-strain property is represented by the dash line for comparison) [143].

The example given above elaborately explains the effect of prior slip on subsequent twinning and vice versa, which is valuable for understanding fatigue plasticity in the presence of various deformation mechanisms in Mg alloy. As discussed in section 3.2 and the preceding paragraph, the fatigue deformation of textured Mg alloys follows twinning and detwinning. As a result, asymmetric hysteresis loop and pseudo-elastic unloading behavior have been reported during cyclic loading of Mg alloy (see Figure 37a [144]). Pseudoelasticity may have several origins such as reversible dislocation motion, phase transformation and twinning. Twinning Pseudoelasticity is caused by the reversible movement of twin boundaries [145]. The complex nature of cyclic plasticity induces a non-zero mean stress (Figure 37b [144]), which markedly affects the fatigue characteristics. The non-elastic unloading and strong asymmetric hysteresis

loop has been attributed to the twinning and detwinning [135, 144, 145]. It is also evident that this material have a noticeable cyclic hardening effect (see Figure 37a [144]).

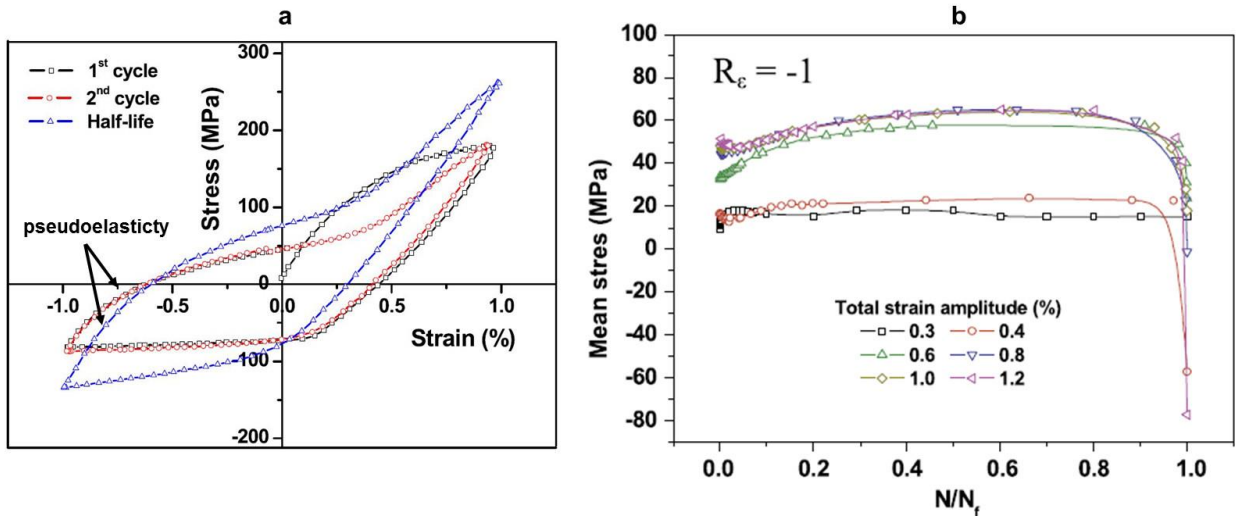

Figure 37 Fatigue cyclic tension-compression behavior under strain control condition (a) stress-strain hysteresis loop for first, second and half-life. (b) Mean stress evolution with life fraction [144].

Although the peculiar shape of the hysteresis loop and, non-zero mean stress and marked strain hardening have been attributed to the twinning-detwinning, but the direct evidence of this phenomena is quite rare. Figure 38 is one of the occasional examples in the literature that shows twinning-detwinning in the same grain in the as-cast Mg AZ91. Twin is formed in bending and some of the partially reverts when the applied load is decreased. Detwinning as a consequence of cyclic loading in Mg alloys occurs from an early stage of deformation, even from compressive unloading. The reason for this is the residual stresses in the material during twinning, which can drive detwinning under compressive unloading [146].

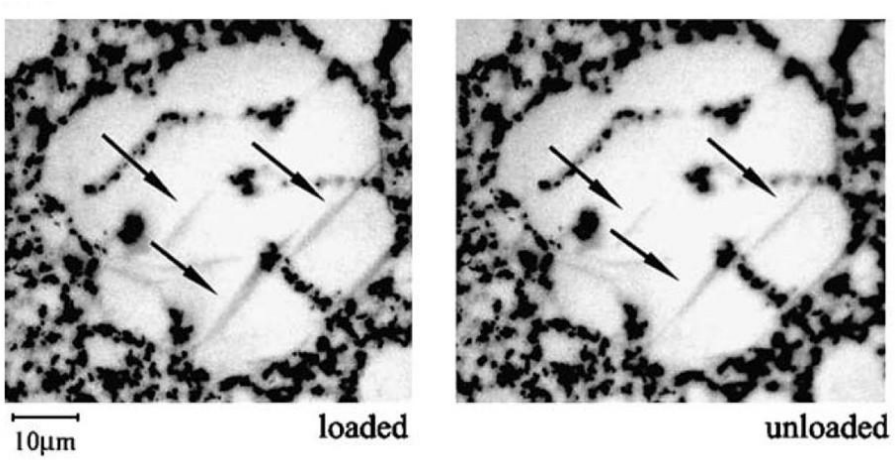

Figure 38 Twin formed during bending and then reverts upon unloading [145].

Fatigue life is greatly dependent on the transition from microstructure small crack initiation and propagation to long crack formation. It has been reported that it is highly probable that inclusions have a major effect on fatigue crack initiation [147-149]. In this regard, it is suggested that fatigue cracks predominantly initiate at cracked particles, thereby suggesting that the driving force for fatigue damage in wrought Mg alloys is related to the brittle intermetallics particles [148] (see Figure 39a). Cracking along twin boundaries has been also reported (Figure 39b [150]). This was the only experimental observation that was found in the literature.

To examine the localized microstructural response of Mg AZ31alloy to crack propagation, Zheng and coworkers [151] monitored the neighboring microstructure of the fatigue crack in a Compact Tension (CT) specimen as it deformed. They noted that crack growth proceeds faster inside smaller grains than in larger grains. This observation was attributed to the difficultly that cracks have in penetrating grain boundaries of the small grains. It is also noted that the slip bands are more apparent in larger sized grains rather than in smaller grains near the transgranular cracks. The SEM image in Figure 40a, by Zheng et al. [151] exhibits two distinct types of striation. In the left hand side of the SEM micrograph (Figure 40a), the striations are parallel to

the direction of the crack. However, at the later stage of the crack propagation, plastic flow proceeds through the inclined V-shape striations (see right hand side Figure 40b).

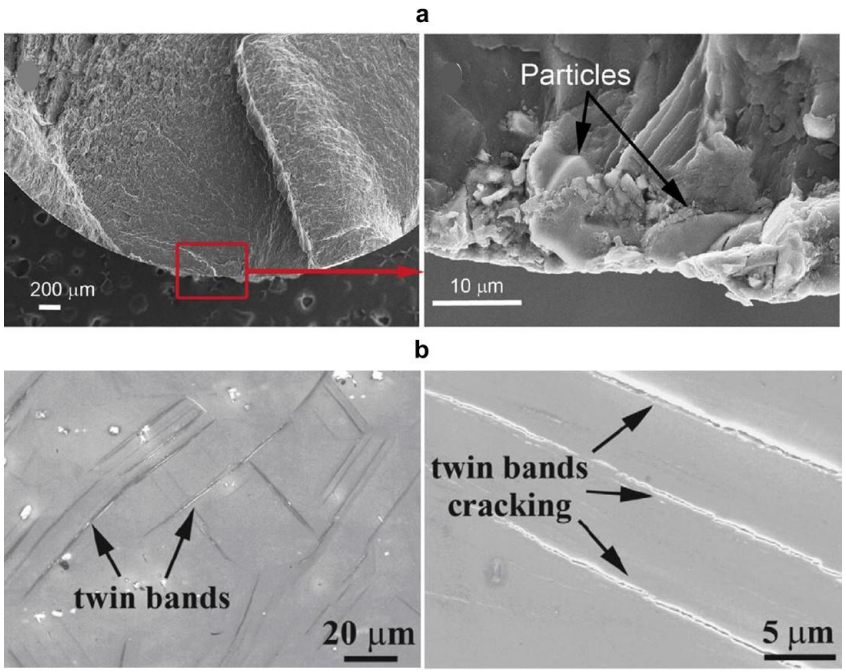

Figure 39 (a) fatigue crack initiates from intermetallic particles in MgAZ3 plate under strain control fatigue condition [152]. (b) Crack initiation along the twin boundary during very high cycle fatigue (stress control condition) of Mg-12Gd-3Y-0.5Zr [150].

A possible explanation for this observation is follow: It is specified earlier that the CRSS for basal slip is very low, meaning that it can be activated easily. It is schematically shown Figure 40b, in addition to the basal slip two sets of $\langle c+a \rangle$ pyramidal slip (marked with left-right arrow) can offer alternative slipping which acts as the driving force for crack growth. During subsequent crack propagation, the recorded V-shaped crack striation pattern is the result of the intersection of the first order pyramidal plane with the propagation plane. It should be also noted that additional alternative slip systems may be activated due to the higher locally concentrated Mode I stress field developed with crack extension.

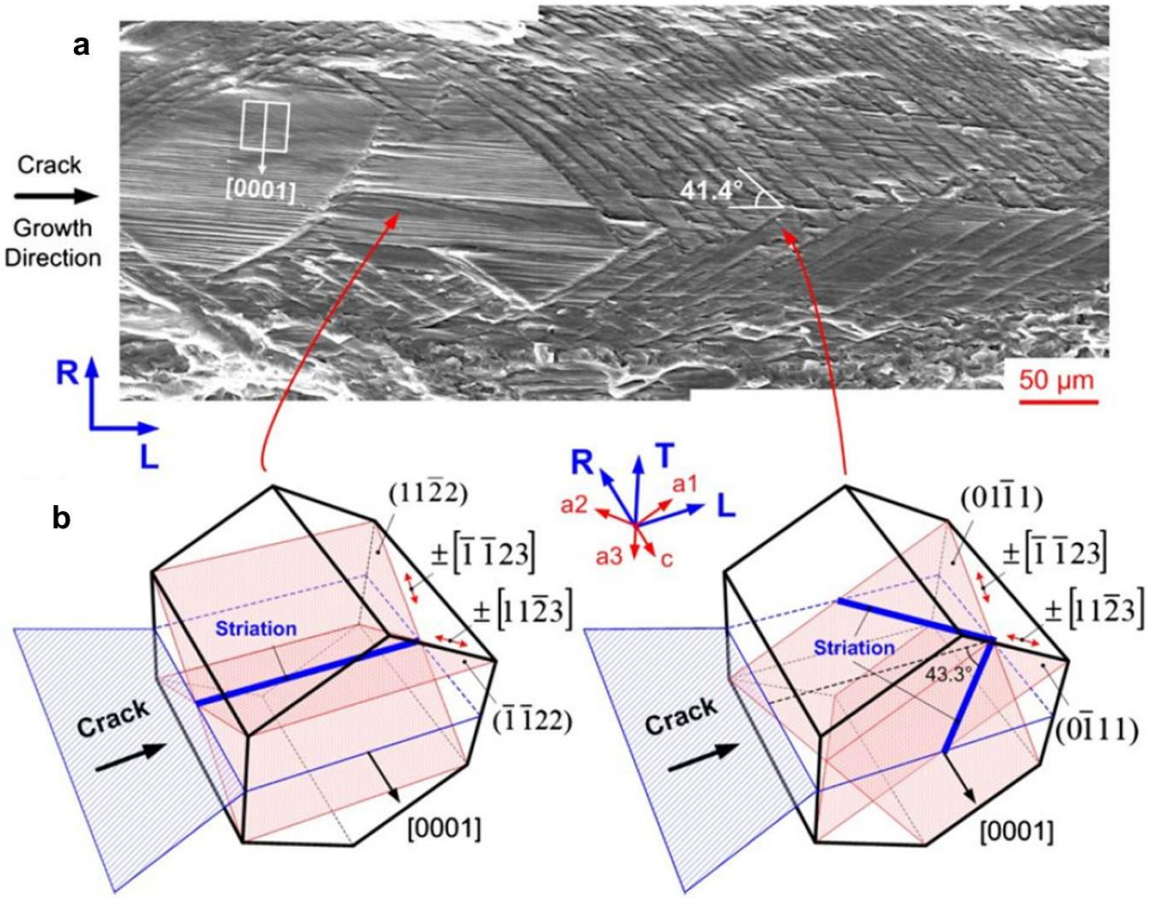

Figure 40 (a) SEM micrograph of fatigue crack growth in the CT sample fabricated from the extruded Mg AZ31. The sample is made in such a manner that the customized pre-crack is parallels the extrusion direction. (b) A possible deformation mechanism as the crack arrives to the microstructure [151].

Chapter 4

The Effect of Twinning on Early Plasticity and Strain Localizations[1]

4. 1 Introduction

This chapter exhibits the recent experimental investigation on the nature of plastic yielding in Mg AZ31 alloy at room temperature. Specifically, it concentrates upon the rules which the heterogeneous deformation obeys and its consequences on the mechanical stress-strain response at the onset of yielding. Pursuant to this aim, material characterization is demonstrated beginning from the macroscopic and extending down to the critical grain scale. Therefore, Digital Image Correlation and Acoustic Emission were simultaneously used to investigate the near yielding behavior of textured samples of a magnesium alloy. Distinct band evolution near-yielding was monitored in situ and directly relatable to profuse local twin formation, verified by ex situ electron back scatter diffraction. The presented results in this chapter demonstrate for the first time quantitatively in both space and time the dominant role of twinning in early stages of plastic deformation of magnesium alloys. The results of this investigation allow prediction of the onset of heterogeneous mode of deformation and importantly, show the underlying mechanism for the mode of deformation.

[1] *K. Hazeli, J. Cuadra, P. A. Vanniamparambil, and A. Kontsos "**In situ Identification of Twin-related Bands near Yielding in a Magnesium Alloy" Scripta Materialia,** Volume 68 January 2013, pages 83-86.*

4.2 Literature review

In chapters 1 and 2, it was specified that due to the high specific strength of Mg based materials, the application of these materials in lightweight structural components has significantly increased. It was also indicated that wrought Mg alloys show better mechanical properties compared to the cast alloys (casting defects such as porosity and inclusion). Thus, wrought Mg alloys have received special attention. The main hurdle in using wrought Mg alloys has been their limited room temperature formability (plastic anisotropy), which, in fact, is rooted in lack of sufficient understanding of their plastic deformation mechanisms [153, 154]. The high texture characteristics activate several deformation systems including slip, twinning and their interactions, thus affecting the deformation mode [29, 155-157]. Polycrystalline plasticity simulations are used to model the observed anisotropy and texture evolution. Strong plastic anisotropy at room temperature is attributed to the initial texture and greater than anticipated non-basal cross-slip of dislocations with $\langle a \rangle$ type Burgers vector [64]. In addition, several experimental investigations of the plastic behavior of HCP metals have been reported using a variety of characterization methods, such as orientation imaging microscopy [158], X-ray diffraction [157], Electron Back-Scattered Diffraction (EBSD) [74, 157-162], TEM/SEM microscopy [74, 157, 159, 160, 162-164], neutron diffraction [156, 165-167], as well indentation-based hardness measurements [158, 163] and nondestructive testing (NDT) including Acoustic Emission (AE) [161, 167-170] and Digital Image Correlation (DIC) [163, 171], there is still lack of fundamental understanding on their microstructure-deformation relations. It is generally accepted that plastic deformation in the pre-hardening zone of such alloys is dominated by deformation twinning, primarily comprising of $\{10\bar{1}2\}\langle\bar{1}011\rangle$ extension twins [162]. However, debate has emerged over both the initiation and dominance region of twinning [74,

162, 167]. Twin nucleation and dislocation glide at the onset of yielding give rise to the characteristic "S-type" stress-strain behavior, preceding the strain hardening region[18, 172]. Nevertheless, little or no attention has been given in quantifying the spatial distribution of twins and its effect on local flow during early stages of deformation, which in light of the limited deformation mechanisms in HCP metals, is expected to influence significantly their plastic behavior [173].

The novel approach in this work is based on situ monitoring plastic deformation of AZ31 alloys using a combination of optical (DIC) and acoustic (AE) NDT methods, targeting quantitative space-time correlations with twinning and its effect on observed plasticity. Early remarks on the ductility of HCP materials made by Kocks and Westlake [174] and subsequently supported by others [29, 175], stated that unlike single crystals, the ductility of polycrystals must be affected by local variations in strain from grain to grain, leading to strain inhomogeneities that are possibly relieved by localized deformation produced by twinning. Plastic strain localization in crystalline metals occurs across a wide variety of materials and loading conditions, and often has a determinative role in influencing the mechanical behavior, and consequently the suitability of a given material for an intended structural application [176]. The localization of plastic deformation into a shear band is defined as a plastic flow instability and a precursor to rupture [177]. Despite the substantial importance of shear band formation in poly- and single crystals for texture control and strength, the mechanisms responsible for their nucleation and development are still unclear [178]. One possible solution is to quantify full-field measurement of plastic strain near growing crystallographically related micro bands. In this framework, by using observations of the cold rolling of HCP metals and microscopy, EBSD, in situ neutron diffraction and AE, Barnett et al. [179] and later Muransky et al. [167] suggested that when

twinning occurs an internal redistribution of stresses is produced, which can be relaxed by "micro-slip" capable to decrease the misfit of twin-dominated grains and their surrounding polycrystalline aggregates. This observation could explain the observed shear banding during cold rolling of Mg alloys, while it implicitly suggests that pre- and post-yielding of these alloys is twin-governed. While there is still no clear understanding of the crystallographic nature of shear banding, it has been suggested. that band formation in FCC metals is preceded by the creation of obstacles to homogeneous deformation [180]. In the case of Mg, plastic deformation when basal slip is restricted and twinning is favorable has been shown to be inhomogeneous and dominated by shear or Lüders-like bands, both at both room [172] and elevated temperatures [157].

4.2 Material

A 25 mm thick AZ31 alloy (Mg–3% Al–1% Zn) rolled sheet manufactured by Magnesium Electron Company was used. To homogenize the grain size and remove all pre-stresses and mechanical twins from rolling, small cubes were first subjected to annealing in salt bath at 350 °C for 30 mins, followed by water quenching. Annealed samples were further compressed parallel to the ND direction up to 5% of total strain. To finalize the re-crystallization process, samples were annealed at a higher temperature (450 ^{o}C) for 50 hours, and a relatively homogeneous grain microstructure with average grain size of ~ 30 µm was obtained Figure 41a. Activation of basal slip during rolling process progressively reorients the basal plane parallel to loading, which leads to the strong basal texture shown in Figure 41b [181, 182].

Cylindrical compression specimens were cut by Electric Discharge Machining (EDM) based on ASTM standard E9 (length to diameter ratio equal to 2 for a 9mm diameter) from two different

directions. As a convention, “TD” refers to samples cut in the plane of the rolling direction and “ND” refers to samples cut perpendicular to the rolling direction.

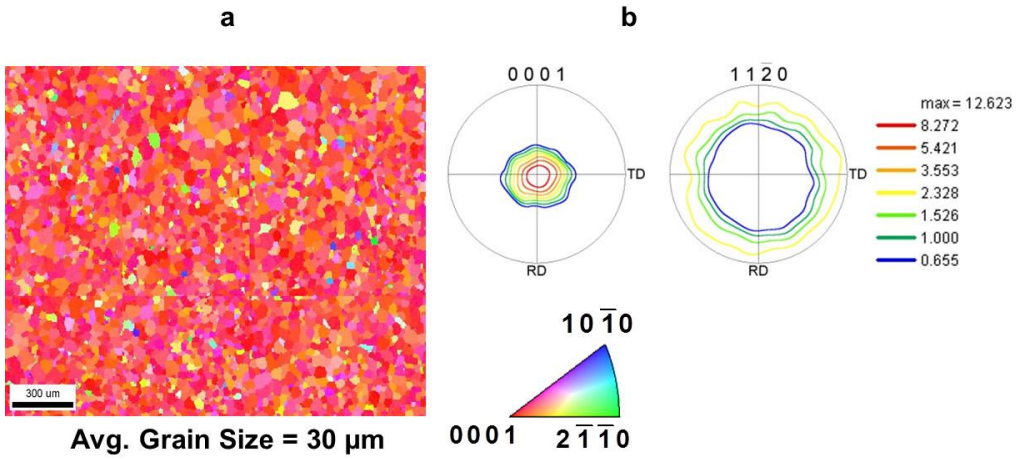

Figure 41 (a) Inverse pole figure map of the microstructure of the AZ31 alloy after the heat treatment and recrystallization processes, and (b) pole figures demonstrating strong basal texture.

In addition to standard cylindrical samples, another group of TD samples was prepared through lateral polishing, to obtain specimens flattened in one side to allow direct DIC analyses coupled with SEM and EBSD. After testing, the lateral sides of the deformed cylindrical specimens were ground using 800, 1200, 1400 and 2500 papers. Polishing was then carried out with alcohol-based (9, 6, 3, and 1 µm) diamond solutions. The process was completed by using ultra-fine (0.05 µm) water-based alumina solution. To reveal the microstructure, specimens were immersed in a chemical etchant (5ml nitric acid, 15 ml acetic acid, 60 ml ethanol, 20 ml distilled water) for 2 sec. EBSD data was then collected by an environmental scanning electron microscope (Philips FEI XL30) equipped with an EBSD (TSL) channel.

4.4 Experimental Procedure

Monotonic compression tests were carried out at constant strain rate of 4.5×10^{-4} sec^{-1} at ambient temperature with an MTS hydraulic load frame. Average, local and full-field strains were computed using the GOM ARAMIS DIC system. For a 50 x 42 mm^2 field of view, the cameras had a separation of 272 mm, an angle of 25^O and were positioned 395 mm from the sample. A speckle pattern was placed on the surface of the material, and the system's sensitivity was measured to ±150 μm/m. For the given tests a picture was taken every 0.33 sec. AE was recorded using an AE data acquisition system (4-channel DiSP system by Physical Acoustics), a piezoelectric transducer (operating frequency range of 200-750 kHz, peak frequency at 500kHz) and a preamplifier (2/4/6-AST, uniform gain of 40dB). The sensor was bonded on the surface of the specimen using a cyanoacrylate adhesive. Pencil-lead break tests were carried out to calibrate the sensitivity of the system, where the threshold of 50-55 dB used minimized the recording of unwanted noise. Signals were band-pass filtered in the frequency range of 100-400 kHz and the peak definition, hit definition and hit lockout settings were 200, 500 and 1000 μsec, respectively.

4.5 Results & discussion

Measured stress-strain curves combined with amplitude of the recorded AE signals for both TD (A) and ND (B) samples are shown in Figure 42a and verify the plastic anisotropy of Mg alloys. TD samples are characterized by a distinct plateau region, immediately after yielding resulting in a "S-type" σ-ε curve. It is interesting to note that the AE amplitude distributions in Figure 42a present distinct increases for strains near yielding in both cases, while it can be further seen that the peak for TD samples is more than 15 dB higher than the peak for ND samples. The AE activity shown in in Figure 42a agrees with several recent research investigations [161, 167, 169] that pointed out the so-called "burst type" AE due to large amounts of energy released during the

crystallographic reorientations caused by twin nucleation, also verified in our experiments. Burst type and twin-related AE activity was additionally reported to be orders of magnitude higher compared to AE from both twin growth and massive (or not) dislocation motion (that further appeared to be of a "continuous-type"). Prior investigations, however, lacked the direct time correlation between AE activity and twinning, which was achieved in the current investigation as shown next.

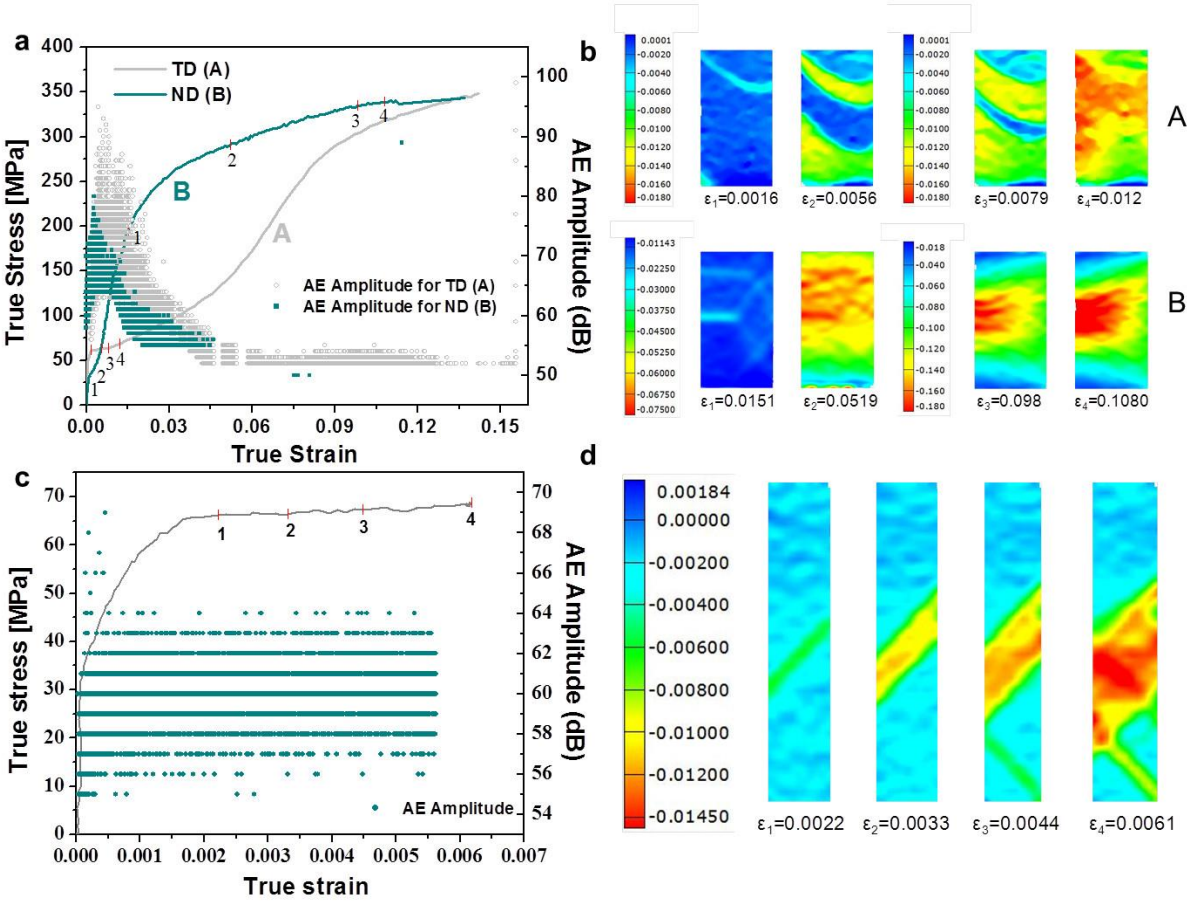

Figure 42 (a) Stress-strain curves for both TD (A) and ND (B) samples and overlaid AE amplitude scatter plots; (b) full-field y-strains for four points of the r–e curve for each sample category; (c) r–e curve for a flattened TD sample; and (d) full-field y-strains for four points of the stress-strain curve in (c).

Full-field y-direction strains are plotted for several points of the σ-ε curve in Figure 42b. For TD samples, DIC strains are presented in the small strain regime (<1.5%), while for ND samples in the 1.5-12% region. The in situ recorded surface strain profiles in this region, which to the best of the author's knowledge is the first time to be reported, reveal Lüders-like bands in TD samples that appear at early strains (<1%) and correlate well with the sharp increase of the AE activity, becoming more pronounced when the AE activity reaches its peak and finally give rise to less-ordered strain localizations for true strains >1% and when the amplitude of AE decreases. Such bands were further found to be always inclined with respect to the loading axis, implying consistent, possibly texture-related behavior. For comparison, the corresponding full field y-strains for a characteristic ND sample are given in Figure 42b; it is seen that they differ significantly from the patterns on the surface of the TD samples, suggesting differences in the deformation mechanisms of the two specimen types, which will be explored next.

The fact that the peak of the AE amplitude distribution, which can be recorded and plotted in situ, was found to relate to both yielding of TD samples and the appearance of strain bands, was taken advantage of in the case of specially prepared flat samples that allow macroscopic mechanical testing followed by microscopic investigations with SEM/EBSD. AE constituted of triggering device for these experiments; used to determine the point in time that the test should be stopped to capture microstructure states within the plateau region, in which the surface bands are readily observable, as shown in Figure 42a. The results obtained from this procedure are presented in Figure 42c and d. It can be clearly seen that the AE amplitude peaks occurred at strain levels of about 0.05%, at which point the stress-strain curve seems to deviate from its initial linear regime, moving towards the yielding and plateau regions. The fixed color map in Figure 42d allows the observation of the evolution of the strain localization as a function of true

strain. The bands in Figure 42d appear to be initially formed again inclined with respect to the loading axis at very small strain levels (~0.22%). As the imposed deformation increased, the bands became more pronounced. The average band strain (ε_{band}) for the ε_2 increment in Figure 42b was measured two times higher than the corresponding ε_{band} for ε_1 and about four times higher than ε_2 itself, indicating strong strain localizations. Interestingly, a new branch with different direction compared to the band at the center of the specimen in Figure 42d, appeared at increment ε_3 and became more pronounced at ε_4. To investigate whether the observed surface bands are related to microstructure, targeted EBSD measurements in six key areas that coincide with: (i) regions away from band boundaries (e.g. 1,6), (ii) regions exactly on boundaries (e.g. 2, 3 and 5), and (iii) regions inside the band structure are shown in Figure 43 for the flat TD specimen of Figure 42c,d at the ε_4 strain increment. Corresponding pole and inverse pole figures are also shown in Figure 43. The results in Figure 43 show that the areas 1 and 6 are almost free of twins, area 2 shows a distinct "twin band" (tensile twins verified by local misorientation analysis which confirmed the ~86^o rotation), same as areas 3 and 5, while area 4 is dominated by a large number of twins almost in all grains. These observations are further supported by the corresponding pole figures that show the appearance of TD components because of twinning. Therefore, twin nucleation and spatial distribution of twinning sites and subsequent twin density evolution appear to initiate near the onset of non-linear deformation shown in Figure 43b, at strain levels significantly lower than previously reported strain regions of 2-4% [74, 162] and in agreement with pertinent neutron diffraction data [167].

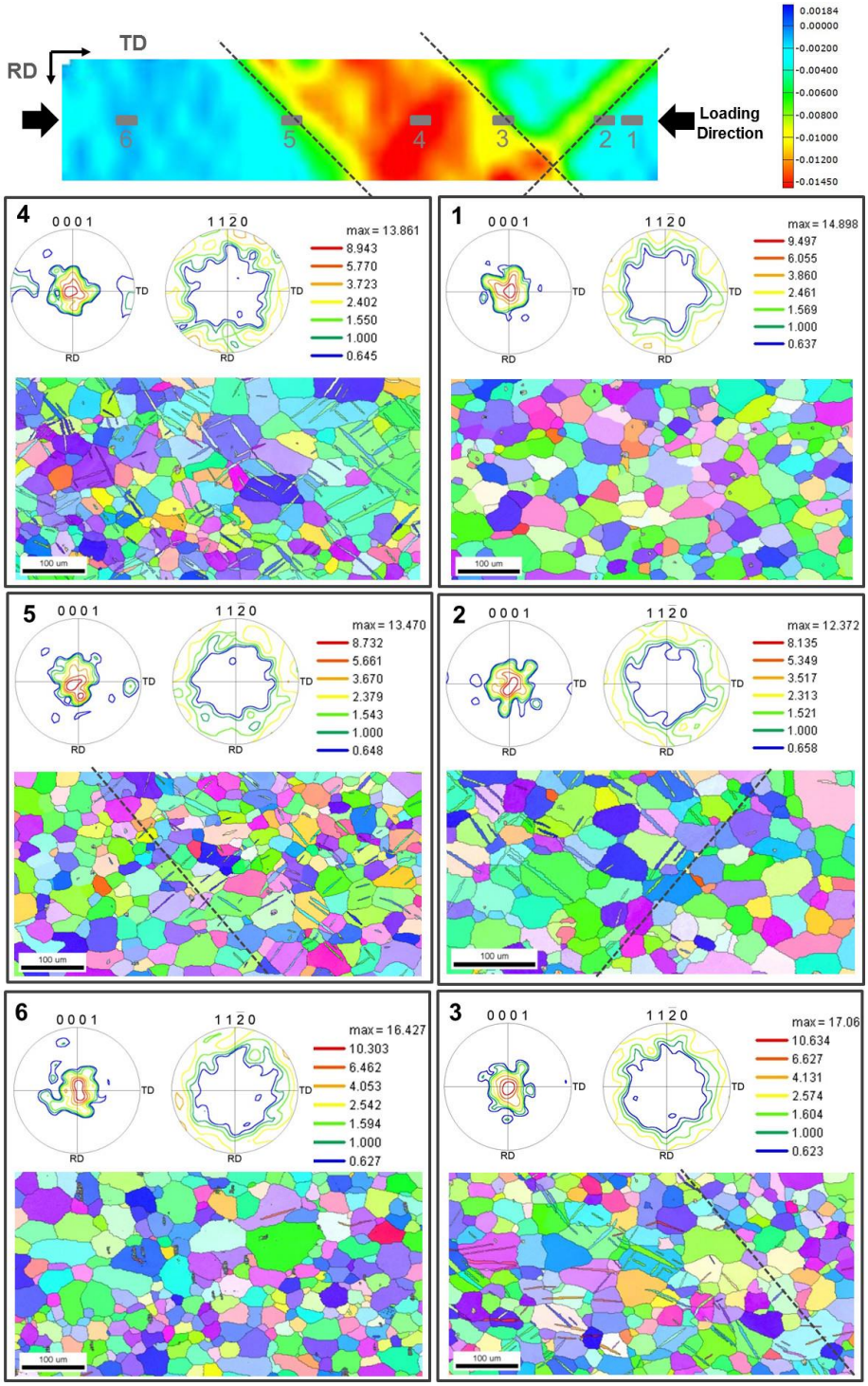

Figure 43 (top) Full-field y-strains for ε_4 4 = 0.61% of the flattened TD sample also shown in Figure 42d. The six areas numbered along the mid-plane of the sample were used to obtain EBSD maps. The dashed lines were artificially placed to assist the identification of the boundaries of the observed surface bands; (bottom) pole and inverse pole figures for the six areas marked on the sample. The dashed lines here are different to the ones placed above and are relevant to each EBSD scanned area to assist the identification of twin dominated vs.twin-free regions.

The rapid nature of twin nucleation, underlying dislocation structure and local strain heterogeneities appear to result in multiple twins within a grain (e.g. in area 4 of Figure 43), which can further cause generation of "secondary" twins with ends attached to other (parent) twins (Figure 44a) as plastic deformation continues. In addition, sites at grain boundaries were found to result into simultaneous twin formation in two adjacent grains (Figure 44b), which have been described as "cross-boundary twins" [172, 173]. Furthermore, in grains with more than one twin in them, twins that have impinged each other (Figure 44c) were found, which agrees with previously reported observations [172]. The fact that large number of grains at relatively small true strain increments are characterized by profuse twinning also agrees with the suggested "autocatalytic" twin process [167], which is independent from the initial "trigger" type twinning [172] that is primarily driven by local strain inhomogeneities in HCP polycrystals, as quantitatively shown here. Therefore, the proposed NDT characterization approach has the potential to directly relate microstructural changes in both time and space with plastic deformation in HCP materials.

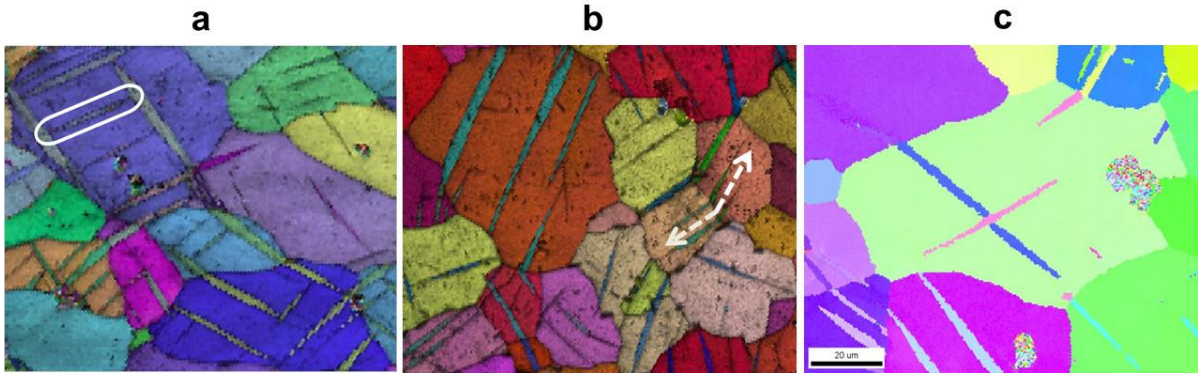

Figure 44 (a) Example of a secondary twin stretching between two thick (primary) twins; (b) example of possible simultaneous “cross boundary twins”; and (c) example of twin impinging within a grain.

4.6 Conclusion

In summary, the results presented in this paper demonstrate that: (a) strain localizations in the form of distinct bands near yielding are directly related to twin nucleation and growth. (b) Twinning in samples with favorable texture appears to initiate very early in the plastic deformation (see the AE amplitude pick in Figure 42C), and evolve in a rather non-uniform, however, topologically ordered way as indicated by the results in Figure 42c. Twinning appears to be responsible for the relative softening observed in the post-yielding (and also post-twin nucleation) regime (ε>0.2%). Therefore flow changes and the onset of possible local "micro-slip" give rise to the plateau region (shown in Figure 42c). Additional slip and further strain localization occur until a critical level of imposed deformation is reached, beyond which hardening tends to initiate.

Chapter 5

Surface and plasticity Effects of Twinning in Magnesium Alloys[1]

5.1 Introduction

This chapter reports directly observed surface effects of twinning and its significant role on surface roughening and plasticity of magnesium alloys. Full field strain monitoring at both micro and macro scales revealed significant strain localizations in areas dominated by tension twin formation. To quantify the surface effects caused by twinning, both interferometry and atomic force microscopy were used. The reported observations were additionally supported by relevant texture measurements performed by using electron backscatter diffraction, as well as Schmid factor and average misorientation analyses. The present investigation demonstrates the three dimensional nature of twinning at early stages of deformation (<1% total strain), and further explains both local and bulk strain localizations and their relationship to plasticity in magnesium alloys. Further, the relationship between surface morphology evolution during compression of magnesium alloys and twinning is discussed. Both *in situ* grain scale observations and *ex situ* but high resolution specimen level measurements demonstrate that twinning is responsible for large intrusions and extrusions that form inside and around twin-favorable grains

[1] *K. Hazeli, J. Cuadra, F. Streller, C. M. Barr, M. L. Taheri, R.W. Carpick, A. Kontsos "**Surface and Plasticity Effect of Twinning in Magnesium Alloys**". Internationa Journal of Plasticity. under review*

5.2 Literature review

Plastic deformation in polycrystalline aggregates occurs by the activation of crystallographic deformation systems [34]. Individual grains, which are constrained by their neighbors, also have variations in their crystallographic orientations even in highly textured materials [183]. Consequently, the state of local stress (or strain) for each individual grain can be highly variable depending on material, processing and applied loading [121, 184]. This crystalline level anisotropy associated with yet to be determined variations in deformation and damage processes in hexagonal close packed (hcp) magnesium (Mg) alloys at both micro and macro scales (shear bands, plastic anisotropy, tension-compression asymmetry, cracking) [184] are the focus of this investigation.

As specified, in Mg alloys the principal deformation mode is basal slip since the critical resolved shear stress (CRSS) for its activation is considerably low (~0.5MPa in pure Mg and ~2MPa in Mg AZ31 [76]). Therefore, even in textured microstructures small misorientations with respect to the loading direction lead to abundant basal slip [185]. Basal slip Burger's vectors are located on the basal plane and therefore no strain can be accommodated along the *c*-axis. $\langle c+a \rangle$ Pyramidal slip and deformation twinning have been reported to contribute to *c*-axis strains. However, they require higher driving force for activation than basal slip at least in ambient temperature. The corresponding CRSS value for $\{10\bar{1}2\}$ twinning is 25 to 35 MPa in pure Mg [186] and 40 to 50 MPa in Mg AZ31 [77]. In fact, $\{10\bar{1}2\}$ twinning can occur at early stages of loading in room temperature [18, 50]. In addition to the major influence of twinning on macroscopic plasticity, twinning results in a rotation of the *c*-axis of not favorably oriented grains for slip by ~86^{o} [187] and creates therefore new boundaries and textures [188], which play

an important role in strain hardening [187]. In addition, this multi-facet nature of twinning creates complex internal stress states which have been recently discussed [186]. Several studies [28, 189] reported that considerable strain (~6.5%) can be theoretically accommodated along the *c*-axis in hcp single crystals of Mg by tension $\left(\left\{10\bar{1}2\right\}\left\langle 10\bar{1}1\right\rangle\right)$ twinning. Accordingly, changes in ductility of Mg alloys have been attributed to the effect of tension twinning [187]. Alloying by e.g. lithium additions as reported by Agnew et al. [88] can cause an increase of non-basal $\frac{1}{3}\left\{11\bar{2}3\right\}$ or $\langle c+a\rangle$ slip and can improve ductility. However, the interplay between twinning, slip and both plasticity and fracture of Mg alloys is not yet fully understood. Grain size also has a considerable effect on the deformation mechanism selectivity. Stanford and Barnett [190]demonstrated that the ratio of the CRSSprism/ CRSSbasal increases by increasing the grain size. Whereas, the ratio of the CRSStwinning/ CRSSbasal remains unchanged by increasing or decreasing the grain size.

In addition to the significant effect of twinning on ductility, a former study by Kocks and Westlake [191] which was later supported by Hutchinson [192], suggested that the ductility of polycrystalline hcp metals is affected by local strain variations in neighboring grains. The basis of this relationship is local strain inhomogeneities, which can be relieved by localized twinning and/or slip [193]. It has also been suggested that twinning is associated with crack formation at later stages of deformation [193-195]. It is thereby concluded that besides the well documented sources of crack initiation, such as surface roughness, inclusions, intermetallics and ductile/brittle phases in polycrystalline alloys [39], twinning, slip and strain inhomogeneities at the grain scale can be also envisioned as an another source of crack incubation and initiation [196]. In this framework, and in agreement with Muransky et al. [18] and Barnett et al. [172], the

authors of this article [50] demonstrated that the onset of the distinct plateau region in the *σ*-*ε* curve obtained during compressive loading perpendicular to the *c*-axis is associated with localized but profuse twinning. In fact, the authors showed the formation of distinct localized strain formations, similar to Lüders bands, before and during elastic-plastic transition which were also verified by neutron diffraction [186]. Similar to the former study by Vaidya and Mahajan [197] in which evidence of slip on $\{11\bar{2}1\}$ planes prior to twinning were reported, Koike et al. [76] demonstrated that twinning occurs in grains with high basal dislocation activity. Therefore, as Hull [194] and more recently Ando et al. [193] argued, localized strain inhomogeneities resulting from the activation of slip can presumably be relieved by twinning. It is also plausible that stress (strain) concentrations due to incompatibilities between twins and their surrounding matrix regions can be relaxed by slip [193, 197] or crack formation [189] which reveals the correlated relationship between these crystallographic deformation mechanisms.

As a result of the lattice reorientations caused by twinning shown by Reed-Hill and Robertson [198] and the strain localizations reported by the authors [50], it is highly probable that fracture originates near twinning sites. Hill and Robertson [198] provided additional evidence of such twin-fracture relationship by removing a thin layer from the fracture surface; they reported the presence of underlying $\{10\bar{1}2\}$ twinning. In this framework, several investigations focused on mechanisms for twin nucleation and growth such as the work by Christian and Mahajan [65] and also [199]. Several models on twin nucleation have been proposed based on Schmid's law [70], distinct strain field formations due to pre-existent slip [76, 198] and recently grain boundary misorientations, as also referenced by pertinent studies [68, 200]. Despite the theoretical and experimental evidence, the role of twinning in local (grain scale) plasticity is still not well described. One reason behind this lack of understanding can be associated to imprecise

information regarding the three dimensional nature of twinning [68]. Consequently, the intricate plastic response [28, 39, 50], as well as the complex microstructure evolution associated to twinning/de-twinning activity [196, 201, 202] has become the focal point of many recent investigations, as a deeper understanding of the plasticity of Mg alloys and the associated anisotropy [161] and asymmetry [203] are required to improve the formability of Mg alloys.

Various sources of heterogeneous deformation have been investigated in recent years [204, 205], and their importance in the bulk behavior of polycrystalline aggregates have been also examined [121, 206-208]. For instance, Becker et al.[208] examined key factors such as strain and strain rate hardening, as well as texture on the spatial distribution of strain and suggested the close relationship between localizations and surface roughening. In this context, grain misorientations due to the collective motion of large numbers of dislocations can induce substantial deformation incompatibilities among individual grains, and they have been recognized as one of the major sources of heterogeneous deformation [209]. In the case of HCP materials, the limited number of slip and operating twinning systems can lead to both plastic instability and strain heterogeneities [210].

In order to explain the relationship between grain scale microstructural changes and deformation or crack initiation in alloys, a number of recent investigations relied on the use of the digital image correlation (DIC) method [121, 128, 129, 205, 211]. Carroll et al. [122] combined ex situ texture measurements with high resolution strain fields obtained by DIC to explain strain localizations near grain boundaries. With this approach they further demonstrated that some grains accumulated significant levels of plastic strain, while some of their immediate neighbors were relatively un-deformed. In addition, a quantitative assessment of the locally heterogeneous material response prior to fatigue crack initiation and its association with fatigue crack formation

has been recently reported [212]. Furthermore, Dave et al. coupled incremental straining of nickel foils with optical microscopy and showed the significant effect of grains boundaries and orientation mismatches on localized strain distributions [128]. Therefore, as a step towards understanding dominating factors that lead to local and global heterogeneous deformation, the present study demonstrates the pronounced effects of twinning on surface morphology by combining compression loading at two different scales with full field surface strain measurements.

5.3 Experimental Procedure

5.3.1 Grain scale strain and surface morphology quantification

In situ measurements of local in-plane strains during compression tests were performed with the aid of an optical microscope and were coupled with an ex situ optical phase-shifting interferometry investigation. The material used was a commercial 25mm thickness Mg AZ31 alloy (Mg-3%Al-1%Zn) plate, which was homogenized using several steps of loading and heat treating, as previously explained in detail by the authors [50]. The average grain size in the microstructures investigated was ~30 μm and a representative initial texture is shown in Figure 45. Strain and morphology measurements were performed in a Region of Interest (ROI) with size of 1 mm^2 which was identified by using fiducial markers created by micro-hardness indentation. The sample was loaded utilizing a MTI/Fullam (SEMaster 1000 EBSD) stage at a compressive displacement rate of 0.5 *mm/min* with the *c*-axis subjected to tension. To this aim, 4x4x5 mm^2 cubes were cut using Electron Discharged Machining (EDM).

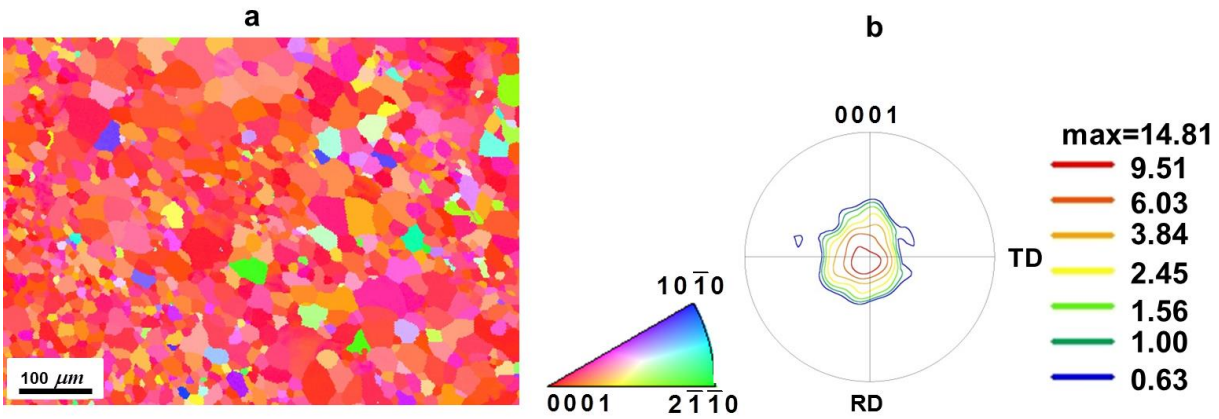

Figure 45 (a) Representative inverse and (b) pole figures showing the strong AZ31 basal texture.

A mirror-like surface was obtained using polishing explained in detail elsewhere [55], to allow texture measurements in the ROI. Loading was applied while an optical microscope (Olympus BH-2) was fixed at 10X magnification to record image sequences during the compression test. The images were recorded by a 10 Megapixels camera with a 25 Hz acquisition rate. The strain field evolution during loading was achieved by direct tracking of the microstructure using the method of DIC [116]. 2D analyses were performed in a field of view of (FOV) of $900\times675\mu m^2$ which resulted in a maximum resolution of 11.25 *μm/pixel*. The gray intensity (contrast) captured by the camera was created by the alloy microstructure and therefore no external patterning method was used. The recorded digital images were post-processed using the commercially available ARAMIS GOM software v6.30-4. Smaller FOV of 196 x 239 μm^2 at specific locations were selected to calculate refined full field and point-to-point strains in order to accurately compute local strain effects caused by microstructural changes during loading. The surface morphology in the ROI was inspected post mortem by non-contact white light interferometry using a Zygo surface profilometer (model 6300) at 20X magnification. As a result of using (20X, Mirau) objective lens, lateral resolution of 750 *nm* and vertical resolution of 0.1*nm* was achieved.

5.3.2 Specimen level strain localizations and surface step quantification

To validate surface morphology observations at the grain scale, compression tests on cylindrical specimens of standard dimensions were also performed. The samples were flattened on one side to allow post loading microstructure analyses. Specimens were cut according to ASTM E9 using EDM from a Mg AZ31 rolled sheet in the plane of rolling direction with ratio equal to 2:1 and had a 10mm diameter. Room temperature compression tests at a strain rate of $4.5\times10^{-4}s^{-1}$ were performed by using a servo-hydraulic (MTS 810, 100kN load cell capacity) mechanical loading frame. Prior testing, the specimens were subjected to the polishing procedure described previously by the authors [55]. The specimens were immersed in chemical etchant (5 ml nitric acid, 15 ml acetic acid, 60 ml ethanol, 20 ml distilled water). Fiducial markers on the polished surface were produced by micro-hardness indentation. The surface morphology in the ROI was quantified using both the interferometry method also used for the grain scale tests, as well as Atomic Force Microscopy (AFM) using a high resolution Dimension FastScan (Bruker). The AFM measurements were conducted in tapping mode utilizing a doped diamond probe with a nominal spring constant of 385 *N/m* and a line speed scan of ~1 *Hz*. It is important to note that concurrently to sample topography provided by the AFM, high resolution imaging was also achieved with minimal distortion due to fine adjustments of the applied force on the specimen's surface. Obtained 2D images were converted to 3D using the Nano Scope Analysis software and the same software was used to analyze the surface roughness.

Local lattice orientations were calculated at intervals of 1 μm on a hexagonal grid by automated acquisition and processing of electron backscatter diffraction patterns in a Scanning Electron Microscope (SEM FEI XL30). The accelerating voltage and working distance were set at 20 *kV* and 19.4 *mm*, respectively. It should be mentioned that in order to prevent changes on the

deformed specimen surface caused by chemical agents, the orientation and topography maps of the marked regions for the deformed samples were performed without any further polishing or etching. Consequently, the presented grain scale surface morphology and orientation maps in some cases do not have optimum quality however they are measured with sufficient accuracy given the observed deformation.

Full-field strain fields were measured using DIC on the cylindrical surface of the tested specimens. To protect the polished side from any contaminants coming from the applied speckle pattern procedure [116], the pattern was placed only on the curvature side of the one-side flatten compression specimens. A 50x42 mm^2 FOV was monitored with a 5 Megapixel 3D DIC system which uses a pair of CCD cameras with a separation of 272 *mm* at an angle of 25°. The full-field strain measurement setup was capable of resolving strains with accuracy ±150 $\mu m/m$ and a resolution of 20 $\mu m/pixel$.

5.4 Results

5.4.1 Grain scale strain measurements and relationship to twin effects

Figure 46 a shows twin nucleation observations made in situ by combining optical microscopy and the SEM compatible MTI stage on cube-shaped samples specially made to be loaded in compression up to ~ 2.31% of total strain. The corresponding localized strain (in the direction of loading) evolution within and across grain boundaries is shown in Figure 46b revealing areas within grains that have unreasonably high both tensile and compressive strains. This is also shown in Figure 46c in which the computed global (average) strains in the used FOV are plotted. It should be noted here that at the early stages of plastic flow (current case) only tension twinning can be activated [193]. The measured local and global strains demonstrate that while the sample undergoes compression (see the black line in Figure 46c), favorable grains (G1 and

G2) for twinning according at least to the reported high Schmid Factor criterion [213], as quantified in Figure 46d, display anomalous large tensile strains exactly at twin locations.

Relevant investigations on the onset of plastic instability indicated that twinning indeed starts at very early stages of deformation (before yielding) for highly textured samples [50]. Furthermore, it was proposed [55] that strain localization as a consequence of twinning first initiates at grains with grain orientation closer to that of the basal plane i.e. at grains with larger SF values [214]. Although the maximum tensile strain caused by twinning has been reported to be only 6.5% [70], the current results appear to provide locally and on average considerably larger values which were suspected to be related to 3D effects of twinning. In fact, out of plane motion severely affects any 2D (in plane) strain measurements such as the ones performed in this test and therefore further investigation was performed and is presented next.

Figure 47a & b show examples of identified by the optical microscope twinned regions and associated pronounced surface morphology changes (differences in height represented by a colorbar) obtained using phase-shifting interferometry. Furthermore, Figure 47c displays height profiles of the roughened free surface as a function of distance measured along two scan lines (labeled i and ii in Figure 47b). The observed sharp changes in the height profile in Figure 47c directly demonstrate the formation of significant surface roughness due to twinning in the cube samples tested in compression. To reveal the 3D surface roughness changes due to twinning

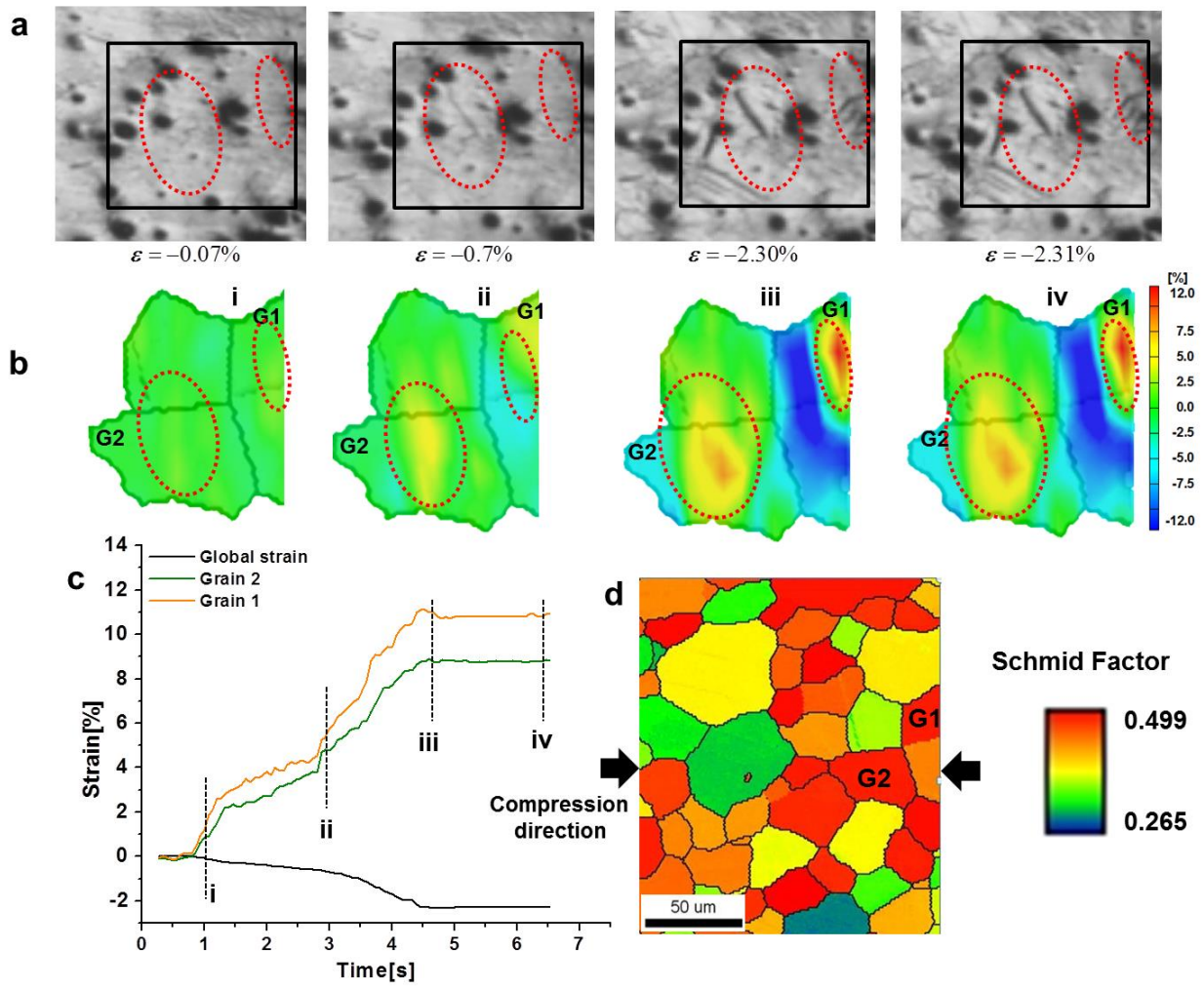

Figure 46 In situ obtained optical microscope images of twin nucleation and growth. (b) Full-field strain maps obtained by DIC with overlaid grain structure. (c) Local (for two different grains) and global (average) strain evolution in time. (d) Measured Schmid Factor values in the region of interest.

Figure 47 d-e show the formation of large extrusions and intrusions in grain regions dominated by twinning. This type of surface steps was previously reported to occur in later stages of plasticity during compression of Mg alloy samples. However, it is the first time, to the authors' best knowledge, that such steps are reported for early stages of deformation as identified by both DIC and concurrent surface morphology measurements.

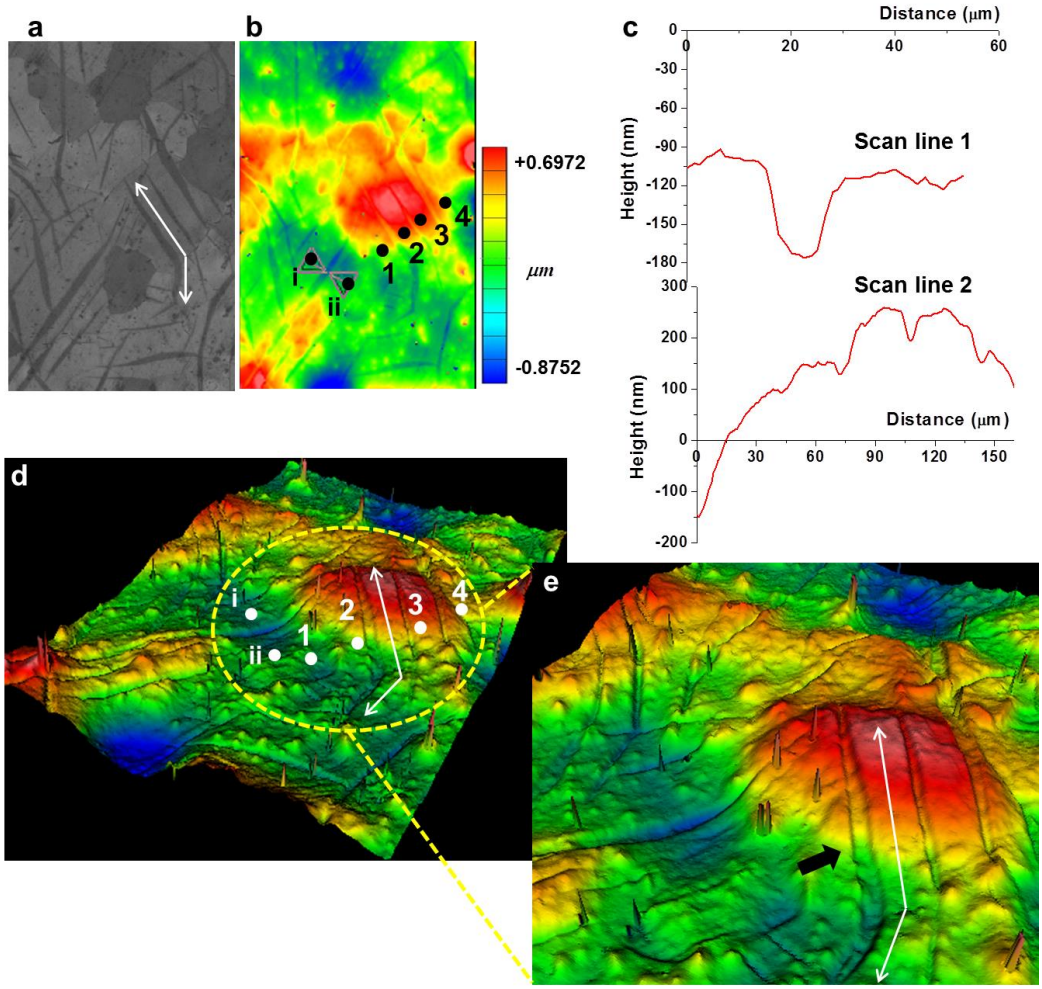

Figure 47 (a) Optical microscopy images obtained from the surface of a deformed specimen showing several twins within multiple grains. (b) Relevant surface morphology contour plot for the same grains obtained using white light interferometry. (c) Surface roughness profiles corresponding to the marked scan lines labeled with roman numerals in (b), and 3D views (d)-(e) of the surface contour displaying grain scale extrusions and intrusions, and their close relationship to twinning.

5.4.2 Specimen level strain localizations and direct relationship to surface steps

To further investigate the association of strain localizations with surface step formation due to twinning in Mg alloys, flattened cylindrical samples were subjected to compression. Figure 48a presents a representative stress versus strain curve. These compression tests were intentionally interrupted at the onset of the plateau region since the authors previously demonstrated that in this region, which plays a key role in metal forming, and for highly textured Mg alloys localized strain accumulations in the form of shear-like bands occur which are directly related to twinning

(see chapter 4 [50]). Figure 48b demonstrates such strain localizations during early deformation. The reason this set of results was required was to validate the effects reported in Figure 46 and Figure 47 in a ROI at the middle of a cylindrical sample (appropriate for compression studies), which as shown in Figure 48b was within the strain band, and therefore it was considered highly probable to contain twins.

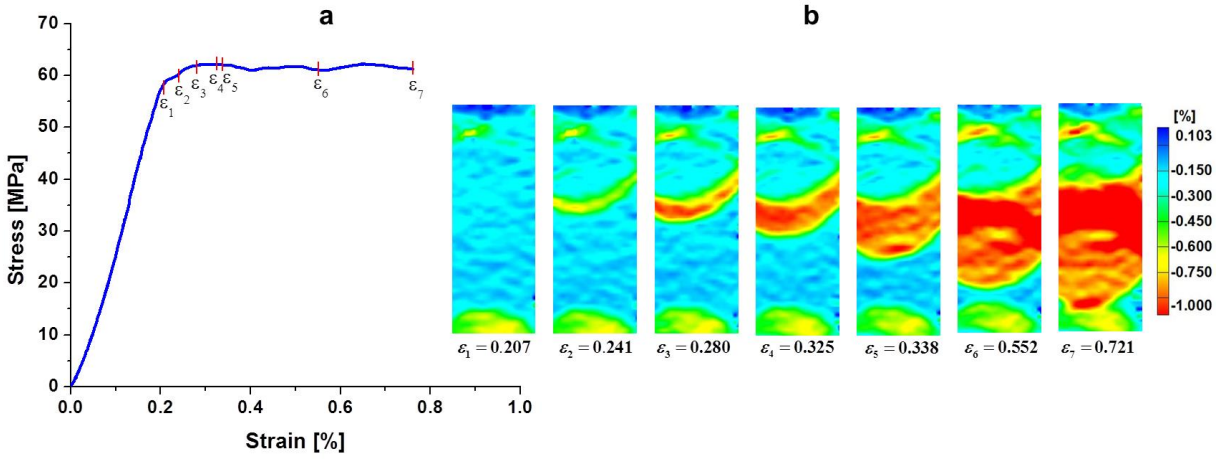

Figure 48 (a) Interrupted stress-strain curve (ε <1% of total strain) for a cylindrical compression sample. (b) Full-field longitudinal (parallel to the loading axis) strains for 7 increments marked on the stress-stain curve.

A scalar indication of the extent of plastic deformation referred to as "effective plastic strain" was defined based on the plastic strain tensor which comprises all three in-plane components. In accordance with Abuzaid et al. [212], the effective plastic strain is calculated as:

$$\varepsilon_{eff}^{p} = \sqrt{\frac{2}{3}(\varepsilon_{ij}\varepsilon_{ij})} \tag{5.1}$$

In fact, DIC measurements allow the simultaneous computation of in-plane longitudinal (ε_{yy}), transversal (ε_{xx}) and shear (ε_{xy}) strains. Since the presented strain fields were measured in situ, they comprise both elastic and plastic parts. However, due to the small contribution of the elastic part in the total strain, the combined elastic and plastic parts were considered as the plastic strain

tensor. Figure 49 illustrates ε_{yy}, ε_{xx}, ε_{xy} and ε_{eff}^{p} for four increments (ε_1, ε_3, ε_5 and ε_7). The results in Fig. 5 show that the effective plastic strain does not comprise a significant strain component in a direction transverse to loading, and it is mostly consisted of the longitudinal strain (ε_{yy}).

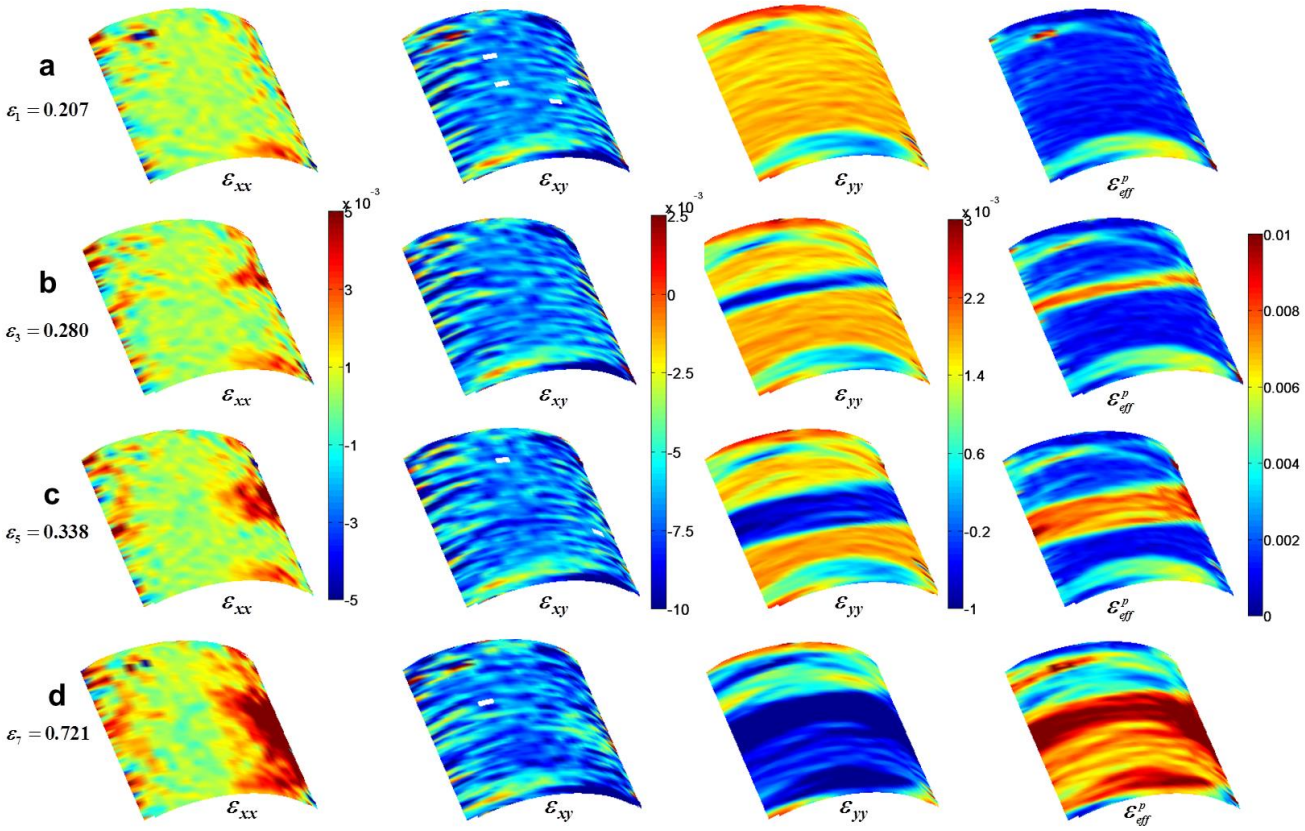

Figure 49 Measured longitudinal ε_{yy}, transversal ε_{xx} and shear ε_{xy} strain fields, as well as effective plastic strain ε_{eff}^{p} for total strain increment (a) $\varepsilon = 0.207$, (b) $\varepsilon = 0.280$, (c) $\varepsilon = 0.338$ and (d) $\varepsilon = 0.721$.

Figure 50 shows the surface topography of the marked ROI before (Figure 50 a) and after Figure 50b deformation obtained from the flattened side of the cylindrical samples. The associated texture measured by EBSD and the surface morphology maps clearly demonstrate the formation of twins in several grains. It is evident that in the initial undeformed state grains are untwinned and no significant surface roughening was measured. The displayed color legend represents the

height of each surface point with respect to a reference point. After deformation a new orientation map and surface topography were calculated. Apparently, even small amounts of plastic deformation (ε <1%) lead to pronounced surface roughening. Figure 50c provides more details about a specific grain (indicated with the solid circle shown in Figure 50b and also marked with the black arrow in the corresponding EBSD map). Careful examination of the results in Figure 50 demonstrates the direct association between twinning and surface steps all of which belong inside the strain band shown in Figure 48. To quantify the surface step profile, the height versus distance plot in Figure 50c contains the scan line results before (blue) and after (red) imposed deformation, which quantify the size of extrusions and intrusions on the surface of the tested one-side flattened specimen.

Several previous studies pointed towards slip-induced roughening during fatigue of polycrystalline materials [215-217]. They attributed such observations to the irreversible nature of slip band motion. It is, however, important to notice that such observations were made for fatigued samples, for which slip bands operate sequentially during tension and compression [218]. Raabe et al. demonstrated the direct relationship between local strain heterogeneities and surface roughness in Al-Mg-Si specimen loaded in both tension and bending [129] and suggested that strain heterogeneities in polycrystals can result in surface defects and roughening [121, 129, 208]. It was additionally hypothesized that the surface roughness evolves with strain and depends on the grain size [219]. For hcp materials, other studies showed that due to the limited number of slip systems the surface tends to experience more pronounced roughening [208, 220].

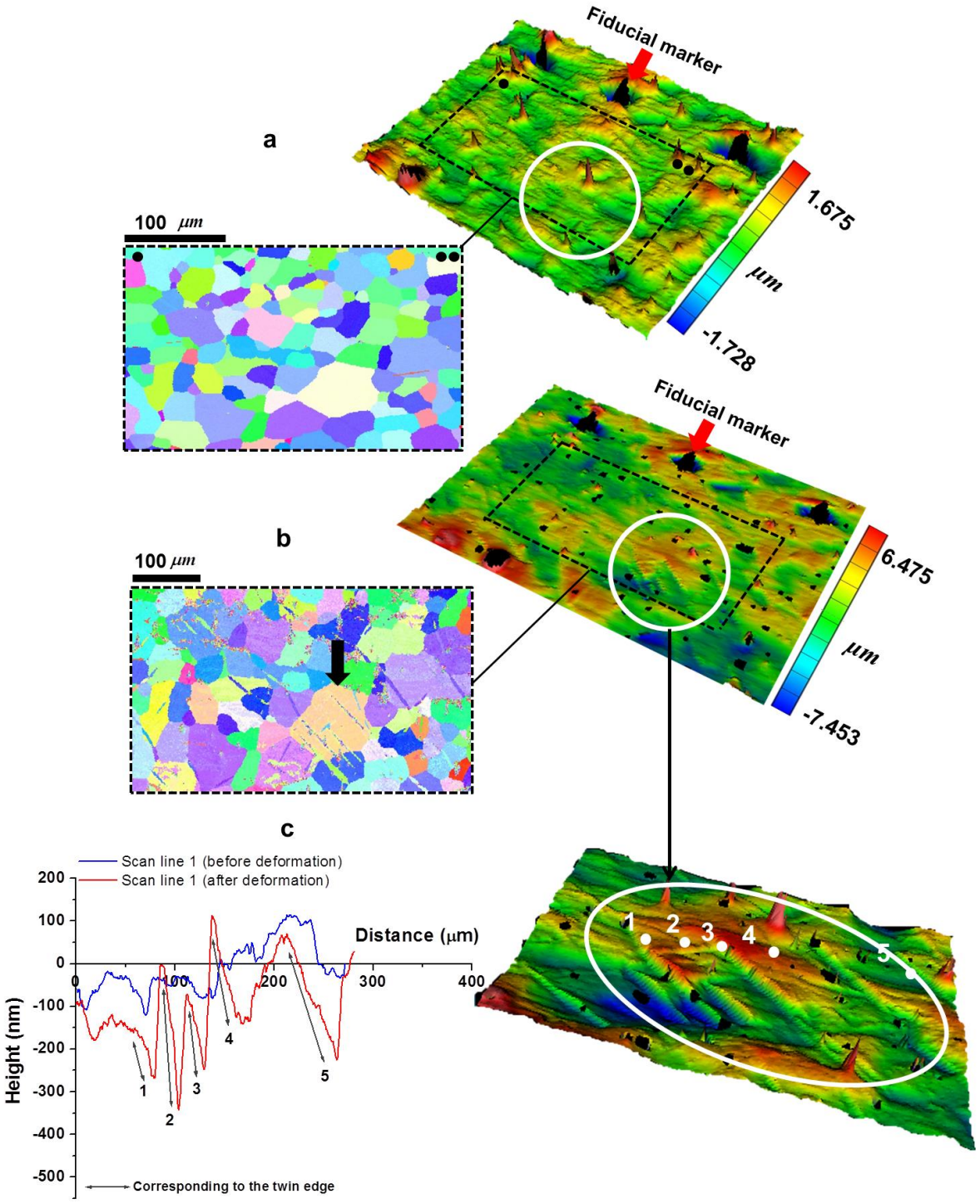

Figure 50 Grain-scale surface morphology maps obtained from optical interferometry and corresponding IPF (a) before and (b) after 0.7 % of total strain. (c) Surface roughness measurements before (Blue) and after (red) straining for the same region. The numbers 1-5 correspond to the grain identified by an arrow in the IPF and by a circle in (b).

The occurrence of noticeable grain scale roughening on Mg alloys was further verified using AFM. Figure 51demonstrates an AFM micrograph of a tension twin in two separate grains. As specified earlier the twin nature was identified using EBSD. The yellow dashed lines (Figure 51a & c) correspond to the twinned region. Figure 50displays clear surface steps. Figure 51b & d present quantitative measurements of the surface extrusions and inclusions due twinning at the onset of plastic deformation. To obtain such plots the cross-sectional profiles and fast Fourier transform of the data along the reference lines shown in Figure 51a & b were used. It is important to notice in Figure 51b that when two twins are formed the generated protrusion is accompanied by an intrusion.

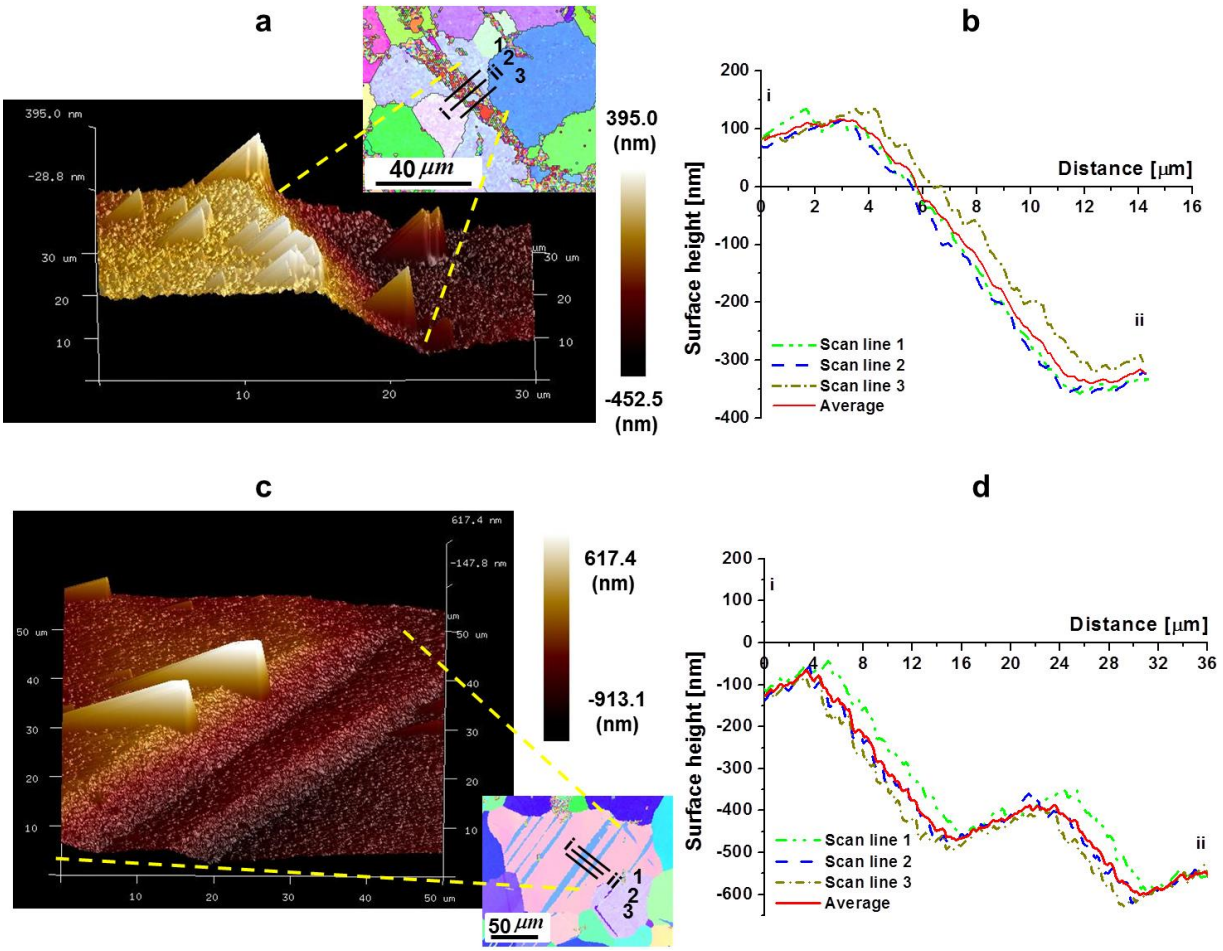

Figure 51 Atomic force microscopy results of surface height for a grain with (a) one twin (c) two twins. Line surface scan profile (b & d) in the twinned grain. These measurements were made across the marked regions from point i to ii in figures (a) and (c) respectively.

In Figure 52 the measured roughness (Figure 52a & b) for a set of grains shown in the IPF of Figure 75c was further used to measure Schmid factor (SF) values in Figure 52d and obtain Kernel Average Misorientation (KAM) in Figure 52e. It can be seen in Figure 52d that the grain with SF equal to 0.25 did not undergo twinning compared to the one with SF equal to 0.47, which contains several twins. Additionally, Figure 52e shows distinct areas with pronounced local misorientation marked with white dashed ellipses near the grain that twinned. Such KAM maps are constructed by measuring the degree of misorientation between a measured point and all its surrounding neighbors and have been related to the stored strain energy [213, 221, 222].

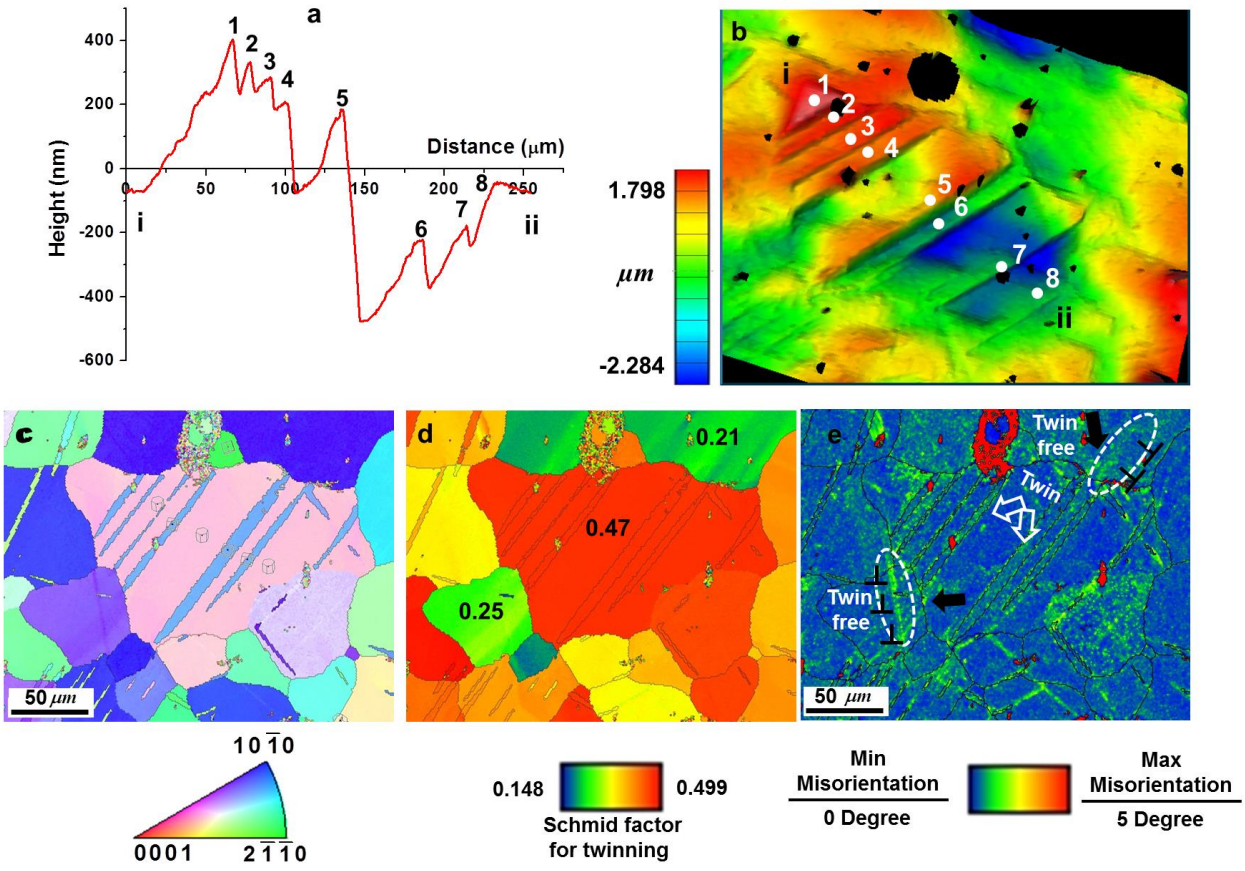

Figure 52 Surface step profile from a line scan identified by points i and ii in the morphology map in (b) obtained from white-light interferometry. (c) IPF for the same set of grains. (d) Corresponding Schmid factor values and (e) Kernel misorientation maps.

It is evident by the KAM map that the density of dislocations at critical intersections of grain boundary and twins (marked with solid black arrows in Figure 52e is relatively higher. This fact can support the probabilistic twin nucleation model for hcp polycrystalline metals proposed by Beyerlein et al. [68], while it further agrees with the model suggested by Meyer et al. [42], and the experimental study by Koike et al. [76] which suggest that stress concentrations are caused by the pronounced activation of basal slip prior to twinning. Similar to a recent study by Balogh et al. [137] where stress gradients in the vicinity of twin boundaries were reported, current experimental results suggest that twin boundaries can have variable states of stress (strain). For example, Figure 52shows the occurrences of several twins in one grain and demonstrates the significant variance in the size of such twin related surface steps, which is a strong indication that twin dislocations are also driven by variable stresses [137]. As a result, the twin density, volume fraction, and morphology can vary widely in grains of the same crystallographic orientation. As such, nucleation is a truly multi-scale event [223].

5.5 Discussion

The grain scale results presented in Figure 46 and Figure 47 which combine in situ observations of twin nucleation with associated strain and morphology measurements, as well as the relevant specimen level results in Figure 50,Figure 51 and Figure 52, suggest that twin formation is directly related to strain inhomogeneities among grains in Mg alloys. In this regard, Ando et al. [193] reported that if a primary twin forms, twinning shear strains are produced and further strain incompatibility is induced between the twin locations and surrounding grains. A closer inspection of the results in Figure 46 and Figure 47 reveals significant strain and morphology gradients within grains and near grain boundaries. Such gradients can be reduced by secondary twins for example [193]. In fact, previous investigations by Korbel and Bochniak [206] provided

insight regarding the onset and consequences of heterogeneous deformation by treating secondary slip systems as the effect of local stress variations; their experimental observations suggested that the increase of local stresses can lead to activation of non-easy slip to lower the total energy of the material system during forming. Therefore, it can be argued that twinning, other grain incompatibilities (e.g. in texture) or pronounced slip activity (e.g. basal in hcp materials) within grains may induce locally high strain regions that may favor further twinning (also higher order twinning or other twin variants). The evolution and exhaustion of such twinning can ultimately lead to fracture as it is discussed in chapter 6.

Former studies pointed out slip-induced surface roughening during fatigue of polycrystalline materials [215-217]. Such effects were attributed to the irreversible nature of the shear strains resulting from slip motion. It is, however, important to notice that the aforementioned observations were recorded for fatigued samples, where slip bands operate sequentially during tension and compression [218]. Raabe et al. demonstrated the direct relationship between micro-strain heterogeneities and surface roughness through straining of Al-Mg-Si samples in tension and bending [129]; they reported that microstructure phenomena leading to strain heterogeneities inside polycrystals aggregates can result in surface defects and roughening [121, 129, 208]. It has been also hypothesized that the surface roughness evolves with strain and depends on the grain size [219]. In hcp materials, other investigations showed that due to their limited slip systems the surface tends to experience greater roughening [208, 220].

The experimental results presented in this article agree with such previous studies [121, 129, 219, 220] and demonstrate the considerable effect of twinning on surface roughness at the onset of plastic deformation, which is extremely important for metal forming [224]. As noted earlier, to the best knowledge of the authors and in relation to former results reported by Moore [225]

Hull [194], as well as to recent detailed TEM observations by Ando et al. [193] and Koike [132], no direct correlation between surface roughening, strain localizations, and twinning in Mg alloys has been made. However, it has been long known that the heights of surface steps in single crystals is equal to the overall shear caused by twinning [194] as schematically shown in Figure 53.

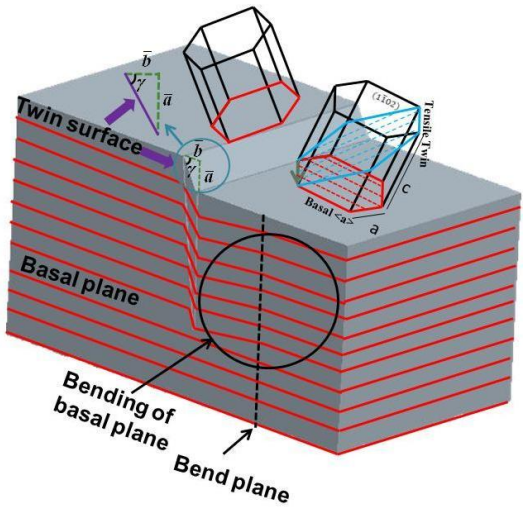

Figure 53 Schematic demonstration of bending on the basal plane and surface step formation due to twinning.

Specifically, Hull [194] described the cleavage-like characteristic morphology when a twin meets the surface. In addition, Jilson [226] described the consequences of shear on the basal plane when twinning occurs. The angle γ, height $\bar{\alpha}$ and size of the twin surface step on the basal plane was measured and it will be outlined next. The corresponding surface step due to twinning for several locations (Grains A, B and C correspond to different regions) were computed based on selecting nine tension twins from three separate grains with different Schmid factor values and reported in Figure 54. The height of the surface step as a function of cleavage angle is shown in Figure 54a. The scatter in the reported values (Figure 54a) indicates that it is very hard to hypothesize a direct relationship between Schmid factor values and surface step. The main reason to this conclusion is related to the unidentified in this study underlying volumetric effects

which directly influence the state of stress (strain) on surface grains. Therefore, a more reliable hypothesis can be drawn only when the collective effect of volumetric (obtained for example using high energy X-rays) and surface grain information for polycrystalline aggregates is available.

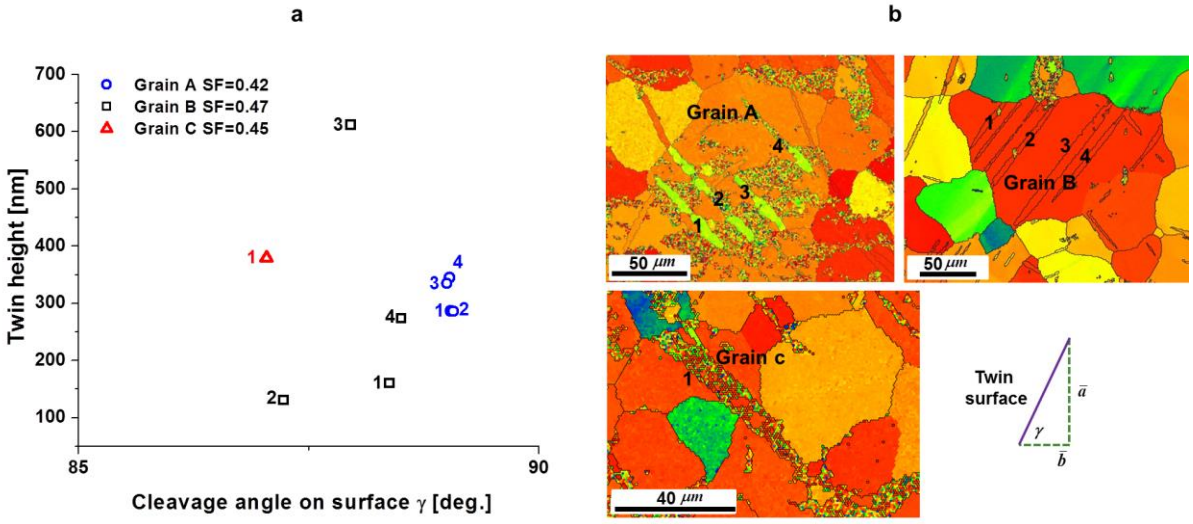

Figure 54 (a) Comparison between surface step height and cleavage angle for (b) three grains with different Schmid factor values and different twin density.

The twin path in relation to local misorientation, Schmid factor, and surface step geometry is presented in Figure 55. The twin appears to form in grains with higher Schmid factor values (0.46-0.48) and it was concluded that thickening occurs in energetically favorable paths (longer side of the grain). It is also important to notice that the green grain in Figure 55c, identified by the black arrow, which was oriented favorably for slip (due to its small SF value), underwent dynamic recrystallization due to pronounced activation of dislocations which can be identified by observing the nucleation of a new grain inside the original grain in the undeformed state (see Figure 55d). It is expected that as local internal stresses increase due to the dislocation pile ups

and reach the CRSS for activation of non-basal slip, dynamic recrystallization nuclei are formed as a result of $\langle a \rangle$ and $\langle c+a \rangle$ dislocation interactions [227].

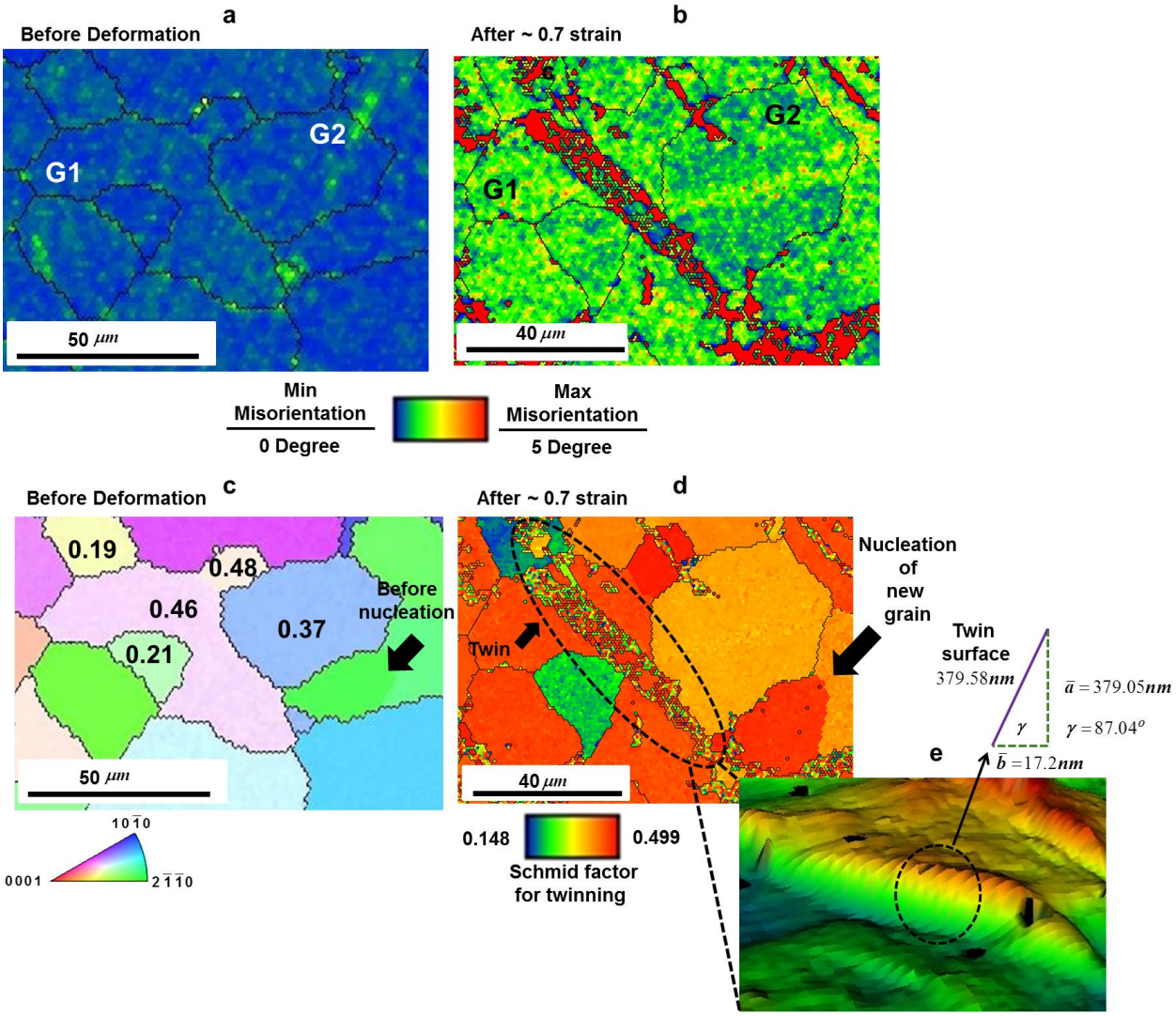

Figure 55 Kernel Average Misorientation for the same grains (a) before (b) after deformation. (c) Inverse pole figure for the same region with corresponding Schmidt factor values. (d) Schmid factor contour. (e) 3D effects of twinning are evident on the surface and its corresponding edges.

5. 6 Conclusion

This article demonstrates the relationship between surface morphology evolution and twinning during compression of magnesium alloys. Both *in situ* grain scale observations and *ex situ* but

high resolution specimen level measurements demonstrate that twinning is responsible for large intrusions and extrusions that form inside and around twin-favorable grains. Direct evidence and quantification were provided to illustrate the three dimensional nature of twinning which can be used to relate such effects with both macroscale plasticity and fracture.

Chapter 6

Microstructure-Sensitive Investigation of Magnesium alloy Fatigue[1]

6.1 Introduction

This chapter describes the critical relationship between measured macroscopic mechanical properties to twinning-detwinning, microplasticity and fatigue crack formation in Magnesium (Mg) AZ31 alloys during Low Cycle Fatigue (LCF) conditions. Experimental fatigue data was obtained by testing standard-sized specimens with an accessible microstructure for direct microstructural quantification and surface morphology evolution analysis. Scanning Electron Microscopy (SEM) alongside with Electron Back Scatter Diffraction (EBSD) analysis was used to examine fractography and texture evolution investigation, respectively. Measured EBSD maps at different stage of fatigue life show repeatable occurrences of Twinning-Detwinning throughout the fatigue life. White-light interferometry was used to study surface morphology evolution and suggest that the surface roughening in Mg alloy is reversible. Therefore, in contrast with FCC metals, no linear relationship between fatigue cycle numbers and surface roughness parameters in Mg with HCP crystalline structure was recognized. It was also found that, although tension twinning contributes considerably on overall plasticity by introducing additional strain components along the c-axis, its boundaries can give rise to crack initiation towards the end of the fatigue life. In addition, in situ nondestructive monitoring of the fatigue

[1] *K. Hazeli, H. Askari, J. Cuadra, F. Streller, R.W. Carpick, M. H. Zbib A. Kontsos "**Microstructure-Sensitive Investigation of Magnesium Alloys Fatigue**". International Journal of Plasticity. under review*

behavior was performed by using the Acoustic Emission (AE) method. The recorded AE signals validated continuous twinning-detwinning occurrences. This test envelope allowed the quantification of the fatigue life in terms of hysteresis loop parameters such as plastic/elastic energy, residual stiffness in addition to maximum, minimum and mean stresses. The targeted mechanical testing combined with high resolution microscopy provided direct evidence on the role of twinning-detwinning and plastic strain localizations near twins as well as surface roughness on the fatigue microcrack formation in Mg alloys. The role of the reported TDR process was additionally explored using a Continuum Dislocation Dynamics Viscoplastic self-consistent (CDD-VPSC) model. The simulation results verified that detwinning is responsible for the anomalous hardening behavior of the sample at various strain amplitudes. This phenomenon was observed for several imposed strain amplitudes and was achieved by properly defining an appropriate boundary condition that allows surface morphology changes. Furthermore, an energy-based relationship for the evaluation of Low Cycle Fatigue (LCF) behavior based on the Ellyin-Kujawski formulation was used and showed a good agreement with experimental information for both half and third quarter-life fatigue predictions.

6.2 Literature review

Improvement of Mg processing, for example cold forming, depends on the understanding of microstructure-property-behavior linkages capable to accurately describe plastic deformation and damage initiation [228, 229]. Although significant progress in this direction has been made [160, 203, 230-242], there is a noticeable gap in information relating microstructure, plasticity and fatigue crack initiation in Mg alloys, which is crucial in a materials-by-design context. To characterize a length-scale microstructure-sensitive fatigue criterion which drives crack formation at microstructure level, a strain-based approach was adopted for several reasons. In

general, engineering components and structures are subjected to a certain degree of constrained loading. Such conditions tend to be similar to strain controlled conditions [243],whereas the strain changes due to cyclic hardening and softening under stress-controlled conditions. In other words, information from a stress-based approach is derived from an unconstrained deformation mode [39]. Moreover, it has been long recognized that cyclic plastic strain is responsible for fatigue damage [244]. Thus, it is significant to determine constrain parameter in strain life relations associated to crack/damage initiation. Finally, because of the crack tip condition, which is commonly identified as elastically strain body [245, 246], strain-life relations to predict fatigue crack initiation should be identified.

Although the effect of microstructural features on the fatigue behavior of polycrystalline materials was documented since the early 1900s [247], the microstructure related mathematical framework for quantitative modeling of fatigue failure has not yet been developed [12, 248]. Microstructures consist of features at length scales ranging from nanometers to several hundred micrometers with complex geometries and varied orientations. Consequently, several spatial correlations and interactions especially under cyclic loading are possible to occur which increase significantly the difficulties associated with both experimental and modeling approaches in microstructure-sensitive fatigue. This article presents information based on the understanding that fatigue and resulting damage initiation are complex evolutionary processes highly dependent on hierarchical microstructural evolution [12, 13]. The effect of local microstructure on macroscopically observed fatigue behavior has been widely researched in the pertinent literature. For example, analysis of the cyclic stress-strain response and the evolution of fatigue hysteresis loop shape showed that the back stress component of the cyclic stress is significantly affected by grain size [249]. Furthermore, the difference in cyclic plasticity behavior between two samples

with different grain size has been related to the effect of grain size on Persistent Slip Band (PSB) morphology. Note that the PSBs are generally characterized as regions of localized deformation arising from intense dislocation activity [250]. In addition, Zhang and Jiang [251] concluded that the fatigue stress-strain response of polycrystalline copper is a strong function of the grain size and texture.

Fatigue crack initiation has been shown to be highly dependent on the degree of strain localization, which in turn depends on both microstructure and active deformation modes [176]. Within this framework, several studies reported that a fatigue crack is formed as the result of localized plastic deformation during cyclic straining [252-256]. In these investigations, evidence is provided on the fact that crack nucleation could occur under cyclic straining due to the formation of irreversible slip bands. Finney and Laird [252] stated that a heavy concentration of strain within PSB structures produces a soft region compared to other regions. This observation is generally referred to as "ductility exhaustion". Basinski et al. [257] further reported gradually increasing PSB intensity as a function of fatigue cycles in copper single crystal. In their study, it appeared that the PSBs begin when the cyclic hardening curve reaches its maximum, while they multiply rapidly and increase in width as stress-strain curve show pronounced softening. In order to develop a stress-life relation [258] considered material responses related to the extrusion-intrusion mechanism produced by PSBs, whose coalescences ultimately lead to crack nucleation. This observation is mostly applicable to FCC metals, however, in which tension-compression asymmetry is usually negligible.

Cyclic experiments on HCP metals are typically more complex compare to other metals due to their dependence on both strong twinning [134, 196, 259] and texture effects [50, 260]. For instance, the relative prevalence of deformation mechanisms strongly depends on the crystal

orientation respect to the loading direction. Consequently, the measured compressive yield stress is significantly less than the corresponding tensile. Studies on the influence of texture on the cyclic response of polycrystals are scarce [255, 261, 262]. For example, Chan [255] showed that texture may enhance fatigue crack initiation if groups of grains are oriented favorably for slip. In highly textured Mg alloys, $\{10\bar{1}2\}$ tension twinning was found to primarily form during the compressive half cycle during cyclic loading [263]. In materials that twin considerably, twinning and its interaction with slip can result in a Bauschinger-like effect [264]. In general, local stress states during plastic deformation of Mg alloys at room temperature greatly depend on twinning [18, 50, 172], which also eventually drives the associated microstructure evolution [74] and has been also recently incorporated into computational models [141, 259].

In agreement with.[172] the authors recently demonstrated [50] that the near yielding behavior is dominated by localized twin-related strain localizations that form characteristic and macroscopically observed band-like structures. Twins were found to propagate from grain to grain, starting from grains with orientation closer to the basal plane [55, 259]. It has been suggested that this effect leads to stress relaxation at the tip of growing twins [172, 193]. A previous study by Partridge [265] shows that twins can disappear or become narrower under reverse loading. In situ bending experiments coupled with Nomarsky interference contrast, directly showed that twins can be partially reverted when the applied load decreases [145]. Despite the frequent reference to twinning-detwinning phenomena and their subsequent effects on tension-compression asymmetry and also strain hardening rate [144, 202, 259, 266-268], many related issues are yet to be addressed. Specifically, it is rare to find direct evidence of the role of twinning-detwinning in fatigue damage initiation [150]. Furthermore, to the author' best

knowledge, the evolution of surface roughness due fatigue loading has not been investigated and associated with evolutionary fatigue incubation conditions.

This article focuses on the role of twinning-detwinning on fatigue damage initiation of Mg alloys. It further examines the effect of local microstructure on both the macroscopic mechanical response during strain-controlled fatigue conditions, as well as on local microstructural changes which are reported herein as key factors to characterize the fatigue behavior of Mg alloys. To accomplish these goals an experimental approach consisting of mechanical testing of standardized-size specimens by also using in situ nondestructive monitoring and ex situ high resolution microstructural characterization tools, was combined with appropriately defined modeling capable to incorporate dominant microstructural observations in its derivation to predict the complicated fatigue behavior of these alloys.

6.3. Experimental Procedure and Modeling Approach

6.3.1 Specimen preparation

Commercial magnesium alloy AZ31 with a nominal composition of 3 wt. % Al and 1 wt. % Zn was used in this study. The alloy was obtained as a 25.4 mm thick plate in the soft annealed condition (O temper). The material was held at 500^{o} C for one hour. Texture, and subsequently the average grain size distribution were measured in metallography samples cut from the normal direction of the plate. Compression, tension, and fatigue specimens were machined from the Mg plate using Electrical Discharged Machining (EDM) according to ASTM E9, E8M and E606 standards, respectively. Tension and fatigue tests were performed for the samples which were fabricated parallel to the Transverse Direction (TD) direction, while compression tests were conducted for specimens cut from the different orientations shown in Figure 56.

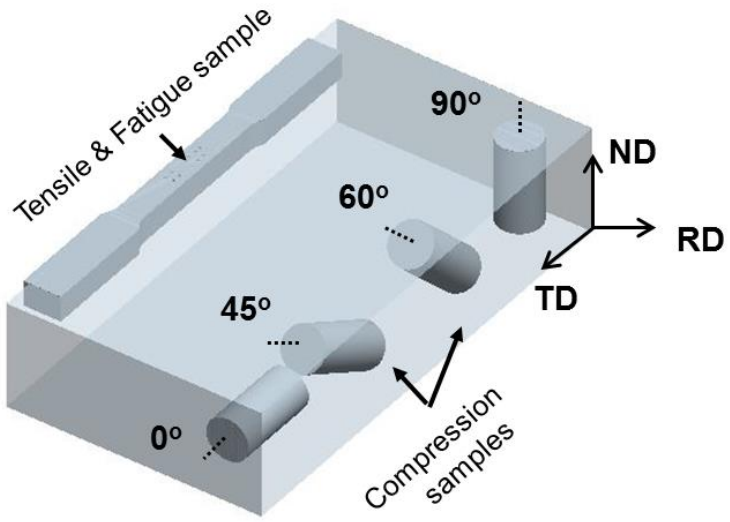

Figure 56 Specimens configuration (compression, tension and fatigue coupons) respect to the Mg plate.

6.3.2 Experimental procedure

Monotonic compression and tension tests were performed in room temperature using a MTS universal testing system at a constant strain rate of $4.5\times10^{-4}s^{-1}$. The same testing system was also used to apply strain-controlled, cyclic compression-tension loading profiles of varying strain amplitude. The fatigue tests were carried out at zero mean strain ($R_{\varepsilon}=-1$, i.e. completely reversed strain cycle), at a constant rate of $5\times10^{-3}s^{-1}$. Saw tooth loading profiles were applied during fatigue tests. To determine fatigue parameters, the fatigue specimens were tested to failure at the following strain amplitudes: 0.25, 0.33, 0.42, 0.50 and 0.58. Furthermore, in situ nondestructive monitoring of the fatigue experiments was provided by Acoustic Emission (AE) measurements. AE signals were recorded using a piezoelectric transducer (Pico) with an operating frequency range of 200-750kHz and a peak frequency at 500kHz connected to a 4-channel data acquisition board (Disp-4, Mistras).

6.3.4 Characterization methods

Fracture surfaces from the fatigued specimens were examined with Scanning Electron Microscopy (SEM). To ex situ study the effect of cyclic strain at the grain scale, fatigue tests were performed on specimens that were polished from one side to a finish acceptable for Electron Back Scatter Diffraction (EBSD) measurements. For this purpose, three regions of interest ($500\times500\mu m^2$ each) were marked by using micro hardness indentation. Local grain information, including lattice orientations, were measured at intervals of $1\mu m$ on a hexagonal grid by automated acquisition and processing of backscatter diffraction patterns in a SEM (FEI XL30). The accelerating voltage and working distance were set at 20 kV and 19.5 mm, respectively. The surface morphology in the marked region was inspected post mortem by non-contact white light interferometry using a Zygo surface profilometer (model 6300) at 20X magnification. As a result of using an objective lens (20X, Mirau), lateral and vertical resolutions of 750 nm and 0.1nm were achieved.

6.3.5 Modeling approach

To quantify the effect of the active deformation mechanisms during cyclic loading of Mg alloys, a modeling approach based on the viscoplastic self-consistent (VPSC) scheme developed by Lebensohn and Tomé [92] was used. Specifically, a Continuum Dislocation Dynamics (CDD) approach was developed in which slip, twinning and detwinning systems are defined by their corresponding normal and Burgers vectors, as well as their associated dislocation densities [269]. Recently, computational models for studying the detwinning mechanism based on twin nucleation and propagation [270], in addition to microstructure evolution during twinning [143] were proposed. In the present study, we use a simplified model based on a phenomenological, power law shear rate formulation that describes both twinning and detwinning as polar

mechanisms. Twinning activity requires positive RSS with respect to twinning Burgers vector while detwinning requires negative RSS with respect to twinning Burgers vector. Detwinning also requires positive twin volume fraction for activation. This is a physical requirement since detwinning is the inverse mechanism of twinning and it cannot be activated if a twinned region does not exist. Therefore we allow twinned volume fraction to recover and add to the untwined volume fraction of the crystal by detwinning activity. We show that for small applied strain amplitudes, this modeling approach can successfully predict the overall fatigue response in the first two cycles.

Details of the VPSC approach are presented in detail the literature [92] . In the following we present a brief explanation of the approach. Since this formulation only determines the plastic part of the deformation, the elastic strains are calculated separately and are then added to the numerical results for plastic deformation. Assuming a homogeneous distribution of elastic strains for all grains, the obtained stresses from the model and the elastic modulus of the polycrystal are used to determine elastic strains at each step. The plastic strain rate in each grain at a given time step is determined according to the shear rates in the slip and the twinning/detwinning systems. Furthermore, the strain rates and stresses in each crystal must conform self-consistently to the corresponding quantities in the homogenized polycrystal which is defined by the boundary conditions. Considering only the plastic part of deformation, the strain rate in each grain in the deviatoric space is represented by summation of shear rates in each deformation system as $\dot{\varepsilon}_{ij} = m_{ij}^{k}\dot{\gamma}^{k}$ where $m_{ij}^{s} = (n_i b_j + n_j b_i)/2$ is the Schmidt factor for slip or twinning system (s) and (n) is the normal vector to the deformation system and (b) is Burgers vector. Given state of

deviatoric stress σ'_{ij}, the shear rate in deformation system (s) is assumed to follow phenomenological expression presented in Eq.(1) and $\tau^s = m^s_{kl}\sigma'_{kl}$ is the resolved shear stress:

$$\dot{\gamma}^s = \dot{\gamma}_0 \left| \frac{\tau^s}{\tau^s_{th}} \right|^{\frac{1}{m}} \mathrm{Sign}(\tau^s) \tag{6.1}$$

In Equation (6.1), m represents strain rate sensitivity, τ^s_{th} is the threshold stress to initiate deformation in system (s) and $\dot{\gamma}_0$ is reference shear rate. The strain rate equation $\dot{\varepsilon}_{ij} = m^k_{ij}\dot{\gamma}^k$ (in five component deviatoric space) contains five equations and ten unknowns. Therefore additional relationships for solving the system are required. The strain rates and stresses in the each crystal must conform self-consistently to the strain rate and stress in the homogeneous media. Therefore, following a linearization of these quantities and by using the equivalent inclusion method [271] a linearized interaction equation between the quantities in the crystal and their pairs in the homogeneous media (shown in capitals) can be obtained using a grain interaction matrix M_{ijkl} and Eigen strains $\dot{\varepsilon}^*_{ij}$.

$$\begin{cases} \dot{\varepsilon}_{ij} = \dot{\gamma}_0 \sum_1^s m^s_{ij} \left(\dfrac{m^s_{kl}\sigma'_{kl}}{\tau^s_{th}} \right)^{\frac{1}{m}} \\ (\dot{\varepsilon}_{ij} - \dot{E}_{ij}) - \dot{\varepsilon}^*_{ij} = M_{ijkl}(\sigma'_{ijkl} - \Sigma'_{ijkl}) \end{cases} \tag{6.2}$$

Equation (6.2) contains a set of ten equations and ten unknowns that can be solved following an iterative process. Different linearization techniques have been developed for Mg alloys and each one leads to a different self-consistent scheme[272, 273]. Among the different schemes, the Affine self-consistent scheme demonstrates the best overall performance and is therefore used in our modeling approach. In the CDD model instead of using the phenomenological model in

Equation (6.1), for describing the shear rate ($\dot{\gamma}$) on each deformation system (s), we use Orowan's relationship for shear rate in a slip system

$$\dot{\gamma}^s = \rho^s \upsilon^s b^s \tag{6.3}$$

where ρ^s, υ^s represent mobile dislocation density and their velocity as a function of stress respectively, and b^s is the corresponding Burgers vector. These quantities are assumed to be constant throughout the grain at each time step. Thus, these parameters represent average quantities and there is no spatial distribution of these quantities inside the grain. In, υ^s for each slip system (s) is computed as follows

$$\mathrm{v}^s = \mathrm{v}_0^s \left| \frac{\tau^s}{\tau_{\mathrm{th}}^s} \right|^{\frac{1}{\mathrm{m}}} \mathrm{Sign}(\tau^s) \tag{6.4}$$

In Equation (6.4), τ^s and τ_{th}^s are resolved shear stress (RSS) and threshold stress, respectively and υ_0^s is a referenced velocity. The shear rate due to twinning or detwinning is assumed to be governed by a power law of the form:

$$\dot{\gamma}^{\mathrm{tw}} = \begin{cases} \dot{\gamma}_0 \left| \dfrac{\tau^{\mathrm{tw}}}{\tau_{\mathrm{th}}^s} \right|^{\frac{1}{\mathrm{m}}} & \tau^{\mathrm{tw}} > 0 \quad \text{(Twinning activity)} \\ -\dot{\gamma}_0 \left| \dfrac{\tau^{\mathrm{tw}}}{\tau_{\mathrm{th}}^s} \right|^{\frac{1}{\mathrm{m}}} & \tau^{\mathrm{tw}} < 0 \text{ and } \mathrm{f}^{\mathrm{tw}} > 0 \quad \text{(Detwinning activity)} \\ 0 & \text{Otherwise} \quad \text{(No twinning or detwinning)} \end{cases} \tag{6.5}$$

Furthermore, assume that plastic deformation is caused by the activation of basal $\{0001\}\langle 11\bar{2}0\rangle$, prismatic $\{1\bar{1}00\}\langle 11\bar{2}0\rangle$, and $\langle c+a\rangle$ pyramidal $\{11\bar{2}2\}\langle 11\bar{2}3\rangle$ slip planes, as well as $\{10\bar{1}2\}\langle 10\bar{1}1\rangle$ tensile twinning system. Detwinning can occur if the resolved shear stress is

negative in the twin system and volume fraction of twins is positive. The negative sign for detwinning shear rate implies that detwinning acts as a recovery mechanism for plastic deformation similar to retreat of the partial dislocations creating the twins. Note that this definition of twinning and detwinning systems automatically prevents activation of both mechanisms simultaneously. According to Equations (6.5) these mechanisms are defined as polar mechanisms that require positive RSS in their plane. Dictated by their geometry, in each twinning and detwinning system of the same character, one of the twinning or detwinning systems will possess negative RSS which ensures zero shear rate in that system. The additional condition defined in Equations (6.5) for the detwinning system ensures that detwinning is only allowed when a positive volume fraction of the twins is available in the corresponding system to be "consumed". The threshold stresses in Equation (6.5) evolve according to the general Voce law [274], but the threshold stresses in Equation (6.4) are represented by

$$\tau_{th}^{s} = \tau_{0}^{s} + \tau_{HP}^{s} + \alpha\mu b\sqrt{\Omega^{sr}\rho^{r}} \tag{6.6}$$

for slip systems where τ_0^s is the initial critical resolved shear stress, τ_{HP}^s is the Hall-Petch hardening parameter and the third term represents the forest dislocation hardening [275]. In the last term in Equation (6.6), captures the latent-hardening and self-hardening as proposed by the Bailey-Hirsch model, with α being a constant, μ shear modulus and Ω^{sr} dislocation interaction matrix that defines the latent hardening effect of system (r) on system (s). Furthermore, the dislocation density ρ^r is the sum of mobile (ρ_m^r) and immobile (ρ_i^r) dislocations in system (r) which evolve according to the following equations:

$$\dot{\rho}_m^{(s)} = \alpha_1 \rho_m^{(s)} \bar{v}_g^{(s)}/\bar{l} - 2\alpha_2 R_c (\rho_m^{(s)})^2 \bar{v}_g^{(s)} - \alpha_3 R_c \rho_m^{(s)} \rho_i^{(s)} \bar{v}_g^{(s)} - \alpha_4 \rho_m^{(s)} \bar{v}_g^{(s)}/\bar{l} + \alpha_5 (|\tau^s|/\tau^*)^r \rho_i^{(s)} \bar{v}_g^{(s)}/\bar{l} \quad (6.7)$$

$$\dot{\rho}_i^{(s)} = \alpha_4 \rho_m^{(s)} \bar{v}_g^{(s)}/\bar{l} - \alpha_3 R_c \rho_m^{(s)} \rho_i^{(s)} \bar{v}_g^{(s)} - \alpha_5 (|\tau^s|/\tau^*)^r \rho_i^{(s)} \bar{v}_g^{(s)}/\bar{l} \quad (6.8)$$

The constants α_1 to α_5 respectively control dislocation generation rate, mutual annihilation of mobile dislocation, annihilation of mobile and immobile dislocations, dipole formation rate and the rate at which immobile dislocations break up from locks and become mobile. These rates for dislocation reactions are a function of dislocation velocities calculated by Equation (6.3). In addition, R_c is the critical distance for dislocation reaction and τ^* is the critical stress for unpinning, which is in the order of threshold stress and dislocation mean free path $\bar{l}$.

Although dislocation hardening is defined through interaction matrix Ω^{sr}, any hardening that arises from dislocation and twin interaction is accounted by the dislocation mean free path. Here we assume that twins are impenetrable regions inside the grain. Therefore, twinning in this formulation is expected to reduce the available space for dislocation glide by reducing the mean free path similar to Kalidindi's approach [91] as presented in the following equation:

$$\bar{l} = \sqrt{\frac{1 - f_{tw}}{\rho_{total}}} \quad (6.9)$$

In Equation (6.9) f_{tw} is volume fraction of twins in the grain and ρ_{total} is the total dislocation density in the grain. The twin volume fraction rate in each grain is calculated by $\dot{f}_{tw} = \sum \dot{\gamma}^{tw}/S^{tw}$ which is the sum of shear rates in twin systems obtained from Equations (6.5) divided by the characteristic shear of the twin S^{tw}. In case of detwinning activity, the volume fraction of the twins will be reduced and subsequently, softening in dislocation glide is expected. The complete specification of the parameters and dislocation evolution laws are presented elsewhere [276].

6.4 Results and discussion

6.4.1 Monotonic behavior

Representative compression and tension stress-strain curves for the samples shown in Fig.1 are plotted in Figure 57. It is evident that compression along the Normal Direction (ND) shows the highest yield stress. Figure 57 displays that remarkable elongation (>20%) can be obtained for the specimens cut at 45^{o} angles with respect to the rolling direction. It should be noted that the flow stress decreases remarkably when the specimen orientation approaches the Transverse Direction (TD). Since the grain size of the specimens was very similar, this observation can be attributed to the significant effect of texture on mechanical response. In fact, the high Schmid's factor (SF) for twinning for TD compression [77] results in the characteristic s-type stress-strain behavior which has been found to be twin-dominated [50, 70, 187].

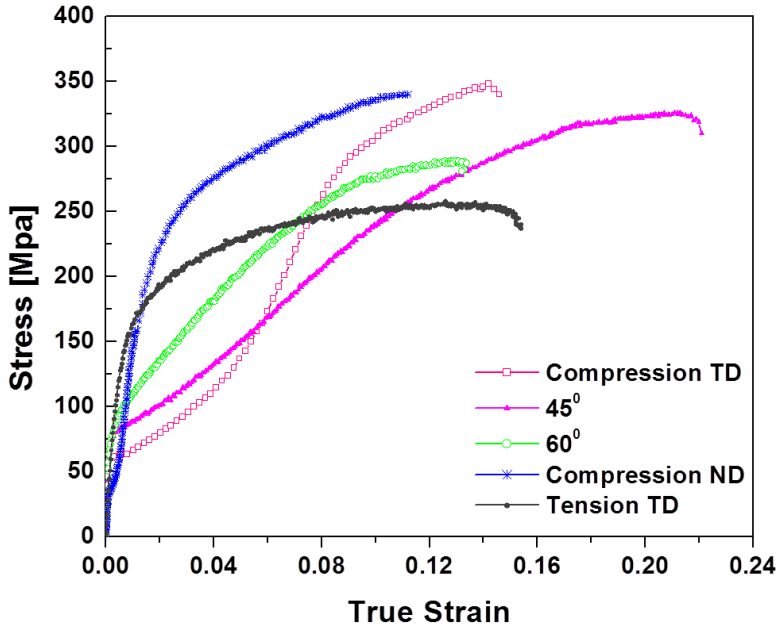

Figure 57 Measured stress-strain curve for compression and tension specimen cutting from different direction

The mechanical behavior results in Figure 57 further show a notable flow stress and strain rate difference between tension and compression (referred to as tension-compression asymmetry). In an extruded magnesium alloy with strong basal texture it is expected that this asymmetry is largely determined by the relative ease with which tension twinning occurs (which dominates yielding in compression) compared to that of prismatic slip (which dominates yielding in tension, [277].

6.4.2 Cyclic behavior

The fatigue deformation behavior during the first, second, half-life and one cycle before failure is shown in Figure 58. As the initial texture is favorable for twinning in the compressive loading path, there is a plateau in the stress-strain curve past the corresponding yielding point in agreement with pertinent fatigue results [203, 232, 233]. The region of constant stress, as mentioned previously, corresponds to twinning [50, 172]. Upon load reversal significant tension-compression asymmetry can be observed [135, 187], which becomes more pronounced with increasing strain amplitude. This increase can be justified by the fact the twin density is expected to also increase by larger imposed strain amplitudes. While the reason for the observed strong Bauschinger effect has proposed to be a result of the twinning-detwinning activity [263, 278], no rigorously tested explanation for its evolution and saturation has been proposed. Twinned regions formed in the compressive loading path reorient under subsequent tensile loading in which detwinning occurs [144], which it is possible to also lead to plastic strain recovery. The compression-tension asymmetry reduces as the number of cycles increases. However, even near the end of fatigue life, and especially at higher strain amplitudes, the hysteresis loop appears to have a noticeable inflection point as the load reverses from compressive to tensile. This could be attributed to detwinning even at the very end of the fatigue

life, which is further investigated later in this article. These inflection points are also indicative of macroscopic strain hardening that has been frequently attributed to dislocation interactions.

In agreement with the relevant literature [144, 202, 266], the current results indicate strong variations in fatigue behavior, especially for the specimens tested at higher strain amplitudes. Further investigation and quantification of the evolution of four fatigue parameters including the compressive and tensile stiffness, as well as the measured stress amplitude and plastic strain energy density is presented next. Figure 59 shows schematically the definitions of these parameters including the characteristic inflection point and pseudoelasticity in the tensile loading path.

The inflection point in Figure 59 is used to describe the point where the strain hardening rate changes from descending to ascending. Figure 60 presents the stress and corresponding strain for such inflection points for different strain amplitudes in the 1^{st} and 2^{nd} fatigue cycles of Figure 58. It is clear that the inflection points shift to higher levels of strain and stress as the strain amplitudes decreases. To explain this result it should be kept in mind that the strain hardening is very sensitive to the strain amplitude and that the increase in hardening rate correlates with exhaustion of twinning-detwinning [135].

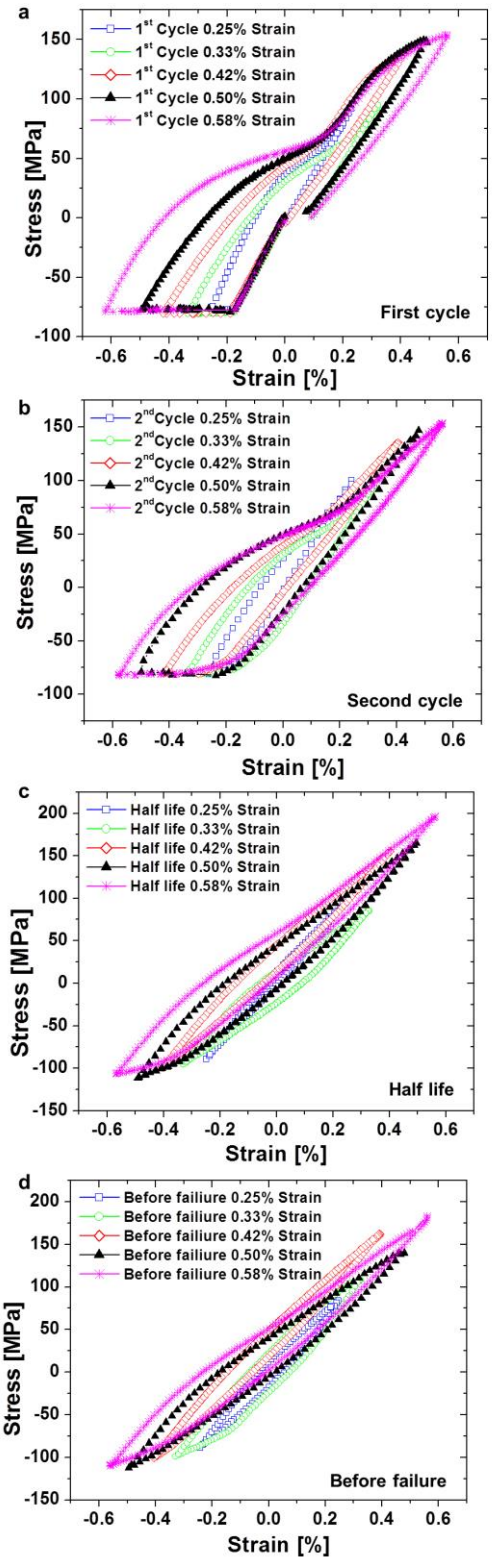

Figure 58 Asymmetric hysteresis loop for varying applied strain amplitudes of 0.25, 0.33, 0.42, 0.5 and 0.58 under $R_\varepsilon = -1$ loading parallel to the transverse direction for (a)1st cycle, (b) 2nd cycle, (c) Half-life (d) last loop before final failure.

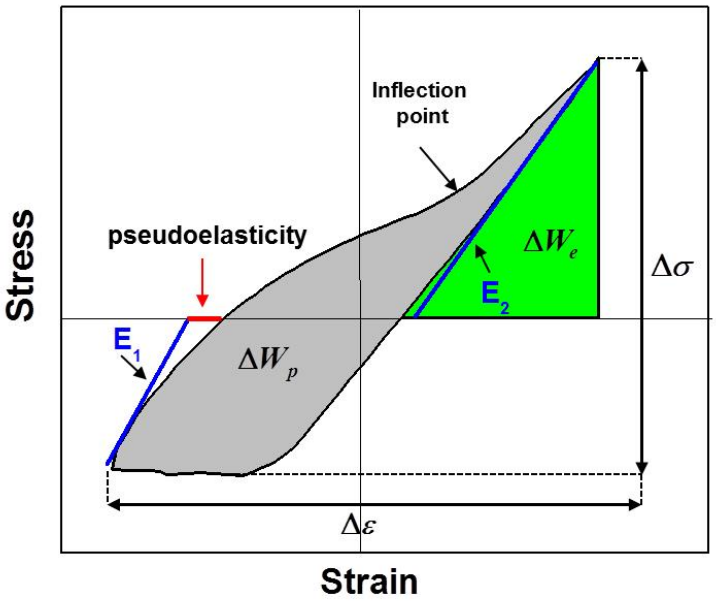

Figure 59 Definition of hysteresis loop parameters

In fact the activation of harder slip systems, such as prismatic slip is needed to accommodate further imposed strain when twinning-detwinning activity cannot accommodate any c-axis strains, and this remark could explain the considerable change in the strain hardening during tensile loading in the 1st fatigue cycle [72]. During the second tensile loading, similar inflection points are found at comparatively larger strains and stresses for each imposed fatigue strain amplitude (Figure 60b). The difference in the corresponding stress recorded for each inflection point between the first and second cycle was found to be more significant for the larger values of the imposed strain amplitude. This observation could be explained by the fact that by imposing larger fatigue strains potentially larger twin volume fractions are also created. Consequently, larger volume fraction of twins is available to be detwinned and thereby more tensile strain can be accommodated by detwinning in accordance with in situ neutron diffraction results, which therefore support this conclusion [135].

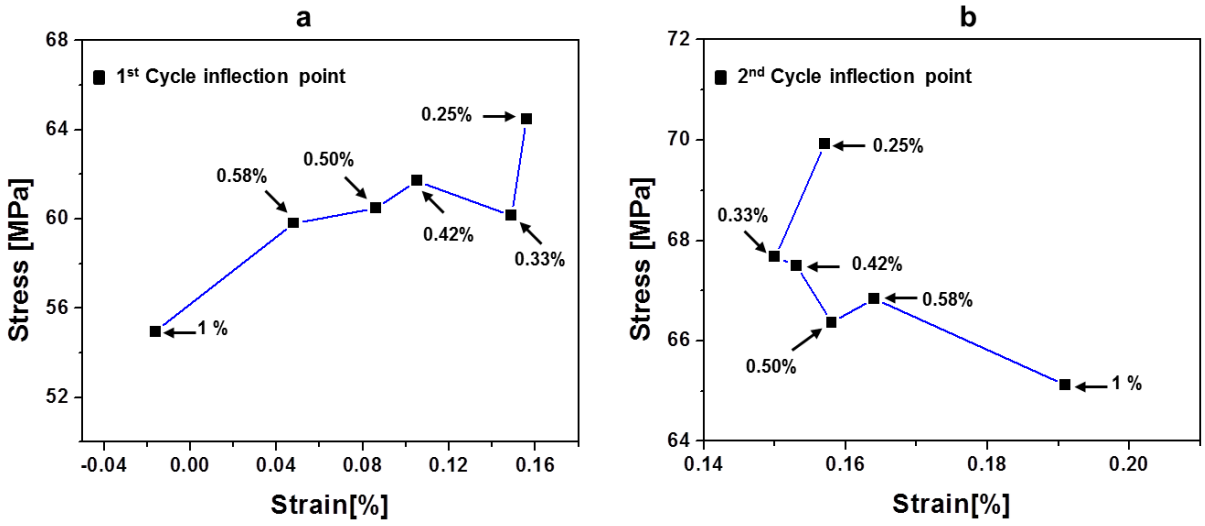

Figure 60 Inflection points measured for (a) first fatigue loop (b) second fatigue loop at different strain amplitude

Figure 61 illustrates the evolution of compressive (E_1) and tensile (E_2) stiffness as a function of fatigue cycles. Both stiffness values were found to have their highest values for the smaller applied strain amplitude. Past the first loading cycle it is observed that there is a sudden drop followed by an almost steady state for E_1 whereas a more gradual change is seen for E_2, in which case a decreasing strain amplitude leads to a corresponding decrease of the measured stiffness.. Similar observations were reported by [202]. The sudden change in stiffness (E_1 and E_2) has been suggested to be the consequence of opening and closing of micro cracks [279, 280]. It can be also seen in Figure 61 that the both stiffness curves change rates with increasing fatigue cycles. The stiffness rate changes indicate that the fatigue behavior of Mg alloys is sensitive to microstructural changes throughout the fatigue process.

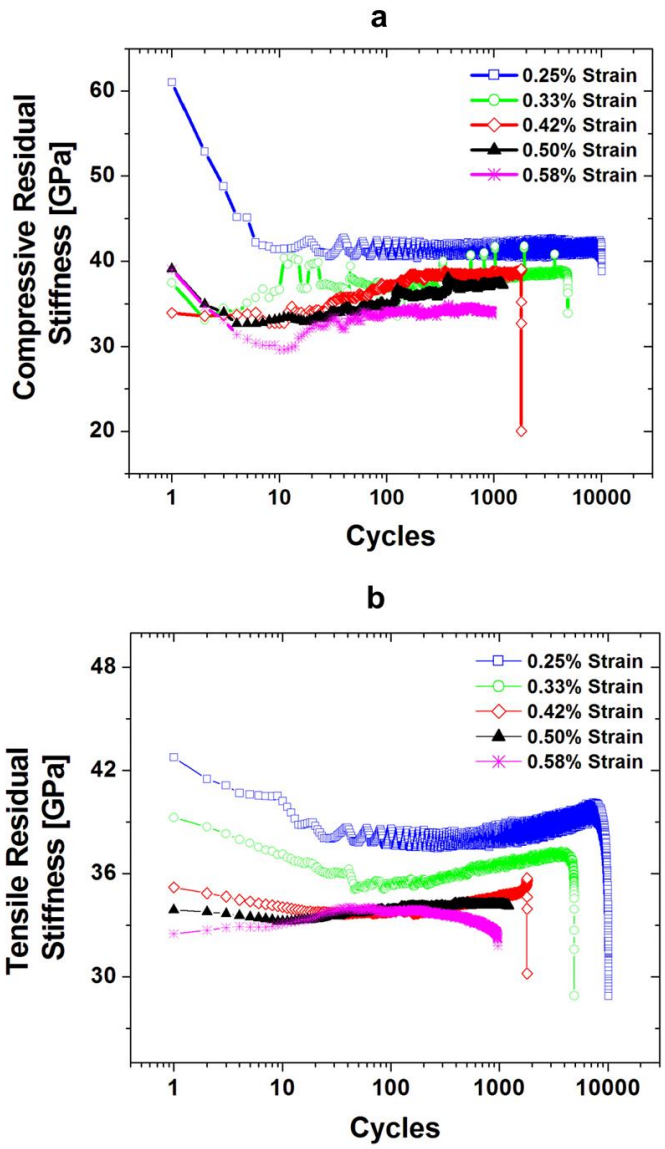

Figure 61 Evolution of (a) compressive, E_1 and (b) tensile, E_2 stiffness as a function of fatigue cycles

Figure 62 shows the effect of different strain amplitudes on the maximum, minimum and mean stress as a function of fatigue life. The results presented in Figure 62a demonstrate that the maximum stress increases, as expected, as the imposed strain amplitudes increase. It is interesting to note that for the lower strain amplitudes (0.25% and 0.33%) the measured maximum stress has a slight decreasing trend during fatigue, whereas the higher imposed strain

amplitudes lead to an increase trend for the maximum stress per cycle as fatigue progresses. Furthermore, Figure 62b demonstrates that the minimum stress per cycle decreases with evolving fatigue. This remark in combination with the observed hysteresis loop shape changes past the 1st fatigue cycle could be attributed to changes in the twinning-detwinning and perhaps in the decrease of the twinning (and consequently the detwinning) activity with fatigue, which promotes the activation of non-basal slip and results in the transition from a "s-type" to a more typical hardening type behavior. Moreover, the mean level of the imposed strain is known to play an important role in influencing the fatigue life [39]. Figure 62c shows that for higher strain amplitudes the mean stress values per cycle initially decrease and then increase. A similar initial reduction and subsequent increase in mean stress is also reported in prior works [202, 281]. It is noted that the drop can be the indication of micro damages [281], which is consistence with sudden stiffness changes discussed earlier. Figure 62 also suggests that the higher the mean stress is the shorter the fatigue life becomes. Interestingly, the higher impose strain amplitudes lead to increasing mean stress values which could be another implicit indication of a more pronounced strain hardening behavior due again to more significant changes in the twinning-detwinning activity compared to the smaller strain amplitudes.

6.4.3 Microstructure-surface evolution and fatigue crack initiation

Crack initiation is, in general, highly dependent upon the degree of localization processes, which themselves are closely related to microstructure and texture. Localized strain, for example, promotes early crack initiation because the macroscopically imposed strain must be carried in relatively few active regions (limited deformation system) [176, 282]. For instance, it has been shown that the Portevin-Le Chatelier (PLC) instabilities, associated with highly localized

deformation, result in strain bursts in the form of bands that have been suggested to play a crucial role in crack initiation [282]. Local deformation heterogeneities induced by the microstructure

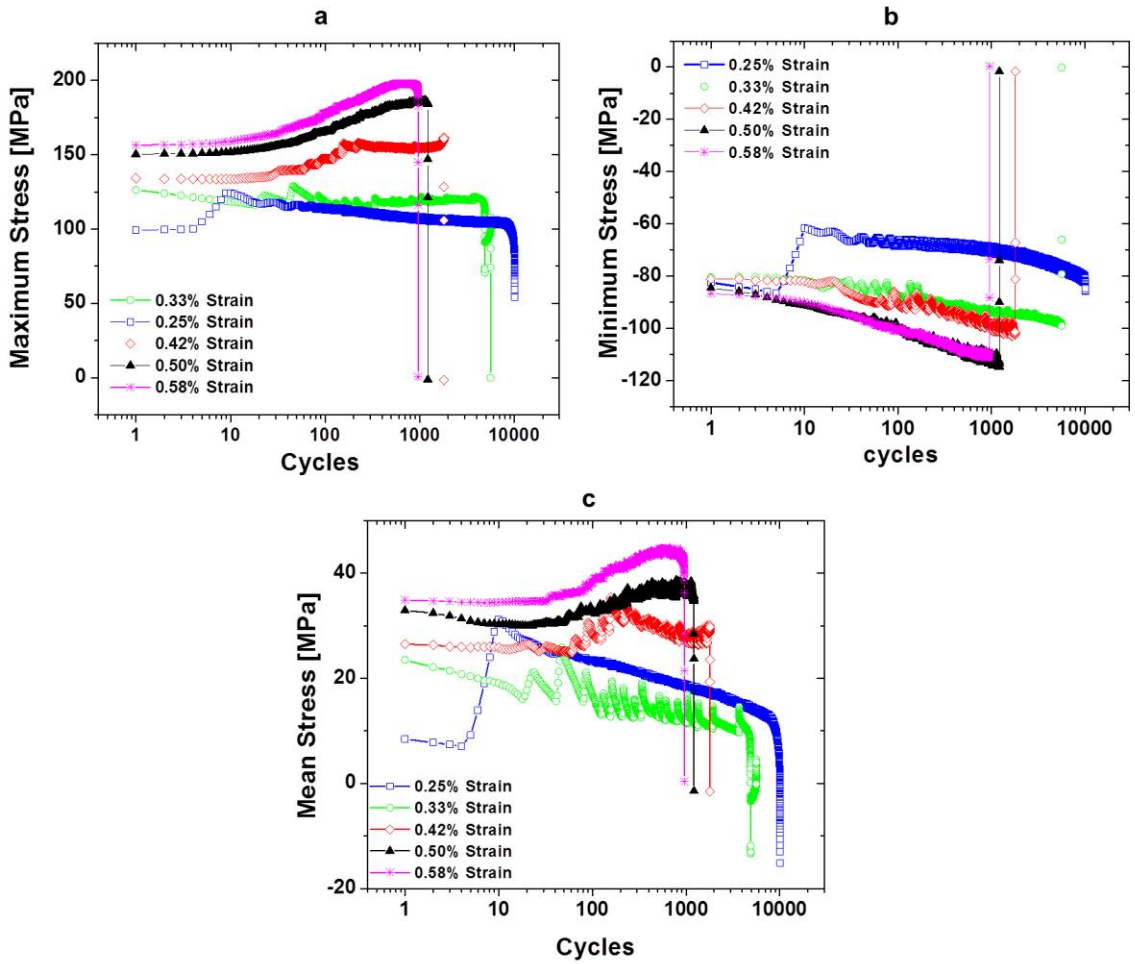

Figure 62 Evolution of (a) maximum, (b) minimum and (c) mean stress for different imposed strain amplitudes.

have been also reported to influence fatigue crack initiation and micro-crack propagation [212]. The same reference also describes the necessary condition and a precursor for the fatigue crack nucleation in polycrystal Hastelloy. Investigation of the fatigue behavior of α-iron polycrystal at a high cyclic strain rate disclosed the development of a surface roughening with the periodicity of the grain size and with stress concentration, leading to fatigue crack initiation [283]. In addition, an elaborate study by Man et al. [40] demonstrated that the cyclic strain localization

leads to PSBs with specific dislocation structure, followed by distinctive surface slip marks (surface extrusion and intrusion) which further promote fatigue cracking. Besides intrusions and extrusions, fatigue crack initiation may occur at grain boundaries or twin boundaries as the result of slip impingement [255]. In the case of Mg, since the grain boundaries are sufficiently strong [132], additional stresses arise to maintain strain compatibility at grain boundaries. Stress incompatibilities lead to the activation of twinning and non-basal slip. It is, however, possible for stress (strain) concentrations due to incompatibilities between twins and their surrounding matrix regions to be relaxed by slip [193, 197] or crack formation [189]. The described complex local plasticity becomes even more complex when twinning-detwinning interchange.

Twinning-detwinning and partially twin removal have been reported in the literature [145, 259]. Recently, the key role of twinning-detwinning on microstructural evolution and cyclic hardening under strain control cyclic condition has been highlighted [235]. However, direct evidence of this phenomenon is rare. Figure 63 shows the occurrence of twinning-detwinning for three microstructural regions as a direct result of a strain-control fatigue experiment with 1% strain amplitude. Each EBSD map in Figure 63a was measured at the points of first zero-stress crossings after load reversal. The results show the twinning-detwinning occurrences in the same fatigue cycle in multiple regions in the material (see Figure 63b). The most important fact to note though is that such measurements were performed using standard-sized specimens which incorporate, therefore, the effect of the bulk and are consequently important both from a statistical and mechanical behavior point of view. Real time volumetric inspection of microstructural changes was conducted through the AE nondestructive method. In Figure 64, the measured triangular stress-time waveform for several fatigue cycles is overlaid with recorded AE signals for two different imposed strain amplitudes. These results show that the AE amplitude

distribution (notice the top row of arrows) exhibits distinct increases near the peak compressive load, which has been previously documented [50, 113] and was directly related to the onset of twinning.

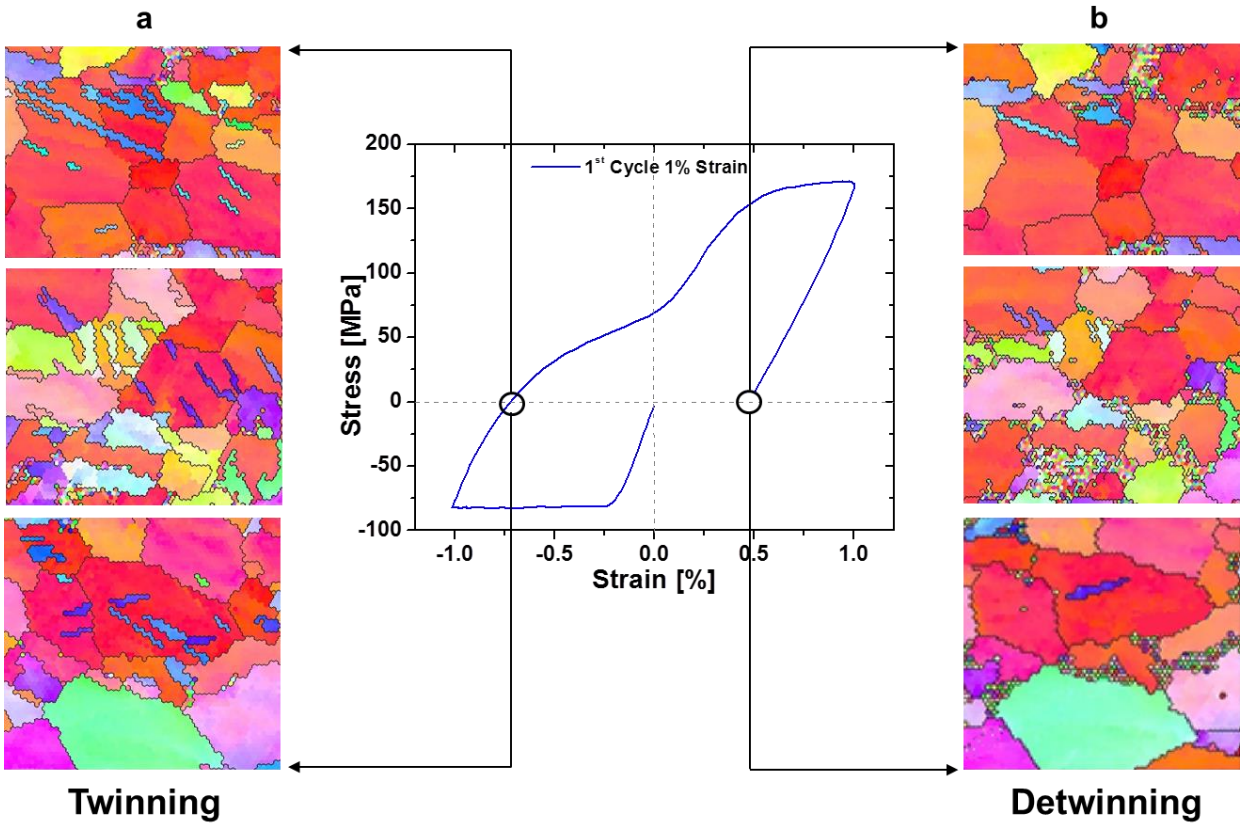

Figure 63 First fatigue cycle for 1% of total strain amplitudes under $R_\varepsilon = -1$. (a) Twinning and (b) detwinning was identified for three different regions.

This diagram suggests that the AE amplitude rises significantly as the samples undergoes compression and the AE amplitudes drops markedly as the loading direction reverses to the tension direction (the maximum amplitude during tension is noted by the bottom row of arrows). This observation can be attributed to the fact that the activation energy for twinning is larger than that for detwinning, presumably because of the need for nucleation. By comparing the decrease of the recorded AE amplitudes as a function of time, it can be concluded that the twinning-

detwinning activity is possible to evolve as fatigue continues. The difference though in AE amplitudes in compression and tension remains nearly constant (~25 dB difference) which might imply that past initial twin nucleation, twinning-detwinning might operate for several cycles. Repeatable occurrences of twinning-detwinning will be further supported next with additional characterization results and constitutes a critical observation for the identification of changes in the fatigue behavior of Mg alloys. As specified earlier, it is important to note that both stiffness and mean stress drop after the first loop, which could be an indication of either micro-cracking or twinning. However, based on the results in Figure 63 and also on the fact that the highest AE peak amplitude appears to occur at the same stage of cyclic compressive loading twinning is the most probable case for this effect.

Twinning is recognized to be a major source of localization phenomena in Mg alloys [50]. In this framework, the authors recently used several experimental characterization techniques to show that twinning leads to considerable surface extrusions and intrusions during monotonic loading [284]. A similar approach was applied in this article to investigate the surface evolution of Mg alloys subjected to fatigue. To this aim, fatigue specimens prepared according to ASTM606-04 were polished to mirror surface finish.

Several regions on the polished surface of each specimen were marked using a micro indenter to study surface parameters by using optical interferometry before and during fatigue. With the aid of these fiducial markers, it was consequently feasible to inspect the same regions of interest at different stages of fatigue life. Figure 65 shows relevant measurements in which the surface topography of a 65 x 85 μm^2 region of the fatigued specimens at quarter-life, half-life and third-quarter life is presented. The color bar in these figures denotes surface height in the millimeter range.

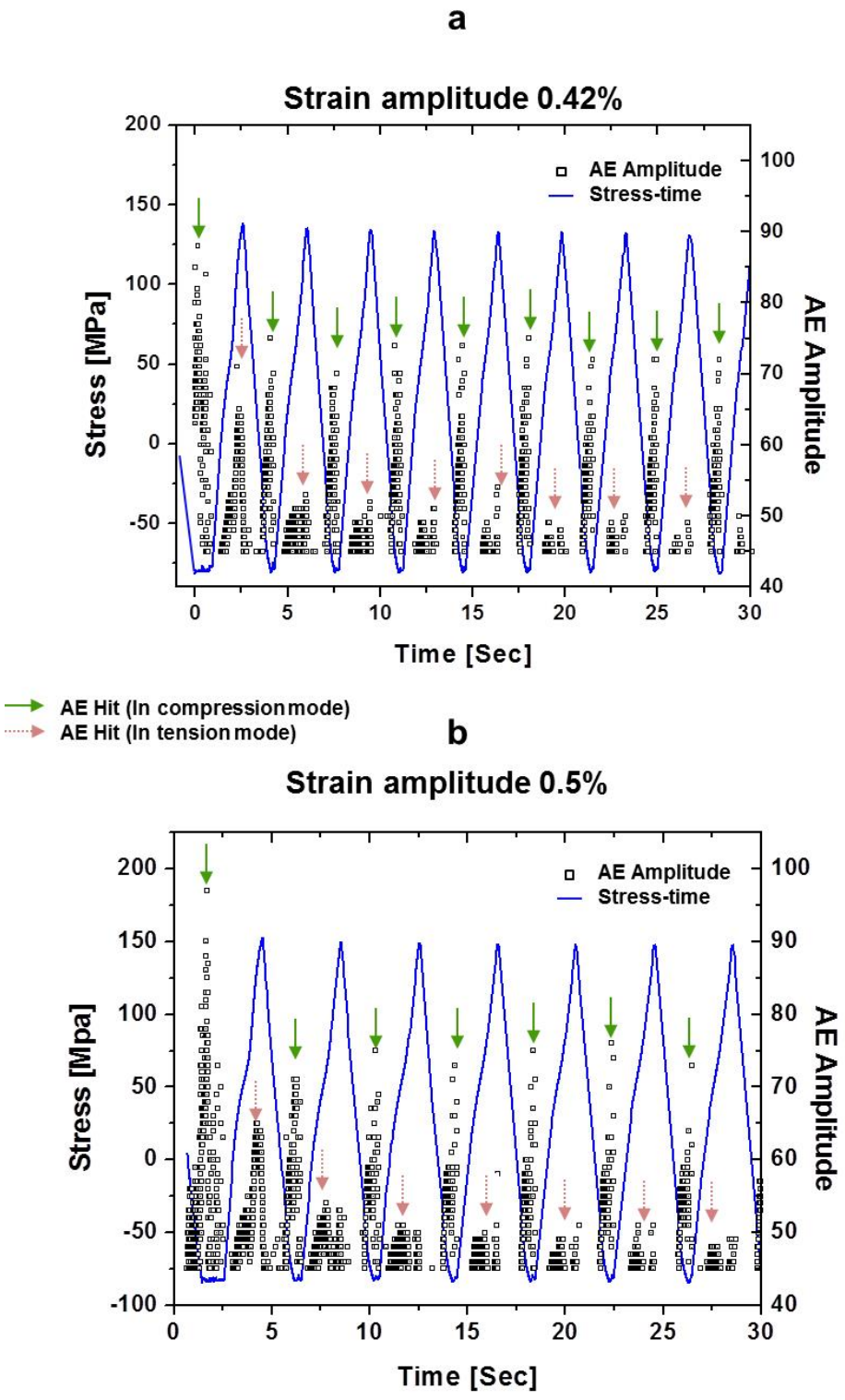

Figure 64 Measured stress-time combined with real time AE activity (a) strain amplitude 0.42 (b) strain amplitude 0.5. Artificially added arrows indicates larger AE activity during compression than tension as a result of twinning detwinning

To quantify the observed surface topography, Figure 65d shows the representative (average) of 3 scan lines across the longer side of the region in the direction of the points from i to ii. Note that for comparison purposes, care was given to terminate the fatigue loading always at the same point of stress ($\sigma = -15MPa$). It is evident from the results in Figure 65 that the surface morphology which was formed at quarter life is relaxed at fatigue half-life, while it becomes more pronounced at the third-quarter. This novel, to the author' best knowledge, measurement demonstrates reversible surface roughening of Mg alloys during strain-control fatigue which based on results previously reported might also be a strong indication of collective macroscopic effects of the twinning-detwinning process.

In addition to the potential effect of twinning-detwinning activity on surface evolution during fatigue of Mg alloys, it was specified earlier in this article that twinning could also be responsible for a non-zero mean stress during cyclic loading. In this regard, it has been suggested that the twins and their parent grains must contain significant internal stresses that can start the detwinning immediately upon unloading [285]. Such large internal strain gradients as a direct result of twinning have been recently identified and quantified [284]. It has been further suggested that the position of the twins in the deformed state is unstable, and that an opposing driving force could cause detwinning upon unloading [145] which is also related to the pseudo-elasticity observed during unloading following compression. In contrast, unloading from the peak tensile stress occurs elastically [135]. Further information on the twinning-detwinning activity during fatigue life is presented in Figure 66 which clearly demonstrates that twinning-detwinning and its repeatable occurrences, called twinning-detwinning-retwinning (TDR) in this article, does not saturate in early stages of fatigue as it was previously reported [266, 281, 286], but it appears past the fatigue half-life.

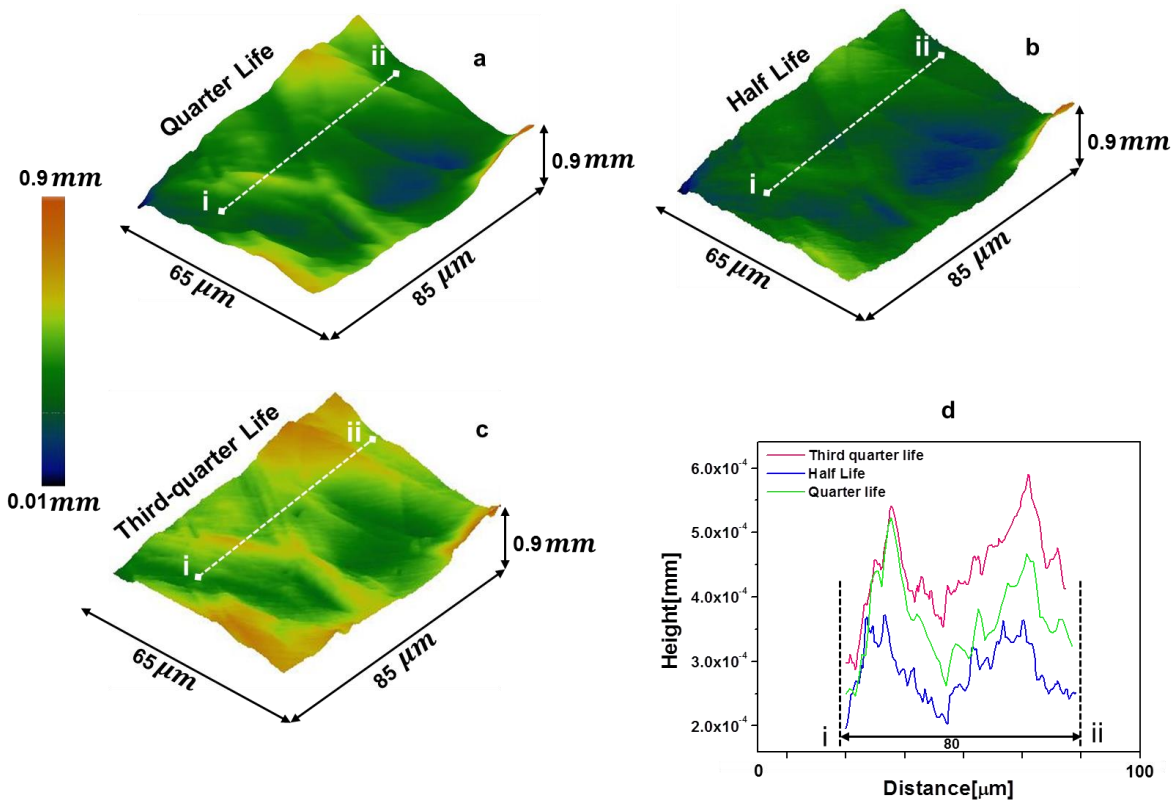

Figure 65 Surface morphology of fatigued samples using strain amplitude of 0.5%, after fatigue (a) at quarter life, (b) half-life and (c) third-quarter life. The data were taken from samples which were polished to a mirror finish prior to cyclic loading. (d) Surface line scan starts from point i to ii. The surface trace lines were obtained from the average of three exact lines in the same neighborhood.

This observation along with the recorded AE amplitude (Figure 64) suggests that the continuous evolution of mean stress (Figure 62c) as noted by Park et al.[263] is mainly governed by slip. However, considering the continuous occurrences of TDR (shown in Figure 66) together with the fact that, slip-slip, slip-twin, slip-twin impingements, texture hardening and probable local softening due to twin reversibility may also affect the strain hardening rate [74, 132], the need for more detailed study of this issue and its relationship to fatigue damage initiation is needed, as presented next.

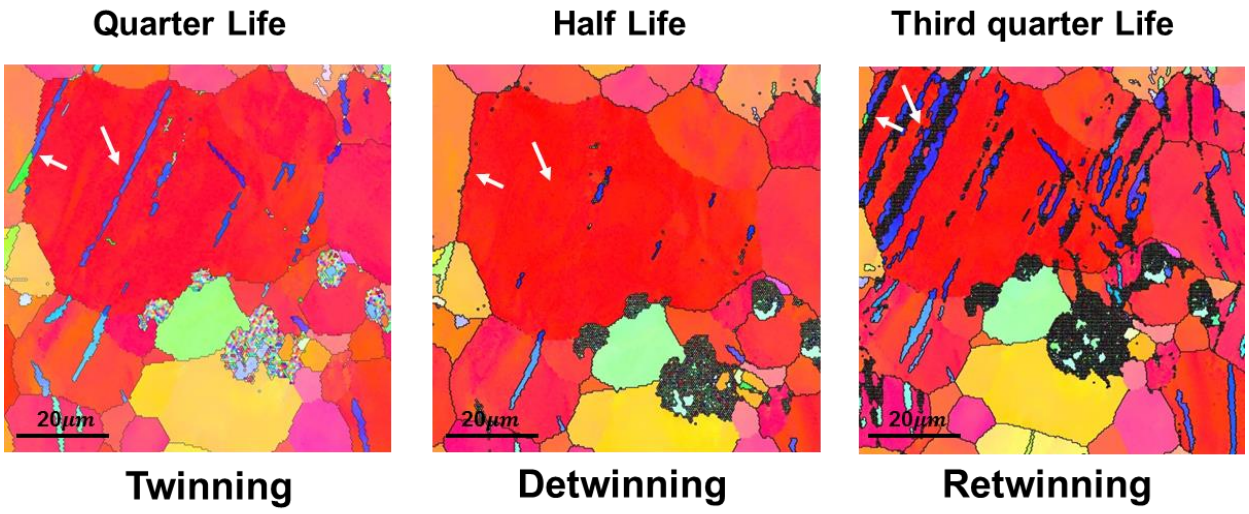

Figure 66 Direct evidence of the Twinning-Detwinning-Retwinning (TDR) activity throughout the fatigue life. The EBSD maps were measured at 2000x with step in the same region.

The effect of slip, twinning and TDR on crack initiation is discussed next. Figure 67presents a detailed analysis of the crack initiation at the grain scale. It can be seen in Figure 67a that in the targeted grain two distinct tensile twins were formed (the nature of the twin was examined by misorientation analysis using EBSD software). In the case of the central twin, due to large surface distortions [284], only five points along the twin region were detected. However, they were sufficient to verify the characteristic ~86^{o} misorientation with respect to the original grain. This measurement was also super imposed on the EBSD pattern quality in Figure 67b, which is dependent on sample topography [287]. The highly distorted region between two twins (quantified in Figure 67d-f) could result from the high activation of slip systems as denoted by the dotted circles in Figure 67b. Moreover, Figure 67c represents a high quality SEM image of the same grain. It should be noted here that aside from the evidence provided by Yang et.al [195] and despite the great interest in identifying crack formation during fatigue of Mg alloys, no other experimental data was found in the relevant literature.

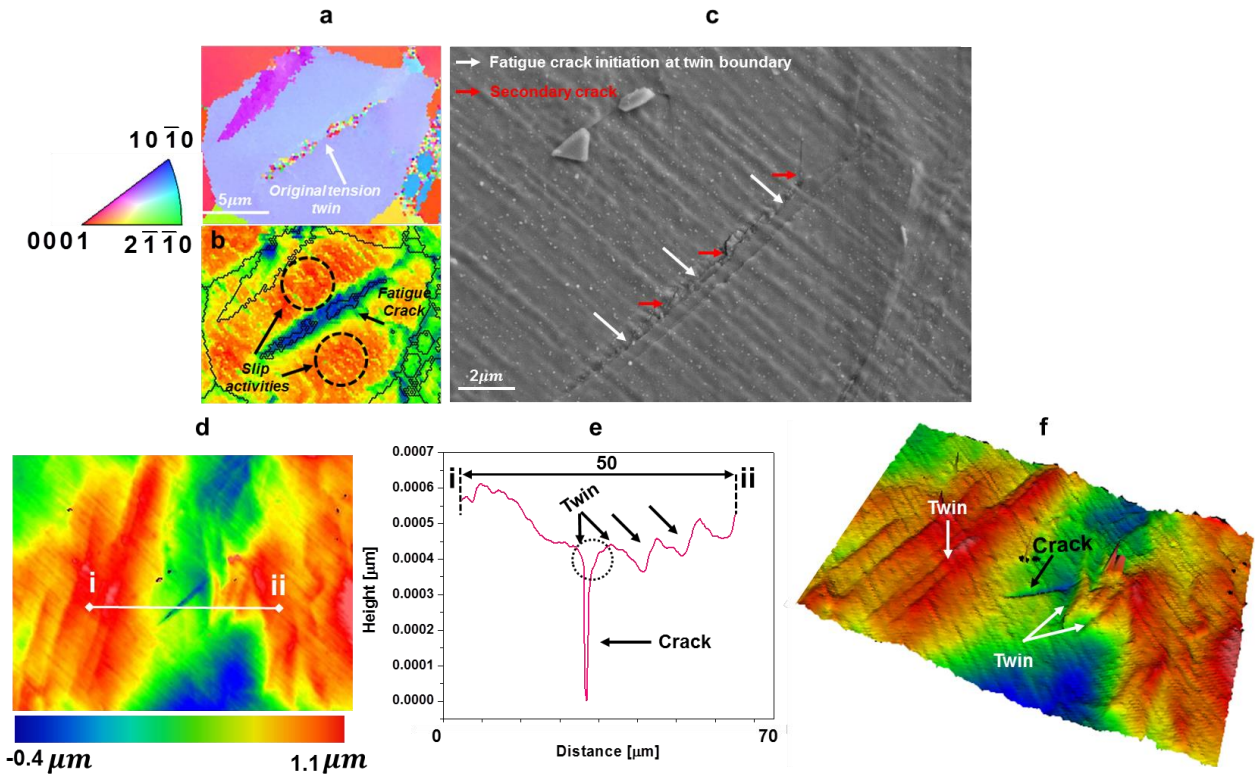

Figure 67 (a) Super-imposed inverse pole figure on grain structure, from the sample fatigued up to its third-quarter of total life. (b) EBSD pattern quality demonstrating surface distortions due to operating deformation mechanisms at the grain scale. (c) High quality SEM image showing crack initiation along the twin boundary. This image also shows submicron cracks that form from larger crack along the twin boundary. (d) Surface morphology contour map. (e) Surface step profile from a line scan (average of three similar scans) along points i and ii. (f) Surface contour in 3D space displaying grain scale extrusions and intrusions due to twinning and fatigue crack formation.

In agreement with Yang et al., Figure 67c clearly shows that fatigue micro cracks originate at twin boundaries. A closer view of Figure 67c shows submicron crack formations at the side of the larger crack, in addition to the large crack along the twin boundary. In this context, Koike [132], followed by Ando et.al [193] found that in polycrystalline Mg, twinning occurs in a grain in which basal dislocations reduce large strains caused by large deformation gradients e.g. such as the ones that could be created by the surface morphology quantified in Figure 67d-f. It was also recently observed that the crystal reorientation as a result of twinning leads to considerable surface steps, which produce a concentrated strain field within the grain [284]. Thus, in order to

satisfy strain compatibility between the slip bands and twin, Yoo [189] and Ando et. al [193] suggested the formation of another slip, crack or secondary twin. The results in Figure 67e-f demonstrate the existence of several 3D steps exactly at twin locations, as well as the formation of a crack in the region between the two twins. Therefore, it can be suggested that the combined effect of twinning, surface morphology, slip and their localized interactions create appropriate conditions for fatigue crack initiation at the subgrain level.

Figure 68 schematically visualizes the sequence of events suggested by the authors that lead to fatigue damage initiation in Mg alloys. As noted earlier, for the favorably oriented grains for twinning, twinning usually occurs in a grain in which slip operates abundantly (Figure 68a). Consequently twin formation may occur as a consequence of a mechanism operated to reduce the stain caused by slip (Figure 68b). Subsequent loading leads to twin boundary disassociation (twin growth in Figure 68c) as function of imposed strain, which can be reversed as the loading direction changes (detwinning in Figure 68d). Additional load reversals could lead to the formation of new twinning (retwinning in Figure 68e) which was the reason this process is referred to as TDR in this article. TDR is suggested in this article to occur for a large portion of the fatigue life as evidence is reported herein that it is active up until the third-quarter of the total fatigue life. The repeatable operation of twinning-detwinning leads to plastic localization within the grain, which could be the result of dislocation accumulation also produced to relax the pronounced surface steps reported in this article and before [284] by the authors. Therefore, it is highly probable that the fatigue crack initiates at twin boundaries as shown in Figure 68f. This postulation is based on the experimental observation given in Figure 67c. As further depicted in Figure 68g-i, the fresh crack can be relaxed with either additional slip or twinning. Besides the

additional slip or twinning, secondary cracks can also form (Figure 68i) to reduce local strain incompatibilities.

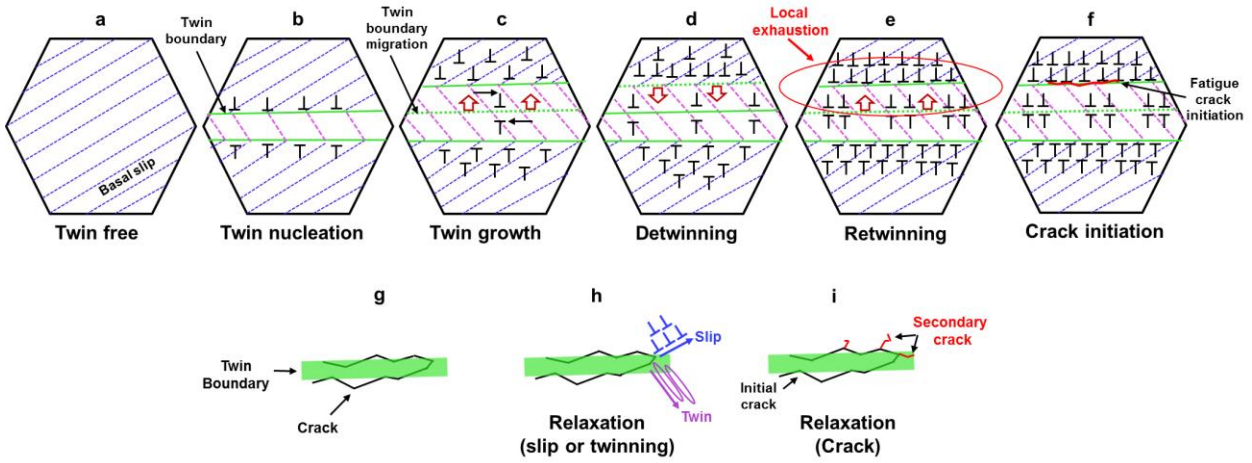

Figure 68 Schematic illustration of a possible grain scale process involving slip and twinning that ultimately leads to formation of fatigue loading induced micro-cracks: (a) Basal slip lines in a grain. (b) Twinning occurring to accommodate strain along the c-axis. (c)Twin growth as a function of macroscopically imposed strain. (d) Twin nucleation and growth can be partially/fully reversed by accumulation of strain inside the twin or by application of reversed macroscopic loading. (e) Exhaustion of twinning – detwinning leading to localized strain accumulations. (f) Twinning-detwinning-retwinning occurs continuously and ultimately leads to micro-crack formation. Once a crack formed (g) the stress field around it can be relaxed by activation of additional slip/twin or (h) secondary cracking.

6.4.4 Fractography

Plastic strain localizations promote crack initiation in metal alloys. The current study suggests that the role of strain localization becomes more pronounced in the case of HCP metals with considerable crystal anisotropy. It is widely accepted that twin mechanisms offer options for plastic accommodation during both monotonic and cyclic loading, with strain incompatibilities due to grain misorientation and basal slip being other major sources [64, 193, 200]. In Mg-based alloys it has been shown that such strain incompatibilities and texture effects cause distinct and twin-related strain localizations [50, 55, 172, 284]. Localized strains near grain boundaries or second phase particles could cause, therefore, very high local stresses [125].

Figure 69 shows SEM fractography information revealing micro crack formation at regions near the surface. To quantify features within this fracture surface, three regions were used in Fig. 14b while higher magnification details are presented in Figure 69c. These regions correspond to nucleation, initiation and are followed by what is termed rapid fracture zone. Higher magnification images in Figure 69c show the formation of microcracks near twin laminas that could consist dominant fracture nucleation sites. In comparison, more ductile type fracture patterns are observed in the rapid fracture zone, which is characterized by dimple formation as a result of e.g. void coalescences. To further quantify features of the fractured surface, a tilted view is used in Figure 69d-f. A noticeable cleavage type fracture at the surface (area numbered as "1") and a dimple pattern at the center of the SEM image (area marked as "2") are shown in Figure 69d. Higher magnification images of these two areas reveal a large number of twins having lamellar structure (Figure 69e), while it was also found that the fatigue cracks are bordered by twins at surface extrusion locations (Figure 69f) in agreement with previous results in this article. Based on this information it is possible to assume that when a crack crosses a twin the microstructure tilts locally, leading to this cleavage topography. This could further indicate that in the presence of twinning, or due to their formation during fatigue, the crack front separates in the plane between the twin and original microstructure [125, 288]. The observed surface fatigue damage appears, therefore, to be composed of twin-assisted cracks.

6.4.5 Crystal plasticity modeling

The experimental information provided in this article shows evidence on the significant role of twinning and detwinning on plasticity and damage initiation of Mg alloys. The modeling framework described in section 6.3.5 was used herein and was compared with the experimental results presented in section 6.4.2, specifically; data obtained from EBSD measurements

including 194 orientations were used to represent the polycrystal in the model. Table 3 presents major parameters used in this approach. These values were found according to the literature and by curve fitting to the monotonic stress-strain curves shown in Figure 57. The strain rate

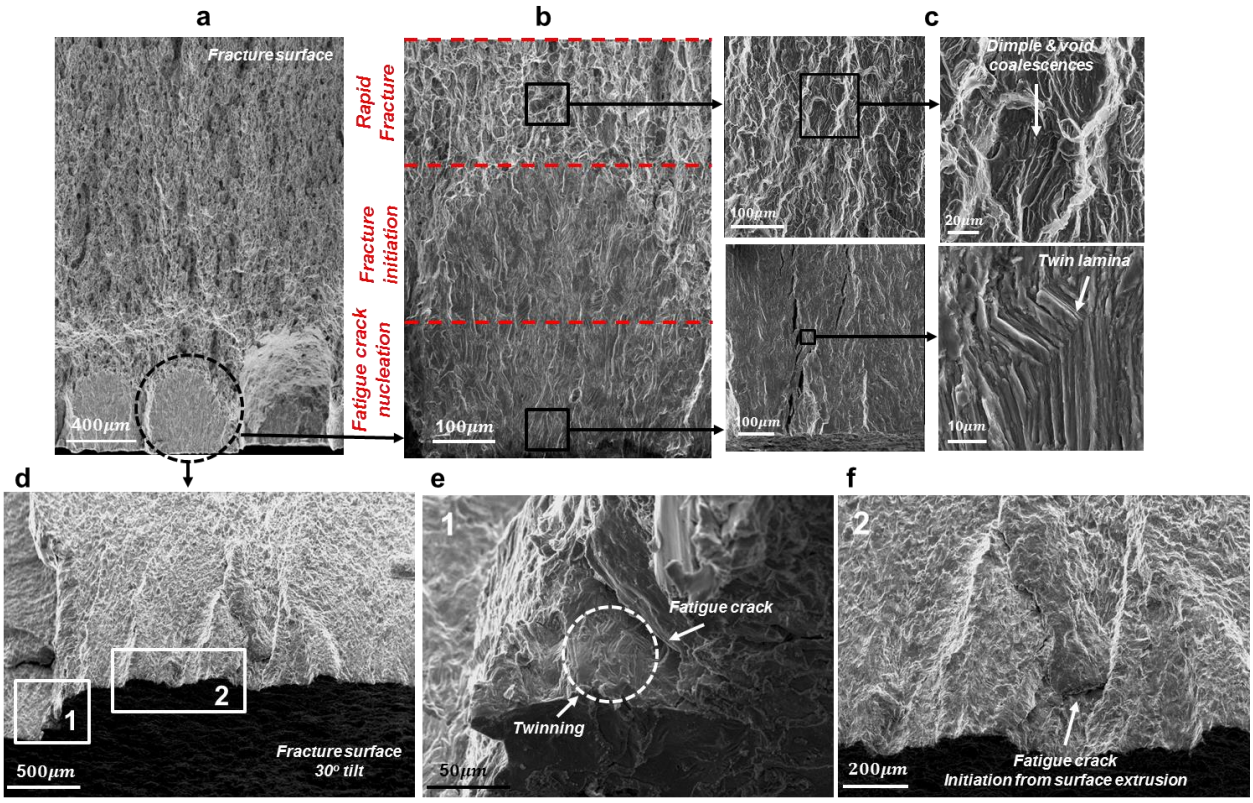

Figure 69 Fracture surface topography of the fatigue specimen tested with 0.5% amplitude, and (b) stages of fatigue damage occurrence labelled as nucleation, initiation and rapid fracture. (c) High magnification SEM images from the crack region showing the existence of lamellar structure due to twinning. Corresponding high magnification SEM observations from the center of the specimen displaying a dimple-like topography. (d) Tilted view of the fracture surface which allowed the observation of 3D features such as surface steps labelled in two numbered areas. (e) High magnification images showing cleavage surface formation across pre-existing twin, and (f) fatigue crack formation along a surface extrusion.

sensitivity (m) was set to be 0.05, while the parameters α_2 =1, and α_3 = 0.02 were used for all slip systems, the critical distance R_c was set to 25b where b is the Burgers vector magnitude (equal to 2.54×10^{-10}m for Mg). The threshold stress for twinning systems was set to 38MPa; for detwinning systems the initial threshold was set to 10MPa at early stages of detwinning, during

which small twinned regions begin to detwin. This value was then rapidly increased to 38 MPa to reach the same threshold stress as the twinning systems. With regards to the applied boundary condition, it is shown in section 6.4.3 that the transverse direction exhibits surface roughening which is an indication of un-deterministic strain rate in these two directions. Therefore, it was essential to define appropriate boundary conditions in the model to reduce deviations from experimental results.

Table 3 CDD-VPSC parameters for AZ31. Values of K are reported from Raeisinia et al.[289]

parameter	Basal	Prismatic	Pyramidal
τ_0 (MPa)	5	55	65
α	0.3	0.6	0.6
α_1	0.2	0.65	0.65
α_4	0.02	0.02	0.05
$\rho_m^o, \rho_i^o (m^{-2})$	4×10^{11}	1.5×10^{11}	0.6×10^{11}
	$\Omega^{basal}=0.2$	$\Omega^{basal}=1.0$	$\Omega^{basal}=1.5$
	$\Omega^{Prismatic}=1.0$	$\Omega^{Prismatic}=0.9$	$\Omega^{Prismatic}=0.9$
	$\Omega^{Pyramidal}=1.5$	$\Omega^{Pyramidal}=0.9$	$\Omega^{Pyramidal}=0.9$
K	0.42	3.72	4.71

To this aim, a strain rate boundary condition in the loading direction was imposed to allow for disturbances of the strain rate in the transverse direction, while enforcing normal stresses to zero. These boundary conditions - in contrast to conventional ones employed in the relevant literature in which the strain rate in the transverse direction is set equal to the negative half of the strain rate in the loading direction – increased the capabilities of the modeling approach and further prevented induced stresses in the transverse direction.

Common practice in modeling cyclic behavior with the VPSC scheme is to start from a completely determined velocity gradient tensor as the boundary condition, i.e. to set the strain

rate in the transverse directions equal to negative half of the applied strain rate. However, the current experimental results (Figure 65) suggest that this boundary condition is not necessarily accurate due to appearance of surface ripples as a direct result of twinning and detwinning. Therefore, stress was used as the boundary condition in the transverse direction while strain rate was computed as a function of load. Due to this assumption more variation was achieved in the strain rate, which is consistent to its physical nature; it is further shown in this section that this approach results in excellent agreement between modeling and experimental results.

Figure 70 compares simulation results with experimental data for different strain amplitudes under compression-tension loading conditions. It is important to note that the good accuracy achieved by using the CDD formulation. For all strain amplitudes, the compression curve starts as a plateau since plasticity is mostly dominated by twinning at these small strains [18, 50, 172]. At this stage basal slip is also active but due to weak interactions of basal dislocations, only small changes in the hardening rate were computed.

Upon load reversal and due to the activation of detwinning, much of the hardening in the compression stage is reversed because of the decrease of twin volume fraction. According to Equation (6.7) this process increases the mean free path for dislocation motion and it can consequently cause easier dislocation glide. After detwinning saturates as a result of consumption of the twinned regions, the hard activated prismatic and pyramidal systems need to be activated to accommodate additional deformation; because of their strong interactions (as defined in Table 3) rapid increase in the hardening rate is observed.

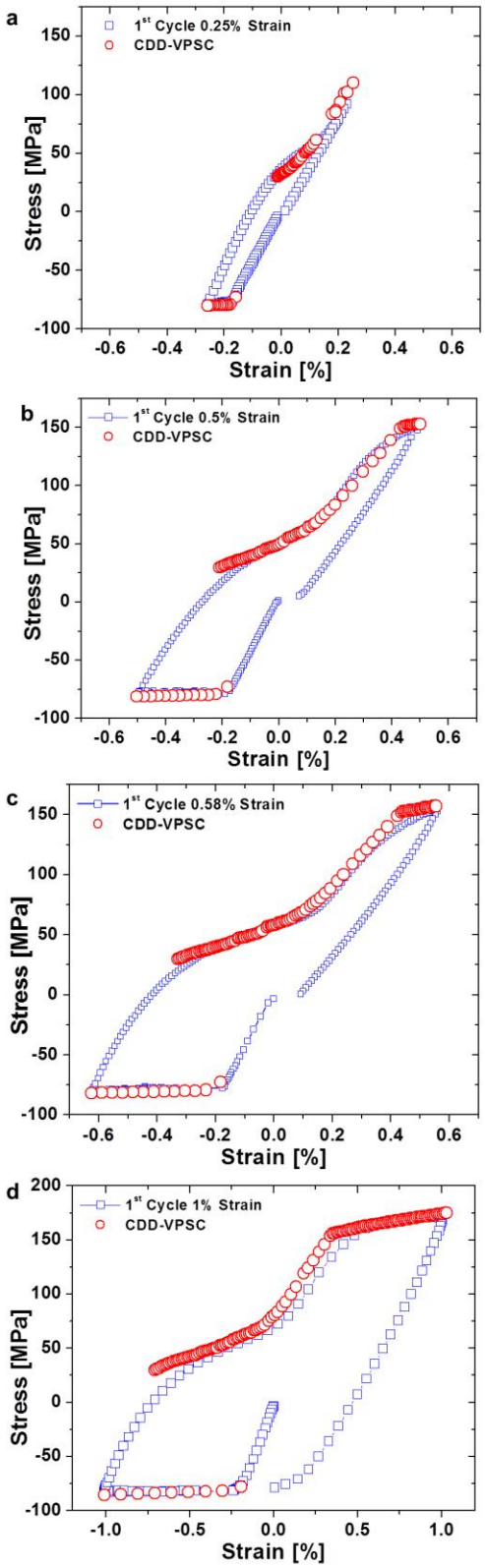

Figure 70 Measured and predicted stress-strain curve under fatigue (Compression-tension): first cycle for (a) 0.25% (b) 0.5 % (c) 0.58% and (d) 1% applied cyclic strain amplitudes.

The modeling results shown in Fig.15 demonstrate the key role of imposed cyclic strain on the shape of the modeled stress–strain curves. For smaller values of imposed strain amplitude, only weak twinning conditions are created which could practically lead to relatively small twinned regions, which quickly vanish due to detwinning after the loading direction reverses. In fact, detwinning is the major reason for the observed pseudoelasticity in the unloading stage. Note that the nucleation-less nature of detwinning could be viewed as the physical reason behind the assumption of relatively small CRSS for initiation of detwinning (10 MPa) compared to the larger CRSS required for twinning (38 MPa). The "s-type" behavior marked by an inflection point at early stages of tensile loading is not observed for the small strain amplitude (Fig. 15a), while a rapid hardening response due to activation of non-basal systems other than twinning is observed for the larger strain amplitudes. Conversely, twinning in compression is active over a longer extent of plastic deformation for the larger strain amplitudes, which leads to thickening of the twinned regions. This could further lead to the presence of small twinned areas alongside the well-defined larger twinned regions. These small twins are very unstable and thus can detwin as soon as unloading starts. The larger twined regions, however, provide enough volume fraction for the detwinning mechanism to "consume" and thereby a well-defined plateau associated with the detwinning activity is observed.

The role of twinning-detwinning is also important in regards to the differences observed between the mechanical response in the first and second fatigue cycle. Generally the second cycle is characterized by an extended plateau region before significant hardening is observed at early tensile loading stages since the twinning mechanism is expected to be activated for a longer period in the preceding compressive stage in the first cycle, as also described by Wang et al. [141]. Figure 71exhabits the results of the simulation for the first and second cycle for strain

amplitude of 0.5%. The extended plateau as consequences of detwinning is due to retardation of the hardening response, because more twinning activity has been stored in last compression stage in the first cycle.

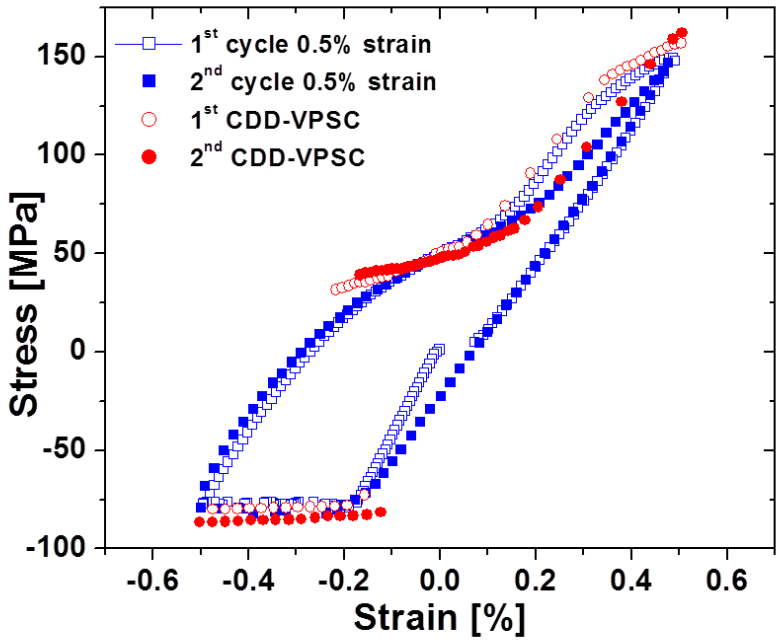

Figure 71: Comparison of experimental and modeling results for the first and second cycle (Strain amplitude of 0.5%)

In Figure 72a & b the details of the active deformation mechanisms in the first cycle and first and second cycle together for strain amplitude of 0.5% are displayed, respectively. In this diagram, the relative activities of various deformation systems are calculated as shear rates in each deformation system divided by the total shear rate at each time step and averaged over all grains. The modeling results show that twinning and basal slips are the most active mechanisms in the compression stage which causes the formation of twinned areas in the grains. Upon load reversal these twinned regions undergo detwinning starting by smaller unstable twins and continuing to larger twinned areas until the twin volume fraction decreases almost to zero. At this stage, non-

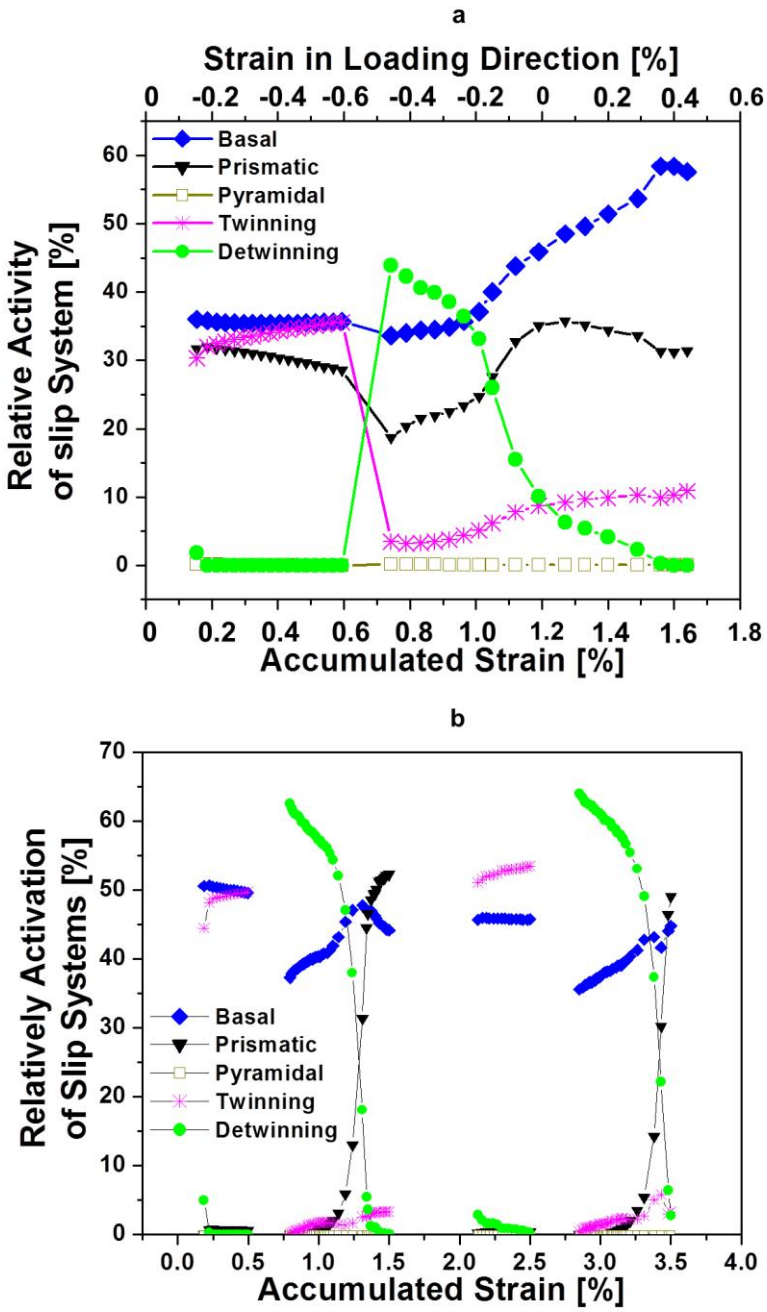

Figure 72 Relative activity of various deformation mechanisms during cyclic compression-tension loading in (a) first cycle (b) first and second cycle combined.

basal dislocation mechanisms become more active and the stress – strain curve shows a transition from the detwinning plateau to a steep hardening curve, arising from the dislocation activities as

displayed in Figure 72. The complete exhaustion of detwinning mechanism leads to behavior similar to the tensile curve presented in Figure 57 for tension results. In the second cycle the twinning activity has the largest participation in the plastic deformation during compression. Therefore, in the following tension stage of the second cycle, detwinning is more active and hard non-basal systems show less activity, causing a decrease in the stress levels in the tension stage of second cycle as shown in Figure 72b.

3.6 Energy-based fatigue life prediction

A strain-based approach is generally used to characterize LCF behavior. This approach considers the plastic deformation that often occurs in localized regions where cracks nucleate [290]. In LCF, the plastic strain amplitude is a quantity that has been related to the initiation of several damage processes, while it also influences the microstructure in a way that eventually also affects strain resistance and fatigue life. The plastic strain energy density per cycle is regarded as a critical fatigue damage parameter, because it is comprised of plastic straining due to the activation of deformation mechanisms and their resistance against their motion [291]. Therefore, energy based fatigue parameters e.g. in Morrow's model has been adopted to incorporate dissipation of strain energy, which occurs as a localized phenomenon at the scale of the material's microstructure and it has been used to predict the fatigue life for wide range of materials including Mg based alloys [202]. Specifically, Morrow's model which relates the number of cycles to failure to plastic strain energy is given as

$$\Delta W_p . N_f^m = C \tag{6.10}$$

Where ΔW_p, N_f and C represent plastic strain energy (shown in Figure 59), fatigue life at half-life and material constant (depends on fatigue exponent and material energy absorption

capacity), respectively. It should be noted, however, that the effect of mean stress which is known to be an important parameters on the fatigue resistance [292], is not regarded in Morrow's model. To this aim, Ellyin and Kujawski [293] incorporated the mean stress effect into a model discussed in Equation (6.10), as

$$\Delta W_t . N_f^m = C \tag{6.11}$$

where $\Delta W_t = (\Delta W_p + \Delta W_e)$ represents the total strain energy at half-life (see Figure 59). Figure 73a & b show predicted by this model total fatigue life (in cycles) as a function of plastic and total strain energy density, for several applied strain amplitudes. It can be observed that the plastic strain energy swiftly decreases for the samples tested using the larger strain amplitude values, while for strain amplitudes equal to 0.25% and 0.33% the plastic strain energy remained fairly constant.

It is, however, important to note that by introducing the (positive) elastic energy (shown in Figure 59) a criterion over the fatigue life can obtained. This trend is given in Figure 73b and as a correlation between the total energy and fatigue life prediction in Figure 73c & d. The results presented in Figure 73a & b together with the evolution of mean stress shown in Figure 62c demonstrate the high sensitivity of the fatigue life to the mean stress especially at higher levels of strain amplitude. This also suggests that the Coffin-Manson approach would not yield an accurate life prediction in strain-control fatigue and especially for high strain amplitudes, since

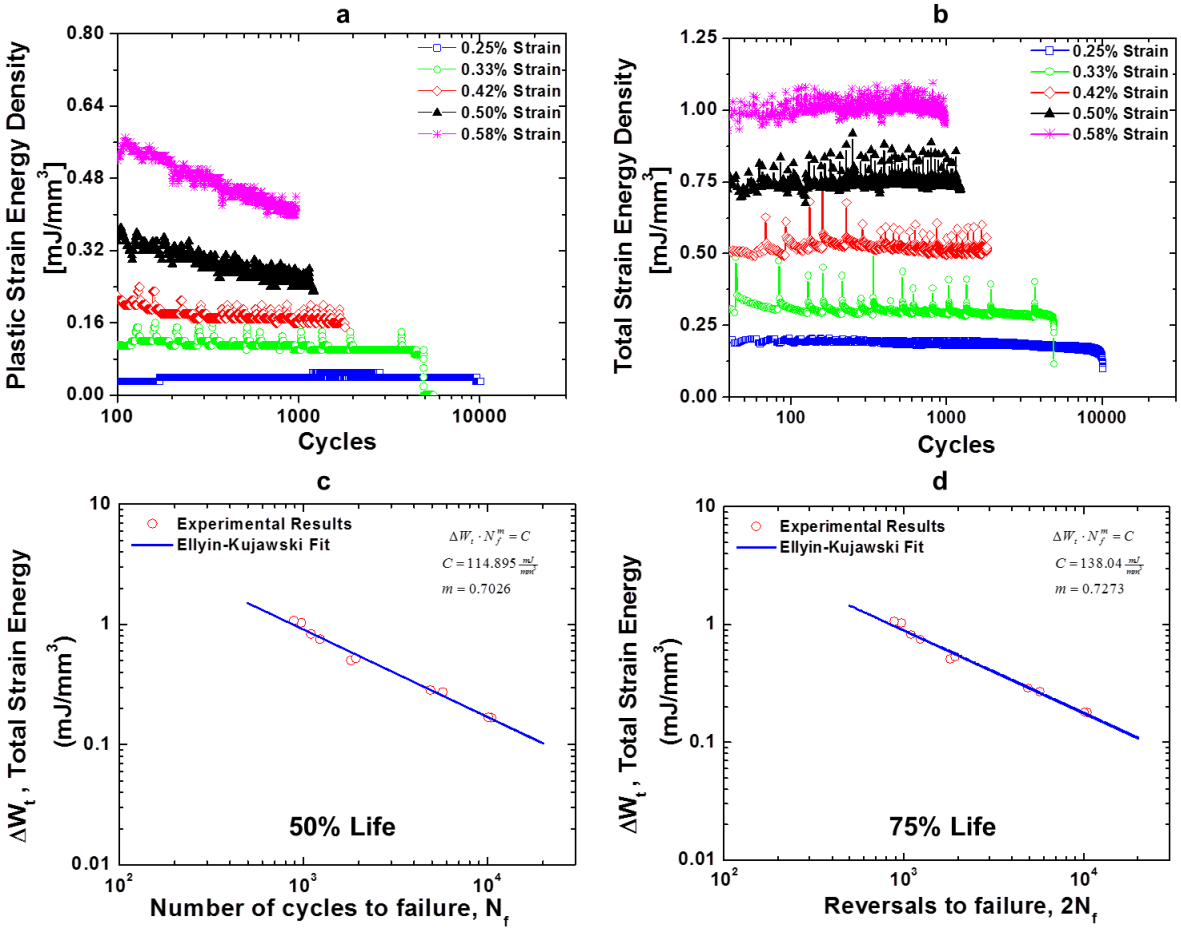

Figure 73 (a) plastic and (b) total strain energy density evolution as a function of number of cycles to failure. Fatigue life prediction with the energy based model according to the (c) half-life criteria (d) third-quarter life criteria.

the effect of mean stress is not included. Figure 73c shows the comparison of the experimental data and the prediction for half-life, whereas Figure 73 d corresponds to the third-quarter life prediction. This comparison shows only insignificant differences between the model predictions for half-life and quarter-life. Since the energy-based approach relies on the collective effect of localized changes it can successfully comprise volumetric effects which cannot be viewed on the surface and therefore serves as a macroscopic estimation approach based on the procedure followed in this article.

6.5 Conclusion

A systematic experimental approach comprising a parametric investigation of the effect that imposed strain has on the low cycle fatigue behavior of Mg alloys was combined in this article with targeted microstructural observations throughout the fatigue life, as well as both crystal plasticity modeling and total life predictions. The dominant role of twinning-detwinning in localized plasticity and damage incubation of Mg alloys was examined in relation to direct observation of surface morphology, texture effects and nondestructive monitoring. Results for the first fatigue cycle were analyzed in conjunction with subsequent cycles, including the half and three-quarters of total life. The evolution of twinning and surface morphology as a function of fatigue cycles provided strong evidence that they are related to the development of damage-prone areas from which microcracks were shown to originate. Accompanying continuum dislocation dynamics crystal plasticity modeling in a viscoplastic self-consistent scheme was successful in incorporating the strong experimental evidence, while it further assisted the explanation of changes in the hardening behavior. These results were further paired with energy based fatigue life predictions that by taking into account means stress effects were capable to provide life estimates based on the obtained experimental fatigue data.

Chapter 7

The Effect of Strontium on Strain Localization, Plastic Anisotropy and Damping Property in Mg Based Alloys[1,2]

7.1 Introduction

The main objective of the current chapter is to identify the effect of the texture and alloying elements on localization, plastic anisotropy and damping in Mg AZ31 alloy. This was achieved by casting AZ31 alloys containing various levels of Sr and then extruding the cast samples at 250^{o}C and 35^{o}C temperature. Results indicate that Sr affects the plastic behavior of the alloys by reducing plastic anisotropy through suppressing twinning, which also affects strain hardening. The mechanical properties depended more on the extrusion temperature than on the Sr concentration. The yield asymmetry of the AZ31+xSr alloys increased with increasing extrusion temperature. Similar twin related band (discussed in chapter 4) in the form of shear band was observed at the onset of yielding. It was, however, found that the localized band tends to decrease by increasing the Sr level. To further investigate the effects of Sr on the mechanical properties and plasticity of Mg alloys, targeted compression tests were performed while simultaneously using digital image correlation and acoustic emission monitoring. The results presented herein reveal direct correlations between the extrusion temperature, as well as Sr

[1] *K. Hazeli, A. Sadeghi, M. O. Pekguleryuz, A. Kontsos "**The Effect of Strontium in Plasticity of Novel Magnesium Alloys**". Material Science and Engineeing A, Volume 578, 20 August 2013, Pages 383-393.*

[2] *K. Hazeli, A. Sadeghi, M. O. Pekguleryuz, A. Kontsos "**Damping and Dynamic Recovery in Magnesium Alloys Containing Strontium**". Material Science and Engineering A, Volume 589, 20 January 2014, Pages 275-279.*

content with the bulk mechanical properties, plasticity and texture evolution of these novel alloys. Furthermore, the addition of Sr was found to be related to distinct strain localizations near yielding which were related to twinning activity, providing a route for quantitative control of their microstructural design. The results suggest that the random grain nucleation caused by Sr reduces plastic anisotropy. Fresh grain nucleation affects the CRSS for non-basal slip systems by decreasing the related Pierls-Nabarro force and as a result, twinning propensity reduces. It was found that the localization starts from the group of the grains which they are oriented in a way that their orientation is closer to the basal plane. In this study, the recrystallization and texture evolution during hot bar extrusion of AZ31-Sr alloys in three sections is also characterized. It was shown that Particle-Stimulated Nucleation (PSN) occurred in the deformed regions around the precipitates in certain hot working conditions at 350^{o}C. Increasing the amount of Al-Sr stringers in AZ31 increased the potential sites for PSN. Moreover, PSN through Al-Sr stringers resulted in the recrystallization of new grains with orientations other than the basal fibre texture, which results in the reduction of fibre texture strength.

Finally, the evidences related to the effect of strontium on damping and dynamic recovery of novel extruded magnesium alloys was investigated. Dynamical mechanical analyses demonstrate a significant plateau region on storage/loss moduli, as well as damping values. Post-mortem electron back scatter diffraction and kernel average misorientation analysis showed that these experimental results are related to both changes in texture and crystallographic recovery due to twinning and pronounced slip activity at higher temperatures.

7.2 Literature review

The demand for fuel efficient, yet high performance vehicles is currently being addressed through research and development on lightweight metallic materials [294-296]. On this subject, crystallographic texture engineering achieved by intelligent processing and alloying has led to the widespread use of light structural alloys made of Aluminum [297, 298]. Beyond Al alloys, Mg with its density of 1.7 g/m^3 (which is 33% less that of Al) is one of the lightest structural metallic materials. Common Mg alloys have higher specific strengths [24, 299, 300] than many Al alloys and several types of steels [301, 302]. Despite considerable efforts to design novel Mg microstructures, it is still largely unknown how alloying elements contribute to yielding and overall plastic deformation. Several attempts have been made to introduce various alloy combinations, which in conjunction with advanced processing techniques have the potential to minimize the formation of strong textures during hot deformation that are responsible for the observed poor formability of Mg alloys. In addition, the low creep resistance of Mg alloys restricts their usage in critical aerospace and automotive parts. To overcome this problem, the effect of several alloying additions, such as Rare Earth (RE) and Alkali Earth (AE) metals on creep resistance has been investigated. Relevant improvements have been reported in the case of RE elements, although they are relatively expensive [303, 304]. Alloys containing the more cost-effective AE elements (Ca, Sr) were developed to replace the RE elements, achieving similar properties for a lower price [305]. Strontium (Sr) had been initially introduced to Mg alloys to replicate the effects of RE elements [306]. It was reported that the Sr in Mg alloys refines the grains in casting alloys [307, 308]. The Mg-Al-Sr alloying system rapidly earned a reputation for its superior creep resistance property [305, 309, 310]. Because of the relative success in these efforts, Sr has been receiving noticeable attention in the design and synthesis of creep resistant

casting alloys for automotive power train applications [305, 310].The enhanced creep performance has been attributed to the formation of thermally stable Al_4Sr precipitates, which suppress the formation of the low melting point $\beta - Mg_{17}Al_{12}$ and reduce the Al concentration in Mg solid solution [305, 310]. The thermal stability of Sr intermetallics due to the low solubility of Sr in Mg is also attributable this property [305]. Later it was reported that the poor creep resistance in Mg-Al based alloy is mainly attributed to softening driven by the $\beta - Mg_{17} - Al_{12}$ intermetallic phase, while the superior resistance of Mg-Al-Sr alloy is attributed to its replacement by Al_4Sr [311]. The residual Al in $\alpha - Mg$ matrix in this case is low enough to prevent the formation of $\beta - Mg_{17} - Al_{12}$. Furthermore, it has been reported that Sr-rich precipitates increase the tensile strength of Mg alloys [305]. However, as the level of Sr increases, the amount of Sr intermetallic network at the grain boundaries increases, inducing brittleness [312]. Notably, the creep resistance characteristic of this alloy has motivated the adoption of it in automotive casting engine blocks [313]. In subsequent efforts, Sr was used to develop wrought Mg alloys and was reported that thermally stable Sr-rich precipitates are effective Particle Stimulated Nucleation (PSN) sites during hot deformation and are capable of reducing texture anisotropy by nucleating randomly orientated grains [314, 315]. However, it has also been noted that when the level of Sr increases above certain values, such precipitates may also act as crack nucleation sites, thereby reducing ductility [316]. Furthermore, the effect of Sr on twinning of a Mg-Al alloy, caused by changes in solid solution composition has also been discussed [315].

It is further known that Sr affects the workability and mechanical properties of Mg alloys in two ways:

(i) *By forming thermally stable precipitates which increase the strength of the alloy and (ii) as described earlier, by acting as nucleation sites for dynamic recrystallization* [314, 315], it induces an effective mechanism to generate new grains with random orientations [317]. Furthermore, it has been reported that this effect reduces the strength of basal texture in AZ31-Sr alloys [314]. High levels of Sr also induce an increased level of brittleness by initiating cracks at the precipitate/matrix interface [316].

(ii) *Sr decreases the solid solubility of Al in Mg and therefore, affects both grain growth and twinning behavior.* Al has two important effects in Mg alloys, First, it increases the mechanical strength of the Mg matrix by pinning dislocations [318]. Second, it has been shown that by increasing the level of Al, both <a> and <c> lattice parameters decrease [319]. However, the slope of decrease is relatively higher for <a> and consequently the c/a ratio increases [320]. Changes in the c/a ratio have been associated with the twinning behavior of Mg as reported, for example, by Yoo et al. [44] who investigated the dependence of twinning shear on the c/a ratio for different twinning modes. Such results indicate that when the c/a ratio increases the twinning shear for $\{10\bar{1}2\}$ tension-twins decreases. On the other hand, for contraction twins the twinning shear increases with increasing c/a [29]. Pekguleryuz et al. [311] studied the effect of c/a ratio on twinning and edge cracking in hot rolling of Mg alloys. They reported that small changes of c/a (e.g. a 0.04% increase) between pure Mg and AZ31 leads to difficulty in atomic reshuffling during double twining, leading to a higher propensity for tension twins which are potent sites for crack nucleation.

7.3 The effect of Strontium in Plasticity of Novel Magnesium alloys

To investigate the effect of twinning and its role in plastic deformation in Sr-containing AZ31 alloys, targeted mechanical tests coupled with in situ non-destructive testing (NDT) provided by both Acoustic Emission (AE) and Digital Image Correlation (DIC) were conducted. The full-field strain measurements achieved by DIC are further assisted in post mortem by characterization and quantification of the microstructures by EBSD analysis. The results reported in this chapter provide further evidence on the effect of Sr on the microstructure of Mg extrusion rods. Additionally, they provide spatially resolved and quantified information on the relationships between inhomogeneous plasticity and both texture and deformation mechanisms activation and development at early stages of plasticity.

7.3.1 Experimental procedure

Synthesizing- Extruded AZ31 bars and Sr-10Al master alloys were used to produce testing specimens. The melt was prepared in a steel crucible using a high frequency induction furnace. Large (8.2cm diameter, 30cm length) cylinders were cast in preheated steel dies.

Table 4 Chemical composition of the alloy

Alloy	Chemical Composition (wt%)				
	Al	Zn	Mn	Sr	Mg
AZ31	3.15	0.89	0.52	-	Balance
AZ31+0.4%Sr	2.76	0.79	0.35	0.34	Balance
AZ31+0.8%Sr	2.83	0.79	0.33	0.81	Balance

The cast cylinders were machined to a final 8cm diameter. Samples were extruded at Applied Magnesium (Nuevo Laredo, Mexico) at 250 ^{o}C and 350 ^{o}C by an extrusion ratio of 1.83 to 1.9 cm bars. The container temperature was fixed at 50 ^{o}C cooler than the samples. The chemical composition of the AZ31 and AZ31 alloys containing Sr are listed in Table 4

Microscopy- Specimens for microscopic investigation were sectioned from extruded bars both perpendicular and parallel to the extrusion direction. Samples were mechanically ground using 800, 1200, 1400 and finally 2500 SiC papers. Subsequent polishing was carried out using an alcohol based diamond solution through a sequence of 3 and 1 µm; polishing was completed by using ultra-fine (0.05 µm) water based alumina solution. Additionally, in each polishing step ultrasonic cleaning was employed to eliminate adhered particles from previous polishing courses. Finally, to reveal the microstructure and perform EBSD measurement, specimens were immersed in a chemical polishing solution comprising of 5% nitric acid, 15% acetic Acid, 20% distilled water and 60% ethanol for 2 sec. EBSD data was collected by a Scanning Electron Microscope (SEM FEI XL30) equipped with EBSD detector and controlled by TSL software. The accelerating voltage and working distance were set at 20 kV and 19.7 mm respectively. Orientations were recorded at intervals of 0.9 µm on a hexagonal grid. To measure macro texture characteristics, a Bruker D8 X-ray diffractometer was used with Co Kα radiation. Three measured incomplete pole figures were converted to orientation distribution functions (ODF) using TextTools texture analysis software. In addition, sub-micron microstructural features were studied using Transmission Electron Microscopy (TEM, Philips CM200), bright field images taken by operating the electron beam at 200 kV. The thin foil specimens were prepared from the cross-sections of the extruded samples containing the extrusion direction (ED-r) by grinding and further thinning via ion milling in a Gatan precision system (PIPS).

Mechanical behavior-To investigate the mechanical properties of the extruded bars, two sets of specimen were machined. The first set consisted of compression samples of cylindrical geometry according to ASTM E8. The samples were prepared both along the extrusion and radial directions with an h/d=2 (see Figure 74). Direct correlations between surface strain maps

obtained by DIC and microstructural changes arising from differences in crystallography were obtained using customized samples manufactured according to the standard geometry but flattened from one side, utilizing the previously described polishing procedure. Prior to compression tests, EBSD maps and corresponding pole figures were obtained.

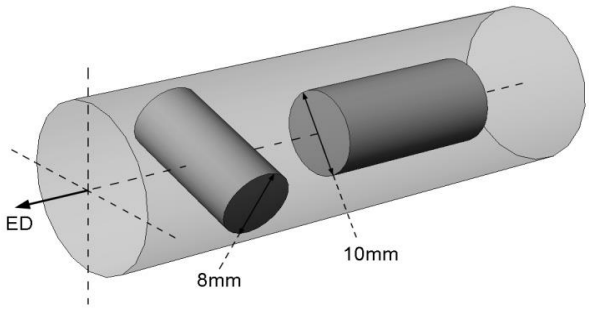

Figure 74 Configuration of the compression samples in the extruded bar

Room temperature compression tests were carried out using a 100 kN load cell on a servo hydraulic testing frame (MTS) at the constant strain rate of 4.5×10^{-4} s^{-1}. Acoustic Emission signals were recorded by a 4-channel digital AE system (Physical Acoustics) using a piezoelectric transducer with an operating frequency range of 200–750 kHz and a preamplifier with a uniform gain of 40 dB. The sensor was bonded on the surface of the specimen using a cyanoacrylate adhesive. Pencil-lead break tests were carried out to calibrate the sensitivity of the system, while the threshold of 50–55 dB minimized the recording of unwanted noise. Signals were band-pass filtered in the frequency range of 100 – 400 kHz and the peak definition, hit definition and hit lockout settings were 200, 500 and 1000 μs, respectively. Average, local and full-field strains were computed using the GOM ARAMIS DIC system. A speckle pattern was placed on the surface of the material. A $50\times42mm^2$ field of view was used, while the facet and step size were 26×26 pixels and 13 pixels respectively, giving a ±150 μm/m sensitivity.

7.3.2 Results and discussion

Figure 75 a & b present the configuration of the $Al-Sr$ precipitates eutectic in the alloys, which was imaged by using Backscattered Electron (BSE) before and after extrusion. The eutectic morphology of the $Al-Sr$ (labeled A in Figure 75c) and $Al-Mn$ precipitates (labeled B in Figure 75c) in the as-cast condition are revealed by precipitate extraction. It has been reported that Sr in Mg-Al based alloys also forms unstable $Al-Sr-Mg$ precipitates [321]. These large Al-Sr inter-dendritic precipitates (Figure 75c).

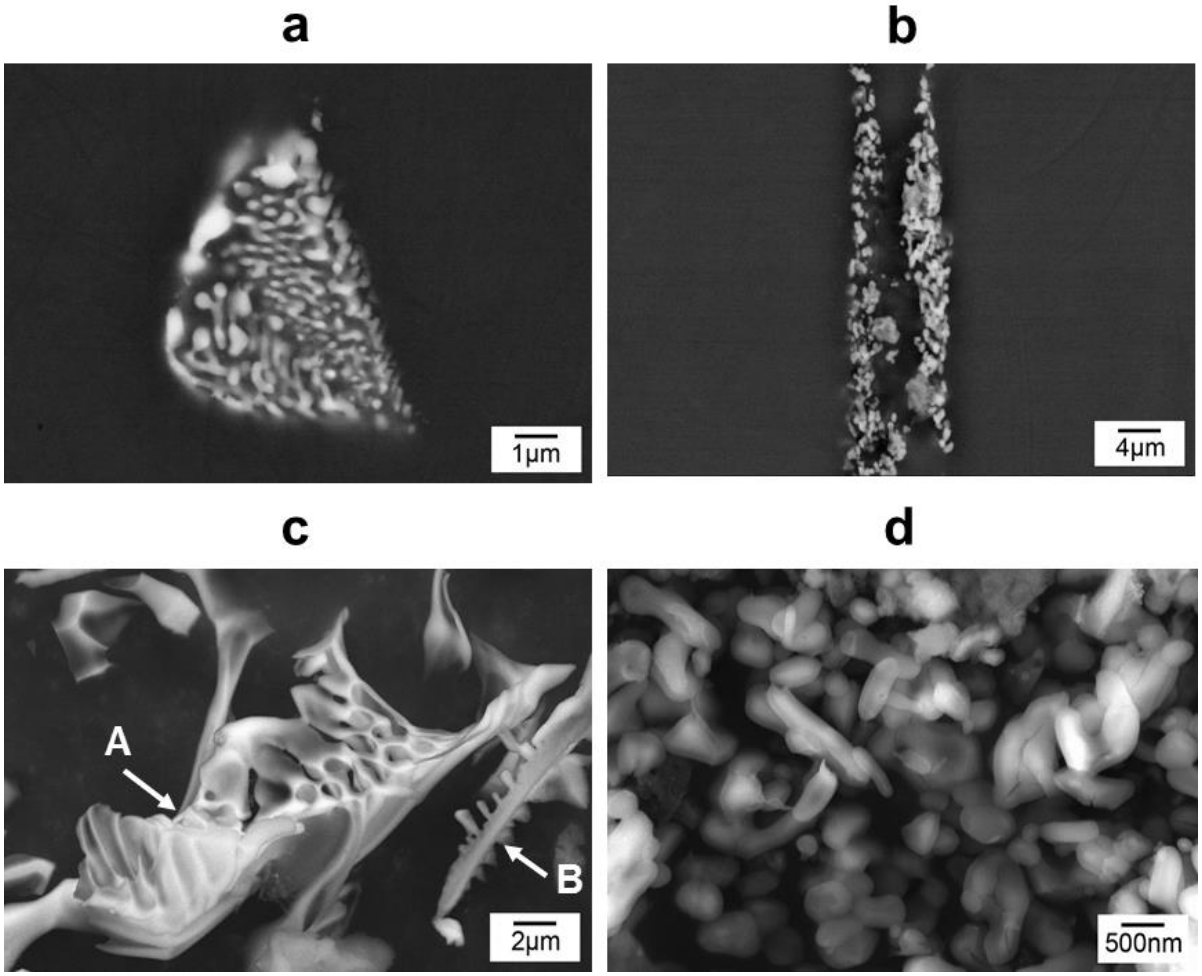

Figure 75 Backscattered electron images of Al-Sr precipitates in AZ31+0.8%Sr, (a) before and (b) after extrusion at 350ºC, and secondary electron images of extracted Al-Sr precipitates (c) before and (d) after same extrusion process.

It is shown (Figure 75d) that during hot deformation, large precipitates break down and the smaller $Al-Sr$ precipitates relocate and form stringers along the grain boundaries and are aligned with the material flow direction [314, 315]. The sizes of the precipitates inside the stringers were measured to be between 0.5-1.5 μm. It should be mentioned that annealing or hot deformation leads to the rejection of the excess Mg in the precipitates which then dissolves additional Al and transform into fine Al_4Sr eutectic precipitates [312, 321].

7.3.2.1 Texture and microstructure

Detailed texture measurements revealed that the $Al-Sr$ intermetallic promotes particle stimulated nucleation (PSN) [315, 322]. Figure 76 a & b show PSN grains at the stringer boundary growing into the parent grain. Figure 76b shows, in particular, that the recrystallized grains have different orientation compared to their parent crystal. Under certain thermo-mechanical conditions, the effect of PSN becomes comparable to that of dynamic recrystallization (DRX) at the grain boundaries and consequently, the texture intensity decreases via the formation and growth of randomly oriented new grains at the precipitate interfaces [317]. Thermodynamic calculations and EDS measurements have also shown that by increasing the level of Sr, Al concentration in Mg solid solution decreases [313, 323]. Furthermore, Figure 76c presents TEM verification of the recrystallized grains (labeled as A and B) grown into the region with high dislocation density (C) at the stringer of $Al-Sr$ precipitates during hot extrusion. The two grains grew starting from the stringer and their convex grain boundaries show that their direction of growth was toward the high dislocation density matrix.

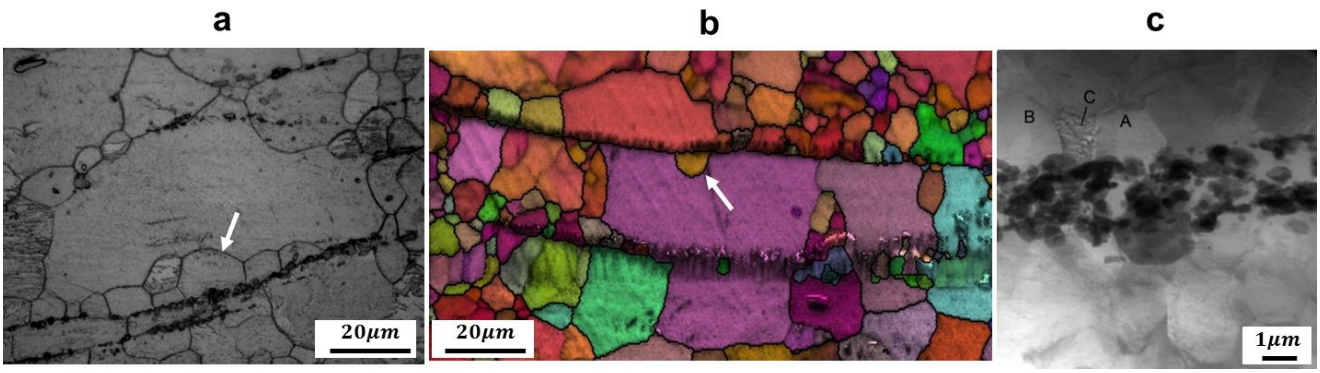

Figure 76 (a) Microstructure, (b) Inverse Pole Figure (IPF) and (c) bright field TEM image of the AZ31+0.8%Sr extruded at 350 ºC, showing recrystallization of grains A and B originating at the Al-Sr stringer and consuming the deformation zone C.

Figure 77 demonstrates optical micrographs of the microstructure of six samples containing 0, 0.4 and 0.8 wt% Sr extruded at 250ºC and 350ºC. It was observed that the amount and thickness of stringers in the extrusion direction increases with increasing levels of Sr. X-ray diffractometry [324] revealed that the stringers comprise metastable $Mg-Al-Sr$ and stable $Al-Sr$ second phases, the formation of which suppresses precipitation of the $\beta-Mg_{17}-Al_{12}$ present in AZ31 [325]. Figure 78 shows relevant EBSD data of the six samples shown in Figure 77. It can be observed, that the grains of the samples extruded at the higher temperature (350ºC) are relatively larger.

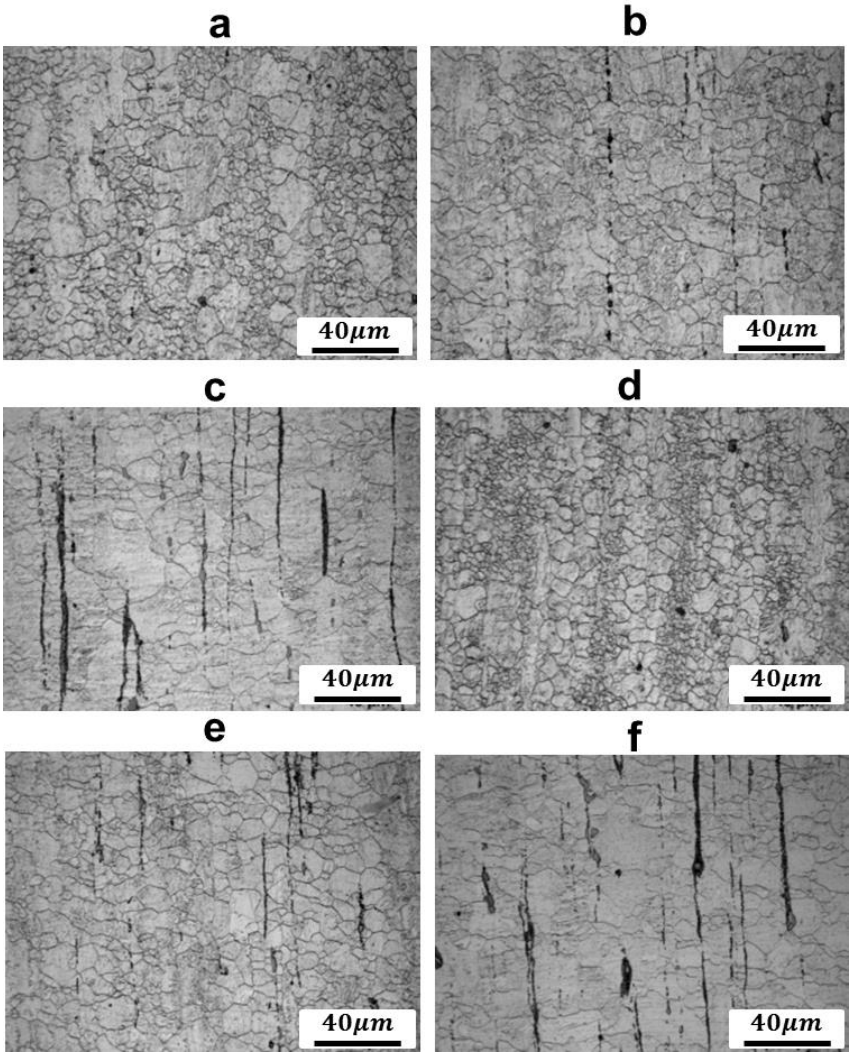

Figure 77 Optical micrographs (scale bar is fixed at 40 μm) showing the microstructure of the as-extruded samples; (a) AZ31, (b) AZ31+0.4%Sr and (c) AZ31+0.8%Sr extruded at 350ºC. (d) AZ31, (e) AZ31+0.4%Sr and (f) AZ31+0.8%Sr extruded at 250ºC.

To quantify this observation, Figure 79 shows the measured average grain size of extruded microstructures using both optical and EBSD information. The results reported indicate that the average grain size increases both with increasing Sr and increasing extrusion temperature. The EBSD measurements in Figure 79 further indicate that the grain size of AZ31 without Sr is less sensitive to extrusion temperature compared to the alloys containing Sr. The dependence of AZ31-Sr alloys on extrusion temperature is a result of the high rate of grain-boundary migration

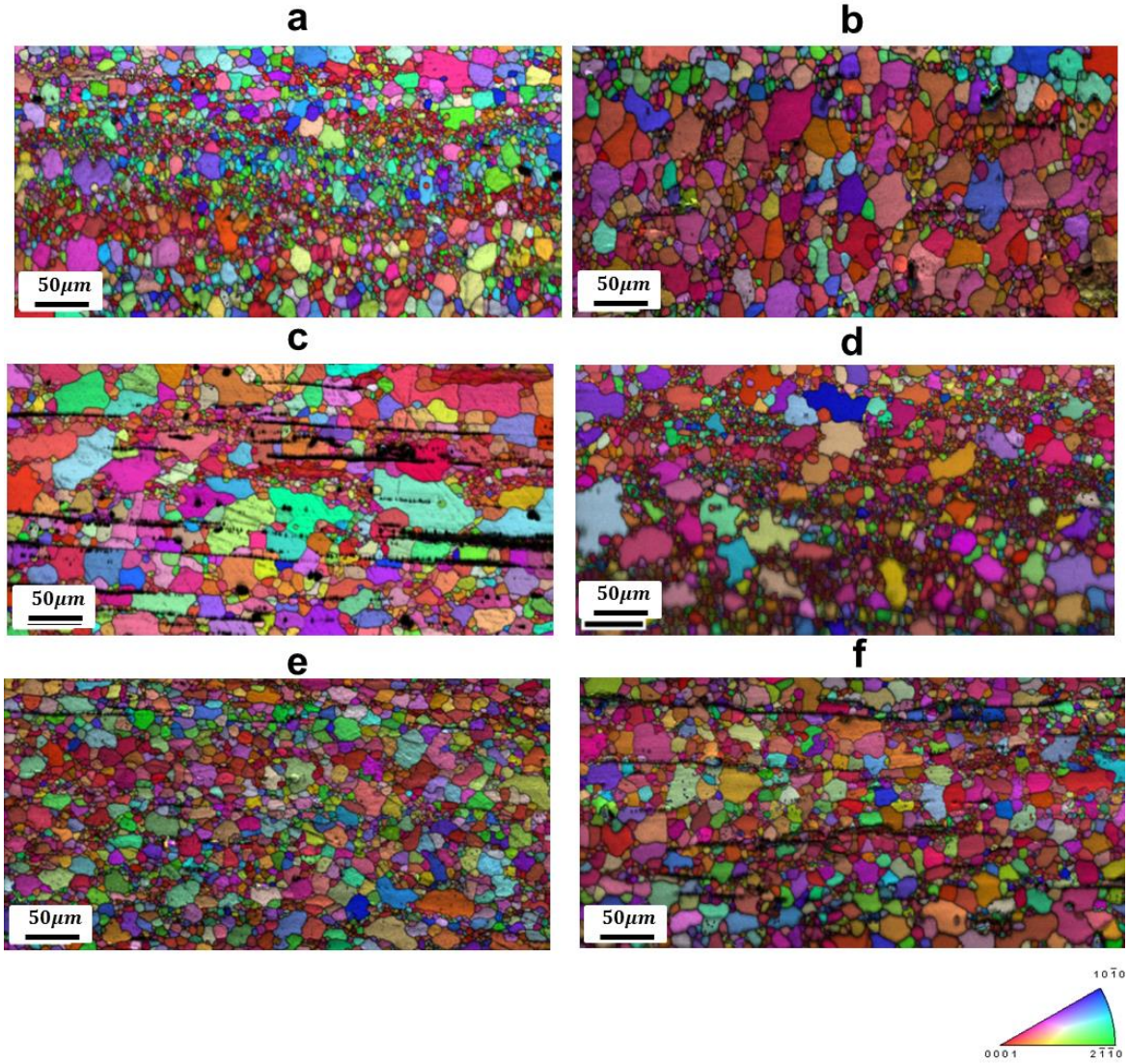

Figure 78 Inverse pole figure and image quality maps of extrudded alloys extruded at 350°C: (a)AZ31, (b)AZ31+0.4%Sr, (c) AZ31+0.8%Sr; extruded at 250°C: (d) AZ31, (e) AZ31+0.4%Sr and (f) AZ31+0.8%Sr.

(see Figure 76c) when Al is depleted in primary Mg. This finding is in agreement with Shahzad et al. [321] who reported that during extrusion at lower temperatures, twinning is more active and the overall grain size is reduced by nucleation of new grains at the twin boundaries. Additionally, the grain size distribution shown in Figure 80 indicates that the fraction of small grains (bellow 10 μm) significantly drops with increasing Sr.

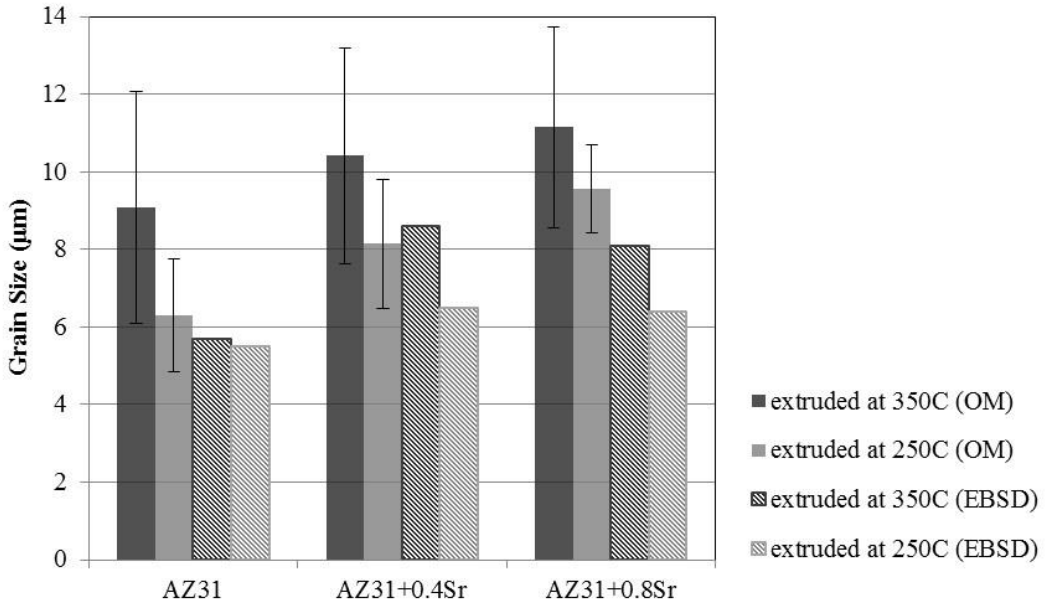

Figure 79 Average grain size in the extruded samples measured using optical micrographs and EBSD.

This result further supports the findings reported in Figure 76 associated with the decrease in Al concentration by increasing the level of Sr [313, 323]. Hence, it can be stated that the reduced amount of Al in solid solution causes a lower degree of work hardening during dynamic recrystallization in the newly recrystallized grains and, therefore, the grains could grow larger. However, when a higher amount of Al is present as a solid solution is present work hardening increases the activation energy for growth and stops the growth of DRX grains; consequently, new grains form on the grain boundaries that stop migrating. The effect of such key microstructural changes induced by the addition of Sr in Mg alloys on the local and bulk mechanical behavior is presented in the following sections.

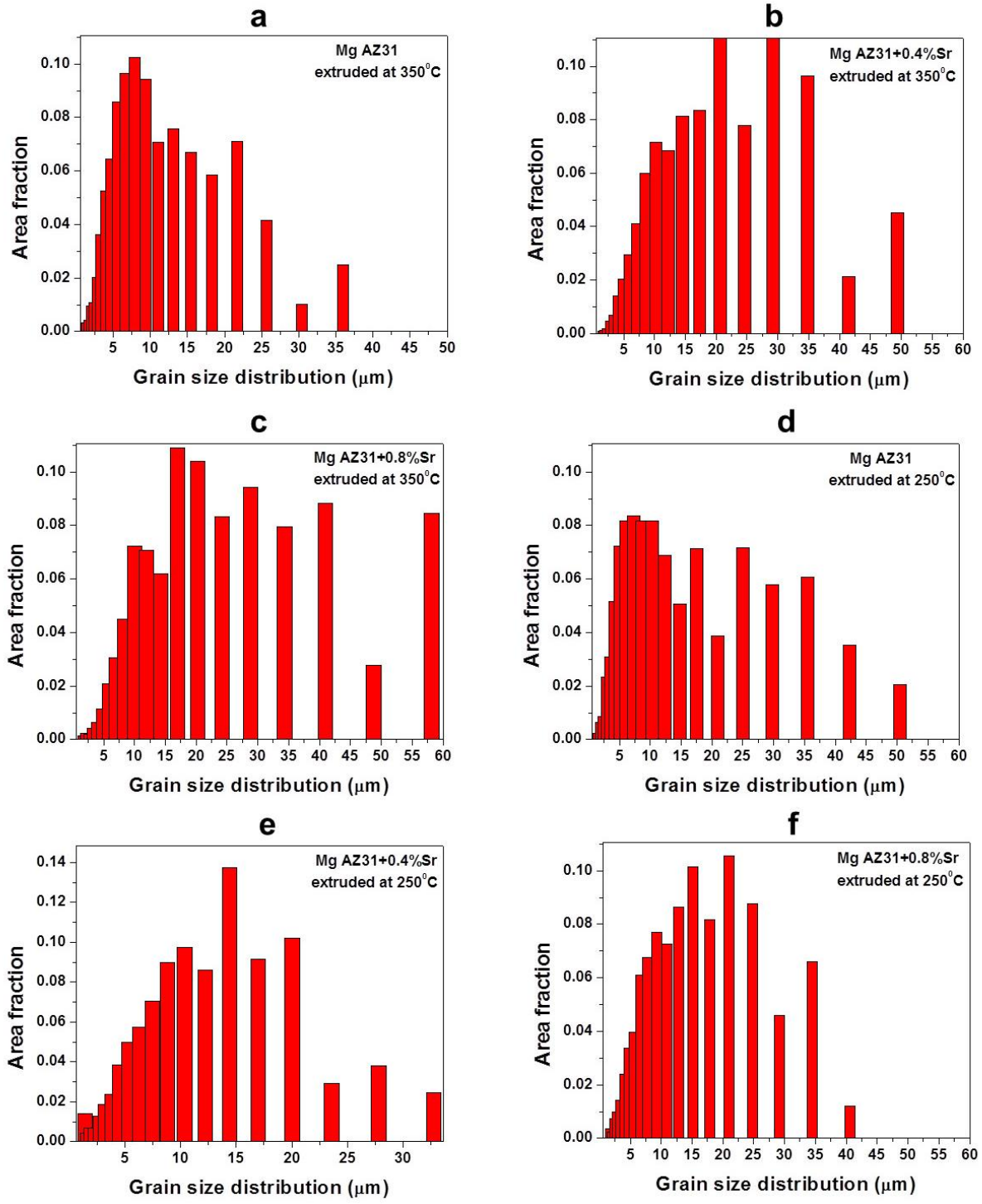

Figure 80 grain size distribution of the extruded alloys (a) AZ31, (b) AZ31+0.4%Sr and (c) AZ31+0.8%Sr extruded at 350ºC. (d) AZ31, (e) AZ31+0.4%Sr and (f) AZ31+0.8%Sr extruded at 250ºC.

7.3.2.2 Texture evolution

Figure 81 shows the basal pole figures of the six extruded samples calculated using EBSD. Mostly during axisymmetric extrusion of AZ31 (Mg-3Al-1Zn) alloy, basal planes become parallel to the extrusion axis, and the c-axes align perpendicularly in the radial orders. In all samples shown in Figure 81, exhibit ring basal texture which represents the crystallographic alignment of prismatic planes perpendicular to the extrusion direction. Figure 81g schematically shows the position of HCP unit cells with respect to the extrusion direction, which lead to the ring basal texture.

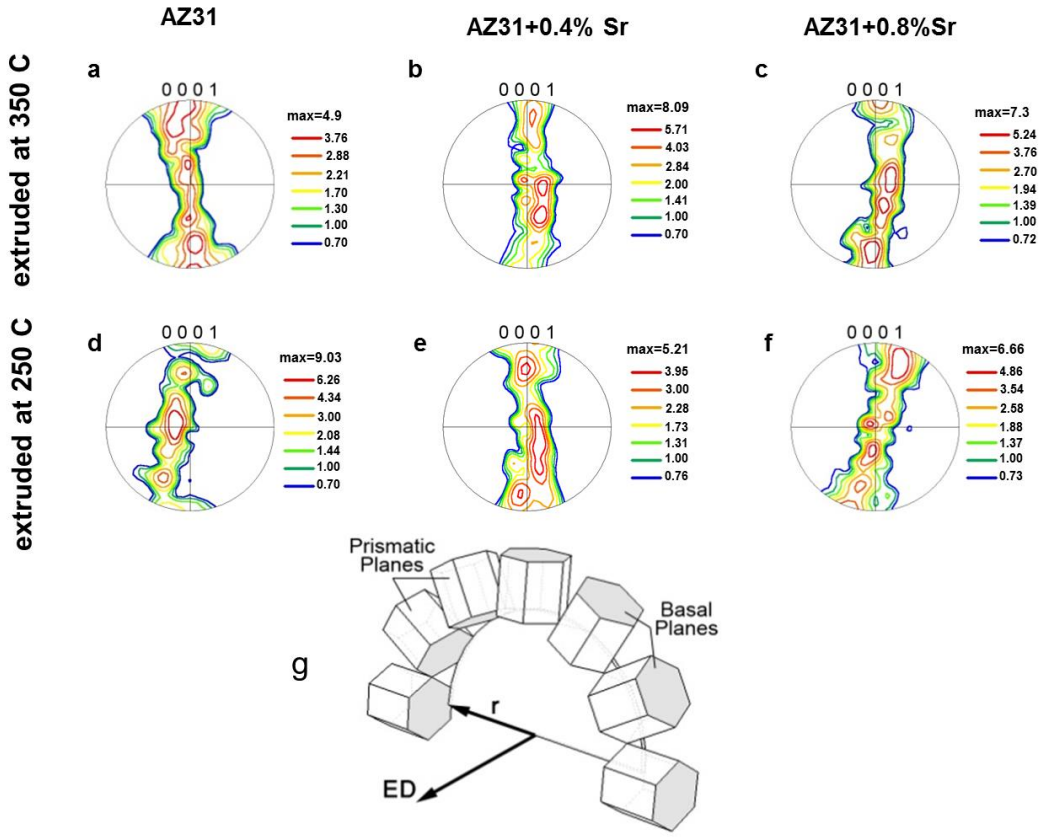

Figure 81 Basal pole figures of extruded at 350ºC: (a)AZ31, (b)AZ31+0.4%Sr, (c) AZ31+0.8%Sr; extruded at 250ºC: (d) AZ31, (e) AZ31+0.4%Sr, (f) AZ31+0.8%Sr (g) The relationship between basal and prismatic planes in Mg basal fiber texture after extrusion according to extrusion direction (ED) and radial direction (r)

Figure 82shows inverse pole figures measured by X-ray diffraction, in which the concentration of poles represents the planes perpendicular to the circular cross section. Notably, for the samples extruded at both temperatures the crystallographic plane perpendicular to the extrusion axis shifts between two different prismatic planes, namely from $[10\bar{1}0]$ to $[11\bar{2}0]$. Similar observations were previously seen as a result of increasing annealing time before the extrusion of AZ31+0.8%Sr [29, 326]. Specifically, increasing annealing time lead to the transformation of a larger amount of the metastable $Mg-Al-Sr$ precipitates to the stable Al_4Sr, and consequently to a more substantial depletion of Al from the Mg solid solution, an effect which further leads to changes in the preferential slip directions in the basal plane due to the reduction of the lattice resistance. Therefore, the grains with low Schmidt factor become work hardened and are consumed in the DRX cycles, while the grains with high Schmidt factor remain stable and appear in the final texture [326] .

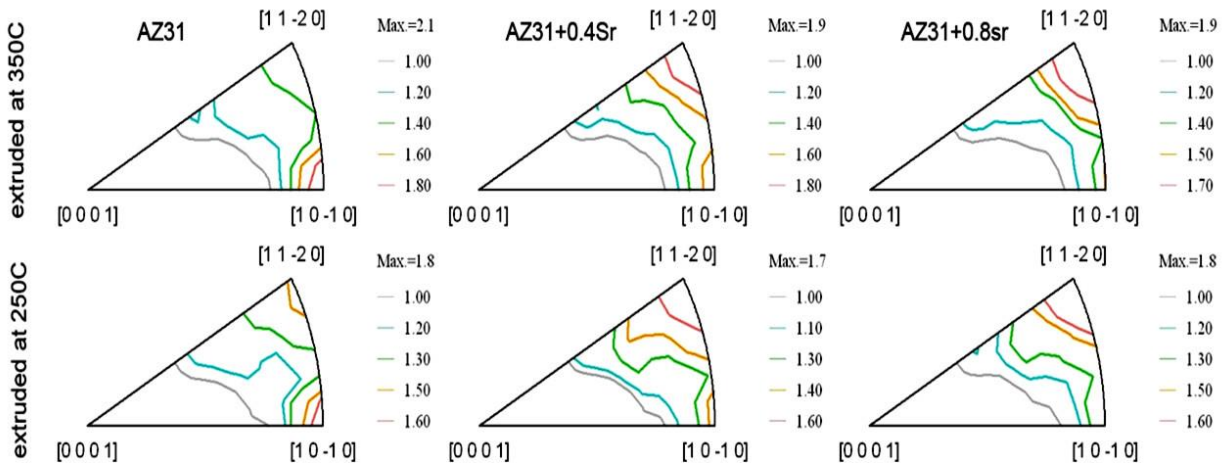

Figure 82 Inverse pole figures of the extruded samples.

7.3.2.3 Mechanical testing

Stress–strain curves and associated mechanical properties of AZ31 and AZ31 containing 0.4% and 0.8% Sr are reported in Figure 83 and Figure 84. The results present the effects of c-axis

orientation, Sr content and extrusion temperature on the mechanical behavior of the alloy samples. The differences in the shape of the stress-strain curves of the "parallel" and "perpendicular" samples are attributed to the plastic anisotropy of Mg alloys. Samples cut parallel to the ED have most of their c-axis perpendicular to the loading direction and consequently result into the characteristic "s-type" bulk behavior (Figure 83a & c), due to the activation of $\{10\bar{1}2\}$ twinning [30, 44, 167, 327]. Furthermore, samples cut perpendicular to the extrusion direction contain grains with c-axis mostly parallel to the loading direction, which leads to the non-linear behavior shown in Figure 83 b&d.

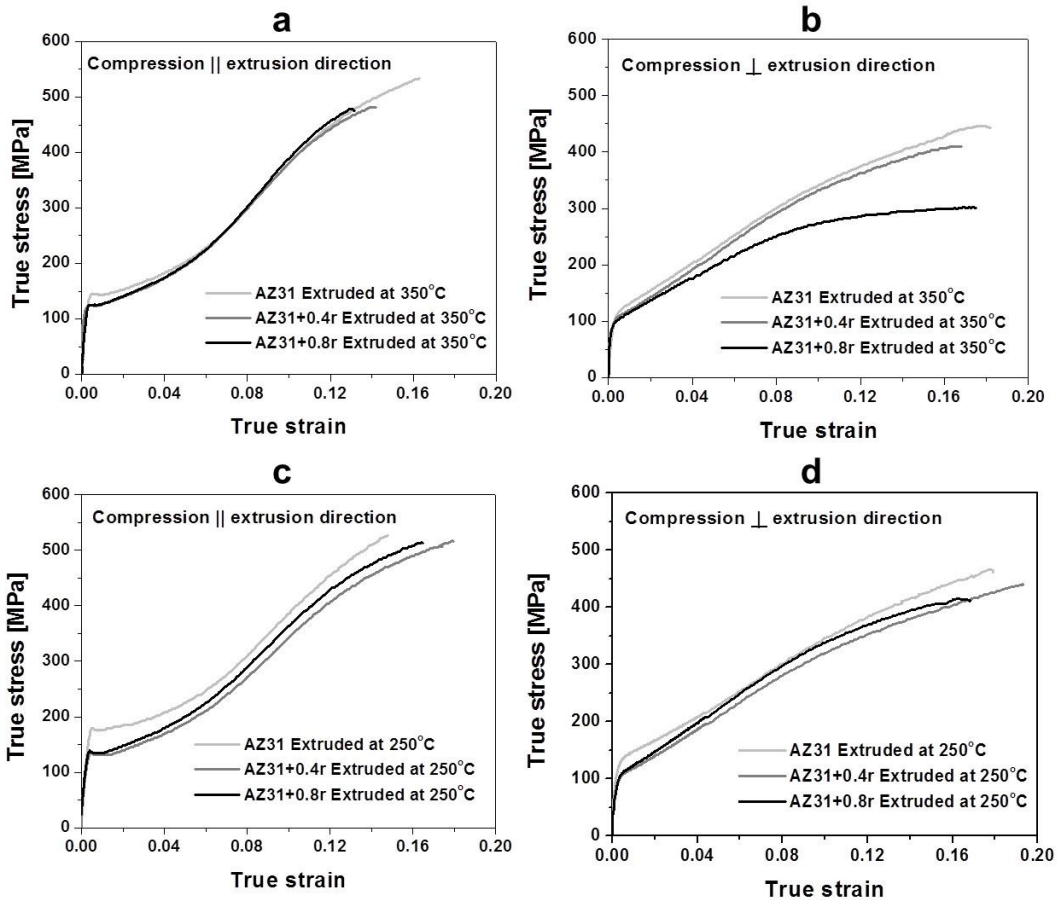

Figure 83 Stress-strain curves obtained by compression tests of AZ31 alloys with various Sr concentrations extruded at 350 ºC and: (a) parallel and (b) perpendicular to the extrusion direction. Similarly, curves for AZ31 samples extruded at 250 ºC and: (c) parallel and (d) perpendicular to the extrusion direction.

Deformation monitoring by loading along the c-axis has been extensively investigated [162, 328, 329] and it has been reported, that it is generally controlled by prismatic and pyramidal slip, which, however, require higher critical resolve shear stresses (CRSS). In this context, the results in Figure 84 demonstrate that as the Sr content increases from 0 to 0.4% for both extrusion temperatures and sample directions, the ultimate (σ_{UCS}) compression strength and yield (σ_y) strength decrease. This effect can be attributed to the depletion of Al from the Mg solid solution, and it is consistent with the Hall-Petch effect caused during the dynamic recrystallization process described earlier in this article. In addition, the results in Figure 84 show that the σ_y of the samples parallel to the extrusion direction at 250°C and the σ_{UCS} of perpendicular samples at 350°C show a more significant dependence on the Sr level compared to the perpendicular samples. On the contrary, increase of the Sr content from 0.4% to 0.8% for extrusion at 250°C leads to an increase of σ_y in the case of parallel samples, which could be attributed to the reinforcement effect of Al-Sr precipitates that overcomes the softening caused by the depletion of Al.

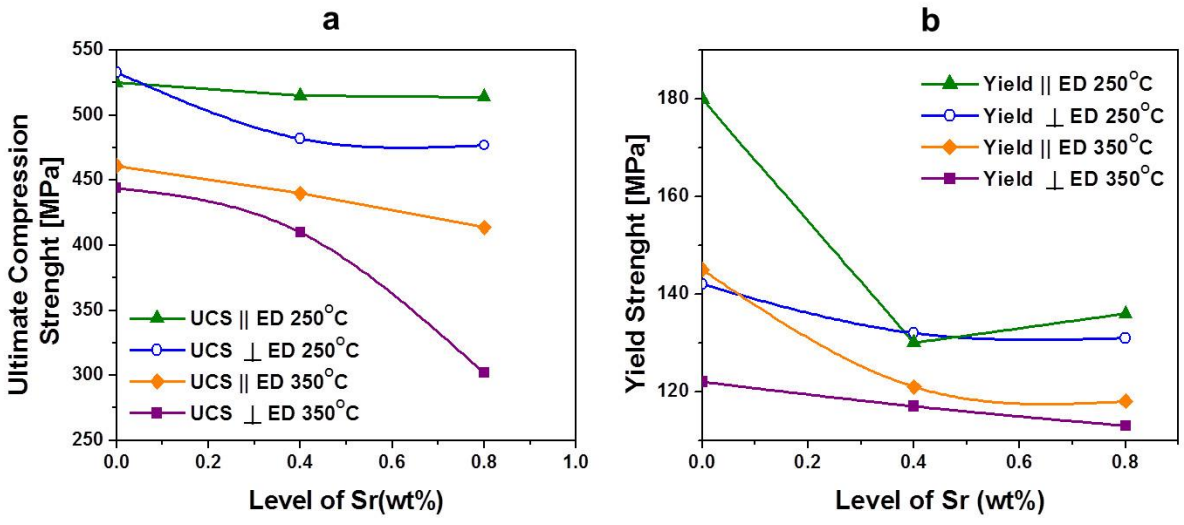

Figure 84 Room temperature mechanical properties (Yield Strength and Ultimate Compressive Strength) of extruded Mg alloys containing different levels of Sr.

The addition of Sr further results in the reduction of the difference in σy between the parallel and perpendicular samples, affecting in this way the observed plastic anisotropy due possibly to suppression of twinning, as further discussed later in this article.

In order to determine the effect of Sr on plastic anisotropy, other quantities can be considered. Akhtar and Teghtsoonian [330] reported that the CRSS of prismatic slip reduces solute additions, which further increases the CRSS for twinning. Clearly such changes in deformation mechanism are expected to have noticeable effects on the mechanical behavior of Mg alloys. In fact, Sr does not meet the Hume-Rothery criteria [331] and therefore the ease of non-basal slip cannot be justified by the direct effect of Sr solubility proposed earlier by Akhtar and Teghtsoonian [330]. On the other hand, Sr is exerts it effect by changing the solubility of other elements. As described previously a high concentrations of Sr favors the formation of $Al-Sr$ intermetallics which reduce the solid solubility of Al in $\alpha-Mg$. Mn solubility also increases with reduced Al in solid solution. These combined effects of Sr on the composition of the solid solution may exert an effect on the non-basal slip systems in an $\alpha-Mg$ matrix. Comparably to the former study by Akhtar and Teghtsoonian [330], increasing the level of Mn in a Mg matrix reduces the CRSS of prismatic slip, while at the same time it increases the CRSS for twinning. It is also interesting to notice that σ_{UCS} of samples perpendicular to extrusion direction drops severely by increasing level of Sr. This is consistent with the reported effect of precipitates related to crack initiation and propagation along the grain boundaries [312].

7.3.2.4 Acoustic Emission Monitoring

The amplitude distributions of real-time recorded AE signals as a function of true strain for alloy samples with no Sr extruded at 350^{o}C and cut in both directions, as well as for parallel samples with 0.8% Sr and both extrusion temperatures are presented in Figure 85. The AE amplitude in

both cases shows a distinct increase at small strain levels (<1%), i.e. well before yielding, which is consistent with recent findings by the authors in the case of rolled AZ31 samples[327]. AE information in this deformation region was found to include primarily burst type waveforms with relatively high amplitudes (>85 dB). This type of AE activity further agrees with pertinent information in the literature [167, 259, 332] and has been related to favorable due to texture and imposed loading, twin nucleation and growth which are macroscopically identified by the distinct mechanical behavior shown in Figure 85. In addition, it can be seen that the AE activity for the "parallel" samples (A) in Figure 85a consists of waveforms with higher amplitudes compared to the "perpendicular" ones (B), which is also consistent with the expected more pronounced twinning (due to texture) in the "parallel" case.

The characteristics of the recorded AE activity changes as plastic deformation continues (strains >1%); significant AE activity with lower amplitudes and more continuous type emissions were recorded in the strain hardening region (~2-8%) for both types of samples compared in Figure 85. It was further observed that the maximum amplitude of AE waveforms for the 350^{o}C samples (I) in Figure 85b is higher compared to the ones extruded in 250^{o}C (II), which can be explained by the fact that larger grain sizes were measured in the 350^{o}C case (see Figures 6 and 7), that result in easier twinning for favorably oriented grains.

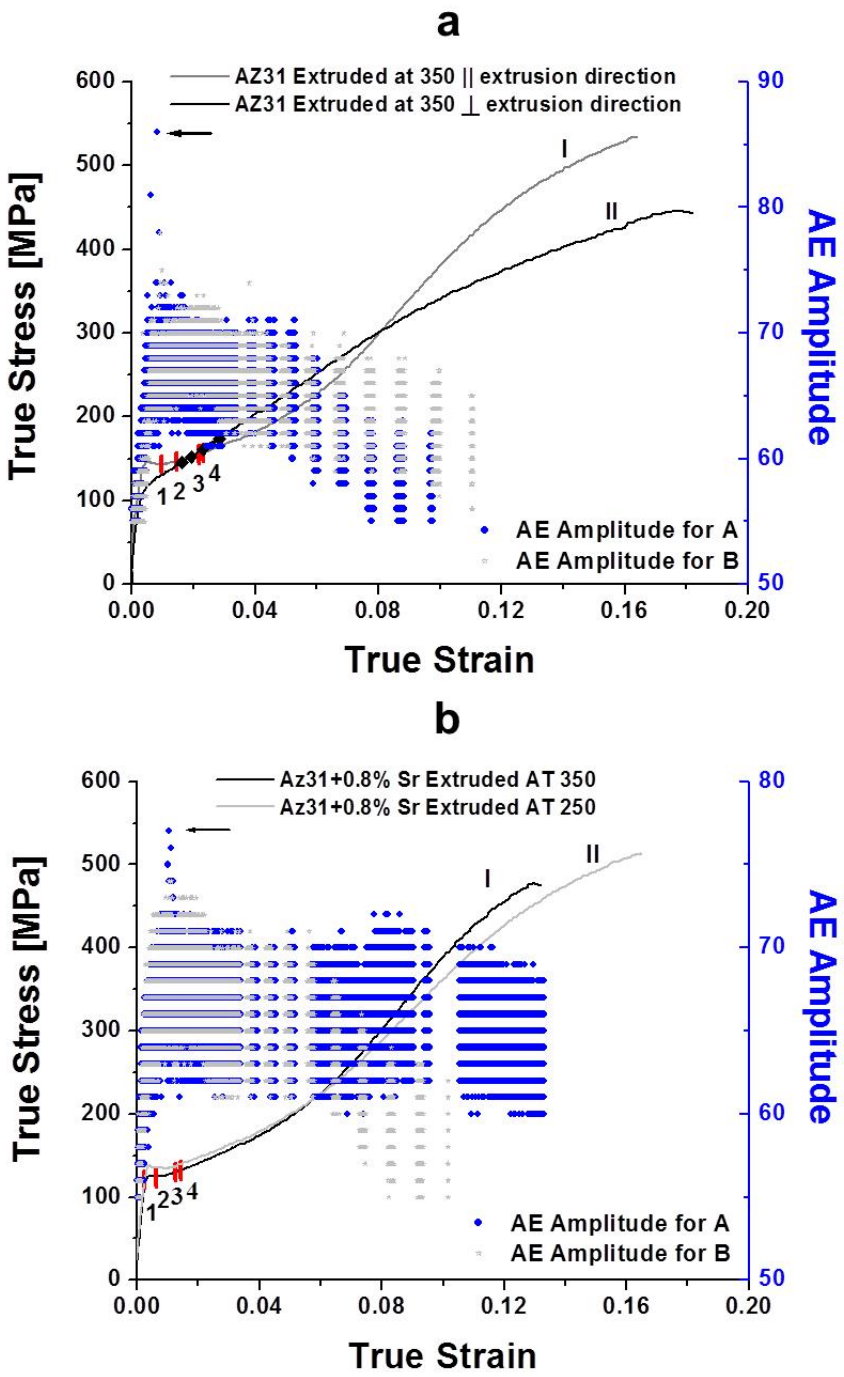

Figure 85 True stress-strain curves correlated with amplitude of AE signals for alloy samples with: (a) no Sr cut parallel (A) and perpendicular (B) to the extrusion direction and extrusion temperature of 350ºC; (b) 0.8%Sr cut parallel to the extrusion direction and extruded at 350°C (I) and 250°C (II).

Interestingly, the amplitude distributions of AE waveforms for both AZ31+0.8% Sr samples in Figure 85b are considerably lower (observe the arrows that point to the maximum in each case)

compared to pure AZ31 samples in Figure 85a, which could be attributed to overall suppression of twinning, as well as induced changes in deformation mechanisms and resulting plastic anisotropy achieved by Sr precipitates, especially for the samples that correspond to 250°C (see Figure 83 and explanations therein).

7.3.2.5 Digital Image correlation

In early stages of deformation, the plastic response of the alloy samples was in situ monitored by full-field surface strain measurements (on the entire samples' surface) provided by DIC. Figure 86 presents strain values in the direction of loading (y-strains) for the two types of samples shown in Figure 56, including: (a) samples without any Sr for both directions and extruded at 350°C, as well as (b) for 0.4% and 0.8%Sr only for the parallel samples extruded at 250°C .

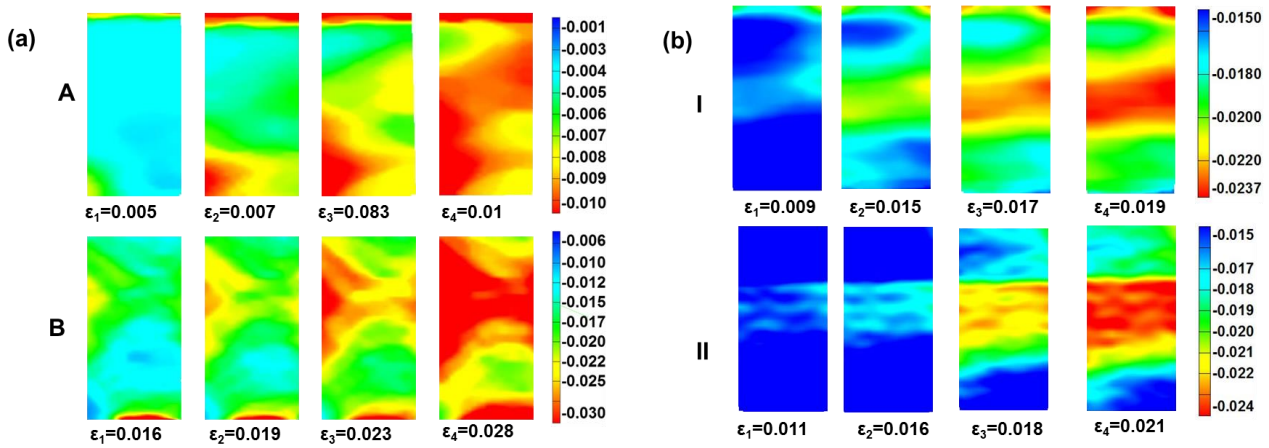

Figure 86 Full field y-strain maps at marked locations along the stress strain curves of samples: (a) no Sr cut parallel (A) and perpendicular (B) to the extrusion direction at extrusion temperature of 350°C(b); (b) 0.8%Sr cut parallel to the extrusion direction and extruded at 350°C (I) and 250°C (II).

Strain values marked as ε_1 to ε_4 correspond to locations 1-4 on the stress-strain curves in Figure 56 and were all measured in the post-yielding region. In Figure 86a, the strain maps obtained for the samples without Sr show no strain accumulations in the case of the "perpendicular" samples (B), while a more distinct band-like pattern is observed in the case of "parallel" (A).

In samples with c-axis parallel to the compression direction (noted with B in Figure 86a), i.e. having what is called "hard" texture [162], non-basal slip has been extensively reported [64, 328, 329] in absence of tension twinning. In addition, slight misalignments ($\pm 10^0$) of the basal plane with respect to the loading direction [77], can lead to the continuous operation of the basal slip mode [70, 77] when the c-axis is both parallel or perpendicular to the loading direction. Therefore work hardening at the onset of plasticity is achieved by simultaneous activation of basal [132, 333] and non-basal slip [64, 328, 329], as well as due to the formation of contraction twins [31, 334]. Such slip systems and their dislocation/dislocation and dislocation/twin [29] interactions could explain the non-organized strain localizations at the sample's surface, as reported in Figure 86a-B.

To further investigate the effect of Sr in the "parallel" ("A" samples in Figure 86a and "I" and "II" in Figure 86b) that as explained based on the results in Figure 85 are favorable for twinning, Figure 86b reveals the formation of strain localization zones on the samples surface, which actually form bands (clearly shaped for the samples "I" extruded at 250°C) that appear, increase and gradually diffuse with further loading. This behavior in association with the mechanical and AE results reported in Figure 85, confirms the effect of Sr on plasticity of Mg alloys, possibly resulting in effects on twinning and the activation of basal and non-basal slip systems. Furthermore, the presence of alloying elements in the AZ31+0.8%Sr samples shown in Figure 86b could be related to disruptions of dislocation movement caused by the solid solution phases [12] (see also Figure 77 and Figure 78). In addition, it is possible that the finer grains at 250°C (see Figure 79 and Figure 80) lead to more pronounced bands due again to increased obstacle density for dislocation motion.

To investigate the yielding and post yielding behavior in such Mg alloys in more detail, and to better understand the origin of localized band formation presented previously, two additional interrupted tests were performed on parallel AZ31+0.8% Sr samples extruded at 350°C and deformed up to 0.73% and 1.57% of total strain. The interruption of these tests at the specified strain increments was based both on previously measured onsets and endings of the convex part in the stress-strain behavior ("s-type" plateau region in Figure 83 and Figure 85) and based on trends on the AE activity similar to Figure 85. Figure 87a & c show the obtained stress-strain responses, as well as the full field strain fields calculated for the marked points. The plotted strain fields were obtained from the polished face of the compression samples and are labeled again ε_1 to ε_4. Note that the analysis of the true strain increment $\varepsilon_1$and ε_2 in Figure 87b & d was chosen for direct comparison. The DIC results in Figure 87c & d clearly show the onset of a strain localization region immediately after yielding, which coincides with the peak AE amplitude values.

In order to characterize the strain localization regions presented in Figure 87, detailed microscopic investigation was carried out using EBSD as shown in Figure 88 and Figure 89. Artificially added rectangular areas in these figures show the location where EBSD maps were collected. The findings suggest that distinct strain localization regions occur in areas where twins are more favorable to occur. To quantify this, the EBSD data in Figure 88 suggests that twins occur in well-defined areas where texture is favorable for twinning. Notice for example that area 1 which is well inside the strain localization region has a parent twin density equal to 44.1% compared to only 0.8% in area 3.

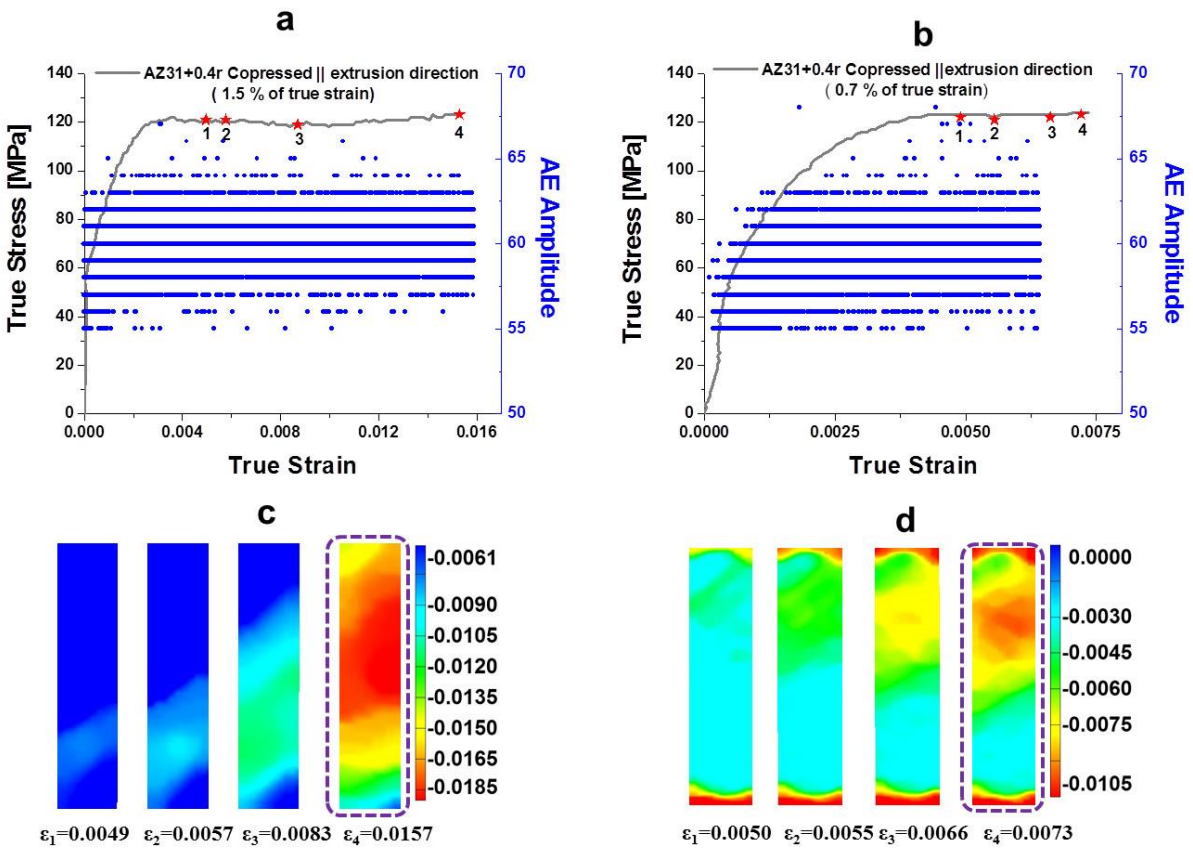

Figure 87 Interrupted stress-strain test of total true strain for AZ31+0.8%Sr extruded at 350°C and correlated with amplitude of AE signals at: (a) 1.5% and (c) 0.7% strain. Corresponding strain fields were calculated for (b) 1.5% and (d) 0.7%

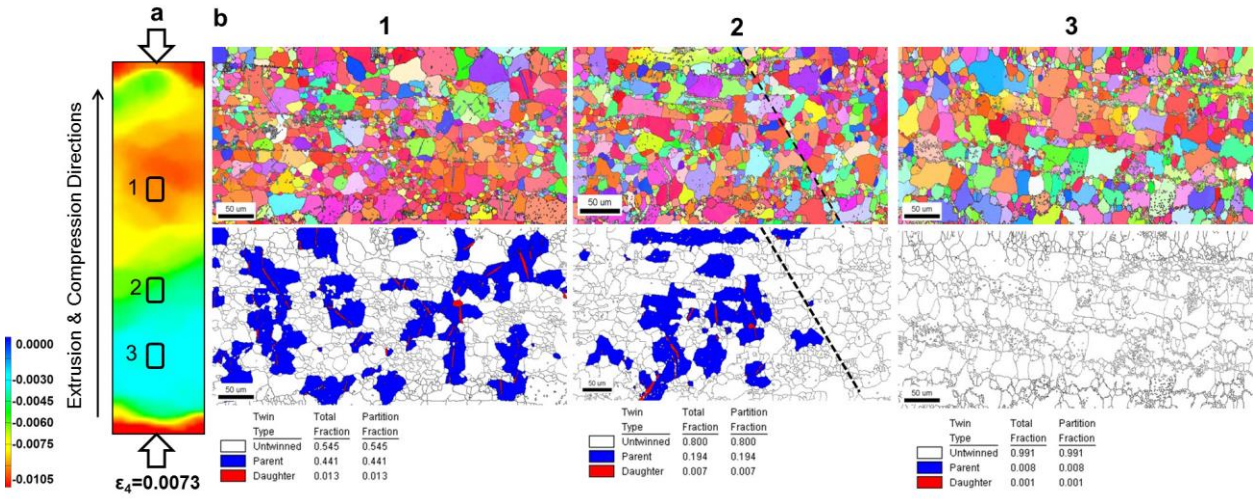

Figure 88 EBSD maps of the regions marked along the length of the sample correlating to the labelled regions in DIC map.

It is also interesting to note the difference between the daughter twin densities in Figure 88 and Figure 89; in the case of the sample tested up to 1.57% this density is more than three times higher (4.5% versus 1.3%) compared to the sample compressed up to 0.73% indicating evolution of twinning as a function of applied loading. The IPF in Figure 89d provides further information related to texture changes associated with straining similar samples to different levels; note the texture evolution due to deformation twinning. To further quantify the observed heterogeneous plastic deformation, a statistical approach based on detailed microscopic analysis was performed. In Figure 90b, grains were classified according to their misorientation with respect to the basal plane.

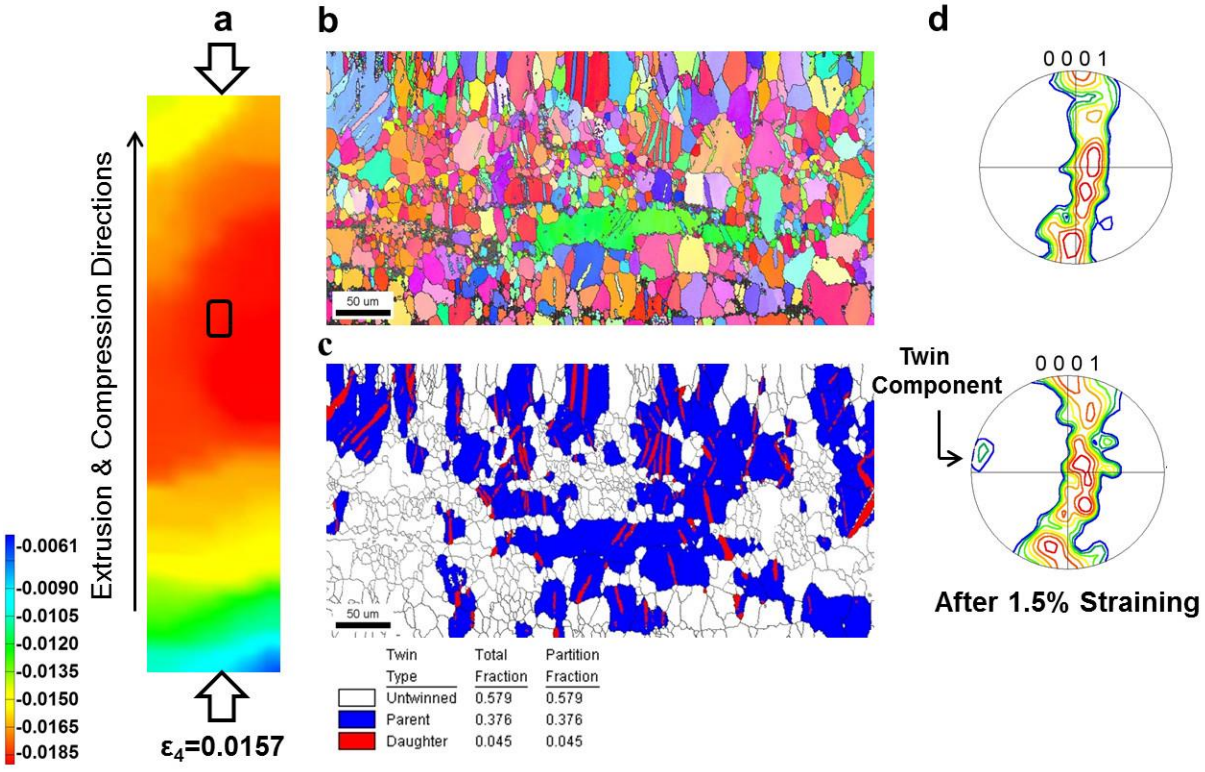

Figure 89 EBSD maps of the regions marked along the length of the sample correlating to the labelled regions in the DIC map.

In the present analysis shown below, 37.4% of the grains (green) have a closer orientation, as seen in Figure 90-1, while only 22.5% of the grains (green) have misorientation of $<30^{o}$ with respect to the basal plane, as seen in Figure 90-2. In this context, Lou et al. [259] reported that the CRSS of twinning is lower when the grain orientation is closer to that of the basal plane. Thus, it can be concluded that more grains in Figure 90-1 are favorable to twin compared to Figure 90-2. Consequently, the region with more favorable grains to deform by twinning causes earlier strain accumulations such as the ones shown in Figure 88, Figure 89 and Figure 90.

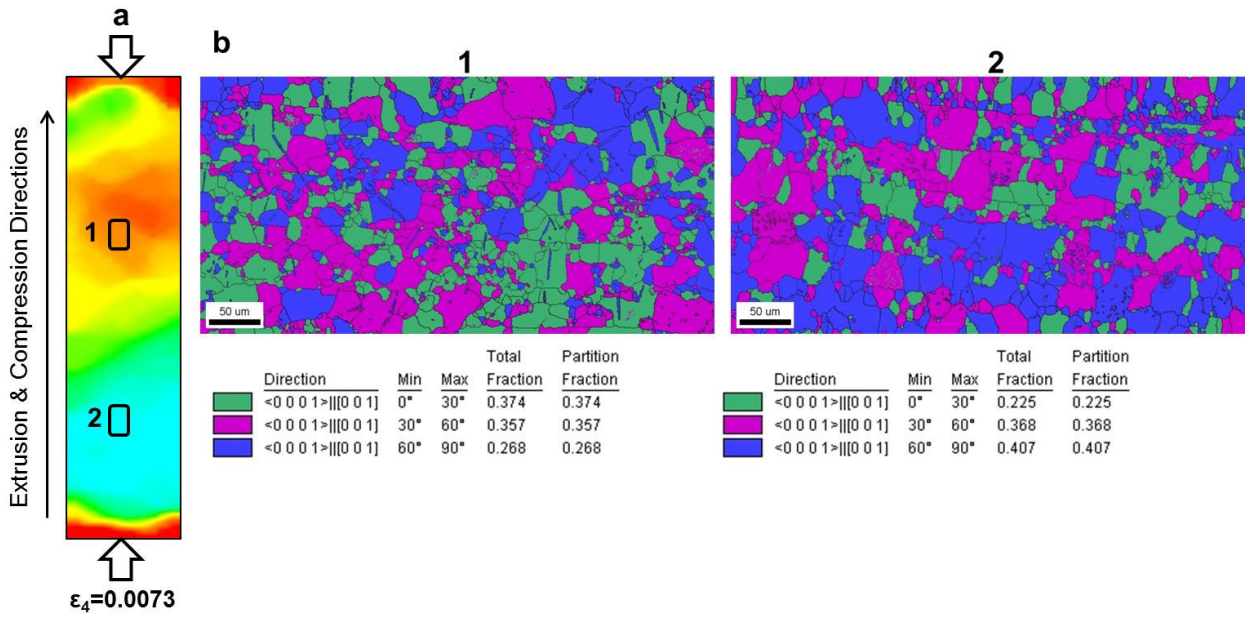

Figure 90 Grain classification according to their misorientation with respect to the basal plane orientation.

The results presented above indicate that Sr can suppress twinning in Mg-Sr alloys in two ways: (i) random nucleation of grain with different texture, and (ii) reduction of the difference in CRSS values between non-basal, basal and twinning mechanisms. Note that although it has been reported that the activity of twinning decreases with decreasing grain size [335], the addition of Sr effectively increases the average grain size (as shown in Figure 79) and therefore the temperature dependent grain distribution cannot explain by itself the reported results in this

article. Unfavorable plastic deformation by basal slip or twinning in some grains leads to activation of non-basal slip systems. In this context, the random grain nucleation caused by Sr (Figure 76), affects the CRSS for non-basal slip systems by decreasing the related Pierls-Nabarro force [330, 336], and as a result, the effect of twinning is reduced as indicated in Figure 85. Moreover, Sr atoms are larger than Mg atoms, so they cannot sit in the interstitial vacancies. Therefore, twinning could be further suppressed since the depleted aluminum caused by the addition of Sr allows dislocations to slip more easily.

7.4 Dynamic and dynamic Recovery in Magnesium Alloys Containing Sr

Although significant efforts have been made to characterize the mechanical behavior of Mg alloys under various loading conditions [148, 337-339], less attention has been given to the quantification of the dynamic properties of Mg alloys at high temperatures, which is critical in manufacturing. With this goal, Dynamic Mechanical Analysis (DMA) was utilized in this investigation to demonstrate the effect of strontium (Sr) on the storage/loss moduli and damping of novel Mg alloys at various temperatures, which was subsequently correlated to distinct crystallographic changes.

7.4.1 Experimental procedure

Material preparation procedure including casting and extrusion steps is described earlier in section (7.3.1). Similar to what was shown earlier, the effect of extrusion on precipitates shape was inspected. To do so, TEM was used to study the precipitate structure before and after extrusion. Figure 62 demonstrates the back scattered image of AZ31+ 0.8% Sr. The formation of the metastable $Mg-Al-Sr$ precipitates are shown in Figure 92 .As a consequence of extrusion $Mg-Al-Sr$ becomes elongated along the extrusion direction (Figure 92b). It is also important

to notice that due to the thermal exposure (during cooling to room temperature), the non-equilibrium $Mg-Al-Sr$ precipitate transforms to an equilibrium eutectic phase shown in Figure 92c by rejection of Mg from precipitate into the matrix. Figure 92d illustrates the elongated Al_4Sr eutectic phase using bright field transmission electron microscopy (TEM, Philips CM200 operating at 200 kV). The thin foil specimens for TEM were prepared from cross sections of extruded samples containing the extrusion direction (ED-r) by grinding and further thinned by ion milling using a Gatan precision ion polishing system (PIPS).

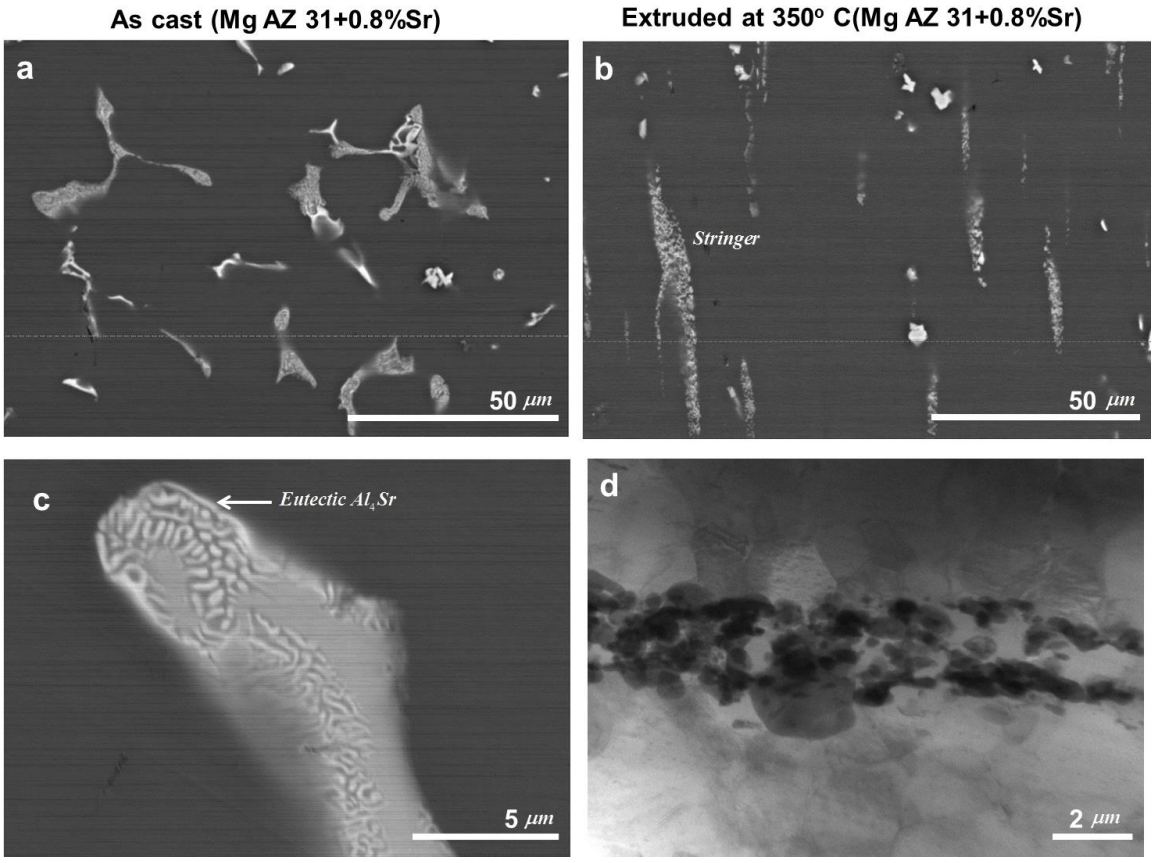

Figure 91 Back scattered electron images of AZ31+0.8wt%Sr (a) as cast $Mg-Al-Sr$ precipitates (b) a partially transformed $Mg-Al-Sr$ metastable phase to stable Al4Sr eutectic (c) the same alloy after extrusion at 350C, and (d) TEM image of an Al_4Sr stringer after extrusion at 350°C.

A DMA Q800 (TA Instruments) was used to obtain loss and storage moduli values as a function of temperature from 25 to 400 °C Figure 92. Temperature scans with 1 Hz oscillation frequency and maximum displacement of 15 μm were performed at a rate of 2°C/min. The center of a two-end supported sample was subjected to a sinusoidal load with a ratio of minimum to maximum load equal to zero. A built-in Linear Variable Differential Transformer (LVDT) provided displacement measurements. Sample dimensions were 30 mm length, 10 mm width, and 2 mm thickness along the extrusion direction. The DMA was set up in the single cantilever mode with flexural loading, while the stress created in the centerline never reached yielding.

In order to correlate underlying microstructural mechanisms including dynamic recovery and texture development during deformation to the observed dynamic mechanical behavior, careful microscopic investigation was conducted by polishing of the lateral side of the long edge of the samples. The details of methodical polishing procedure can be found elsewhere [340]. Texture, grain size and misorientation angles were measured before and after deformation using Electron Backscatter Diffraction (EBSD) in selected $500 \times 500 \mu m^2$ regions identified by using fiducially markers created by Vickers indentation. Environmental Scanning Electron Microscope (FEI XL30) equipped with an EBSD detector was used to characterize the microstructure. The accelerating voltage and working distance were set at 20 kV and 19.7 mm respectively. Local lattice orientations were calculated at intervals of 1 μm on a hexagonal grid utilizing the TSL software.

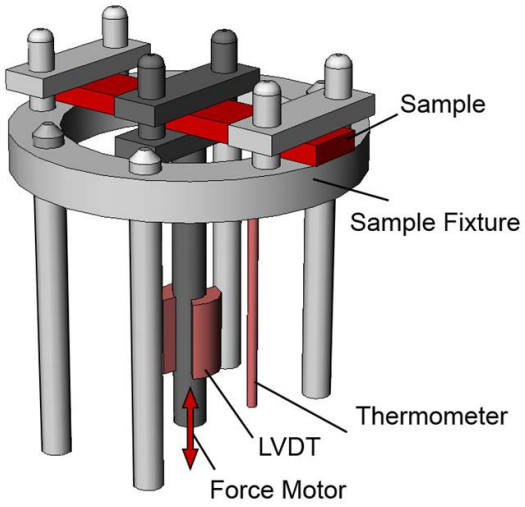

Figure 92 Single cantilever loading set up. Middle clamp is movable while the sample is fixed at the ends.

7.4.2 Results and Discussion

DMA is a widely used technique to characterize dynamic properties as a function of temperature, time, frequency, stress or the combination of these parameters for a wide range of materials [341-344]. Measured stiffness and damping values in DMA tests are typically presented by the storage and loss moduli. The ratio of the loss to the storage modulus is known as tan delta (δ). Tan delta is often used to measure the energy dissipation of materials [345]. For measurements in this investigation, the center of a two-end supported sample (see Figure 92) was subjected to a constant sinusoidal oscillating stress, shown in Equation (7.**1**)

$$\sigma(t) = \sigma_0 \sin(\omega t + \delta) \tag{7.1}$$

where $\sigma(t)$ is the stress at time t, σ_0 is the maximum stress, and ω is the frequency of oscillation. Strain values have a phase lag equal to δ, and therefore

$$\varepsilon(t) = \varepsilon_0 \sin(\omega t) \tag{7.2}$$

where ε_0 is the strain at the maximum stress. Based on Equation (7.**1**) and Equation (7.**2**) the storage modulus (E^*) and loss modulus (E^{**}) are defined as [344]:

$$E^{*} = \frac{\sigma_o}{\varepsilon_o} \sin\delta \tag{7.3}$$

And

$$E^{**} = \frac{\sigma_o}{\varepsilon_o} \cos\delta \tag{7.4}$$

The storage modulus E^{*} characterizes the stored energy and the loss modulus the energy dissipated by the material [346].

Figure 93 demonstrates the effect of temperature on storage modulus and tan delta over the range of 25 to 400 °C as measured by DMA. It is evident (Figure 93a), along with the values in Table 5 that the storage modulus decreases with increasing level of Sr at room temperature. Referring to a recent investigation [299], Sr content in Mg alloys has a close relationship with mechanical properties at room temperature. AZ31 alloys containing Sr exhibit lower yield and ultimate strength at ambient temperature than Mg AZ31, which agree with the results in Figure 93 that show a decrease in the storage modulus values with increasing Sr in the alloy.

This effect of Sr on the mechanical properties of Mg alloys has been attributed to the influence of Al depletion from the Mg solid solution, which is also consistent with the Hall-Petch effect due to average grain size increase with increase of Sr content, caused during the dynamic recrystallization process observed in such alloys due to particle stimulated nucleation near grain boundaries. The effect of Sr on the dynamic behavior of Mg alloys was further investigated by studying the inflection points of the obtained DMA curves. The artificially added arrows in Figure 93a were placed exactly at points where the storage modulus drops significantly. Results (see Table 5) suggest that by increasing the Sr level, these inflections points shift to higher temperatures.

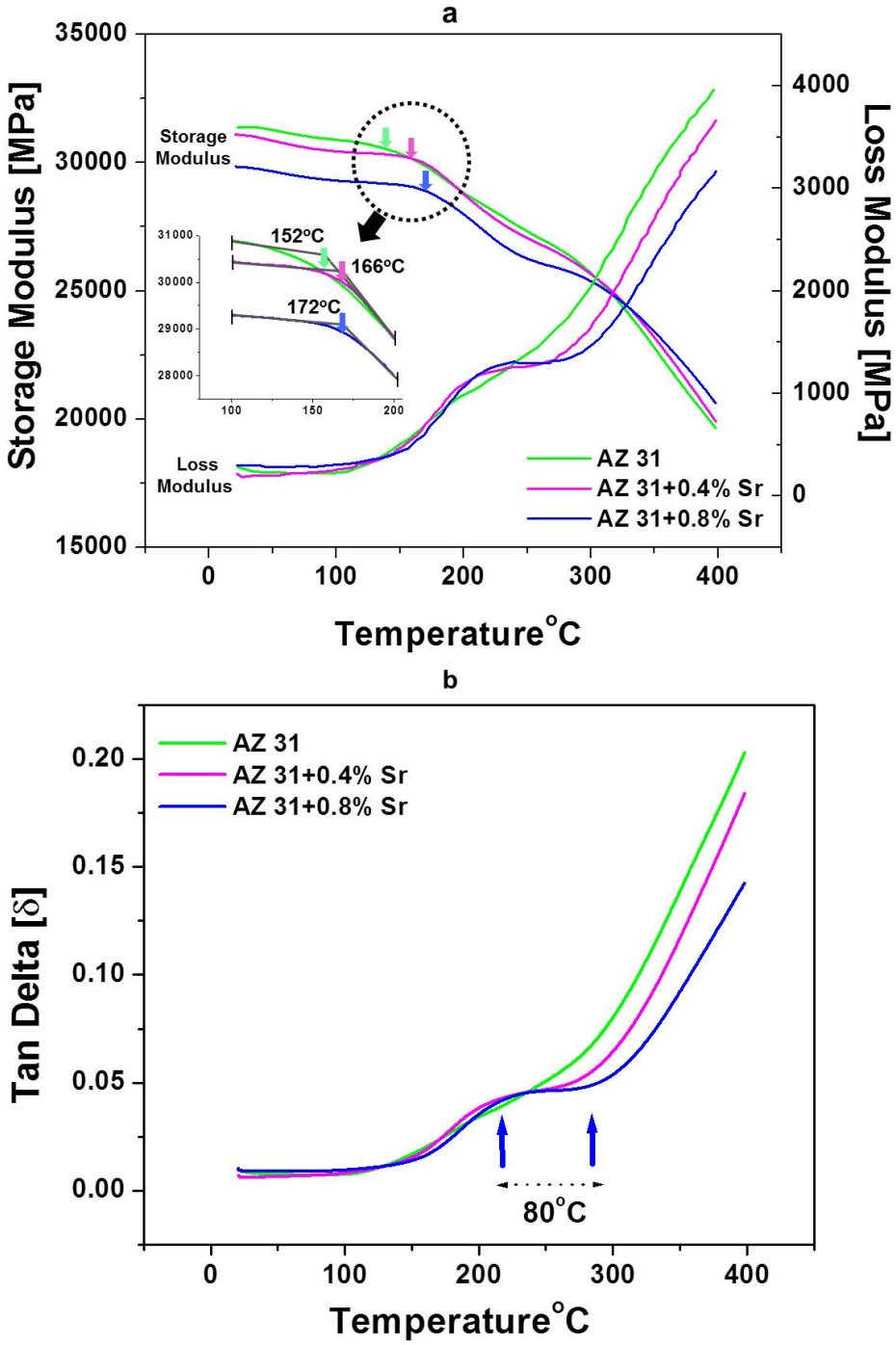

Figure 93 (a) Storage modulus and loss modulus with increasing temperature. (b) Tan delta (δ) versus temperature.

Additionally, by increasing the level of Sr, the storage modulus decreases, whereas the loss modulus and tan delta increase with a lower rate. This observation can be attributed to the

smaller amounts of low melting point $\beta - Mg_{17} - Al_{12}$ precipitates in the microstructure when Sr is added in Mg alloys [322].

Table 5 Effect of temperature on storage modulus and damping

Alloy	Measured Mechanical Properties				
	E^* MPa (25^OC)	E^* MPa (400^OC)	δ (25^OC)	δ (300^OC)	Inflection temp (^oC)
AZ31	30400	1980	0.009	0.203	152
AZ31+0.4%Sr	29800	2240	0.007	0.184	166
AZ31+0.8%Sr	29600	4440	0.01	0.142	172

Another major effect of Sr, evident in Figure 93a & b, is the observed plateau regions in both the loss modulus and tan delta (δ) curves. Specifically, the results indicate that while the applied temperature is being increased overand the loss modulus and tan delta values remain nearly constant for an interval of approximately 80^oC. Former studies suggest that the damping capacity generally exhibits an increase with increasing temperature, especially above 200^oC [342, 345]. This agrees with the case of AZ31 without Sr in Figure 93a & b, which exhibits a different behavior compared to the alloys that contained Sr. Indeed, the plateau regions become more pronounced by increasing the level of Sr and therefore it can be stated that the viscoelastic behavior of such alloys exhibits lower dependence to temperature for a significant temperature range.

To explain these results, EBSD measurements were performed for samples tested at temperatures corresponding to prior (Figure 94a & b) and post (Figure 94c & d) plateau regions. Interestingly, the Inverse Pole Figure (IPF) comparison reveals the formation of new texture components at [10-10] in the sample interrupted at 180^oC, i.e. right before the plateau region. This new texture component is also present though at a much lower extent, in the sample halted at higher temperature (250^oC). Analysis of the microstructures shown in Figure 94 showed that these new

texture components are a direct result of twinning which is evident in Figure 94b (i.e. for the sample stopped at 180 ^{o}C) but not in Figure 94d (i.e. for the sample stopped at 250 ^{o}C).

Furthermore, Figure 95 presents EBSD Kernel Average Misorientation (KAM) maps of the DMA samples. The KAM maps are constructed by measuring the degree of misorientation between a measured point and all its surrounding neighbors. Such misorientation has been related to the stored strain energy [213, 221]. Figure 95 demonstrates that regions with the maximum KAM of 7^{o} correspond to areas with the highest dislocation density. In highly deformed materials which consequently have high stored energy, the dislocation density at grain boundaries has been related to eventual recrystallization [347]. Such recrystallization is reported to occur either at higher temperatures or in samples with higher dislocation activity [348, 349]. Figure 94 exhibits no sign of dynamic recrystallization in the microstructures. Nevertheless, the KAM maps reveal a relaxation of the localized stored strain energy for the sample tested up to 250^{o}C (i.e. inside the plateau); contrary, the sample interrupted at 180^{o}C (i.e. before the plateau) has higher activation energy for recovery and consequently shows areas of high dislocation density with almost no evidence of restoration.

Mg has been characterized as a high stacking-fault energy material, and therefore, climb and cross slip would occur easily and it is expected to soften by recovery [350, 351]. Moreover, it has been noted that when Al solutes are present, the stress exponent values [350] have a lower magnitude compared to pure Mg [352], indicating that a solute drag control mechanism is activated. Thus, dislocation movement is restricted due to the presence of solute atoms [352]. Besides, it has been reported that by increasing the level of Sr in Mg-Al alloys the Al solid solubility is reduced due to the formation of $Al-Sr$ precipitates [322], which has also been confirmed by thermodynamic calculations [353].

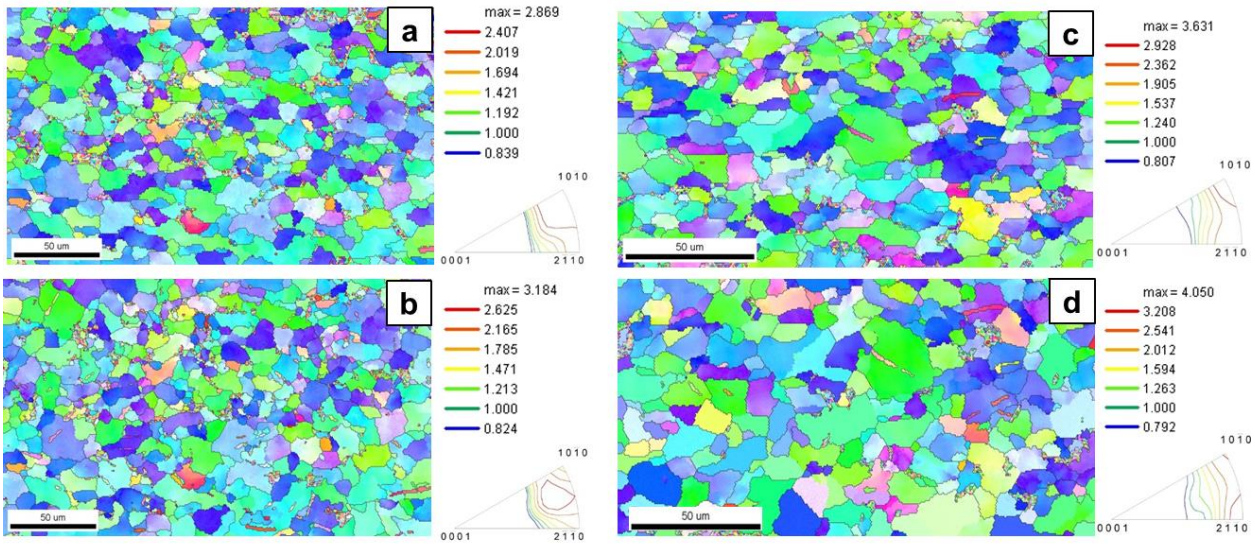

Figure 94 Inverse Pole Figure (IPF) for AZ31 with 0.8% Sr before and after the plateau region in Fig.2: (a)&(c) demonstrate the microstructure and texture before running DMA. (b) DMA was performed and test was interrupted to measure IPF for a sample tested up to 180^{o}C, i.e. before the plateau, while in (d) the test was interrupted to measure IPF for a different sample tested up to 250^{o}C which is inside the plateau region

Such evidence suggests that in the samples containing higher levels of Sr, dislocations could move more easily either by glide or climb resulting in lower drag stress and enhanced recovery. Easier dislocation movement in AZ31-Sr alloys by annealing at higher temperature has also been reported elsewhere [354]. Note, since Sr has a negligible solubility, does not provide significant drag stress [299].

Closer inspection of the current results shows that the observed plateau regions can be attributed to the activation of additional dislocation systems in alloys, which have more Sr (and therefore less Al). It is well documented that the CRSS of pyramidal and prismatic slip systems become comparable with basal CRSS at temperatures above 200^{o}C [300]. These additional non-basal systems assist slip in non-basal systems and therefore enhance recovery. In fact, lower amounts of dissolved Al give rise to additional dislocation activity and pile-ups.

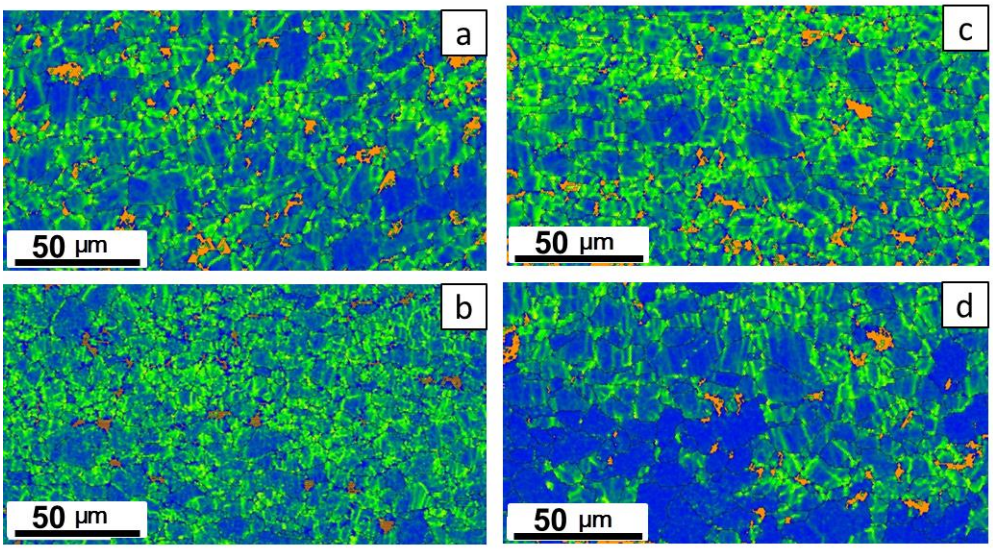

Figure 95 Kernel Average Misorientation (KAM) maps for AZ31 with 0.8% Sr. The maps at (a)&(c) correspond to measurements before running the DMA tests, while the (b) and (d) to the IPF for the sample tested up to 180ºC at 250ºC, respectively.

In the case of AZ31 where no plateau is observed, dislocations are not able to climb to such non-basal planes since they are pinned by Al atoms. In contrast, this investigation suggests that in Mg alloys with Sr, dislocations could move more easily, enabling enhanced and rapid recovery. This type of strontium-induced dynamic recovery needs to consider when designing thermo-mechanical processing of Sr containing Mg-Al based alloys.

7.5 Conclusion

The effect of adding small amounts of Sr in AZ31 alloys was investigated using a novel mechanical characterization procedure involving targeted mechanical testing coupled with the use of two nondestructive techniques that provide in situ combined surface and volume monitoring of microstructural changes. The results presented demonstrate the role of Sr in inducing microstructural changes relating to grain size, stringer formation, twinning suppression and dislocation activity, all of which cause distinct changes in the bulk mechanical behavior investigated by compression both parallel and perpendicular to the c-axis. From a macroscopic

perspective, the extrusion temperature combined with the amount of Sr in these novel Mg alloys results in changes of their overall stress-strain curves and both their yield and ultimate strength that improve their plastic anisotropy. In addition, noticeable changes on the plastic flow identified through digital image correlation were cross-referenced with acoustic emission activity and validated by microstructure quantification, revealing correlations with twinning. The results presented in this article can be used to control and optimize the microstructure in novel Mg alloys, opening the way for tailoring their mechanical behavior to specific commercial applications. The novel NDT approach reported in this article offers a powerful multi-scale characterization method with the potential to link, in real time, microstructural changes with bulk mechanical behavior, as recently shown by the authors in the case of twin-related bands near yielding in AZ31 alloys [327].

In addition, three different Mg-Al-Zn alloys containing 0, 0.4 and 0.8wt% Sr were tested by DMA and the following conclusions were made. First, distinct plateau regions at higher temperatures were observed for stored moduli, as well as damping measurement. Relevant EBSD measurements suggest the formation of new texture components possibly due to twinning before and not after these plateaus. This effect was attributed to enhanced dislocation activity at higher temperatures which can be explained by the depletion of Al in solid solution due to Sr. Al depletion further promotes dislocation movement in non-basal slip systems and consequently higher recovery rates are observed, as demonstrated by the reported Kernel Average Misorientation maps.

Chapter 8

Conclusion

Ensuring the reliability of industrial devices in general will require a fundamental description of their mechanical behavior in different working and processing conditions. To be truly predictive, this description must be based on a deep understanding of the operative deformation mechanisms. A relatively poor understanding of these mechanisms in low symmetry crystalline materials such as HCP metals is currently exacerbated by the limitation that many existing plasticity models, developed to describe FCC materials, are known to fail at predicting non-homogeneous behavior. Indeed, twinning is a key constituent in unraveling this enigma. When a cylindrical compression specimen is subjected to the simple compression test, the full-field strain map remains relatively constant until the stress reaches a yield value (corresponding to 0.15% of total strain). At this point load drops dramatically and remains rather constant until ~2% of the total strain. It is observed that the deformation at the onset of plasticity, elastic-plastic transition, is noticeably heterogeneous. The strong heterogeneous plasticity characteristic appears in the form shear band and it is attributed to the localized profuse twinning. The presented results also suggest that localized twinning give rise to high AE activity at the onset of plasticity. The high AE activity occurs as soon as shear bands begin to appear on the macrostructure. Twin-related shear bands develop and consume the entire sample as the imposed strain increases. It appears that localized band tend to originate from locations where a considerable number of grains collectively has a closer orientation to the basal plane. Furthermore, the results indicate that tailoring random texture can reduce the known plastic anisotropy, which is related to twinning.

In the current study, Sr appeared to be an effective alloying element to reduce plastic anisotropy through formation and growth of randomly oriented new grains at the precipitate interfaces. The present investigation demonstrates that the three dimensional nature of twinning at early stages of deformation (<1% total strain) is responsible for the considerable strain heterogeneity. Moreover, a relationship between surface morphology evolution during compression of magnesium alloys and twinning is found. Both *in situ* grain scale observations and *ex situ* high-resolution specimen level measurements show that twinning is responsible for large surface intrusions and extrusions that form inside and around twin-favorable grains. It is observed that the similar tension twinning variant can occur in grains with different morphology. It is assumed that the mechanical state of stress for a targeted grain is influenced by several criteria including Schmid's factor and the mechanical state of the neighboring grains through the surface and bulk. Consequently, similar twinning variants may cause different surface steps. Thus, it will be difficult to create a single criterion to relate a crystallographycal quantity such as Schmid's factor to the surface step as a function of strain increments, unless the bulk properties are considered.

The combined results obtained from low cycle fatigue and targeted microstructure investigation indicates the strong effect of detwinning upon the reversal loading. As a result, previous reports of asymmetric hysteresis loops and pseudoelastic unloading behavior during cyclic loading of Mg alloys are verified. In addition, the dominant role of twinning-detwinning in localized plasticity and damage incubation of Mg alloys is examined in relation to direct observation of surface morphology, texture effects and nondestructive monitoring. The evolution of twinning and surface morphology as a function of fatigue cycles provided strong evidence that they are related to the development of damage-prone areas from which micro-cracks were shown to originate. It was found that, although tension twinning contributes considerably on overall

plasticity by introducing additional strain components along the c-axis, its boundaries could give rise to crack initiation towards the end of the fatigue life. In contrast with FCC metals, no linear relationship was found between fatigue cycle numbers and surface roughness parameters in Mg with HCP crystalline structure. Accompanying continuum dislocation dynamics crystal plasticity modeling in a viscoplastic self-consistent scheme successfully incorporated the experimental evidence, while it further assisted the explanation of changes in the hardening behavior. These results were further paired with energy based fatigue life predictions that by taking into account means stress effects were capable to provide life estimates based on the obtained experimental fatigue data.

Chapter 9

Future work

The experimental and analytical investigations presented in this dissertation have explicitly defined gaps in the current understanding of early stage plasticity in meso- and micro scale of polycrystalline Mg alloys during quasi-static and cyclic loading. Further investigations can be designed to address several unresolved concerns. These are as follows:

9.1 Deformation induced in single crystal

The most pertinent issue to be answered following this experimental and analytical investigation is determining and quantifying the mechanisms responsible for single crystal straining. This task is extremely valuable for establishing existing and general understanding of deformation field as a result of deformation by slip or twinning. Such understanding coupled with the current knowledge of meso and micro scale, originated from the current dissertation findings as well as pertinent literature, can potentially create a hierarchical physic based framework. In the proposed framework, information is passed sequentially at smaller length scale at progressively larger length scale. This task can be divided to two separate phases.

9.1.1 Single crystal compression

In single crystal plasticity it is assumed that continuum shear deformation occurs on certain slip planes and in specific slip direction [355], which define a set of slip system. It would be of great value to directly measure the contribution of each slip system on local strain field obtained by DIC during the compression of Mg single crystal. The objective would be to determine

underlying dislocation structure (using TEM) and density responsible for the measured strain field.

9.1.2 Nanoindentation

Despite the complexity tests parameters arises from the complicated boundary and kinematic conditions during nanoindentation, such as microstructural size effects, anisotropy, and heterogeneity of the deformation and stress fields as well as from the corresponding dislocation arrangements that are created below and around an indent [356, 357]. There are two main benefits from an improved understanding of nanoindentation. First, the material parameters, which are commonly extracted from the force versus displacement curves, could be placed on a more solid theoretical ground. This applies in particular to the field of plasticity where a more detailed comprehension of the contact area, rate and relaxation effects, three-dimensional (3D) stress state and material anisotropy might render the data acquisition more detailed. Second, an enhanced understanding of indentation mechanics might enable one to extract and address a larger spectrum of constitutive material parameters than before. For instance it is conceivable to obtain tensorial rather than only scalar data, residual stresses, flow anisotropy, or small-scale damage effects from nanoindentations at amore quantitative scale than currently possible. For instance, Kysar et al. [358] conducted a wedge indentation experiments on nickel single crystal from which they measured Geometrical Necessary Dislocation density (GND) onto the effective individual slip systems. Figure 96 shows GND on two different slip systems in Ni single crystal, which further allows for connecting dislocation level to the macroscale behavior. Therefore, it would be useful to perform in situ nanoindentation, particularly wedge indentation, so several image can be recorded during indentation. This measurement could be also coupled with detailed TEM investigation.

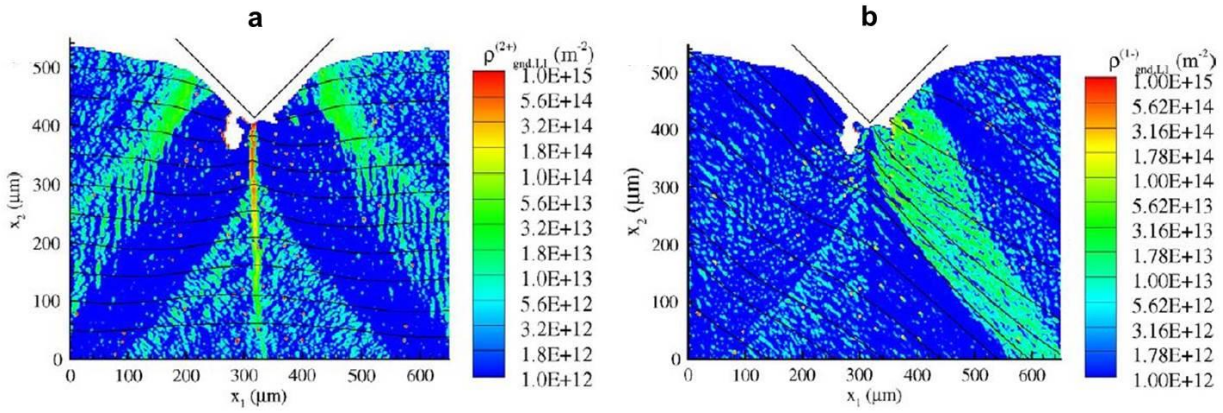

Figure 96 Geometrical dislocation density on effective plane strain on two different slip systems [358].

9.2 Determining mechanical state of stress for a crystal in polycrystalline aggregate

In order to study internal stress (strain) induced plasticity and crack initiation, it is critical to extend the investigation by considering the volumetric effects (grains interaction). In this regard, x-ray [19, 184, 359] and neutron diffraction [360, 361] have been suggested to study polycrystalline aggregates, in particular to measure in situ lattice strain during mechanical loading. Although neutron diffraction benefits from its larger penetration depth, the great interest in using high-energy synchrotron X-rays is motivated by the capability to simultaneously examine many families of crystal planes orientated in various directions. In this way, the 3-D mechanical response of a polycrystalline aggregate can be measured. For example, Figure 97 exhibits average lattice strain for several macroscopic stress values of thin (0.5mm) iron-copper, axially strained beyond their respective macroscopic yield strengths using a mechanical loading frame. The loading was stopped at different points to conduct diffraction experiments. Specifically, Figure 97 displays lattice strain pole figures for Fe and Cu both phases in different

level of stress. From the diagram, it is apparent that the strain development along loading direction for all $\{hkl\}$'s generally evolves to compression for scattering vectors near the transverse and normal directions. Such observations are important for developing a deeper understanding of the spatial relationship between grains as an individual and aggregate.

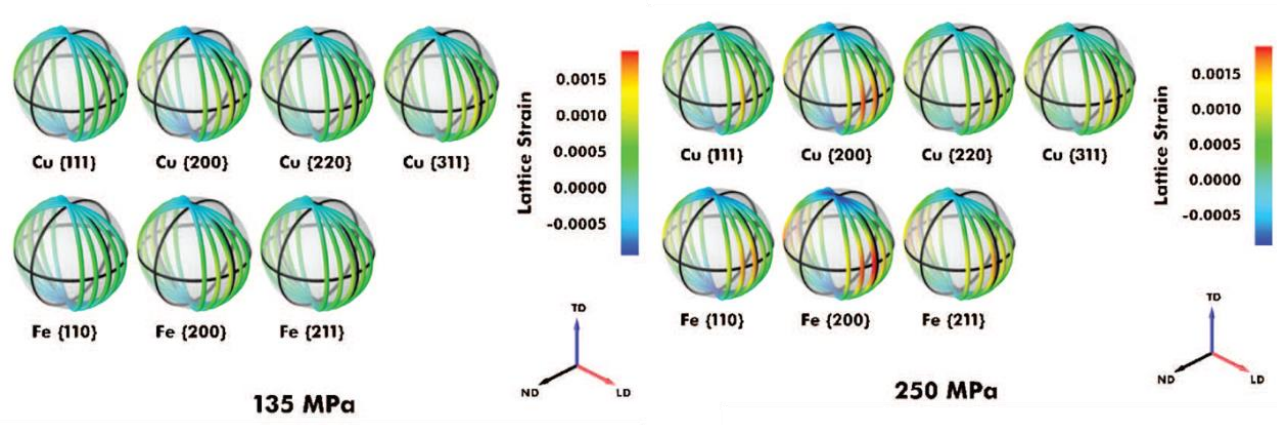

Figure 97 Lattice strain pole figures for Cu and Fe elements [19].

A better understanding of the multi scale micromechanical response of metallic alloys can be obtained by quantifying the underlying deformation mechanisms and monitoring the distortion of the crystalline aggregates under load. More importantly, the history of twinning, plastic slip and lattice strain data can be used to motivate and validate predictive material response models. Together, high fidelity lattice strain and simulation data can be employed to develop a deeper understanding of behaviors such as multiphase elastic-plastic deformation and eventually processes such as microcrack initiation.

References

1. Kojima Y: **Platform science and technology for advanced magnesium alloys**. In: *Materials Science Forum: 2000*. Trans Tech Publ: 3-18.

2. Avedesian MM, Baker H: **ASM specialty handbook: magnesium and magnesium alloys**. *ASM international* 1999, **274**.

3. Mutua JM: **Use of magnesium alloys in optimizing the weight of automobile: Current trends and opportunities**. *Sustainable Research and Innovation Proceedings* 2011, **3**.

4. Mukai T, Yamanoi M, Watanabe H, Higashi K: **Ductility enhancement in AZ31 magnesium alloy by controlling its grain structure**. *Scripta Materialia* 2001, **45**(1):89-94.

5. Kleiner M, Geiger M, Klaus A: **Manufacturing of lightweight components by metal forming**. *CIRP Annals-Manufacturing Technology* 2003, **52**(2):521-542.

6. Shadanbaz S, Dias GJ: **Calcium phosphate coatings on magnesium alloys for biomedical applications: A review**. *Acta Biomaterialia* 2012, **8**(1):20-30.

7. Witte F, Kaese V, Haferkamp H, Switzer E, Meyer-Lindenberg A, Wirth CJ, Windhagen H: **In vivo corrosion of four magnesium alloys and the associated bone response**. *Biomaterials* 2005, **26**(17):3557-3563.

8. Hakamada M, Furuta T, Chino Y, Chen Y, Kusuda H, Mabuchi M: **Life cycle inventory study on magnesium alloy substitution in vehicles**. *Energy* 2007, **32**(8):1352-1360.

9. Jensen DJ, Hansen N, Humphreys F: **Texture development during recrystallization of aluminium containing large particles**. *Acta Metallurgica* 1985, **33**(12):2155-2162.

10. Watanabe H, Mukai T, Ishikawa K: **Effect of temperature of differential speed rolling on room temperature mechanical properties and texture in an AZ31 magnesium alloy**. *Journal of Materials Processing Technology* 2007, **182**(1):644-647.

11. Adams BL, Henrie A, Henrie B, Lyon M, Kalidindi SR, Garmestani H: **Microstructure-sensitive design of a compliant beam**. *Journal of the Mechanics and Physics of Solids* 2001, **49**(8):1639-1663.

12. McDowell DL: **Simulation-based strategies for microstructure-sensitive fatigue modeling**. *Materials Science and Engineering: A* 2007, **468**:4-14.

13. Shan Z, Gokhale AM: **Digital image analysis and microstructure modeling tools for microstructure sensitive design of materials**. *International Journal of Plasticity* 2004, **20**(7):1347-1370.

14. Parks DM, Ahzi S: **Polycrystalline plastic deformation and texture evolution for crystals lacking five independent slip systems**. *Journal of the Mechanics and Physics of Solids* 1990, **38**(5):701-724.

15. Mughrabi: **On the life-controlling microstructural fatigue mechanisms in ductile metals and alloys in the gigacycle regime**. *Fatigue & Fracture of Engineering Materials & Structures* 1999, **22**(7):633-641.

16. Sha J, Hirai H, Tabaru T, Kitahara A, Ueno H, Hanada S: **High-temperature strength and room-temperature toughness of Nb–W–Si–B alloys prepared by arc-melting**. *Materials Science and Engineering: A* 2004, **364**(1–2):151-158.

17. Roberts T, Talebzadeh M: **Acoustic emission monitoring of fatigue crack propagation**. *Journal of Constructional Steel Research* 2003, **59**(6):695-712.

18. Muránsky O, Barnett M, Carr D, Vogel S, Oliver E: **Investigation of deformation twinning in a fine-grained and coarse-grained ZM20 Mg alloy: Combined< i> in situ</i> neutron diffraction and acoustic emission**. *Acta Materialia* 2010, **58**(5):1503-1517.

19. Miller M, Bernier J, Park J-S, Kazimirov A: **Experimental measurement of lattice strain pole figures using synchrotron x rays**. *Review of scientific instruments* 2005, **76**(11):113903-113903-113911.

20. Syed B, Geng J, Mishra R, Kumar K: **[0001] Compression Response at Room Temperature of Single Crystal Magnesium**. *Scripta Materialia* 2012.

21. Ando S, Tonda H: **Non-basal slip in magnesium-lithium alloy single crystals**. *Materials Transactions, JIM(Japan)* 2000, **41**(9):1188-1191.

22. Ye J, Mishra RK, Sachdev AK, Minor AM: **In situ TEM compression testing of Mg and Mg–0.2 wt.% Ce single crystals**. *Scripta Materialia* 2011, **64**(3):292-295.

23. Agnew S, Tomé C, Brown D, Holden T, Vogel S: **Study of slip mechanisms in a magnesium alloy by neutron diffraction and modeling**. *Scripta Materialia* 2003, **48**(8):1003-1008.

24. Gehrmann R, Frommert MM, Gottstein G: **Texture effects on plastic deformation of magnesium**. *Materials Science and Engineering: A* 2005, **395**(1):338-349.

25. Yi SB, Davies CHJ, Brokmeier HG, Bolmaro RE, Kainer KU, Homeyer J: **Deformation and texture evolution in AZ31 magnesium alloy during uniaxial loading**. *Acta Materialia* 2006, **54**(2):549-562.

26. Atwell DL, Barnett MR, Hutchinson WB: **The effect of initial grain size and temperature on the tensile properties of magnesium alloy AZ31 sheet**. *Materials Science and Engineering: A* 2012, **549**(0):1-6.

27. Kocks U: **The relation between polycrystal deformation and single-crystal deformation**. *Metallurgical and Materials Transactions B* 1970, **1**(5):1121-1143.

28. Schmid E, Boas W: **Plasticity of crystals**. 1950.

29. Yoo M: **Slip, twinning, and fracture in hexagonal close-packed metals**. *Metallurgical and Materials Transactions A* 1981, **12**(3):409-418.

30. Barnett MR: **Twinning and the ductility of magnesium alloys: Part I: "Tension" twins**. *Materials Science and Engineering: A* 2007, **464**(1–2):1-7.

31. Barnett M: **Twinning and the ductility of magnesium alloys: Part II."Contraction" twins**. *Materials Science and Engineering: A* 2007, **464**(1):8-16.

32. Hosford WF: **Mechanical behavior of materials**: Cambridge University Press; 2010.

33. Hull D, Bacon DJ: **Introduction to dislocations**, vol. 37: Access Online via Elsevier; 2011.

34. Abbaschian R, Abbaschian L, Hill RER: **Physical metallurgy principles**: CengageBrain. com; 2009.

35. Yang Y, Wang L, Bieler T, Eisenlohr P, Crimp M: **Quantitative atomic force microscopy characterization and crystal plasticity finite element modeling of heterogeneous deformation in commercial purity titanium**. *Metallurgical and Materials Transactions A* 2011, **42**(3):636-644.

36. Thompson N, Wadsworth N, Louat N: **Xi. The origin of fatigue fracture in copper**. *Philosophical Magazine* 1956, **1**(2):113-126.

37. Mughrabi H: **Cyclic slip irreversibilities and the evolution of fatigue damage**. *Metallurgical and Materials Transactions B* 2009, **40**(4):431-453.

38. Winter A: **A model for the fatigue of copper at low plastic strain amplitudes**. *Philosophical Magazine* 1974, **30**(4):719-738.

39. Suresh S: **Fatigue of materials**: Cambridge university press; 1998.

40. Man J, Vystavěl T, Weidner A, Kuběna I, Petrenec M, Kruml T, Polák J: **Study of cyclic strain localization and fatigue crack initiation using FIB technique**. *International Journal of Fatigue* 2012, **39**:44-53.

41. Zhang J, Laird C: **Cyclic saturation and fatigue fracture of tungsten monofilament-reinforced multicrystalline copper composites**. *Materials Science and Engineering: A* 2001, **314**(1–2):150-156.

42. Meyers M, Vöhringer O, Lubarda V: **The onset of twinning in metals: a constitutive description**. *Acta Materialia* 2001, **49**(19):4025-4039.

43. Venables J: **Deformation twinning in face-centred cubic metals**. *Philosophical Magazine* 1961, **6**(63):379-396.

44. Yoo M, Lee J: **Deformation twinning in hcp metals and alloys**. *Philosophical Magazine A* 1991, **63**(5):987-1000.

45. El-Danaf E, Kalidindi SR, Doherty RD: **Influence of grain size and stacking-fault energy on deformation twinning in fcc metals**. *Metallurgical and Materials Transactions A* 1999, **30**(5):1223-1233.

46. Karaman I, Sehitoglu H, Chumlyakov Y, Maier H: **The deformation of low-stacking-fault-energy austenitic steels**. *JOM* 2002, **54**(7):31-37.

47. Chen M, Ma E, Hemker KJ, Sheng H, Wang Y, Cheng X: **Deformation twinning in nanocrystalline aluminum**. *Science* 2003, **300**(5623):1275-1277.

48. Muzyk M, Pakiela Z, Kurzydlowski KJ: **Generalized stacking fault energy in magnesium alloys: Density functional theory calculations**. *Scripta Materialia* 2012, **66**(5):219-222.

49. Brown D, Agnew S, Bourke M, Holden T, Vogel S, Tomé C: **Internal strain and texture evolution during deformation twinning in magnesium**. *Materials Science and Engineering: A* 2005, **399**(1):1-12.

50. Hazeli K, Cuadra J, Vanniamparambil PA, Kontsos A: **In situ identification of twin-related bands near yielding in a magnesium alloy**. *Scripta Materialia* 2013, **68**(1):83-86.

51. Barnett MR, Nave MD, Bettles CJ: **Deformation microstructures and textures of some cold rolled Mg alloys**. *Materials Science and Engineering: A* 2004, **386**(1–2):205-211.

52. Watanabe H, Mukai T, Kohzu M, Tanabe S, Higashi K: **Effect of temperature and grain size on the dominant diffusion process for superplastic flow in an AZ61 magnesium alloy**. *Acta Materialia* 1999, **47**(14):3753-3758.

53. Jain A, Duygulu O, Brown D, Tomé C, Agnew S: **Grain size effects on the tensile properties and deformation mechanisms of a magnesium alloy, AZ31B, sheet**. *Materials Science and Engineering: A* 2008, **486**(1):545-555.

54. Agnew S, Horton J, Yoo M: **Transmission electron microscopy investigation of< c+ a> dislocations in Mg and α-solid solution Mg-Li alloys**. *Metallurgical and Materials Transactions A* 2002, **33**(3):851-858.

55. Hazeli K, Sadeghi A, Pekguleryuz MO, Kontsos A: **The effect of strontium in plasticity of magnesium alloys**. *Materials Science and Engineering: A* 2013, **578**(0):383-393.

56. Jain A, Agnew SR: **Modeling the temperature dependent effect of twinning on the behavior of magnesium alloy AZ31B sheet**. *Materials Science and Engineering: A* 2007, **462**(1–2):29-36.

57. Ishikawa K, Watanabe H, Mukai T: **High strain rate deformation behavior of an AZ91 magnesium alloy at elevated temperatures**. *Materials Letters* 2005, **59**(12):1511-1515.

58. Püschl W: **Models for dislocation cross-slip in close-packed crystal structures: a critical review**. *Progress in Materials Science* 2002, **47**(4):415-461.

59. Yoshinaga H, Horiuchi R: **Deformation mechanisms in magnesium single crystals compressed in the direction parallel to hexagonal axis**. *Trans JIM* 1963, **4**:1-8.

60. Taylor GI: **Plastic strain in metals**. *J Inst Met*, 1938, **62**:307-338.

61. Cazacu O, Plunkett B, Barlat F: **Orthotropic yield criterion for hexagonal closed packed metals**. *International Journal of Plasticity* 2006, **22**(7):1171-1194.

62. Obara T, Yoshinga H, Morozumi S: **{1122}〈1123〉 Slip system in magnesium**. *Acta Metallurgica* 1973, **21**(7):845-853.

63. Yoshinaga H, Horiuchi R: **Deformation mechanisms in magnesium single crystals compressed in the direction parallel to hexagonal axis**. *Trans JIM* 1963, **4**:1.

64. Agnew SR, Duygulu Ö: **Plastic anisotropy and the role of non-basal slip in magnesium alloy AZ31B**. *International Journal of Plasticity* 2005, **21**(6):1161-1193.

65. Christian JW, Mahajan S: **Deformation twinning**. *Progress in Materials Science* 1995, **39**(1):1-157.

66. Li B, Sui M, Li B, Ma E, Mao S: **Reversible twinning in pure aluminum**. *Physical review letters* 2009, **102**(20):205504.

67. Yu Q, Qi L, Chen K, Mishra RK, Li J, Minor AM: **The nanostructured origin of deformation twinning**. *Nano letters* 2012, **12**(2):887-892.

68. Beyerlein I, Tomé C: **A probabilistic twin nucleation model for HCP polycrystalline metals**. *Proceedings of the Royal Society A: Mathematical, Physical and Engineering Science* 2010, **466**(2121):2517-2544.

69. Mendelson S: **Dislocation dissociations in hcp metals**. *Journal of Applied Physics* 2003, **41**(5):1893-1910.

70. Kleiner S, Uggowitzer P: **Mechanical anisotropy of extruded Mg–6% Al–1% Zn alloy**. *Materials Science and Engineering: A* 2004, **379**(1):258-263.

71. Jiang L, Jonas JJ, Mishra RK, Luo AA, Sachdev AK, Godet S: **Twinning and texture development in two Mg alloys subjected to loading along three different strain paths**. *Acta Materialia* 2007, **55**(11):3899-3910.

72. Park SH, Hong S-G, Lee CS: **Activation mode dependent {1 0 −1 2} twinning characteristics in a polycrystalline magnesium alloy**. *Scripta Materialia* 2010, **62**(4):202-205.

73. Hong S-G, Park SH, Lee CS: **Strain path dependence of {10− 12} twinning activity in a polycrystalline magnesium alloy**. *Scripta Materialia* 2011, **64**(2):145-148.

74. Jiang L, Jonas J, Mishra R, Luo A, Sachdev A, Godet S: **Twinning and texture development in two Mg alloys subjected to loading along three different strain paths**. *Acta Materialia* 2007, **55**(11):3899-3910.

75. Kelley EW, Hosford WF: **The plastic deformation of magnesium: technical report**. 1967.

76. Koike J, Sato Y, Ando D: **Origin of the Anomalous (1012) Twinning during Tensile Deformation of Mg Alloy Sheet**. *Materials transactions* 2008, **49**(12):2792.

77. Wang Y, Huang J: **The role of twinning and untwinning in yielding behavior in hot-extruded Mg–Al–Zn alloy**. *Acta Materialia* 2007, **55**(3):897-905.

78. Reed-Hill R, Robertson W: **Additional modes of deformation twinning in magnesium**. *Acta Metallurgica* 1957, **5**(12):717-727.

79. Yoshinaga H, Obara T, Morozumi S: **Twinning deformation in magnesium compressed along the C-axis**. *Materials Science and Engineering* 1973, **12**(5):255-264.

80. Wonsiewicz B, Backofen W: **Independent slip systems and ductility of hexagonal polycrystals**. *Transaction of Metallurgical Soc AIME* 1967, **239**:1422-1433.

81. Barnett MR, Keshavarz Z, Beer AG, Ma X: **Non-Schmid behaviour during secondary twinning in a polycrystalline magnesium alloy**. *Acta Materialia* 2008, **56**(1):5-15.

82. Ma Q, El Kadiri H, Oppedal AL, Baird JC, Horstemeyer MF, Cherkaoui M: **Twinning and double twinning upon compression of prismatic textures in an AM30 magnesium alloy**. *Scripta Materialia* 2011, **64**(9):813-816.

83. Martin É, Capolungo L, Jiang L, Jonas JJ: **Variant selection during secondary twinning in Mg–3% Al**. *Acta Materialia* 2010, **58**(11):3970-3983.

84. Chun YB, Davies CHJ: **Twinning-induced negative strain rate sensitivity in wrought Mg alloy AZ31**. *Materials Science and Engineering: A* 2011, **528**(18):5713-5722.

85. Hartt W, Reed-Hill R: **The irrational habit of second-order/1011/-/1012/twins in magnesium**. 1967.

86. Roters F, Eisenlohr P, Bieler TR, Raabe D: **Crystal plasticity finite element methods**: Wiley. com; 2010.

87. Raabe D: **Cellular automata in materials science with particular reference to recrystallization simulation**. *Annual review of materials research* 2002, **32**(1):53-76.

88. Agnew S, Yoo M, Tome C: **Application of texture simulation to understanding mechanical behavior of Mg and solid solution alloys containing Li or Y**. *Acta Materialia* 2001, **49**(20):4277-4289.

89. Choi SH, Kim D, Seong B, Rollett A: **3-D simulation of spatial stress distribution in an AZ31 Mg alloy sheet under in-plane compression**. *International Journal of Plasticity* 2011, **27**(10):1702-1720.

90. Hazeli K, Cuadra J, Vanniamparambil P, Kontsos A: **In situ Identification of Twin-related Bands near Yielding in a Magnesium Alloy**. *Scripta Materialia* 2012.

91. Kalidindi SR: **Incorporation of deformation twinning in crystal plasticity models**. *Journal of the Mechanics and Physics of Solids* 1998, **46**(2):267-290.

92. Lebensohn R, Tomé C: **A self-consistent anisotropic approach for the simulation of plastic deformation and texture development of polycrystals: application to zirconium alloys**. *Acta Metallurgica et Materialia* 1993, **41**(9):2611-2624.

93. Taylor GI, Quinney H: **The plastic distortion of metals**. *Philosophical Transactions of the Royal Society of London Series A, Containing Papers of a Mathematical or Physical Character* 1932, **230**:323-362.

94. Hutchinson J: **Bounds and self-consistent estimates for creep of polycrystalline materials**. *Proceedings of the Royal Society of London A Mathematical and Physical Sciences* 1976, **348**(1652):101-127.

95. Walde T, Riedel H: **Modeling texture evolution during hot rolling of magnesium alloy AZ31**. *Materials Science and Engineering: A* 2007, **443**(1):277-284.

96. Kulekci MK: **Magnesium and its alloys applications in automotive industry**. *The International Journal of Advanced Manufacturing Technology* 2008, **39**(9):851-865.

97. Marciniak Z, Kuczyński K: **Limit strains in the processes of stretch-forming sheet metal**. *International Journal of Mechanical Sciences* 1967, **9**(9):609-620.

98. Barsom JM, Rolfe ST: **Fracture and fatigue control in structures: Applications of fracture mechanics**, vol. 41: Astm International; 1999.

99. Przybyla C, McDowell D: **Microstructure-sensitive extreme-value probabilities of high-cycle fatigue for surface vs. subsurface crack formation in duplex Ti–6Al–4V**. *Acta Materialia* 2012, **60**(1):293-305.

100. Barnett MR: **Influence of deformation conditions and texture on the high temperature flow stress of magnesium AZ31**. *Journal of Light Metals* 2001, **1**(3):167-177.

101. Miller RK, McIntire P: **Acoustic emission testing**: American Society for Nondestructive Testing; 1987.

102. Shull PJ: **Nondestructive evaluation: theory, techniques, and applications**, vol. 142: CRC; 2002.

103. Prakash R: **Non-Destructive Testing Techniques**: New Age Science; 2009.

104. Bassim MN, Lawrence SS, Liu CD: **Detection of the onset of fatigue crack growth in rail steels using acoustic emission**. *Engineering Fracture Mechanics* 1994, **47**(2):207-214.

105. Roberts TM, Talebzadeh M: **Fatigue life prediction based on crack propagation and acoustic emission count rates**. *Journal of Constructional Steel Research* 2003, **59**(6):679-694.

106. Fang D, Berkovits A: **Fatigue design model based on damage mechanisms revealed by acoustic emission measurements**. *Journal of engineering materials and technology* 1995, **117**(2):200-208.

107. Priestley MB: **Spectral analysis and time series**. 1981.

108. Vinogradov A, Patlan V, Hashimoto S: **Spectral analysis of acoustic emission during cyclic deformation of copper single crystals**. *Philosophical Magazine A* 2001, **81**(6):1427-1446.

109. Vinogradov A, Merson D, Patlan V, Hashimoto S: **Effect of solid solution hardening and stacking fault energy on plastic flow and acoustic emission in Cu–Ge alloys**. *Materials Science and Engineering: A* 2003, **341**(1):57-73.

110. Friesel M, Carpenter SH: **Determination of the source of acoustic emission generated during the deformation of magnesium**. *Journal of acoustic emission* 1984, **3**:11-17.

111. Lu Y, Gharghouri MA, Taheri F: **Effect of texture on acoustic emission produced by slip and twinning in AZ31B magnesium alloy**. 2008.

112. Kontsos A, Loutas T, Kostopoulos V, Hazeli K, Anasori B, Barsoum MW: **Nanocrystalline Mg–MAX composites: Mechanical behavior characterization via acoustic emission monitoring**. *Acta Materialia* 2011, **59**(14):5716-5727.

113. Lu Y, Gharghouri M, Taheri F: **Effect of texture on acoustic emission produced by slip and twinning in AZ31B magnesium alloy—part II: clustering and neural network analysis**. *Nondestructive Testing and Evaluation* 2008, **23**(3):211-228.

114. Chu T, Ranson W, Sutton M: **Applications of digital-image-correlation techniques to experimental mechanics**. *Experimental mechanics* 1985, **25**(3):232-244.

115. Pan B, Qian K, Xie H, Asundi A: **Two-dimensional digital image correlation for in-plane displacement and strain measurement: a review**. *Measurement science and technology* 2009, **20**(6):062001.

116. Sutton MA, Orteu J-J, Schreier HW: **Image correlation for shape, motion and deformation measurements: basic concepts, theory and applications**: Springer; 2009.

117. Halim H, Wilkinson DS, Niewczas M: **The Portevin–Le Chatelier (PLC) effect and shear band formation in an AA5754 alloy**. *Acta Materialia* 2007, **55**(12):4151-4160.

118. Niendorf T, Dadda J, Canadinc D, Maier H, Karaman I: **Monitoring the fatigue-induced damage evolution in ultrafine-grained interstitial-free steel utilizing digital image correlation**. *Materials Science and Engineering: A* 2009, **517**(1):225-234.

119. Lagattu F, Brillaud J, Lafarie-Frenot M-C: **High strain gradient measurements by using digital image correlation technique**. *Materials characterization* 2004, **53**(1):17-28.

120. Carroll J, Clark B, Buchheit TE, Boyce B, Weinberger CR: **An Experimental Statistical Analysis of Stress Projection Factors in BCC Tantalum**. *Materials Science and Engineering: A* 2013.

121. Zhao Z, Ramesh M, Raabe D, Cuitino A, Radovitzky R: **Investigation of three-dimensional aspects of grain-scale plastic surface deformation of an aluminum oligocrystal**. *International Journal of Plasticity* 2008, **24**(12):2278-2297.

122. Carroll JD, Abuzaid W, Lambros J, Sehitoglu H: **High resolution digital image correlation measurements of strain accumulation in fatigue crack growth**. *International journal of fatigue* 2013, **57**(0):140-150.

123. Leng Y: **Materials characterization: introduction to microscopic and spectroscopic methods**: Wiley. com; 2009.

124. Sharpe Jr WN, Sharpe J, William N: **Springer handbook of experimental solid mechanics**: Springer; 2008.

125. Hull D: **Fractography: observing, measuring and interpreting fracture surface topography**: Cambridge University Press; 1999.

126. Engler O, Randle V: **Introduction to texture analysis: macrotexture, microtexture, and orientation mapping**: CRC press; 2010.

127. Schwartz AJ: **Electron backscatter diffraction in materials science**: Springer; 2009.

128. Dave S, Song X, Hofmann F, Dragnevski K, Korsunsky A: **Digital image correlation and finite element analysis of inter-and intra-granular deformation**. *Procedia Engineering* 2009, **1**(1):197-200.

129. Raabe D, Sachtleber M, Weiland H, Scheele G, Zhao Z: **Grain-scale micromechanics of polycrystal surfaces during plastic straining**. *Acta Materialia* 2003, **51**(6):1539-1560.

130. Agnew S, Horton J, Yoo M: **Transmission electron microscopy investigation of⟨ c+ a⟩ dislocations in Mg and α-solid solution Mg-Li alloys**. *Metallurgical and Materials Transactions A* 2002, **33**(3):851-858.

131. Máthis K, Nyilas K, Axt A, Dragomir-Cernatescu I, Ungár T, Lukáč P: **The evolution of non-basal dislocations as a function of deformation temperature in pure magnesium determined by X-ray diffraction**. *Acta Materialia* 2004, **52**(10):2889-2894.

132. Koike J: **Enhanced deformation mechanisms by anisotropic plasticity in polycrystalline Mg alloys at room temperature**. *Metallurgical and Materials Transactions A* 2005, **36**(7):1689-1696.

133. Stanford N, Sotoudeh K, Bate PS: **Deformation mechanisms and plastic anisotropy in magnesium alloy AZ31**. *Acta Materialia* 2011, **59**(12):4866-4874.

134. Khan AS, Pandey A, Gnäupel-Herold T, Mishra RK: **Mechanical response and texture evolution of AZ31 alloy at large strains for different strain rates and temperatures**. *International Journal of Plasticity* 2011, **27**(5):688-706.

135. Wu L, Agnew S, Brown D, Stoica G, Clausen B, Jain A, Fielden D, Liaw P: **Internal stress relaxation and load redistribution during the twinning–detwinning-dominated cyclic deformation of a wrought magnesium alloy, ZK60A**. *Acta Materialia* 2008, **56**(14):3699-3707.

136. Gharghouri M, Weatherly G, Embury J, Root J: **Study of the mechanical properties of Mg-7.7 at.% Al by in-situ neutron diffraction**. *Philosophical Magazine A* 1999, **79**(7):1671-1695.

137. Balogh L, Niezgoda S, Kanjarla A, Brown D, Clausen B, Liu W, Tomé C: **Spatially resolved in situ strain measurements from an interior twinned grain in bulk polycrystalline AZ31 alloy**. *Acta Materialia* 2013, **61**(10):3612-3620.

138. Proust G, Tomé CN, Kaschner GC: **Modeling texture, twinning and hardening evolution during deformation of hexagonal materials**. *Acta Materialia* 2007, **55**(6):2137-2148.

139. Agnew SR, Duygulu O: **A mechanistic understanding of the formability of magnesium: Examining the role of temperature on the deformation mechanisms**. In: *Materials Science Forum: 2003*. Trans Tech Publ: 177-188.

140. Clausen B, Tomé C, Brown D, Agnew S: **Reorientation and stress relaxation due to twinning: Modeling and experimental characterization for Mg**. *Acta Materialia* 2008, **56**(11):2456-2468.

141. Wang H, Wu P, Wang J, Tomé C: **A Crystal Plasticity Model for Hexagonal Close Packed (HCP) Crystals including Twinning and De-twinning Mechanisms**. *International Journal of Plasticity* 2013.

142. Wadsworth N: **The Fatigue of Metals**. Ph. D. Thesis, University of Bristol; 1955.

143. Proust G, Tomé CN, Jain A, Agnew SR: **Modeling the effect of twinning and detwinning during strain-path changes of magnesium alloy AZ31**. *International Journal of Plasticity* 2009, **25**(5):861-880.

144. Hyuk Park S, Hong S-G, Ho Lee B, Bang W, Soo Lee C: **Low-cycle fatigue characteristics of rolled Mg–3Al–1Zn alloy**. *International Journal of Fatigue* 2010, **32**(11):1835-1842.

145. Caceres C, Sumitomo T, Veidt M: **Pseudoelastic behaviour of cast magnesium AZ91 alloy under cyclic loading–unloading**. *Acta Materialia* 2003, **51**(20):6211-6218.

146. Hong S-G, Park SH, Lee CS: **Enhancing the fatigue property of rolled AZ31 magnesium alloy by controlling {10-12} twinning-detwinning characteristics**. *Journal of Materials Research* 2010, **25**(04):784-792.

147. Jordon JB, Gibson JB, Horstemeyer MF, Kadiri HE, Baird JC, Luo AA: **Effect of twinning, slip, and inclusions on the fatigue anisotropy of extrusion-textured AZ61 magnesium alloy**. *Materials Science and Engineering: A* 2011, **528**(22–23):6860-6871.

148. Jordon J, Brown H, Kadiri HE, Kistler H, Lett R, Baird J, Luo A: **Investigation of Fatigue Anisotropy in an Extruded Magnesium Alloy**. *International Journal of Fatigue* 2013, **51**:8-14.

149. Bernard JD, Jordon JB, Horstemeyer MF, Kadiri HE, Baird J, Lamb D, Luo AA: **Structure–property relations of cyclic damage in a wrought magnesium alloy**. *Scripta Materialia* 2010, **63**(7):751-756.

150. Yang F, Lv F, Yang X, Li S, Zhang Z, Wang Q: **Enhanced very high cycle fatigue performance of extruded Mg–12Gd–3Y–0.5 Zr magnesium alloy**. *Materials Science and Engineering: A* 2011, **528**(6):2231-2238.

151. Zheng S, Yu Q, Jiang Y: **An experimental study of fatigue crack propagation in extruded AZ31B magnesium alloy**. *International Journal of Fatigue* 2012.

152. Lugo M, Jordon JB, Solanki KN, Hector Jr LG, Bernard JD, Luo AA, Horstemeyer MF: **Role of different material processing methods on the fatigue behavior of an AZ31 magnesium alloy**. *International Journal of Fatigue* 2013, **52**(0):131-143.

153. Eliezer D, Aghion E, Froes FH: **Magnesium Science, Technology and Applications**. *Advanced Performance Materials* 1998, **5**:201-212.

154. Agnew SR: **Wrought Magnesium: A 21st Century Outlook**. *JOM* 2004, **56**(5):20-21.

155. Obara T, Yoshinga H, Morozumi S: **Slip system in magnesium** *Acta Metallurgica* 1973, **21**:845-853.

156. Brown DW, Agnew SR, Bourke MAM, Holden TM, Vogel SC, Tome CN: **Internal strain and texture evolution during deformation twinning in magnesium**. *Materials Science & Engineering A* 2005, **399**:1-12.

157. Gehrmann R, Frommert MM, Gottstein G: **Texture effects on plastic deformation of magnesium**. *Materials Science & Engineering A* 2005, **395**:338-349.

158. Kalidindi S, Salem AA, Doherty RD: **Role of deformation twinning on strain hardening in cubic and hexagonal polycrystalline metals**. *Advanced Engineering Materials* 2003, **5**(4):229-232.

159. Barnett BR, Keshavarz Z, Beer AG, Atwell D: **Influence of grain size on the compressive deformation of wrought Mg-3Al-1Zn**. *Acta Materialia* 2004, **52**:5093-5103.

160. Agnew SR, Duygulu O: **Plastic anisotropy and the role of non-basal slip in magnesium alloy AZ31B**. *International Journal of Plasticity* 2005, **21**:1161-1193.

161. Lou XY, Li M, Boger RK, Agnew SR, Wagoner RH: **Hardening evolution of AZ31B Mg sheet**. *International Journal of Plasticity* 2007, **23**:44–86.

162. Knezevic M, Levinson A, Harris R, Mishra RK, Doherty RD, Kalidindi SR: **Deformation twinning in AZ31: Influence on strain hardening and texture evolution**. *Acta Materialia* 2010, **58**(19):6230-6242.

163. Marya M, Hector LG, Verma R, Tong w: **Microstructural effects of AZ31 magnesium alloy on its tensile deformation and failure behaviors**. *Materials Science & Engineering A* 2006, **418**:341-356.

164. Ando D, Koike J, Sutou Y: **Relationship between deformation twinning and surface step formation in AZ31 magnesium alloys**. *Acta Materialia* 2010, **58**:4316-4324.

165. Agnew SR, Brown DW, Tome CN: **Validating a polycrystal model for the elastoplastic response of magnesium alloy AZ31 using in situ neutron diffraction**. *Acta Materialia* 2006, **54**:4841-4852.

166. Muránsky O, Carr D, Barnett MR, Oliver E, Sittner P: **Investigation of deformation mechanisms involved in the plasticity of AZ31 Mg alloy: In situ neutron diffraction and EPSC modelling**. *Materials Science & Engineering A* 2008, **496**:14-24.

167. Muránsky O, Barnett M, Carr D, Vogel S, Oliver E: **Investigation of deformation twinning in a fine-grained and coarse-grained ZM20 Mg alloy: Combined in situ neutron diffraction and acoustic emission**. *Acta Materialia* 2010, **58**(5):1503-1517.

168. Bohlen J, Chmelik F, Dobron P, Letzig D, Lukac P, Kainer KU: **Acoustic emission during tensile testing of magnesium AZ alloys**. *Journal of Alloys and Compounds* 2004, **378**:214-219.

169. Mathis K, Chmelık F, Janecek M, Hadzima B, Trojanova Z, Luka P: **Investigating deformation processes in AM60 magnesium alloy using the acoustic emission technique**. *Acta Materialia* 2006, **54**:5361–5366.

170. Bohlen J, Dobron P, Swiostek J, Letzig D, Chmelık F, Luka P, Kainer KU: **On the influence of the grain size and solute content on the AE response of magnesium alloys tested in tension and compression**. *Materials Science and Engineering A* 2007, **462**:302–306.

171. Ahn B, Nutt SR: **Strain mapping of Al-Mg alloy with multi-scale grain structure using Digital Image Correlation Method**. *Experimental mechanics* 2010, **50**:117-123.

172. Barnett MR, Nave MD, Ghaderi A: **Yield point elongation due to twinning in a magnesium alloy**. *Acta Materialia* 2012, **60**(4):1433-1443.

173. Beyerlein IJ, Capolungo L, Marshall PE, McCabe RJ, Tome CN: **Statistical analyses of deformation twinning in magnesium**. *Philosophical Magazine* 2010, **90**(16):2161-2190.

174. Kocks UF, Westlake DG: **Importance of twinning for ductility of CPH polycrystals**. *Metallurgical Society of American Institute of Mining, Metallurgical and Petroleum Engineers -- Transactions* 1967, **239**(7):1107-1109.

175. Hutchinson J: **Creep and plasticity of hexagonal polycrystals as related to single crystal slip**. *Metallurgical and Materials Transactions A* 1977, **8**(9):1465-1469.

176. Antolovich SD, Armstrong RW: **Plastic strain localization in metals: origins and consequences**. *Progress in Materials Science* 2014, **59**:1-160.

177. Rice JR: **The localization of plastic deformation**: Division of Engineering, Brown University; 1976.

178. Paul H, Morawiec A, Driver JH, Bouzy E: **On twinning and shear banding in a Cu–8at.% Al alloy plane strain compressed at 77K**. *International Journal of Plasticity* 2009, **25**(8):1588-1608.

179. Barnett M, R., Nave MD, Bettles CJ: **Deformation microstructures and textures of some cold rolled Mg alloys**. *Materials Science & Engineering A* 2004, **386**:205-211.

180. Paul H, Morawiec A, Driver JH, Bouzy E: **On twinning and shear banding in Cu-8 at.% Al alloy plane strain compressed at 77 K** *International Journal of Plasticity* 2009, **25**:1588-1608.

181. Zhang P, Watzinger B, Kong Q, Blum W: **Microstructural Evolution during Creep of the Mg-Al-Alloy AZ91hp**. *Key Engineering Materials* 1999, **171**:609-616.

182. Jin Q, Shim S-Y, Lim S-G: **Correlation of microstructural evolution and formation of basal texture in a coarse grained Mg–Al alloy during hot rolling**. *Scripta Materialia* 2006, **55**(9):843-846.

183. Nave MD, Barnett MR: **Microstructures and textures of pure magnesium deformed in plane-strain compression**. *Scripta Materialia* 2004, **51**(9):881-885.

184. Park J-S, Revesz P, Kazimirov A, Miller MP: **A methodology for measuring in situ lattice strain of bulk polycrystalline material under cyclic load**. *Review of scientific instruments* 2007, **78**(2):023910-023910-023911.

185. Kelley E, HOSFORD W: **The deformation characteristics of textured magnesium**. *TRANS MET SOC AIME* 1968, **242**(4).

186. Brown DW, Agnew SR, Bourke MAM, Holden TM, Vogel SC, Tomé CN: **Internal strain and texture evolution during deformation twinning in magnesium**. *Materials Science and Engineering: A* 2005, **399**(1–2):1-12.

187. Barnett M: **Twinning and the ductility of magnesium alloys: Part I:"Tension" twins**. *Materials Science and Engineering: A* 2007, **464**(1):1-7.

188. Tomé C, Maudlin P, Lebensohn R, Kaschner G: **Mechanical response of zirconium—I. Derivation of a polycrystal constitutive law and finite element analysis**. *Acta materialia* 2001, **49**(15):3085-3096.

189. Yoo M: **Slip, twinning, and fracture in hexagonal close-packed metals**. *Metallurgical Transactions A* 1981, **12**(3):409-418.

190. Stanford N, Barnett M: **Solute strengthening of prismatic slip, basal slip and twinning in Mg and Mg-Zn binary alloys**. *International Journal of Plasticity* 2013.

191. Kocks U, Westlake D: **The importance of twinning for the ductility of CPH polycrystals**. *AIME MET SOC TRANS* 1967, **239**(7):1107-1109.

192. Hutchinson J: **Creep and plasticity of hexagonal polycrystals as related to single crystal slip**. *Metallurgical Transactions A* 1977, **8**(9):1465-1469.

193. Ando D, Koike J, Sutou Y: **Relationship between deformation twinning and surface step formation in AZ31 magnesium alloys**. *Acta Materialia* 2010, **58**(13):4316-4324.

194. Hull D: **Twinning and fracture of single crystals of 3% silicon iron**. *Acta Metallurgica* 1960, **8**(1):11-18.

195. Yang F, Yin S, Li S, Zhang Z: **Crack initiation mechanism of extruded AZ31 magnesium alloy in the very high cycle fatigue regime**. *Materials Science and Engineering: A* 2008, **491**(1):131-136.

196. Zeng R, Han E, Ke W, Dietzel W, Kainer KU, Atrens A: **Influence of microstructure on tensile properties and fatigue crack growth in extruded magnesium alloy AM60**. *International Journal of Fatigue* 2010, **32**(2):411-419.

197. Vaidya S, Mahajan S: **Accommodation and formation of {11$\bar{2}$1} twins in Co single crystals**. *Acta Metallurgica* 1980, **28**(8):1123-1131.

198. Reed-Hill RE, Robertson WD: **The crystallographic characteristics of fracture in magnesium single crystals**. *Acta Metallurgica* 1957, **5**(12):728-737.

199. Staroselsky A, Anand L: **A constitutive model for hcp materials deforming by slip and twinning: application to magnesium alloy AZ31B**. *International Journal of Plasticity* 2003, **19**(10):1843-1864.

200. Beyerlein I, Capolungo L, Marshall P, McCabe R, Tomé C: **Statistical analyses of deformation twinning in magnesium**. *Philosophical Magazine* 2010, **90**(16):2161-2190.

201. Wu L, Jain A, Brown DW, Stoica GM, Agnew SR, Clausen B, Fielden DE, Liaw PK: **Twinning–detwinning behavior during the strain-controlled low-cycle fatigue testing of a wrought magnesium alloy, ZK60A**. *Acta Materialia* 2008, **56**(4):688-695.

202. Begum S, Chen D, Xu S, Luo AA: **Low cycle fatigue properties of an extruded AZ31 magnesium alloy**. *International journal of fatigue* 2009, **31**(4):726-735.

203. Wu L, Agnew SR, Ren Y, Brown DW, Clausen B, Stoica GM, Wenk HR, Liaw PK: **The effects of texture and extension twinning on the low-cycle fatigue behavior of a rolled magnesium alloy AZ31B**. 2010.

204. Bhattacharyya A, El-Danaf E, Kalidindi SR, Doherty RD: **Evolution of grain-scale microstructure during large strain simple compression of polycrystalline aluminum with quasi-columnar grains: OIM measurements and numerical simulations**. *International Journal of Plasticity* 2001, **17**(6):861-883.

205. Tatschl A, Kolednik O: **A new tool for the experimental characterization of micro-plasticity**. *Materials Science and Engineering: A* 2003, **339**(1):265-280.

206. Korbel A, Bochniak W: **The structure based design of metal forming operations**. *Journal of Materials Processing Technology* 1995, **53**(1–2):229-237.

207. Bach F-W, Rodman M, Rossberg A, Behrens B-A, Kurzare G: **Macroscopic damage by the formation of shear bands during the rolling and deep drawing of magnesium sheets**. *JOM* 2005, **57**(5):57-61.

208. Becker R: **Effects of strain localization on surface roughening during sheet forming**. *Acta Materialia* 1998, **46**(4):1385-1401.

209. Miguel M, Vespignani A, Zapperi S, Weiss J, Grasso J-R: **Complexity in dislocation dynamics: model**. *Materials Science and Engineering: A* 2001, **309**:324-327.

210. Barnett M, Nave M, Bettles C: **Deformation microstructures and textures of some cold rolled Mg alloys**. *Materials Science and Engineering: A* 2004, **386**(1):205-211.

211. Raabe D, Sachtleber M, Zhao Z, Roters F, Zaefferer S: **Micromechanical and macromechanical effects in grain scale polycrystal plasticity experimentation and simulation**. *Acta Materialia* 2001, **49**(17):3433-3441.

212. Abuzaid W, Sehitoglu H, Lambros J: **Plastic strain localization and fatigue micro-crack formation in Hastelloy X**. *Materials Science and Engineering: A* 2013, **561**(0):507-519.

213. Takayama Y, Szpunar JA: **Stored energy and Taylor factor relation in an Al-Mg-Mn alloy sheet worked by continuous cyclic bending**. *Materials transactions* 2004, **45**(7):2316-2325.

214. Park SH, Hong S-G, Lee JH, Lee CS: **Multiple twinning modes in rolled Mg–3Al–1Zn alloy and their selection mechanism**. *Materials Science and Engineering: A* 2012, **532**:401-406.

215. Forsyth P: **Exudation of material from slip bands at the surface of fatigued crystals of an aluminium-copper alloy**. *Nature* 1953, **171**:172-173.

216. Mott N: **A theory of the origin of fatigue cracks**. *Acta Metallurgica* 1958, **6**(3):195-197.

217. Forsyth P, Stubbington C: **A Slip-band Exudation Effect observed in Pure Aluminium**. 1955.

218. Cottrell A, Hull D: **Extrusion and intrusion by cyclic slip in copper**. *Proceedings of the Royal Society of London Series A Mathematical and Physical Sciences* 1957, **242**(1229):211-213.

219. Fukuda M, Yamaguchi K, Takakura N, Sakano Y: **Roughening phenomenon on free surface of products in sheet metal forming**. *Journal of the Japan Society for Technology of Plasticity* 1974, **15**(167):994-1002.

220. OsAKADA K, OYANE M: **On the roughening of free surface in deformation processes**. *Bulletin of JSME* 1971, **14**(68):171-177.

221. Yi S, Brokmeier H-G, Letzig D: **Microstructural evolution during the annealing of an extruded AZ31 magnesium alloy**. *Journal of Alloys and Compounds* 2010, **506**(1):364-371.

222. Hazeli K, Sadeghi A, Pekguleryuz M, Kontsos A: **Damping and Dynamic Recovery in Magnesium Alloys Containing Strontium**. *Materials Science and Engineering: A* 2013, **589**:275-279.

223. Niezgoda SR, Kanjarla AK, Beyerlein IJ, Tomé CN: **Stochastic modeling of twin nucleation in polycrystals: An application in hexagonal close-packed metals**. *International Journal of Plasticity* 2013, **56**:119-138.

224. Hosford WF, Caddell RM: **Metal forming: mechanics and metallurgy**: Cambridge University Press; 2011.

225. Moore AJW: **Twinning and accommodation kinking in zinc**. *Acta Metallurgica* 1955, **3**(2):163-169.

226. Jillson D: **An experimental survey of deformation and annealing processes in zinc**. *Trans Aime* 1950, **188**:1009.

227. Yin D, Zhang K, Wang G, Han W: **Warm deformation behavior of hot-rolled AZ31 Mg alloy**. *Materials Science and Engineering: A* 2005, **392**(1):320-325.

228. Barnett MR, Nave MD, Bettles CJ: **Deformation microstructures and textures of some cold rolled Mg alloys**. *Materials Science & Engineering A (Structural Materials: Properties, Microstructure and Processing)* 2004, **A386**(1-2):205-211.

229. Al-Maharbi M, Karaman I, Beyerlein IJ, Foley D, Hartwig KT, Kecskes LJ, Mathaudhu SN: **Microstructure, crystallographic texture, and plastic anisotropy evolution in an Mg alloy during equal channel angular extrusion processing**. *Materials Science and Engineering A* 2011, **528**(25-26):7616-7627.

230. Hasegawa S, Tsuchida Y, Yano H, Matsui M: **Evaluation of low cycle fatigue life in AZ31 magnesium alloy**. *International Journal of Fatigue* 2007, **29**:1839-1845.

231. Ishihara S, Nan Z, Goshima T: **Effect of microstructure on fatigue behavior of AZ31 magnesium alloy**. *Materials Science and Engineering A* 2007, **468-470**:214-222.

232. Wu L, Agnew SR, Brown DW, Stoica GM, Clausen B, Jain A, Fielden DE, Liaw PK: **Internal stress relaxation and load redistribution during the twinning-detwinning-dominated cyclic deformation of a wrought magnesium alloy, ZK60A**. *Acta MATERIALIA* 2008, **56**:3699-3707.

233. Wu L, Jain A, Brown DW, Stoica GM, Agnew SR, Clausen B, Fielden DE, Liaw PK: **Twinning-detwinning behavior during the strain-controlled low-cycle fatigue testing of a wrought magnesium alloy, ZK60A**. *Acta MATERIALIA* 2008(688-695).

234. Yang F, Yin SM, Li SX, Zhang ZF: **Crack initiation mechanism of extruded AZ31 magnesium alloy in the very high cycle fatigue regime**. *Materials Science and Engineering A* 2008, **491**:131-136.

235. Yin SM, Yang HJ, Li SX, Wu SD, Yang F: **Cyclic deformation behavior of as-extruded Mg-3%Al-1%Zn**. *Scripta Materialia* 2008, **58**:751-754.

236. Yin SM, Yang F, Yang XM, Wu SD, Li SX, Li GY: **The role of twinning-detwinning on fatigue fracture morphology of Mg-3%Al-1%Zn alloy**. *Materials Science and Engineering A* 2008, **494**:397-400.

237. Begum S, Chen DL, Xu S, Luo AA: **Low cycle fatigue properties of an extruded AZ31 magnesium alloy**. *International Journal of Fatigue* 2009, **31**:726-735.

238. Fan CL, Chen DL, Luo AA: **Dependence of the distribution of deformation twins on strain amplitudes in an extruded magnesium alloy after cyclic deformation**. *Materials Science and Engineering A* 2009, **519**:38-45.

239. Lv F, Yang F, Duan QQ, Luo TJ, Yang YS, Li SX, Zhang ZF: **Tensile and low-cycle fatigue properties of Mg-2.8%Al-1.1.%Zn-0.4% Mn alloy along the transverse and rolling directions**. *Scripta Materialia* 2009, **61**:887-890.

240. Matsuzuki M, Horibe M: **Analysis of fatigue damage process in magnesium alloy AZ31**. *Materials Science and Engineering A* 2009, **504**:169-174.

241. Koike J, Fujiyama N, Ando D, Sutou Y: **Roles of deformation twinning and dislocation slip in the fatigue failure mechanism of AZ31 Mg alloys**. *Scripta Materialia* 2010, **63**:747-750.

242. Lv F, Yang F, Duan QQ, Yang YS, Wu SD, Li SX, Zhang ZF: **Fatigue properties of rolled magnesium alloy (AZ31) sheet: Influence of specime orientation**. *International Journal of Fatigue* 2011, **33**:672-682.

243. Stephens RI, Fatemi A, Stephens RR, Fuchs HO: **Metal fatigue in engineering**. *John Wiley and Sons, Inc, New York* 2001.

244. Potzies C, Kainer KU: **Fatigue of Magnesium Alloys**. *Advanced Engineering Materials* 2004, **6**(5):281-289.

245. Carlson RL, Kardomateas GA: **Introduction to Fatigue in Metals and Composites**: Springer; 1995.

246. Manson S, Halford GR: **Fatigue and durability of structural materials**: ASM International (OH); 2006.

247. Ewing J, Humfrey J: **The fracture of metals under repeated alternations of stress**. *Philosophical Transactions of the Royal Society of London Series A, Containing Papers of a Mathematical or Physical Character* 1903, **200**:241-250.

248. McDowell DL, Dunne FPE: **Microstructure-sensitive computational modeling of fatigue crack formation**. *International Journal of Fatigue* 2010, **32**:1521-1542.

249. Morrison DJ, Moosbrugger JC: **Effects of grain size on cyclic plasticity and fatigue crack initiation in nickel**. *International Journal of Fatigue* 1997, **19**(93):51-59.

250. Venkataraman G, Chung Y, Mura T: **Application of minimum energy formalism in a multiple slip band model for fatigue—I. Calculation of slip band spacings**. *Acta metallurgica et materialia* 1991, **39**(11):2621-2629.

251. Zhang J, Jiang Y: **Fatigue of polycrystalline copper with different grain sizes and texture**. *International Journal of Plasticity* 2006, **22**(3):536-556.

252. Finney J, Laird C: **Strain localization in cyclic deformation of copper single crystals**. *Philosophical Magazine* 1975, **31**(2):339-366.

253. Ritchie R, Suresh S: **Some considerations on fatigue crack closure at near-threshold stress intensities due to fracture surface morphology**. *Metallurgical Transactions A* 1982, **13**(5):937-940.

254. Harvey S, Marsh P, Gerberich W: **Atomic force microscopy and modeling of fatigue crack initiation in metals**. *Acta metallurgica et materialia* 1994, **42**(10):3493-3502.

255. Chan KS: **Roles of microstructure in fatigue crack initiation**. *International Journal of Fatigue* 2010, **32**(9):1428-1447.

256. Peralta P, Choi SH, Gee J: **Experimental quantification of the plastic blunting process for stage II fatigue crack growth in one-phase metallic materials**. *International Journal of Plasticity* 2007, **23**(10–11):1763-1795.

257. Basinski Z, Pascual R, Basinski S: **Low amplitude fatigue of copper single crystals—I. The role of the surface in fatigue failure**. *Acta Metallurgica* 1983, **31**(4):591-602.

258. Tanaka K, Mura T: **A theory of fatigue crack initiation at inclusions**. *Metallurgical Transactions A* 1982, **13**(1):117-123.

259. Lou X, Li M, Boger R, Agnew S, Wagoner R: **Hardening evolution of AZ31B Mg sheet**. *International Journal of Plasticity* 2007, **23**(1):44-86.

260. Barnett M: **Influence of deformation conditions and texture on the high temperature flow stress of magnesium AZ31**. *Journal of light metals* 2001, **1**(3):167-177.

261. Llanes L, Rollett A, Laird C, Bassani J: **Effect of grain size and annealing texture on the cyclic response and the substructure evolution of polycrystalline copper**. *Acta metallurgica et materialia* 1993, **41**(9):2667-2679.

262. Le Biavant K, Pommier S, Prioul C: **Local texture and fatigue crack initiation in a Ti-6Al-4V titanium alloy**. *Fatigue & Fracture of Engineering Materials & Structures* 2002, **25**(6):527-545.

263. Park SH, Hong S-G, Bang W, Lee CS: **Effect of anisotropy on the low-cycle fatigue behavior of rolled AZ31 magnesium alloy**. *Materials Science and Engineering: A* 2010, **527**(3):417-423.

264. Karaman I, Sehitoglu H, Chumlyakov YI, Maier HJ, Kireeva I: **The effect of twinning and slip on the Bauschinger effect of Hadfield steel single crystals**. *Metallurgical and Materials Transactions A* 2001, **32**(13):695-706.

265. Partridge P: **Cyclic twinning in fatigued close-packed hexagonal metals**. *Philosophical Magazine* 1965, **12**(119):1043-1054.

266. Matsuzuki M, Horibe S: **Analysis of fatigue damage process in magnesium alloy AZ31**. *Materials Science and Engineering: A* 2009, **504**(1):169-174.

267. Lv F, Yang F, Duan Q, Yang Y, Wu S, Li S, Zhang Z: **Fatigue properties of rolled magnesium alloy (AZ31) sheet: Influence of specimen orientation**. *International Journal of Fatigue* 2011, **33**(5):672-682.

268. Lugo M, Jordon J, Solanki K, Hector Jr L, Bernard J, Luo A, Horstemeyer M: **Role of Different Material Processing Methods on the Fatigue Behavior of AZ31 Magnesium Alloy**. *International Journal of Fatigue* 2013.

269. Li D, Zbib H, Sun X, Khaleel M: **Predicting Plastic Flow and Irradiation Hardening of Iron Single Crystal with Mechanism-based Continuum Dislocation Dynamics**. *International Journal of Plasticity* 2013.

270. Wang H, Wu P, Tomé C, Wang J: **A constitutive model of twinning and detwinning for hexagonal close packed polycrystals**. *Materials Science and Engineering: A* 2012, **555**:93-98.

271. Eshelby JD: **The Determination of the Elastic Field of an Ellipsoidal Inclusion, and Related Problems**. *Proceedings of the Royal Society of London Series A, Mathematical and Physical Sciences* 1957, **241**(1226):376-396.

272. Wang H, Raeisinia B, Wu P, Agnew S, Tomé C: **Evaluation of self-consistent polycrystal plasticity models for magnesium alloy AZ31B sheet**. *International Journal of Solids and Structures* 2010, **47**(21):2905-2917.

273. Wang H, Wu Y, Wu P, Neale K: **Numerical analysis of large strain simple shear and fixed-end torsion of HCP polycrystals**. *Computers Materials and Continua* 2010, **19**(3):255.

274. Voce E: **A practical strain-hardening function**. *Metallurgia* 1955, **51**(307):219-226.

275. Ohashi T, Kawamukai M, Zbib H: **A multiscale approach for modeling scale-dependent yield stress in polycrystalline metals**. *International Journal of Plasticity* 2007, **23**(5):897-914.

276. Askari H, Young J, Field D, Kridli G, Li D, Zbib H: **A study of the hot and cold deformation of twin-roll cast magnesium alloy AZ31**. *Philosophical Magazine* 2013(ahead-of-print):1-23.

277. Robson J, Stanford N, Barnett M: **Effect of precipitate shape on slip and twinning in magnesium alloys**. *Acta MATERIALIA* 2011, **59**(5):1945-1956.

278. Jordon J, Gibson J, Horstemeyer M, Kadiri HE, Baird J, Luo A: **Effect of twinning, slip, and inclusions on the fatigue anisotropy of extrusion-textured AZ61 magnesium alloy**. *Materials Science and Engineering: A* 2011, **528**(22):6860-6871.

279. Eisenmeier G, Holzwarth B, Höppel HW, Mughrabi H: **Cyclic deformation and fatigue behaviour of the magnesium alloy AZ91**. *Materials Science and Engineering: A* 2001, **319–321**(0):578-582.

280. Yin SM, Yang HJ, Li SX, Wu SD, Yang F: **Cyclic deformation behavior of as-extruded Mg–3%Al–1%Zn**. *Scripta Materialia* 2008, **58**(9):751-754.

281. Hasegawa S, Tsuchida Y, Yano H, Matsui M: **Evaluation of low cycle fatigue life in AZ31 magnesium alloy**. *International Journal of Fatigue* 2007, **29**(9):1839-1845.

282. Wang H, Berdin C, Mazière M, Forest S, Prioul C, Parrot A, Le-Delliou P: **Portevin–Le Chatelier (PLC) instabilities and slant fracture in C–Mn steel round tensile specimens**. *Scripta Materialia* 2011, **64**(5):430-433.

283. Mughrabi H, Herz K, Stark X: **Cyclic deformation and fatigue behaviour of α-iron mono-and polycrystals**. *International Journal of Fracture* 1981, **17**(2):193-220.

284. Hazeli K, Cuadra J, Streller F, Barr CM, Carpick RW, Taheri ML, Kontsos A: **Surface and Plasticity Effects of Twinning in Magnesium Alloys**. *International Journal of Plasticity* 2014, **Submitted**.

285. Wu L, Jain A, Brown D, Stoica G, Agnew S, Clausen B, Fielden D, Liaw P: **Twinning–detwinning behavior during the strain-controlled low-cycle fatigue testing of a wrought magnesium alloy, ZK60A**. *Acta MATERIALIA* 2008, **56**(4):688-695.

286. Geng CJ, Wu BL, Du XH, Wang YD, Zhang YD, Wagner F, Esling C: **Low cycle fatigue behavior of the textured AZ31B magnesium alloy under the asymmetrical loading**. *Materials Science and Engineering: A* 2013, **560**(0):618-626.

287. Trager-Cowan C, Sweeney F, Trimby P, Day A, Gholinia A, Schmidt N-H, Parbrook P, Wilkinson A, Watson I: **Electron backscatter diffraction and electron channeling contrast imaging of tilt and dislocations in nitride thin films**. *Physical Review B* 2007, **75**(8):085301.

288. Brooks CR, Choudhury A: **Failure analysis of engineering materials**: McGraw-Hill New York; 2002.

289. Raeisinia B, Agnew SR, Akhtar A: **Incorporation of solid solution alloying effects into polycrystal modeling of Mg alloys**. *Metallurgical and Materials Transactions A* 2011, **42**(5):1418-1430.

290. Roessle ML, Fatemi A: **Strain-controlled fatigue properties of steels and some simple approximations**. *International Journal of Fatigue* 2000, **22**(6):495-511.

291. Morrow J: **Cyclic plastic strain energy and fatigue of metals**. 1965.

292. Kujawski D, Ellyin F: **A unified approach to mean stress effect on fatigue threshold conditions**. *International Journal of Fatigue* 1995, **17**(2):101-106.

293. Ellyin F, Kujawski D: **A multiaxial fatigue criterion including mean-stress effect**. *ASTM SPECIAL TECHNICAL PUBLICATION* 1993, **1191**:55-55.

294. Hirsch J, Al-Samman T: **Superior light metals by texture engineering: Optimized aluminum and magnesium alloys for automotive applications**. *Acta Materialia* 2013, **61**(3):818-843.

295. Ashby MF, Jones DRH: **Engineering Materials 2: An Introduction to Microstructures and Processing**. Kidlington, Oxford: Butterworth-Heinemann; 2012.

296. Musfirah A, Jaharah A: **Magnesium and Aluminum Alloys in Automotive Industry**. *Journal of Applied Sciences Research* 2012, **8**(9):4865-4875.

297. Giribaskar S, Suresh K, Suwas S: **Evolution of Microstructure and Crystallographic Texture in AA2014 Aluminium Alloy during Equal Channel Angular Extrusion**. In: *Materials Science Forum: 2012*. Trans Tech Publ: 97-100.

298. Moy CKS, Weiss M, Xia J, Sha G, Ringer SP, Ranzi G: **Influence of heat treatment on the microstructure, texture and formability of 2024 aluminium alloy**. *Materials Science and Engineering: A* 2012, **552**(0):48-60.

299. Hazeli K, Sadeghi A, Pekguleryuz MO, Kontsos A: **The effect of Strontium in Plasticity of Magnesium alloys**. *Material Science and Engineering A* 2013, **578**:383-389.

300. Agnew S, Mehrotra P, Lillo T, Stoica G, Liaw P: **Texture evolution of five wrought magnesium alloys during route A equal channel angular extrusion: Experiments and simulations**. *Acta Materialia* 2005, **53**(11):3135-3146.

301. Miller W, Zhuang L, Bottema J, Wittebrood AJ, De Smet P, Haszler A, Vieregge A: **Recent development in aluminium alloys for the automotive industry**. *Materials Science and Engineering: A* 2000, **280**(1):37-49.

302. Tmukai M, Y, Watanabe H, Highashi K: **Ductility enhancement in AZ31 magnesium alloy by controlling its grain structure [J]**. *Scripta Materialia* 2001, **45**(1):89-94.

303. Bohlen J, Nürnberg MR, Senn JW, Letzig D, Agnew SR: **The texture and anisotropy of magnesium–zinc–rare earth alloy sheets**. *Acta Materialia* 2007, **55**(6):2101-2112.

304. Pettersen G, Westengen H, Høier R, Lohne O: **Microstructure of a pressure die cast magnesium—4wt.% aluminium alloy modified with rare earth additions**. *Materials Science and Engineering: A* 1996, **207**(1):115-120.

305. Baril E, Labelle P, Pekguleryuz M: **Elevated temperature Mg-Al-Sr: creep resistance, mechanical properties, and microstructure**. *JOM Journal of the Minerals, Metals and Materials Society* 2003, **55**(11):34-39.

306. Baril E, Labelle P, Pekguleryuz MO: **Elevated Temperature Mg-Al-Sr : Creep Resistance , Mechanical Properties , and Microstructure**. 2003(November).

307. King H: **Solid solution and intermetallic phases containing strontium**. In*: 1973*. 213.

308. Koubichek L: **Effect of small additions of elements on grain size and the refinement of the mg4al3 [mg17al12] phase in ml5 alloy**. *Metallurgy of Non-Ferrous Metals* 1959, **6**.

309. Pekguleryuz MO, Kaya AA: **Magnesium diecasting alloys for high temperature applications**. *Magnesium Technology* 2004, **TMS Annual Meeting,Symposium on Magnesium Technology, Charlotte, NC**:281-287.

310. Pekguleryuz M, Celikin M: **Creep resistance in magnesium alloys**. *International Materials Reviews* 2010, **55**(4):197-217.

311. Pekguleryuz M, Celikin M, Hoseini M, Becerra A, Mackenzie L: **Study on edge cracking and texture evolution during 150°C rolling of magnesium alloys: The effects of axial ratio and grain size**. *Journal of Alloys and Compounds* 2012, **510**(1):15-25.

312. Zeng X, Wang Y, Ding W, Luo AA, Sachdev AK: **Effect of strontium on the microstructure, mechanical properties, and fracture behavior of AZ31 magnesium alloy**. *Metallurgical and Materials Transactions A* 2006, **37**(4):1333-1341.

313. Pekguleryuz MO, Kaya AA: **Magnesium Diecasting Alloys for High Temperature Applications**. 2004.

314. Sadeghi A, Pekguleryuz M: **Recrystallization and texture evolution of Mg–3%Al–1%Zn–(0.4–0.8)%Sr alloys during extrusion**. *Materials Science and Engineering: A* 2011, **528**(3):1678-1685.

315. Sadeghi A, Hoseini M, Pekguleryuz M: **Effect of Sr addition on texture evolution of Mg–3Al–1Zn (AZ31) alloy during extrusion**. *Materials Science and Engineering: A* 2011, **528**(7–8):3096-3104.

316. Sadeghi A, Shook S, Pekguleryuz M: **Yield asymmetry and fracture behavior of Mg–3%Al–1%Zn–(0–1)%Sr alloys extruded at elevated temperatures**. *Materials Science and Engineering: A* 2011, **528**(25-26):7529-7536.

317. Humphreys FJ, Hatherly M: **Recrystallization and related annealing phenomena**: Pergamon press; 2004.

318. Rovera DM: **Solid solution strengthening in concentrated Mg ± Al alloys**. 2001, **1**:151-156.

319. Raynor GV: **The physical metallurgy of magnesium and its alloys**, vol. 5: Pergamon; 1959.

320. Park J, Chang YW: **The Effect of Alloying Elements on the c/a Ratio of Magnesium Binary Alloys**. *Advanced Materials Research* 2007, **26**:95-98.

321. Shahzad M, Wagner L: **Influence of extrusion parameters on microstructure and texture developments, and their effects on mechanical properties of the magnesium alloy AZ80**. *Materials Science and Engineering: A* 2009, **506**(1-2):141-147.

322. Sadeghi A, Pekguleryuz M: **Microstructure, mechanical properties and texture evolution of AZ31 alloy containing trace levels of strontium**. *Materials characterization* 2011, **62**(8):742-750.

323. Dargusch MS, Zhu SM, Nie JF, Dunlop GL: **Microstructural analysis of the improved creep resistance of a die-cast magnesium–aluminium–rare earth alloy by strontium additions**. *Scripta Materialia* 2009, **60**(2):116-119.

324. Zhao P, Wang QD, Zhai CQ, Zhu YP: **Effects of strontium and titanium on the microstructure, tensile properties and creep behavior of AM50 alloys**. *Mat Sci Eng a-Struct* 2007, **444**(1-2):318-326.

325. Sadeghi A, Pekguleryuz M: **Microstructural investigation and thermodynamic calculations on the precipitation of Mg–Al–Zn–Sr alloys**. *Journal of Materials Research* 2011, **26**(07):896-903.

326. Sadeghi A, Pekguleryuz M: **Effect of pre-deformation anneal on the microstructure and texture evolution of Mg–3Al–1Zn–0.7Sr alloy during hot extrusion**. *Journal of Materials Science* 2012, **47**(14):5374-5384.

327. Hazeli K, Cuadra J, Vanniamparambil PA, Kontsos A: **In situ identification of twin-related bands near yielding in a magnesium alloy**. *Scripta Materialia* 2012(0).

328. Obara T, Yoshinga H, Morozumi S: **{11$\bar{2}$2}< 1123> Slip system in magnesium**. *Acta Metallurgica* 1973, **21**(7):845-853.

329. Yoshinaga H, Horiuchï R: **On the nonbasal slip in magnesium crystals**. *Transactions of the Japan Institute of Metals* 1963, **5**:14-21.

330. Akhtar A, Teghtsoonian E: **Solid solution strengthening of magnesium single crystals—ii the effect of solute on the ease of prismatic slip**. *Acta Metallurgica* 1969, **17**(11):1351-1356.

331. Reed-Hill RE, Abbaschian R: **Physical metallurgy principles**. 1973.

332. Máthis K, Chmelik F, Janeček M, Hadzima B, Trojanová Z, Lukáč P: **Investigating deformation processes in AM60 magnesium alloy using the acoustic emission technique**. *Acta Materialia* 2006, **54**(20):5361-5366.

333. Agnew SR, Tomé CN, Brown DW, Holden TM, Vogel SC: **Study of slip mechanisms in a magnesium alloy by neutron diffraction and modeling**. *Scripta Materialia* 2003, **48**(8):1003-1008.

334. Cizek P, Barnett M: **Characteristics of the contraction twins formed close to the fracture surface in Mg–3Al–1Zn alloy deformed in tension**. *Scripta Materialia* 2008, **59**(9):959-962.

335. Bohlen J, Dobron P, Meza Garcia E, Chmelík F, Lukáč P, Letzig D, Kainer KU: **The effect of grain size on the deformation behaviour of magnesium alloys investigated by the acoustic emission technique**. *Advanced Engineering Materials* 2006, **8**(5):422-427.

336. Cáceres CH, Rovera DM: **Solid solution strengthening in concentrated Mg–Al alloys**. *Journal of Light Metals* 2001, **1**(3):151-156.

337. Barnett M, Keshavarz Z, Beer A, Atwell D: **Influence of grain size on the compressive deformation of wrought Mg–3Al–1Zn**. *Acta Materialia* 2004, **52**(17):5093-5103.

338. Boehlert C, Chen Z, Gutiérrez-Urrutia I, Llorca J, Pérez-Prado M: **< i> In situ</i> analysis of the tensile and tensile-creep deformation mechanisms in rolled AZ31**. *Acta Materialia* 2012, **60**(4):1889-1904.

339. Wu W, Lee SY, Paradowska AM, Gao Y, Liaw PK: **Twinning–detwinning behavior during fatigue-crack propagation in a wrought magnesium alloy AZ31B**. *Materials Science and Engineering: A* 2012, **556**(0):278-286.

340. Hazeli K, Cuadra J, Vanniamparambil P, Kontsos A: **In situ Identification of Twin-related Bands near Yielding in a Magnesium Alloy**. *Scripta Materialia* 2013, **68**(1):83-86.

341. Vaidyanathan TK, Vaidyanathan J, Cherian Z: **Extended creep behavior of dental composites using time–temperature superposition principle**. *Dental Materials* 2003, **19**(1):46-53.

342. Sastry S, Krishna M, Uchil J: **A study on damping behaviour of aluminite particulate reinforced ZA-27 alloy metal matrix composites**. *Journal of Alloys and Compounds* 2001, **314**(1–2):268-274.

343. Srikanth N, Gupta M: **Damping characterization of Mg–SiC composites using an integrated suspended beam method and new circle-fit approach**. *Materials Research Bulletin* 2002, **37**(6):1149-1162.

344. Menard KP: **Dynamic mechanical analysis: a practical introduction**. Broken Sound Parkway NW: CRC PressI Llc; 2008.

345. Elomari S, Boukhili R, Skibo M, Masounave J: **Dynamic mechanical analysis of prestrained Al2O3/Al metal-matrix composite**. *Journal of Materials Science* 1995, **30**(12):3037-3044.

346. Goertzen WK, Kessler MR: **Dynamic mechanical analysis of carbon/epoxy composites for structural pipeline repair**. *Composites Part B: Engineering* 2007, **38**(1):1-9.

347. McQueen H, Konopleva E: **Creep and hot working of Mg alloy AZ 91**. *Magnesium Technology* 2001:227-234.

348. Myshlyaev MM, McQueen HJ, Mwembela A, Konopleva E: **Twinning, dynamic recovery and recrystallization in hot worked Mg–Al–Zn alloy**. *Materials Science and Engineering: A* 2002, **337**(1–2):121-133.

349. Mwembela A, Konopleva E, McQueen H: **Microstructural development in Mg alloy AZ31 during hot working**. *Scripta Materialia* 1997, **37**(11):1789-1795.

350. Ravi Kumar N, Blandin J, Desrayaud C, Montheillet F, Suéry M: **Grain refinement in AZ91 magnesium alloy during thermomechanical processing**. *Materials Science and Engineering: A* 2003, **359**(1):150-157.

351. Beer A, Barnett M: **Microstructural development during hot working of Mg-3Al-1Zn**. *Metallurgical and Materials Transactions A* 2007, **38**(8):1856-1867.

352. Vagarali SS, Langdon TG: **Deformation mechanisms in hcp metals at elevated temperatures—I. Creep behavior of magnesium**. *Acta Metallurgica* 1981, **29**(12):1969-1982.

353. Sadeghi A, Pekguleryuz M: **Microstructural investigation and thermodynamic calculations on the precipitation of Mg-Al-Zn-Sr alloys**. *Journal of Materials Research* 2011, **26**(7):896.

354. Sadeghi A, Pekguleryuz M: **Effect of pre-deformation anneal on the microstructure and texture evolution of Mg–3Al–1Zn–0.7 Sr alloy during hot extrusion**. *Journal of materials science* 2012, **47**(14):5374-5384.

355. Kysar JW, Briant CL: **Crack tip deformation fields in ductile single crystals**. *Acta Materialia* 2002, **50**(9):2367-2380.

356. Bahr DF, Kramer DE, Gerberich WW: **Non-linear deformation mechanisms during nanoindentation**. *Acta Materialia* 1998, **46**(10):3605-3617.

357. Zaafarani N, Raabe D, Singh RN, Roters F, Zaefferer S: **Three-dimensional investigation of the texture and microstructure below a nanoindent in a Cu single crystal using 3D EBSD and crystal plasticity finite element simulations**. *Acta Materialia* 2006, **54**(7):1863-1876.

358. Kysar J, Saito Y, Oztop M, Lee D, Huh W: **Experimental lower bounds on geometrically necessary dislocation density**. *International Journal of Plasticity* 2010, **26**(8):1097-1123.

359. Schuren J, Miller M, Kazimirov A: **A mechanical testing capability for measuring the microscale deformation behavior of structural materials**. *Experimental mechanics* 2012, **52**(5):461-479.

360. Agnew SR, Brown DW, Tomé CN: **Validating a polycrystal model for the elastoplastic response of magnesium alloy AZ31 using in situ neutron diffraction**. *Acta Materialia* 2006, **54**(18):4841-4852.

361. Muránsky O, Carr D, Barnett M, Oliver E, Šittner P: **Investigation of deformation mechanisms involved in the plasticity of AZ31 Mg alloy:< i> In situ</i> neutron diffraction and EPSC modelling**. *Materials Science and Engineering: A* 2008, **496**(1):14-24.